The feedback between basin and strait processes in the Mediterranean Sea and similar marginal seas – a process study

Stephan Matthiesen

Doctor of Philosophy

The University of Edinburgh

2001

Declaration

This thesis has been composed by myself, and all work reported herein is my own except where otherwise stated.

Acknowledgements

I would like to thank Keith Haines for the excellent opportunity to work with him, for his support and patience, and the wealth of new ideas throughout the project that often lead to new insights and inspiring discussions. Thanks also to the members of the Department of Meteorology, who created a very friendly and motivating atmosphere. Special thanks goes to the oceanographers in the Department – although only a small group, we always had interesting meetings.

I am indebted to Paul Myers for comments and discussions, and for providing the figures in section 7.7 which contribute an important aspect to this thesis. For the work on the 3-layer system in chapter 8, I enjoyed – and profited greatly from – discussions with David Smeed.

Innumerable other people have helped me with their intellectual or moral support, and only few can be mentioned here. I would particularly like to thank Ingrid Ittner, whose friendship I have enjoyed for many years. Our dust-scraping adventures in Macedonia and elsewhere will always be a source for many happy memories.

Last but not least I want to thank my parents who always supported me in everything I did. I hope that I can some day return all the good things they did for me.

This research was funded by the European Union under the *Training and Mobility of Researchers* programme through a *Marie Curie Research Training Grant*, contract number ERBFMBICT961814.

Abstract

The Strait of Gibraltar limits the exchange between the Atlantic and the Mediterranean Sea and therefore plays an important role in determining the water properties of the evaporation-dominated Mediterranean Sea. On the other hand, the strait dynamics depends on the boundary conditions set by the basin. To investigate this fundamental feedback between strait and basin processes, a 3-box model of the Mediterranean with a hydraulically controlled strait was programmed. It accommodates both maximal and submaximal strait exchange and does not impose steady state budget constraints, making it particularly useful for investigating transitional and non-equilibrium situations.
The model is used in an explorative study to find new dynamical aspects of the system. First, the response of the system to changing air-sea-fluxes is modelled. Increasing evaporation shifts the steady state of the system to a more saline and – as a secondary effect – slightly warmer state. Increased heat loss leads to a colder and slightly less saline basin. Besides shifting the steady state, changes in heat flux and net evaporation can also lead to a nonlinear response in which the pycnocline deepens considerably for a transitional period of decades or centuries before returning to its steady state depth. Second, the effect of rising sea levels since the Last Glacial Maximum (18 kyr BP) was modelled. At times of rapid sea level rise, the long residence time leads to stronger stratification and reduced circulation in the basin, providing a possible mechanism for the formation of sapropel S1.
Finally the effect of mixing in the hydraulic jump between the Mediterranean and the Strait of Gibraltar is included in the model. The entrainment of inflowing water into the outflow reduces the effective exchange between Atlantic and Mediterranean, and the system develops multiple equilibria. After a comparatively short perturbation (e. g. a 20% larger evaporation for 10 years), the system can move from the stable, well-ventilated state to an almost stagnant meta-stable state which persists for centuries before the well-ventilated state is reestablished. Under different conditions, oscillating behaviour between the two states is found. This mechanism is also found in GCM experiments, although its relevance for realistic situations remains unclear.

Contents

Chapter 1

Introduction

Although the ocean plays a crucial role in controlling climatic variations on time scales of months to centuries, we still know very little about the variability of ocean circulation due to internal dynamics and external forcing. The (Eurafrican) Mediterranean Sea (figure 1.1) can serve as a laboratory in which we can develop our understanding of ocean dynamics, as it shows many of the important physical processes that occur in the global ocean, like a thermohaline circulation with deep and intermediate water formation and passage through straits. Its topography with several sub-basins and different water formation sites makes it in principle possible that the circulation shows complex dynamical behaviour. Indeed, the geological record shows drastic changes in the circulation in the past, and recent observations also hint to changing conditions at present.

Beside being a test basin for the global ocean, the Mediterranean is of great importance as a regional climate factor. Furthermore, the saline outflow from the Mediterranean Sea forms an important water mass in the North Atlantic – the Mediterranean Overflow Water (MOW) or the Eurasian Mediterranean Water (EMW) – that may interact with the global thermohaline circulation and therefore may play an important role in the global climate system.

Therefore, a good understanding of the fundamental behaviour of the Mediterranean Sea is of great interest, both for the climate history of the Mediterranean region and the stability of the global thermohaline circulation. This study aims to clarify some of the basic mechanisms that govern the Mediterranean.

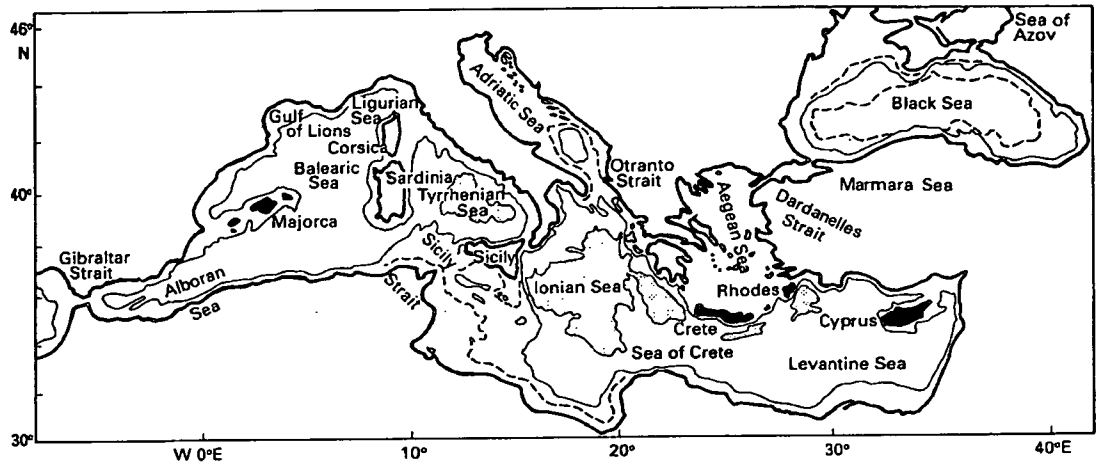

Figure 1.1: The Eurafrican Mediterranean Sea and its sub-basins (from Tomczak and Godfrey 1994)

The Mediterranean Sea is a marginal basin to the World Ocean that is connected to the Atlantic only through the narrow and shallow Strait of Gibraltar. Its area is approximately $2.4 \times 10^{12}\,\mathrm{km}^2$, and its average depth is 1500 m. It may be roughly divided by the Straits of Sicily and Messina into the Western Mediterranean with depths down to 3200 m in the Tyrrhenian Sea, and the Eastern Mediterranean, with its deepest point being a narrow trench off the Coast of Greece at 5100 m, and large parts of the Ionian Sea between 3000 m and 4200 m (Tomczak and Godfrey 1994).

Situated in a predominantly arid area, it has a freshwater deficit, as evaporative losses are not balanced by precipitation and river runoff. Modern estimates of the net evaporation $E - P$ (where P includes both precipitation and river runoff) range from from 50 cm/year to 100 cm/year averaged over the whole basin (Bryden and Kinder 1991, Bethoux 1979). However, in some sub-basins there is considerable inflow of freshwater from humid regions, e. g. through the Nile and Po rivers as well as the Black Sea and the Dardanelles Strait. In this thesis, generally a value of 75 cm/year is used. The heat budget is also negative with a net heat loss to the atmosphere of approximately $7\,\mathrm{W/m}^2$ averaged over the basin.

Typical for a marginal sea under arid conditions, the main overall circulation is a thermohaline anti-estuarine or lagoonal circulation (see figure 1.2), with comparatively fresh water of approximately 36 psu flowing in at the surface through the Strait of Gibraltar, and saltier (ca. 38 psu) intermediate and deep water flowing out at greater

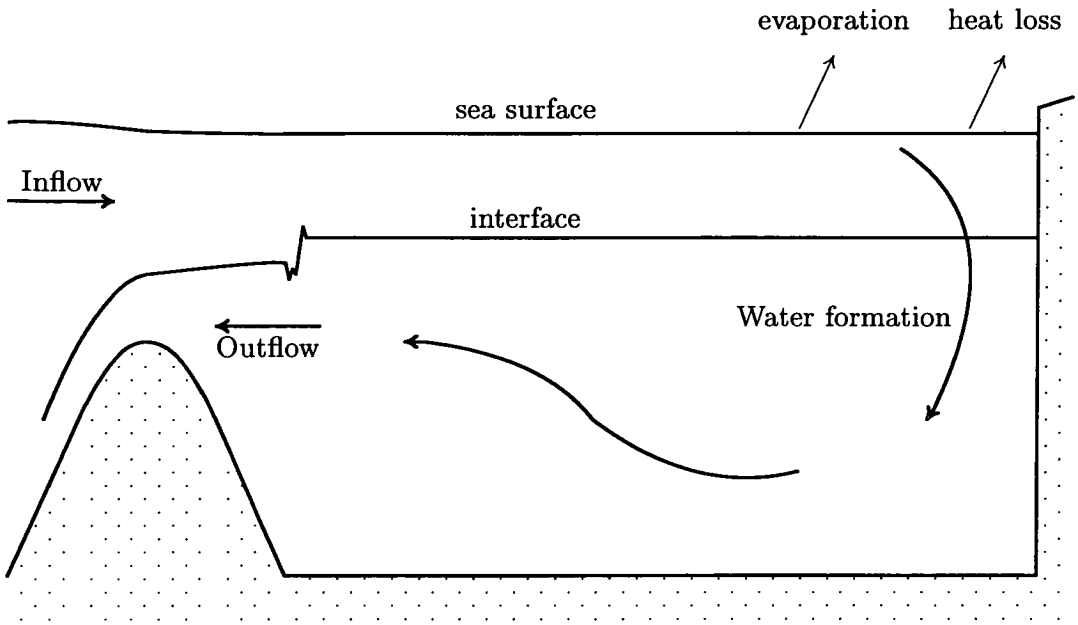

Figure 1.2: The Mediterranean shows an anti-estuarine or lagoonal thermohaline circulation, in which inflowing surface water is transformed into intermediate and deep water and subsequently flows out through the Strait.

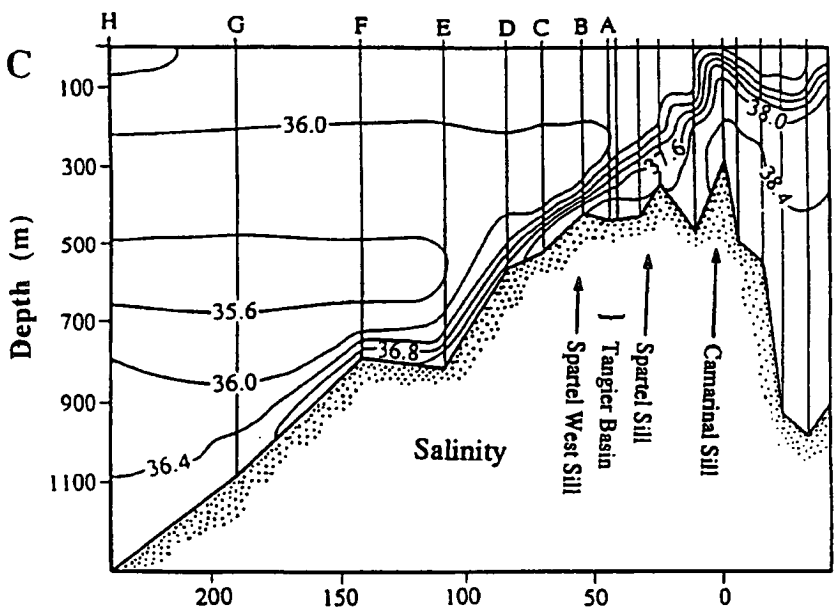

Figure 1.3: Observed salinity along the Strait of Gibraltar, showing the outflow of denser Mediterranean Overflow Water (MOW) (from Baringer and Price 1997).

depth, so that the Strait of Gibraltar shows a 2-layer exchange (1.3). The outflowing water sinks to approximately 1000 m in the Atlantic, where it forms a distinct water mass, the so-called Mediterranean Overflow Water (MOW) or Eurasian Mediterranean Water (EMW) (Tomczak and Godfrey 1994).

The amount of MOW may have significant effects on the circulation in the North Atlantic and the global circulation. The inflow of highly saline water into the North Atlantic makes the North Atlantic saltier than the Pacific and facilitates the formation of North Atlantic Deep Water (NADW) in the Norwegian Sea, which is a driving force of the global thermohaline circulation (Reid 1979). On the other hand, it has been suggested that an increase in the Mediterranean outflow due to the damming of river systems and global warming may lead to a stronger stratification in the North Atlantic, inhibiting the deep water formation in the Norwegian Sea and thus leading to a collapse in the global thermohaline circulation, but this is still very controversial[1] (Rahmstorf 1998).

Inside the basin, intermediate water is predominantly formed during winter in the Levantine Sea and therefore called Levantine Intermediate Water (LIW). In the Adriatic or Aegean Sea, deep water is formed and fills the Eastern Mediterranean as Eastern Mediterranean Deep Water (EMDW), while Western Mediterranean Deep Water (WMDW) is predominantly formed in the Gulf of Lyons.

The Strait of Gibraltar, being the only significant connection to the world ocean, plays an important role in determining the water properties of the Mediterranean. The Strait of Gibraltar (see figure 1.4) has a narrows of 12 km at Tarifa, and a shallow sill – the Camarinal Sill – with a depth of 284 m further to the west. Its limited size restricts the water exchange with the global ocean, making the Mediterranean saltier than the global ocean. On the other hand, in the long term, the water, salt and heat transports through the strait also have to balance the equivalent air-sea-fluxes over the basin. It has been noted decades ago by Stommel and Farmer (1953) that these constraints allow a minimal salinity difference between inflow and outflow to be calculated for the steady state. In other words, the water properties of the Mediterranean can be said to

[1]Nonetheless, this prospect has prompted Johnson (1997) to suggest somewhat provocatively to build a huge dam at Gibraltar to reduce the outflow of MOW.

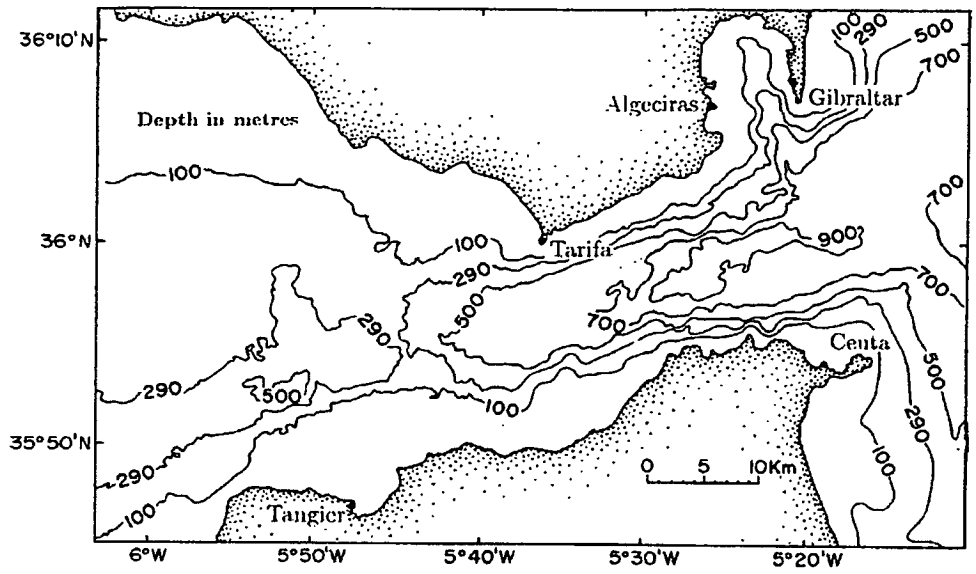

Figure 1.4: Bathymetry of the Strait of Gibraltar (from Garrett et al. 1990)

be *controlled* by the Strait, as the actual salinity difference must be larger than this minimum.

Therefore, the dynamics of sea straits with a 2-layer exchange (figure 1.5) has received some attention, and the fluid dynamics of systems of this type has been investigated by many researchers (see chapter 2 for details). These studies allow the calculation of the transport in the two layers as a function of the boundary conditions in the connected reservoirs, and confirm that – for a given density difference between the layers and a net transport specified by the evaporation over the basin – there is maximal possible exchange transport through the strait. These fluid dynamical studies have generally focussed on the strait, and regarded the basin primarily as a reservoir which determines the boundary conditions for the strait dynamics.

However, while budget studies see the strait as controlling the basin, and fluid dynamical studies assume that the basin only determines the boundary conditions of the strait dynamics, little attention has been directed to the fact that there is a feedback between the strait and the basin, which may lead to interesting dynamical behaviour. In particular, the budget considerations are only valid in the steady state, but are unable to predict transitional states.

This thesis therefore tries to focus on the feedback between the strait dynamics and

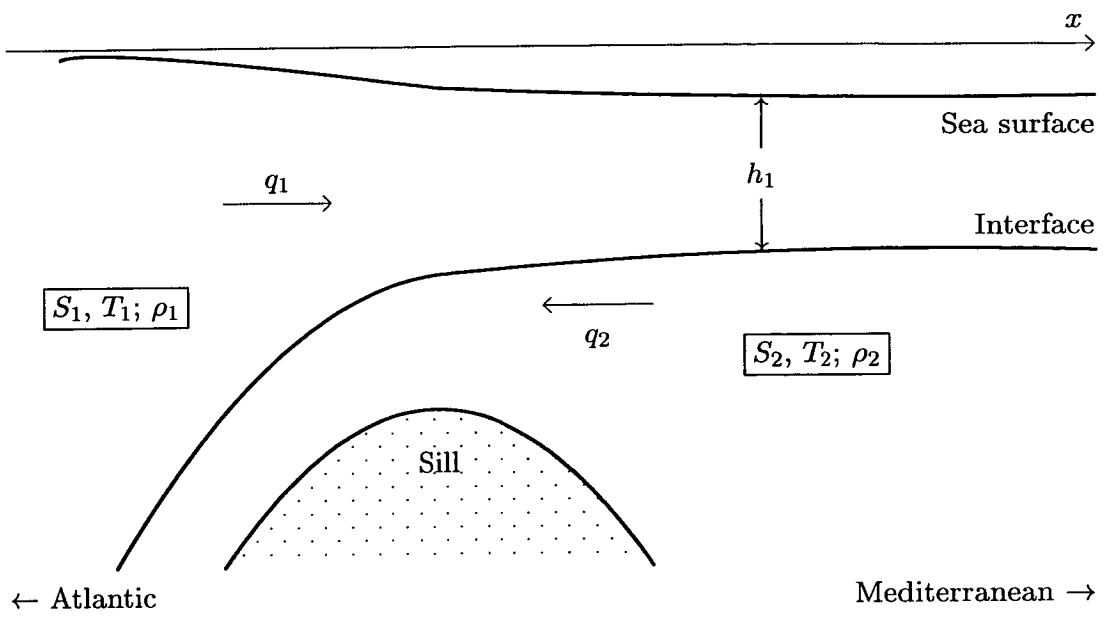

Figure 1.5: Two layer exchange.

the basin properties. For most of this study, a box model of the Mediterranean was used. This model was given the name HYCOBOX and reflects the basic feedback through its combination of a hydraulically controlled strait with a simple 3-box representation of the Mediterranean basin. Although other researchers, e. g. Tziperman and Speer (1994), have used box models with an unresponsive strait, this is – to the best of our knowledge – the first model that couples a box model to a strait with full hydraulics that allows both maximal and submaximal situations. The model does not impose any budget constraints on the system other than the fundamental conservation laws, and the volume of all boxes and the sea surface are allowed to change freely.

Simple models like HYCOBOX can complement the use of more detailed General Circulation Models (GCMs). In particular, while primitive equation GCMs are very good at reproducing observations in detail, they cannot easily be used to develop a physical understanding of the relevant processes. Simpler box models, on the other hand, specifically focus on a few physical mechanisms and can therefore be used to investigate their relevance for the system and their qualitative behaviour. Thus simpler models are appropriate tools for understanding both the observations and GCM results.

Simpler models are also particularly useful for the investigation of past climatic conditions, where observational data are less abundant, and more competing scenarios

are possible. Simple box models have the advantage of being able to simulate several thousands of years in only a few minutes computing time, so that it is possible to scan a large number of different scenarios and filter out inconsistent scenarios, while GCMs are so computationally expensive that such experiments would not be feasible with GCM runs.

Although all calculations in this study were performed with Mediterranean values, the results are qualitatively applicable to any basin-strait-system with an anti-estuarine circulation and a 2-layer exchange at the strait. Furthermore, it is hoped that enough information about numerical scaling arguments is given to enable readers to apply the results quantitatively to other sea straits.

The outline of this thesis is as follows. Chapter 2 summarises hydraulic control theory, i. e. the fluid dynamics of straits, and introduces and defines all the necessary quantities. Chapter 3 describes the design details of the HYCOBOX model. A particular problem for the model is the parameterisation of the water formation rate, for which no established method exists. Therefore, a number of different water formation parameterisations are implemented, so that their behaviour can be compared. Chapter 4 discusses the main feedback mechanisms that act in the strait-basin-system, and calculates the relevant timescales.

Chapter 5 uses a set of 24 HYCOBOX experiments to address the question of how the system reacts to changing air-sea-fluxes, a question relevant both for recently observed changes and for transitions from earlier climate regimes at the end of the pleistocene. For the steady state, a simple but useful equation, the SQE-equation, is derived that links the changes in salinity (S) and strait transport (q) to changes in net evaporation ($E - P$). While the steady state changes in an easily predictable way, the transitional states can develop complex behaviour. An important result of the experiments is the fact that relatively small changes in air-sea-fluxes may not only lead to a simple shift of the steady state, but push the system into a transitional phase for several centuries during which the circulation is significantly different from both the initial and the final steady state.

As a case study, the transition from the Last Glacial Maximum (LGM) 18000 years ago to the present day is investigated in chapter 6. Of particular interest is a time

in the early holocene (9600 – 6400 BP)[2], during which the presence of sapropels, i. e. dark carbon rich sediments, may indicate a collapse in the Mediterranean circulation. HYCOBOX is used to investigate possible mechanisms. The opening of the Black Sea may have lead to an additional input of fresh water and thus increased the stratification – and at least in one scenario the transitional effects discussed in the previous chapter are again relevant –, but the timing of the event is not without problems. Therefore, a new mechanism is also proposed, which has – to the best of our knowledge – not received attention before: During times of rapid sea level rise, the inflow of fresher Atlantic water increased, whereas the salinity in the basin may have considerably lagged behind, leading to a stronger stratification in the basin. The size of this effect is estimated and shown to be of similar importance to the Black Sea opening – with the added advantage that the sapropels date to a period after an important meltwater peak, but possibly before the opening of the Black Sea.

The subsequent chapter 7 introduces a speculative idea into the feedback system. When the exchange in the strait is maximal, the connection to the basin is not smooth, but a hydraulic jump (or smoother hydraulic transition) occurs. As this is a turbulent process, we introduce the idea that the hydraulic jump leads to entrainment of inflowing water into the outflow, thus reducing the effective net exchange with the basin. This modification introduces an additional feedback mechanism into the system. The system now develops multiple states or even oscillatory behaviour. By a comparatively small event, e. g. an increase in evaporation by 20% for 10 years, the system can jump into a meta-stable state that persists for times of the order of centuries before decaying back into the original state. While this is an intriguing idea, its validity can only be established with future laboratory experiments or observations, but it is argued that similar mechanisms do occur in GCM experiments and should therefore be taken seriously.

Finally, chapter 8 leaves the Mediterranean Sea and provides an insight into the Red Sea. The Red Sea system is not unlike the Mediterranean, with an evaporative basin connected to the Gulf of Aden by the shallow Strait of Bab al Mandab. However, while the circulation is simply anti-estuarine in winter, in summer the monsoon leads

[2]BP: radiocarbon age before present, see chapter 6.

to upwelling of Gulf of Aden Intermediate Water (GAIW), which forms a third layer in the strait, and at the same time the surface flow reverses direction. Therefore, the HYCOBOX model has to be modified considerably to accommodate the switch between a 2-layer and a three-layer exchange. In this chapter, the theory of three layer exchange is outlined, and previous work by Smeed (2000) supplemented by the consideration of a free surface, a necessary requirement if a box model similar to the Mediterranean HYCOBOX is to be built. Unfortunately, the actual implementation of the full model is at present only a promising outlook to the future.

Chapter 2

Hydraulic control theory

Overall, the Mediterranean shows an anti-estuarine circulation with comparatively fresh Atlantic surface water entering through the Strait of Gibraltar, which is then converted into more saline intermediate and deep water inside the Mediterranean, and subsequently flows out through the Strait of Gibraltar. The Strait of Gibraltar therefore essentially exhibits a 2-layer exchange flow.

This chapter describes the basic features of a nonrotating, frictionless exchange flow with two uniform layers and develops the mathematical framework necessary for the model used in this study. Although the basin determines the boundary conditions for the strait dynamics, the discussion of the feedback between strait and basin will be kept separate and will be dealt with in the following chapters. The chapter starts with a short qualitative overview of the physical properties of a 2-layer exchange in sea straits. Following a summary of previous work on 2-layer exchange, the mathematical framework is then developed and the main features of the solution discussed. While the description of 2-layer systems is an interesting mathematical problem in its own right, it is also important to establish whether the nonrotating, frictionless 2-layer description is an appropriate approximation to the actual exchange in sea straits like the Strait of Gibraltar. The last sections of this chapter therefore discuss the influence of friction and rotation and try to summarise observational studies in the Strait of Gibraltar.

2.1 Qualitative features of a 2-layer exchange flows

Before describing the mathematical framework for 2-layer exchange flows, it is useful to list the relevant physical mechanisms in the strait. We assume a situation in which the strait connects two basins which are stratified with a layer of less dense water overlying a layer of denser water. Both layers are assumed to be of uniform density with no friction at the interface, and rotational effects in the strait are neglected[1]. The strait is characterised by a sill and/or narrows which restrict the exchange between the two basins. Such a point is called a (geometric) *control*. The flow in the strait is driven by the difference in sea level and interface depth between the basins, so that the flow rates are determined by the available potential energy in the basin and the kinetic energy of the flow in the strait. Therefore the following factors have to be taken into account:

Strait geometry: In general, a smaller cross-section will reduce the flow. However, the precise relation between all aspects of strait geometry and flow is a nontrivial problem.

Sea level and interface depth: These factors play a double role:

1. The differences in sea surface height and interface depth between basin and Atlantic determine the available potential energy.
2. Sea level and interface depth in the adjacent basins determine the layer thicknesses in the strait. The thickness of each layer in the strait, i. e. the cross-section of each layer, then determines the kinetic energy for the flows. Obviously this factor means that for both very high and very low interface depth the exchange will be low, so that the maximal exchange will be reached for some intermediate interface depth.

Density difference: The available potential energy increases with the density difference between the two layers, therefore a higher density difference will lead to stronger exchange flow.

[1] Whether these simplifications are appropriate for the Strait of Gibraltar will be discussed in section 2.5.

These considerations are the basis for hydraulic control theory, whose mathematical framework and detailed results are outlined below. For the convenience of the reader, all symbols that are used in the text are also listed and explained alphabetically in appendix A.

2.2 A very short history of hydraulic control

Hydraulic control has been used in a number of studies as a simple means of estimating water properties in different systems. One of the earliest studies is Stommel's and Farmer's work on the processes that determine the salinity of an estuary (Stommel and Farmer 1953). For a basin with anti-estuarine circulation, Bryden and Stommel (1984) used a strait with rectangular cross-section of width W_s with a sill of depth D and combined the dynamic equations in the strait with budget considerations for the basin to calculate constraints on the properties of Mediterranean water. They suggested that — for a negligible net transport $Q = q_1 + q_2 \approx 0$ (where $q_1 > 0$ and $q_2 < 0$ are the transports in the upper and lower layer respectively) — the total transport $q = q_1 - q_2$ reaches a maximum when the interface between the layers h_{1s} is at half sill depth

$$h_{1s} = 0.5D \tag{2.1}$$

$$q = 0.5\sqrt{g'D}DW_s \tag{2.2}$$

where g' is the reduced gravity.

Assuming that the salt budget is balanced, this maximal exchange can only be reached when the salinity difference $S_2 - S_1$ between inflowing and outflowing water is at its minimum of

$$S_2 - S_1 = S_1 \sqrt[3]{8\frac{\rho_2}{g\beta S_1} \cdot \frac{(E-P)^2}{W_s^2 D^3}} \tag{2.3}$$

for a given excess evaporation $(E - P)$. The factor β is $\frac{\partial \rho}{\partial S}$ from the equation of state of seawater. This minimal salinity difference will be reached if the mixing in the basin is sufficiently strong (the so called *overmixing solution*). If mixing is too weak, a bigger salinity difference can be realised, and the interface between inflowing and outflowing layer will also be lower than for the maximal solution.

A number of studies used these results to estimate, for example, the depth of the interface in the basin (Rohling 1991b,a, Rohling and Hilgen 1991, Rohling and Bryden

1994) or – for the Bosphorus as the controlling strait – the timescale of the flushing of the Black Sea during the sea level rise after the last deglaciation (Lane-Serff et al. 1997, see also chapter 6).

More detailed fluid dynamical studies of two layer exchange (Armi 1986, Armi and Farmer 1985, 1986, 1987, 1988, Farmer 1981, Farmer and Armi 1986, 1988, Farmer and Denton 1985) and in particular by Dalziel (1991) showed, however, that the solution (2.1, 2.2, 2.3) with an interface at half the sill depth is not realisable because it cannot continuously be connected to the interface away from the sill (see the discussion below in section 2.4). Therefore the maximally realisable flow has an interface below half sill depth, and the transport is reduced accordingly. For a rectangular channel of constant width, negligible net transport and infinite depth of the basin this maximally realisable flow is given by (Bryden and Kinder 1991)

$$h_{1s} = 0.62544D \tag{2.4}$$

$$q = 0.416\sqrt{g'D}DW_s \tag{2.5}$$

i. e., the total flow is about 20% lower than for the calculation based on an interface at half sill depth (2.2), and accordingly the minimal salinity difference between inflowing and outflowing water is larger. Further work on systems with more than one geometric control, e.g with separate sill and narrows (Dalziel 1991, Bormans and Garrett 1989b), show that the flow rates shows the same dependency

$$q \propto \sqrt{g'D}DW_s \tag{2.6}$$

where the constant of proportionality depends on the geometry of the system. For net transport $Q > 0$ the maximal realisable flow cannot be derived in closed form but has to be calculated numerically.

2.3 The Hydraulic functional

The most versatile mathematical description of stratified flows is the functional approach, in which a hydraulic functional is defined from which the features of the flow can be derived. This functional method was first introduced by Gill (1977) for single layer flows and later applied by Dalziel (1991, 1992) to 2-layer flows, and by Smeed (2000) to

3-layer systems. These studies have assumed rectangular channel cross-sections, except for Dalziel (1992) who applied the formalism to parabolic (and, as a limiting case, triangular) cross-sections[2]. Here we derive the equations for more general cross-sections. Although the formalism may seem unnecessarily abstract for the purpose of the 2-layer model described in this work (chapter 3), it can immediately and easily be applied to the more complicated 3-layer case (chapter 8).

In the functional approach in its abstract form, one uses the kinematic equations for constructing a functional $J(w_1(x), \ldots, w_n(x), Q, q, G; h_1(x))$ which embodies a relevant conservation law, e. g. the conservation of energy. The variables $w_1(x), \ldots, w_n(x)$ are parameters representing the geometry along the channel, Q is the net exchange, q is the total transport, and $h_1 x$ is the depth of the interface between the layers. The physical significance of the constant G depends on the actual representation of J; for the explicit representation constructed below, it is the difference in Bernoulli potential across the interface.

The hydraulic functional is defined such as to satisfy

$$J(w_1(x), \ldots, w_n, Q, q, G; h_1) = 0 \tag{2.7}$$

for any allowed configuration. For a given system, J is not uniquely defined. For regions without a hydraulic jump or sharp geometric features, J can be assumed to be continuous in all arguments.

The main purpose of (2.7) is that now the interface depth $h_1(x)$ is defined as an implicit function of $w_1(x), \ldots, w_n(x)$, Q, q and G. To symbolise the special significance of the variable $h_1(x)$, it is separated by semicolon rather than a comma in (2.7). In general, $J(\cdot; h_1)$ is not a one-to-one functional of $h_1(x)$, so that there are several functions $h_1(x)$ for which (2.7) is satisfied. Points at which different branches of $h_1(x)$ meet are called *control points*. The different branches of h_1 meet where J has a zero of higher order, i. e.

$$J = 0 \qquad \text{and} \qquad \frac{\partial J}{\partial h_1} = 0 \tag{2.8}$$

[2]Bryden and Kinder (1991) have also calculated results for a triangular cross-section using different methods, but including budget considerations.

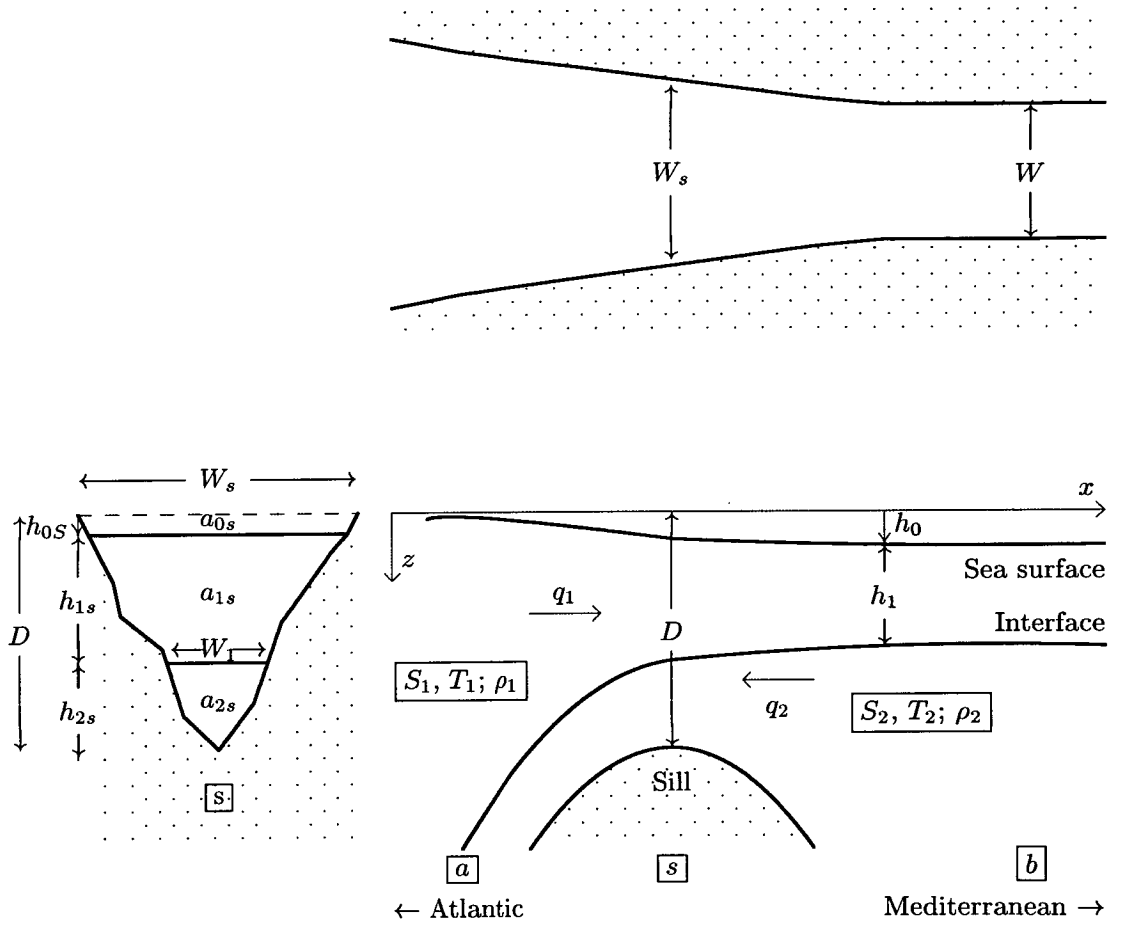

Figure 2.1: Definition sketch of the relevant variables. The different views are: side view (bottom right), top view (top right) and cross section at the sill (left).

After this abstract introduction of the hydraulic functional, an explicit form has to be constructed from the dynamic equations in the strait. In the following, rotational and frictional effects are neglected. We consider a channel of varying cross section, using coordinates x for the alongchannel coordinate and z as the vertical coordinate, measured from a reference level downwards (see figure 2.1). The total depth is given by $d(x)$, and the shallowest section in the channel is a sill of depth D. The thickness of each layer is denoted by $h_1(x)$ and $h_2(x)$, where the subscript 1 refers to the top layer, and 2 to the bottom layer. Then h_{1b} is the thickness of the upper layer inside the Mediterranean basin (point b in figure 2.1), h_{1a} is the thickness towards the Atlantic (point a), and h_{1s} the thickness at the shallowest point above the sill (point s). The sea surface depression is given by h_0 and is measured downwards relative to a fixed reference level, usually the average sea level in the Atlantic.

At the sill, we also define the cross-sectional area of each layer as a_i (see the left insert in figure 2.1), and the total cross-sectional area

$$a_{\text{tot}} = \sum_{i=0}^{2} a_i \tag{2.9}$$

For any particular geometry, there is a one-to-one mapping between the a_i and the h_{is}, so that $a_i = a_i(h_{0s}, h_{1s}, h_{2s})$. In the case of a rectangular cross-section, the relation is simply

$$a_i = W_s \cdot h_i \qquad \text{for} \quad i = 0 \ldots 2 \tag{2.10}$$

$$a_{\text{tot}} = W_s \cdot D \tag{2.11}$$

while for triangular cross-section

$$a_0 = \frac{1}{2} \cdot W_s \cdot h_0 \cdot (2 - \frac{h_0}{D})$$

$$a_1 = \frac{1}{2} \cdot W_s \cdot h_1 \cdot (2 - \frac{h_1}{D} - 2\frac{h_0}{D}) \tag{2.12}$$

$$a_2 = \frac{1}{2D} \cdot W_s \cdot h_2^2 \tag{2.13}$$

$$a_{\text{tot}} = \frac{1}{2} \cdot W_s \cdot D \tag{2.14}$$

The velocities for each layer are $\vec{u}_1(x)$ and $\vec{u}_2(x)$, the respective transports q_1 and q_2, with positive values denoting inflow into the basin, so that $q_2 < 0$. Furthermore, we define the total transport $q = q_1 - q_2$ and the net exchange $Q = q_1 + q_2$.

variable	symbol	dimensionalisation	$c(\cdot)$ for $S_2 = 37 \ldots 38.5$
horizontal coord.	$x = c(x) \cdot \tilde{x}$	$c(x) := W$	1.2×10^4 m
vertical coord.	$z = c(z) \cdot \tilde{z}$	$c(z) := D$	284 m
time	$t = c(t) \cdot \tilde{t}$	$c(t) := \frac{W}{\sqrt{Dg'}}$	$8.29 \ldots 5.26 \times 10^3$ s
cross-section	$a = c(a) \cdot \tilde{a}$	$c(a) := D \cdot W$	3.4×10^6 m^2
time	$t = c(t) \cdot \tilde{t}$	$c(t) := \frac{W}{\sqrt{Dg'}}$	$8.29 \ldots 5.26 \times 10^3$ s
velocity	$u = c(u) \cdot \tilde{u}$	$c(u) := \sqrt{Dg'}$	$1.45 \ldots 2.28$ m/s
pressure	$p_i = c(p_i) \cdot \tilde{p_i}$	$c(p_i) := \rho_i D g'$	$\approx 2.15 \ldots 5.34$ kPa
density	$\rho_i = c(\rho_i) \cdot \rho_i$	$c(\rho_i) := \frac{\rho_1 + \rho_2}{2}$	$\approx 1026.4 \ldots 1027.0$ kg/m^3
flow rate	$q_i = c(q) \cdot \tilde{q_i}$	$c(q) := WD\sqrt{Dg'}$	$4.94 \ldots 7.78 \times 10^6$ m^3/s

Table 2.1: Dimensionalisation of variables. The typical values for the dimensionalisation represent realistic values for Gibraltar for $S_1 = 36$ and $S_2 = 37$ and 38.5 respectively. $g' := g \cdot \frac{2(\rho_2 - \rho_1)}{\rho_1 + \rho_2}$ is the reduced gravity ($g' = 7.32 \ldots 18.3 \times 10^{-3}$ m/s^2 for $S_2 = 37 \ldots 38.5$).

The momentum and continuity equations for each layer are

$$\frac{\partial \vec{u}_i}{\partial t} + (\vec{u}_i \cdot \vec{\nabla})\vec{u}_i = -\vec{\nabla}\left(\frac{p}{\rho_i} - gz\right) \tag{2.15}$$

$$\frac{\partial a_i}{\partial t} + \vec{\nabla} \cdot (a_i \vec{u}_i) = 0 \tag{2.16}$$

The following derivation can be simplified by replacing all quantities h_i, u_i, p_i and ρ_i by appropriately nondimensionalised quantities $\tilde{h_i}$ etc. (see table 2.1). For simplicity we will omit the tilde and continue to use the same symbols, except when confusion with the dimensional variables is possible.

In the Boussinesq approximation ($\rho_2 - \rho_1 \ll \rho_1$), the momentum equation becomes

$$\frac{\partial \vec{u}_i}{\partial t} + (\vec{u}_i \cdot \vec{\nabla})\vec{u}_i = -\vec{\nabla}\left(\frac{p}{\rho_i} - \frac{\rho_i z}{\rho_2 - \rho_1}\right) \tag{2.17}$$

If rotational effects are neglected, the flow can be assumed to be mainly along the channel, so that the y and z components of (2.17) can be ignored. Integration yields Bernoulli's equation in the form

$$B_i = \frac{\partial \Phi_i}{\partial t} + \frac{1}{2}u_i^2 + \frac{p}{\rho_i} - \frac{\rho_i z}{\rho_2 - \rho_1} \tag{2.18}$$

in which Φ_i is defined by $\vec{u}_i = \vec{\nabla}\Phi_i$. We will assume a steady state, for which the time derivative vanishes. Using the Boussinesq approximation $\frac{p}{\rho_1} = \frac{p}{\rho_2}$ again, the difference in Bernoulli potentials at the depth of the interface $h_0 + h_1$ is given by

$$\Delta B := B_1(z = h_0 + h_1) - B_2(z = h_0 + h_1) = \frac{1}{2}(u_1^2 - u_2^2) + (h_1 + h_0) \tag{2.19}$$

In order to construct a hydraulic functional from this statement of conservation of the difference in Bernoulli potentials (2.19), the continuity equation has to be used to express the layer velocities in terms of flow rates and geometric quantities

$$u_1 = \frac{q_1}{a_1} \tag{2.20}$$

$$u_2 = \frac{q_2}{a_2} = \frac{q_2}{a_{\text{tot}} - a_1 - a_0} \tag{2.21}$$

which leads to the definition of the hydraulic functional as

$$J(q_1, q_2, \Delta B; h_0 + h_1) := \Delta B - \frac{1}{2}\left[\left(\frac{q_1}{a_1(h_i)}\right)^2 - \left(\frac{q_2}{a_2(h_i))}\right)^2\right] - (h_1 + h_0) \tag{2.22}$$

For a rectangular cross-section, the functions $a_i(h_i)$ are known ((2.10), note that $D = W_s = 1$ in the nondimensional form), and the hydraulic functional simplifies to

$$J(q_1, q_2, \Delta B; h_0 + h_1) := \Delta B - \frac{1}{2}\left[\left(\frac{q_1}{h_1}\right)^2 - \left(\frac{q_2}{(1 - h_1 - h_0)}\right)^2\right] - (h_1 + h_0) \tag{2.23}$$

In order to make the functional well defined, we have to assume the rigid lid approximation, in which $h_0(x)$ and a_0 are assumed to be known[3]. For this choice of J the composite Froude number is given by[4]

$$F^2 = 1 + \frac{\partial J}{\partial h_1} = \left(\frac{\tilde{q_1}^2}{\tilde{a_1}^3} + \frac{\tilde{q_2}^2}{\tilde{a_2}^3}\right) \cdot \frac{\partial \tilde{a_1}}{\partial \tilde{h_1}} = \left(\frac{\tilde{q_1}^2}{\tilde{a_1}^3} + \frac{\tilde{q_2}^2}{\tilde{a_2}^3}\right) \cdot W_1 \tag{2.24}$$

[3]Note however, that the results remain valid for a free surface, as varying sea surface heights may be interpreted as varying pressure in (2.15). For the more algebraically-minded, if one uses a functional on a two dimensional domain with interface depth and free surface height as the two independent dimensions (similar to the procedure used in the 3-layer case, section 8), it can be shown – with some algebraic effort – that the resulting Froude number condition is (2.24) plus a term with a factor of g'/g, i. e. negligibly small.

[4]Note that $\frac{\partial a_1}{\partial h_1} + \frac{\partial a_2}{\partial h_1} = 0$ if $h_0 = \text{const}$ by (2.9).

and for the rectangular cross-section (Dalziel 1991)

$$F^2 = 1 + \frac{\partial J}{\partial h_1} = \frac{\tilde{q_1}^2}{\tilde{h_1}^3} + \frac{\tilde{q_2}^2}{\tilde{h_2}^3} = \frac{u_1^2}{g'h_1} + \frac{u_2^2}{g'h_2} \tag{2.25}$$

This links the functional approach to the Froude number formalism (Armi and Farmer 1986, Armi 1986, Armi and Farmer 1987, Farmer and Armi 1986) and shows that control sections (defined as transitions from one sheet of h_1 to another, i. e. $\frac{\partial J}{\partial h_1} = 0$) correspond to critical conditions with $F^2 = 1$.

The hydraulic functional (2.23) is cubic in h_1 and therefore can have one, two or three roots. In the case of three roots, the highest and lowest have $\frac{\partial J}{\partial h_1} > 0$, i. e. $F^2 > 1$, and therefore represent supercritical flow, whereas the other root is subcritical ($F^2 < 1$). At a control point two roots coincide, leaving one critical and one supercritical solution. If J has only one root, this represents a supercritical solution.

2.4 The solution for 2-layer exchange

Finding the interface depth $h_1(x)$ from (2.22) is in general a nontrivial problem that can only be tackled numerically. In this section we discuss some of the main features of the solution using the mathematically simpler case of the rectangular cross-section with $D = 1$ and $W_s = 1$. For other cross-sections, the qualitative behaviour is similar, but numerical values are different. Different cross-sections are compared in the section 3.5 below.

To get the solution $h_1(x)$ along the channel, one has to start with the interface depth at the control point, where $F^2 = 1$. For a given net exchange Q the flow rates q_1 and $q_2 = Q - q_1$ can then be obtained from the simple quadratic Froude number equation (2.25). Under the simplifying assumption of no net exchange $q_1^2 = q_2^2$ and $h_0 \ll h_1$, one finds

$$q_1^2 = \frac{1}{(\frac{1}{h_1})^3 + (\frac{1}{1-h_1})^3} \tag{2.26}$$

This function is plotted in figure 2.2.

Using the flow rates, one can then calculate ΔB at the control section, which makes it possible to calculate the roots of J as functions along the channel and connect them continuously. The result for a channel of depth $d(x) = 1 + x^2$ and constant width

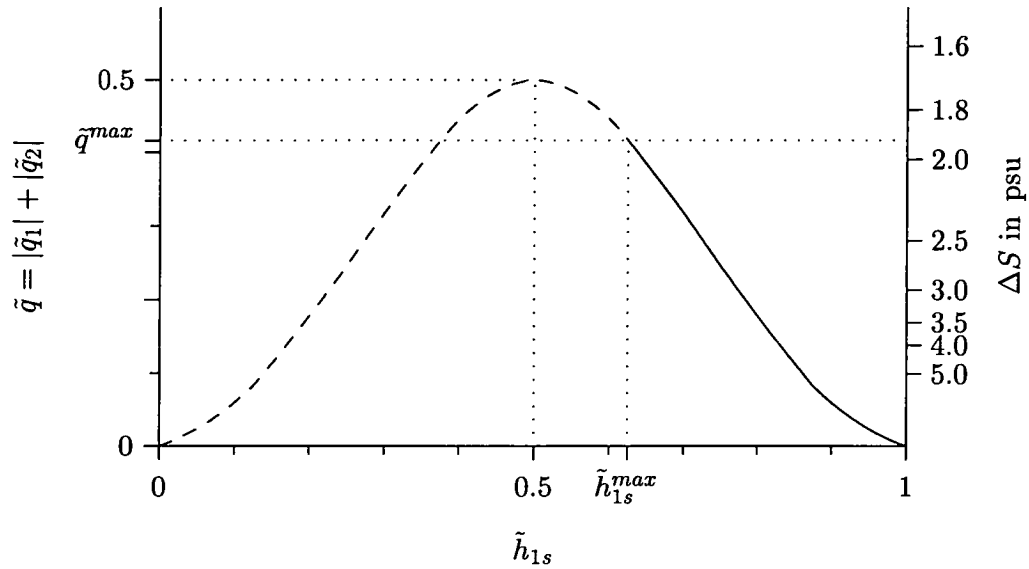

Figure 2.2: The flow rate $\tilde{q}_1$ as a function of the interface depth in the strait $\tilde{h}_{1s}$ for $Q \ll q$. The dashed curve represents solutions at the control point that cannot be matched through to the basin. The right axis shows the salinity difference for which the salt budget is balanced, if Q balances an excess evaporation of $E-P = 100\,\mathrm{cm/year}$ over the whole basin.

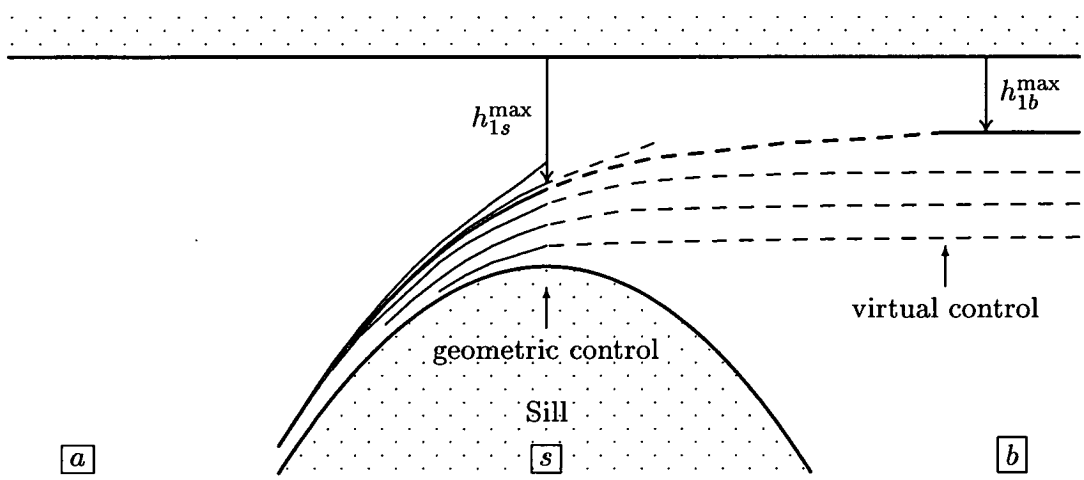

Figure 2.3: The interface depth along the channel $d(x) = 1 + x^2$ for a net exchange of $Q = 0$. The thick line represents the interface for maximal exchange, thin lines mean submaximal exchange. Supercritical flow is shown with solid lines, subcritical flow is dashed. Note that for interfaces higher than the maximal exchange the flow cannot be matched through. Arrows show the position of control sections.

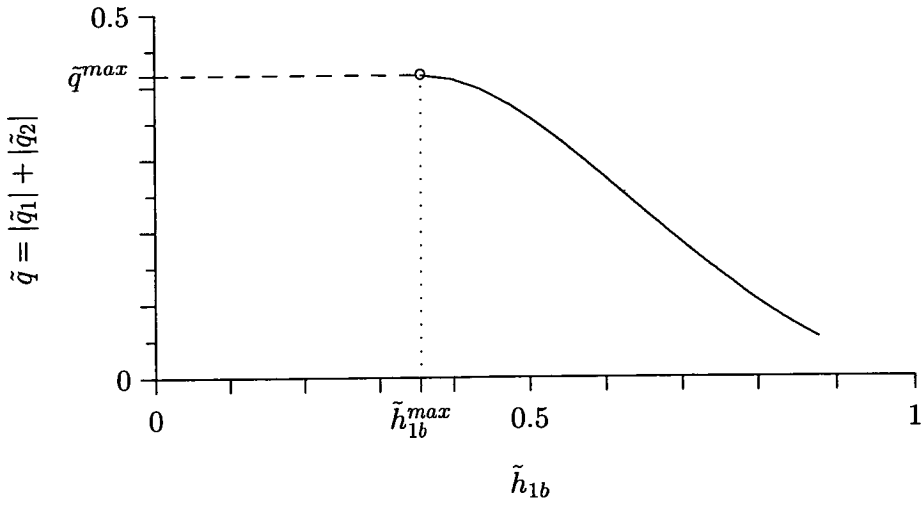

Figure 2.4: The flow $\tilde{q}_1$ as a function of the interface depth in the basin $\tilde{h}_{1b}$ for $Q \ll q$. Note that for interfaces higher than $\tilde{h}_{1b}^{\max}$ the exchange is maximal (dashed line).

$W_s = 1$ is shown in figure 2.3. From these results, a relation between the flow rate and the interface in the basin h_{1b} can be obtained. This is plotted in figure 2.4.

From (2.26) and figure 2.2 one might assume that maximal exchange occurs at $h_{1s} = 0.5$ with $q_1 = 0.25$. However, this solution is not realisable. From (2.23) the difference in Bernoulli potentials for this solution has to be $\Delta B = 0.5$. But at the entrance to the strait, where $h_2 \to \infty$, the hydraulic functional (2.23) leads to

$$\Delta B = \frac{q_1^2}{2h_{1b}^2} + h_{1b} \tag{2.27}$$

which has an absolute minimum given by

$$1 = \frac{q_1^2}{h_1^3} \tag{2.28}$$

For $q_1 = 0.25$, ΔB at has an absolute minimum at $h_{1b} = (q_1)^{2/3} \approx 0.40$ with $\Delta B = 0.59 > 0.5$. Therefore the solution with $h_{1s} = 0.5$ and $\Delta B = 0.5$ cannot be connected continuously to the basin. The physical reason for this problem is that, as d increases, the contribution of the lower layer to the kinetic energy in (2.23) decreases. To balance this, h_1 must decrease. This, however, increases the kinetic energy of the upper layer. For a sufficiently shallow interface, a balance can no longer be reached.

Therefore there is minimum interface depth at the control somewhat below half sill depth, denoted by $h_{1s}^{\max}$, for which the flow can be connected to the upstream basin,

where the interface is at $h_{1b}^{\max}$. For shallower interfaces, there is no continuous solution between sill and basin (see also figure 2.2)[5]. As this solution has a higher transport than solutions with deeper interface, it is called the *maximal solution.*

The maximal solution can be found from the following considerations. As noted above, the Bernoulli potential at the entrance to the strait has a minimum with $\Delta B > 0$. On the other hand, from (2.23) and 2.26), the Bernoulli potential at the sill is a monotonically increasing function with $\lim_{h_{1s}\to 0} \Delta B = 0$ and $\lim_{h_{1s}\to 1} \Delta B = 1$. Therefore, the problem of finding the maximal solution is equivalent to finding the minimum of ΔB at the strait entrance. In general, this can only be calculated iteratively. Dalziel (1991) describes a solution process. For a simple sill in a channel of constant width and infinite depth towards the basin, with no net exchange $Q = 0$, the interface at the control point for maximal exchange is $h_{1s}^{\max} = 0.62544$ (see also (2.4)). An iteration method for the general geometry and non-negligible net transport $Q \neq 0$ is also described below in section 3.1.

For the minimum of ΔB at the strait entrance, the condition 2.28 holds. As this is equivalent to a Froude number condition $F^2 = 1$, this proves that the maximal exchange has a second, so-called *virtual control.* By the same argument, solutions away from the maximal solution, i. e. solutions for which the interface is deeper, do not have a second, virtual control.

The system therefore shows two qualitatively different regimes, and the interface depth in the basin determines the nature of the flow:

Submaximal flow: If the interface in the basin is lower than the maximal solution, i. e. $h_{1b} > h_{1b}^{\max}$, then only submaximal exchange can be realised, with the exchange flow determined by the interface depth in the basin. The flow is subcritical between the basin and the control point at the sill and supercritical towards the Atlantic, where a hydraulic jump will occur. This solution with only one control is called a *partially controlled* solution.

Maximal flow: If the $h_{1b} < h_{1b}^{\max}$, then maximal exchange will occur. The maximal

[5]There are also solutions with shallower interface. But as these solutions require the interface in the Atlantic to be approximately as shallow as in the basin, this case will not be considered further. The flow in this case is subcritical everywhere, and the solution is called *uncontrolled* (Dalziel 1991)

solution has two control points, one at the geometric contraction of the sill, and a second, virtual control towards the basin, whose position is usually not at some geometric characteristics of the channel[6]. Between these controls the flow is subcritical, outside it is supercritical with the wave velocity pointing away from the controls.

As disturbances can only travel away from the strait, disturbances in the basins will not influence the strait. In this sense this solution with two control sections is said to be *fully controlled*. The interface in the basin will be connected to the interface in the strait through a hydraulic jump (or smoother non-conservative transition), so that the interface at the mouth of the strait will be $h_{1b}^{\max}$.

For a rectangular strait, the critical interface depth at which the switchover between the two regimes takes place is $h_{1b}^{\max} = 0.355D$, with a nondimensional transport of $\tilde{q} = |\tilde{q}_1| + |\tilde{q}_2| = 0.416$. It is important to note, however, that the actual value of the maximal exchange flow still depends on the density difference and will increase with the density difference, as $q \propto \sqrt{\rho_2 - \rho_1}$ from (2.5). Therefore, if the density in the basin is allowed to change freely, there is no upper limit to the total transport, and the term "maximal" should be understood to refer to the nondimensional transports, but not to the actual dimensional transports.

2.5 Complicating effects and comparison with observations

These calculations are based on the assumptions that effects of rotation and friction can be neglected, and that the two layers are uniform. While these assumptions simplify the mathematics considerably, it is necessary to establish whether they lead to reasonable results when applied to realistic situations. This section therefore is an attempt to justify each of these assumptions for the case of the Strait of Gibraltar.

To consider the effects of rotation we note that the Rossby radius of deformation is approximately 16 km so that rotational effects are not expected to be very relevant.

[6] A more general case of several geometric controls, like a sill and a narrows at different points is not considered here.

Based on more detailed experimental and theoretical studies, Whitehead et al. (1974), Whitehead (1989) suggested that straits with two layer exchange flows can be in either of two regimes. For a low-rotation regime, the flow rates are given by (2.5). However, the interface is not horizontal across the channel, but slopes downwards from south to north. Whitehead's high-rotation regime sets in when – in a rectangular channel – the interface slopes so strongly that it intersects the bottom and surface rather than the sides of the channel. The low rotation regime is appropriate when the channel width $W < W_0$, where the parameter W_0 is given by

$$W_0 = \frac{\sqrt{g'D}}{2f} \tag{2.29}$$

For the Strait of Gibraltar, using the values given in table 2.1, $W_0 \approx 10 - 12\,\mathrm{km}$ (depending on the density difference between the layers). As the Strait of Gibraltar is 15 km wide at the Tarifa Narrows and 25 km at the Camarinal Sill, it is possible that rotational effects are relevant. However, as the strait has a roughly triangular cross-section, the channel is considerably narrower at the depth of the interface, so Whitehead's results for the rectangular cross-section may be misleading. Bormans and Garrett (1989a) compare results from the theory for rotating hydraulics (Gill 1977) with the non-rotating case and find that the non-rotating theory is appropriate for the Strait of Gibraltar. Thorpe and Bigg (1998) also investigated this problem and found that the results from a GCM study for Gibraltar are consistent with the low-rotation regime. Furthermore, observations (reviewed in Garrett et al. (1990)) show that the slope of the interface is shallower than would be expected for Whitehead's high-rotation regime. Therefore the evidence seems to indicate that the non-rotating theory is sufficient for the Strait of Gibraltar and can be used in this study, while possible benefits of a more complicated rotational theory are dubious.

Friction has several effects. Firstly, the transports through the straits are reduced, as not all the available potential energy is converted into kinetic energy. Secondly, bottom friction and friction at the interface lead to non-uniform velocity distribution, so that the assumption of two uniform layers has to be challenged. Thirdly, friction at the interface can also lead to mixing, which again has implications for the 2-layer approximation. Several studies have addressed the effect of friction. Assaf and Hecht

(1974) used a two layer model with interfacial and bottom friction and found that the best fit to observational data is achieved with a friction coefficients[7] of the order of $k_{\text{interface}} = 10^{-3}$ and $k_{\text{bottom}} = 10^{-2}$, but they also note that the calculated bottom friction coefficient is an order of magnitude larger than most direct measurements suggest. Pratt (1986) showed that – for a realistic bottom friction coefficient of $k_{\text{bottom}} = 10^{-3}$ – the friction term is approximately 10% of the acceleration term in the equations of motion. Bormans and Garrett (1989b) suggest that a bottom friction coefficient of $k_{\text{bottom}} = 3.0 \times 10^{-3}$ is the best fit to observations, and that this will reduce the flow rates by 30% compared to the frictionless theory.

While these studies still assume 2-layer systems with uniform layers, observational data presented by Wesson and Gregg (1994) indicate that there is considerable mixing at the interface, and that a three-layer model with a nonuniform interface layer of considerable thickness and intermediate density is more appropriate. Figure 2.5 show typical observed profiles of the water properties in the Strait (Baringer and Price 1997, Bray et al. 1995). The salinity profile taken at the Camarinal Sill shows the 2-layer system, with a constant salinity of approximately 38 psu below 120 m, and a constant salinity of approximately 36 psu above 80 m. The two layers are separated by an interface layer with a salinity gradient due to shear and mixing between in- and outflow. This interface layer has a thickness of $20 - 40$ m and is centred at a depth of approximately 100 m in spring and 80 m in autumn. However, given that the sheared interface layer is thin compared to the total depth of the Strait (284 m), most of the in- and outflow occurs in uniform layers above and below the interface. The temperature shows a similar layering, but it is also strongly affected by seasonal changes in the upper layer, with a seasonal thermocline developing in summer.

Both theoretical and observational studies therefore indicate that the 2-layer model is a reasonable approximation, but that it is necessary to include friction in a third, sheared layer if one is interested in realistic values for the exchange. However, the aim of this study is not to provide precise numerical predictions, but to study the relevant mechanisms and processes in the strait. Therefore it seems justified to neglect

[7]The friction coefficients are nondimensional factors in a friction term $k_{\text{bottom}} \frac{u_2^2}{z} + k_{\text{interface}} \frac{\Delta u^2}{z}$ that is to be added to the momentum equation 2.15.

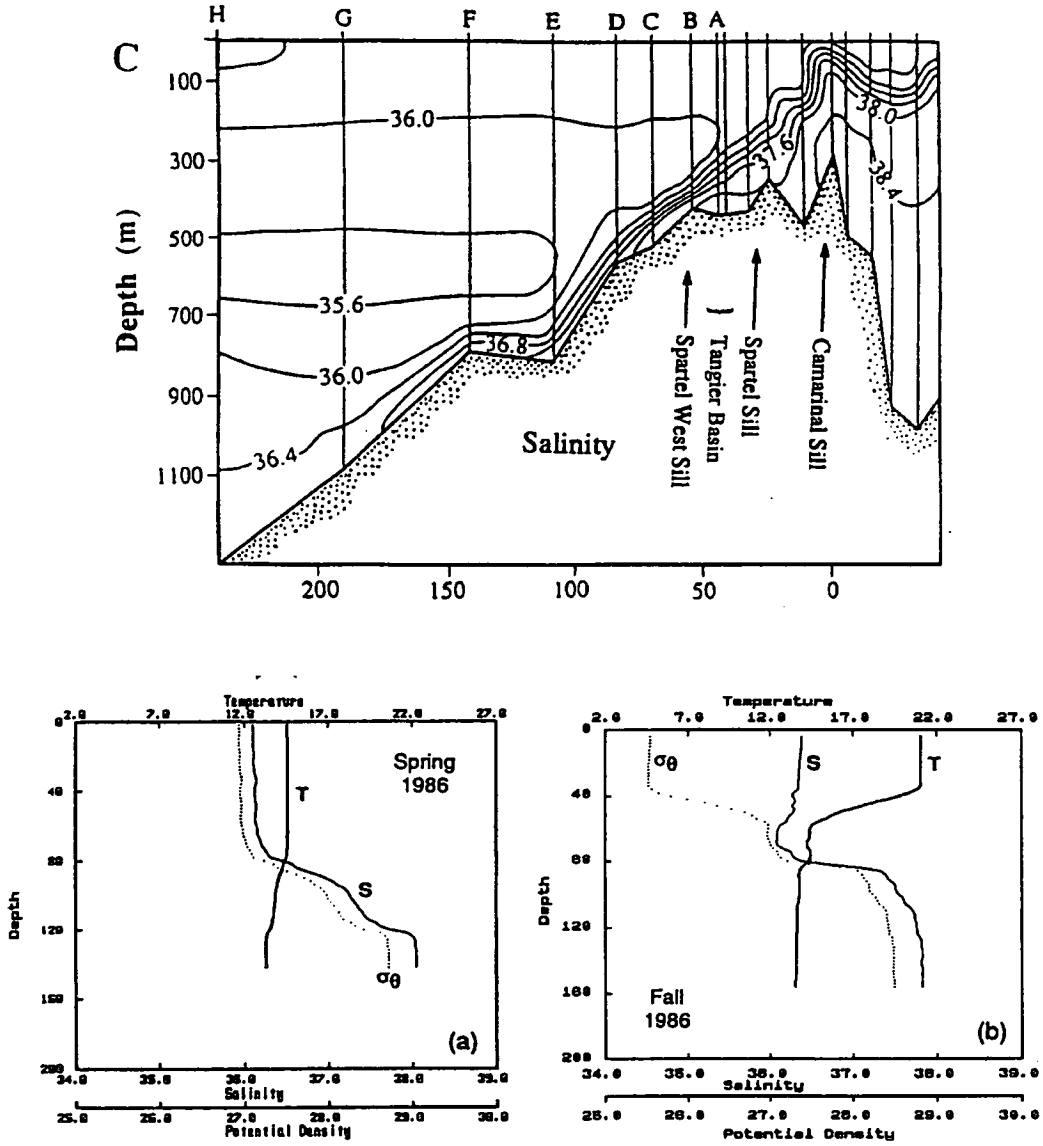

Figure 2.5: Top: Observed salinity along the strait (from Baringer and Price 1997). Bottom: Typical profiles of salinity, temperature and density from a station near the Camarinal Sill in spring and autumn (from Bray et al. 1995).

friction at this point and accept the numerical error of 10-30% introduced through this simplification.

The problem of mixing in the strait, and in particular in the hydraulic jump between the strait and the Mediterranean basin will be taken up again in chapter 7, where possible implications for the dynamical behaviour of the system are discussed.

Chapter 3

The HYCOBOX model

In chapter 2, the mathematical framework and some analytical results for a 2-layer exchange was described. However, analytical work is limited: Only a few interesting quantities (e. g. the flow rates for maximal exchange) can be derived explicitly for simple cases, while analytical solutions for most other situations are not easily found or do not exist. Furthermore, hydraulic control theory describes only the strait processes, but treats the basin only as a fixed boundary condition to the strait equations. In reality, basin and strait interact, as the water properties in the basin determine the boundary conditions for the strait, and the in- and outflow through the strait influences the water properties in the basin. Some of the budget studies described in chapter 2, e. g. Bryden and Kinder (1991, and references therein), have included this basin-strait-feedback, however they only look at the steady state in a maximal exchange situation.

This study tries to improve our understanding of sea straits by focussing on the dynamical aspects of the basin-strait-feedback. As this cannot be easily done analytically, a numerical model was programmed that combines a simple box model with a hydraulically controlled strait. To the best of our knowledge, a coupled model with the features described in this chapter has not been used before, although box models or strait models including some aspects of the feedback have been used by other researchers. The model was programmed using the programming package Modelmaker[1]

[1] Cherwell Scientific Computing Ltd., Version 3.0.2. The Modelmaker software package is specifically designed to simplify the programming of box models and process studies which do not need much computing power.

and was given the name HYCOBOX, an acronym for "HYdraulically COntrolled BOX model". Details of the model design are shown graphically in appendix D.1, where also the full programme code is listed.

HYCOBOX is a box model with three boxes (see figure 3.1), representing an essentially layered Mediterranean basin. Water from the upper layer is mixed into a water formation box (representing either a thin surface layer or a water mass formation region), from which it is transformed into denser and more saline deep water in the lower layer[2]. The upper and lower layer are in contact with the Atlantic, which serves as an infinite reservoir of fresher water, through a strait with a two layer exchange. Only the sea surface in the Atlantic, the excess evaporation in the basin and the salinity and temperature of Atlantic water are specified independently, and the water formation rate, expressed as an exchange velocity c_{FL}, is parameterised in terms of the conditions in the basin. From these input parameters the model calculates the time evolution of the sea surface and the interface depth in the strait and in the basin, the salinity difference between the two layers and the flow rates.

HYCOBOX has two distinctive parts: One submodel calculates the reaction of the strait to the boundary conditions imposed by the basin, whereas a second part then calculates the evolution of the conditions in the basin when the flows in the strait are determined. Thus the design of HYCOBOX reflects the basic feedback loop between the basin and the strait.

The strait submodel uses the steady state hydraulic control and therefore uses time-independent equations. The basin submodel, on the other hand, is defined in terms of differential equations with time as the independent variable. The use of steady state strait dynamics is justified here by the fact that the timescales for the strait dynamics are of the order of hours and therefore considerably shorter than the timescales in the basin, which are of the order of days to millennia (see section 4.2). Furthermore, this study does not focus on short time dynamics of the strait, e. g. tidal dynamics.

To distinguish between strait and basin quantities, the strait variables are denoted by subscripted arabic numbers 1 or 2 according to the layer, whereas basin quantities

[2]On may also regard the water formation box as a "part" of the upper layer, so that the model could be seen as a two-box-model with a differentiated upper layer box.

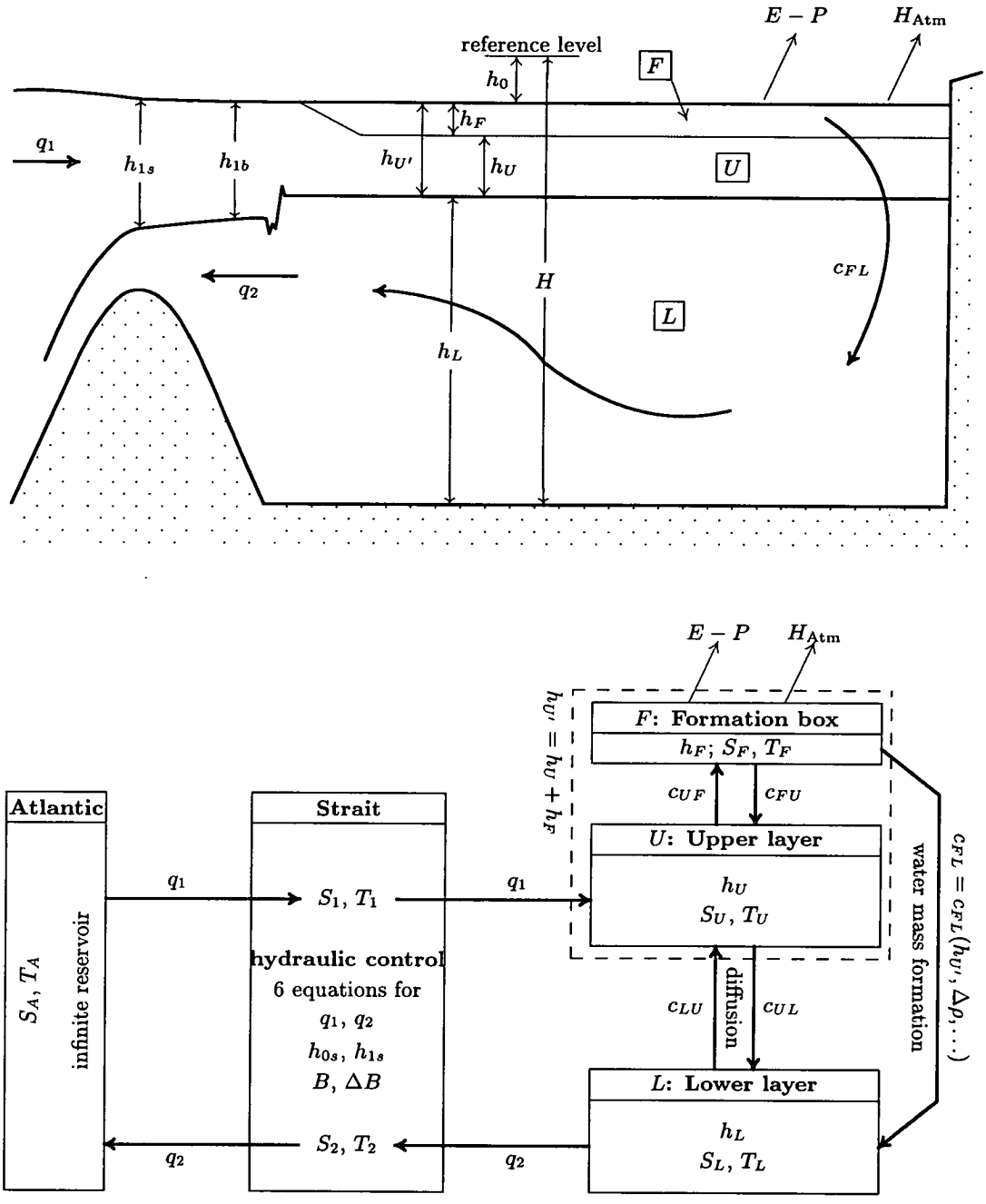

Figure 3.1: HYCOBOX, the hydraulically controlled box model, consists of a basin with three boxes F (water formation box), U (upper layer box) and L (lower layer box), connected to an infinite reservoir through a hydraulically controlled strait. Only the water formation box F interacts with the atmosphere. Boxes F and U together can be regarded as an effective upper layer U'.

are subscripted by the Roman letters F, U or L. The strait submodel uses nondimensional quantities, whereas the submodel for the basin uses dimensional quantities. All variables exchanged between the two submodels are converted accordingly. This has to be done at every timestep, as the dimensionalisation changes with density changes.

3.1 Representation of the strait

The submodel for the strait uses the hydraulic functional (2.22) to calculate the flow rate in both layers. The boundary conditions or input parameters for this calculation are the densities in both layers, the sea surface and the interface at the entrance of the strait on the basinside, all of which are provided by the basin submodel, and the sea surface towards the Atlantic, which is imposed. As auxiliary quantities the sea surface and the interface at the control point, i. e. the sill are calculated.

The equations used by the model are kept in a form general enough to accommodate a variety of different strait geometries, so that the model is not restricted to simple cross-sections. The following assumptions are made (see also figure 3.2):

- The channel cross-section is such that the width decreases with depth (i. e. no overhanging walls).
- The geometric control is situated at the shallowest section of the sill with $d(x_s) = D$, i. e. $\tilde{d}(x_s) = 1$.
- The channel is deep at the entrance towards the basin, i. e. $h_{2b} \gg h_{1b}$. Note that this also means that the cross-section is essentially rectangular at the strait entrance (but not necessarily at the sill), so that $a_{ib} = h_{ib}$.
- The interface in the Atlantic falls to great depths, i. e. $h_{1a} \to \infty$.

The model does not assume a simple (e. g. rectangular or triangular) channel cross-section. A description of the cross-sections used in this thesis and a comparison of different cross-section will be discussed below in section 3.5.

The strait equations are in nondimensional form (see table 2.1), where the depth dimensionalisation is taken at the sill, and the width at the basin-side strait exit.

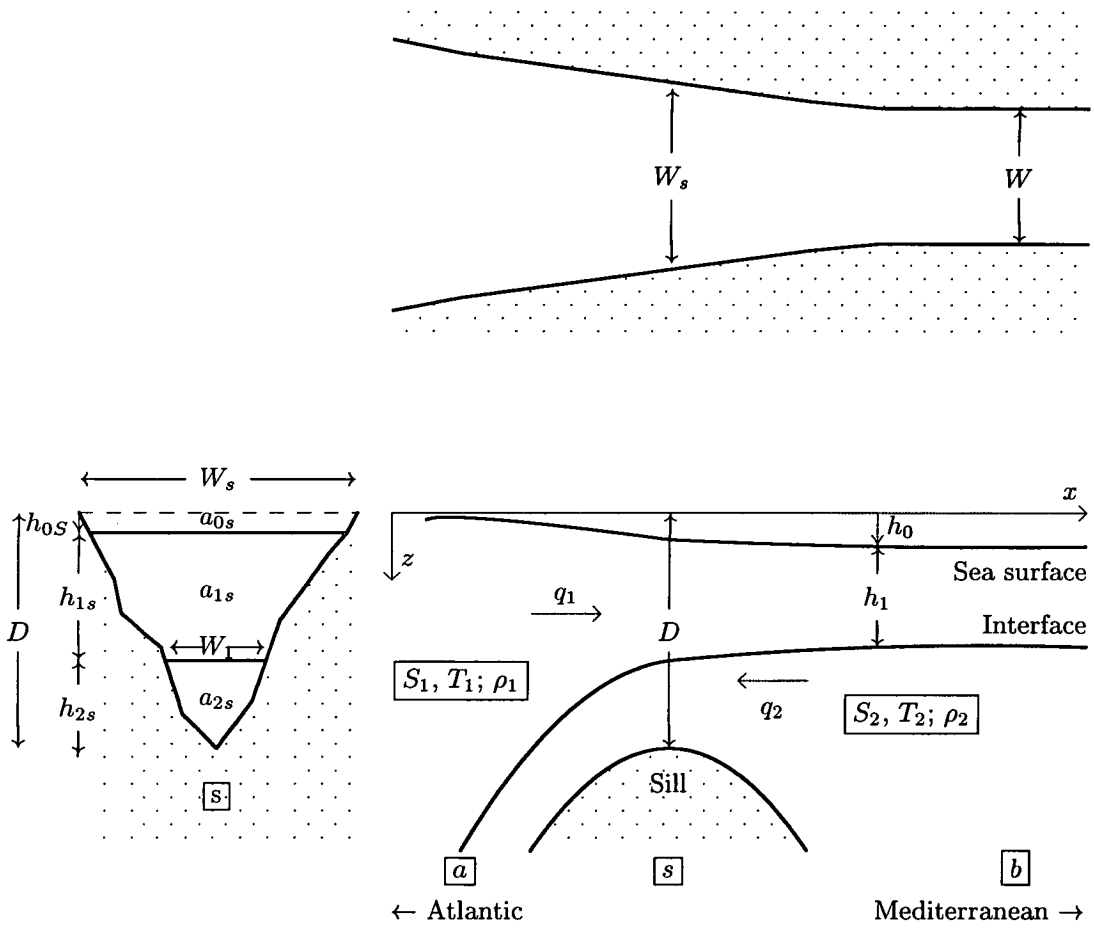

Figure 3.2: Definition sketch of the relevant variables in the strait. The different views are: side view (bottom right), top view (top right) and cross section at the sill (left). This figure is equivalent to figure 2.1.

From the hydraulic functional (2.22) and the control condition at the sill (2.24), we get a set of 6 nondimensional equations:

$$0 = B + \frac{\rho_1 h_{0a}}{\rho_2 - \rho_1} \tag{3.1}$$

$$0 = B - \frac{1}{2}\left(\frac{q_1}{a_{1s}}\right)^2 + \frac{\rho_1 h_{0s}}{\rho_2 - \rho_1} \tag{3.2}$$

$$0 = B - \frac{1}{2}\left(\frac{q_1}{h_{1b}}\right)^2 + \frac{\rho_1 h_{0b}}{\rho_2 - \rho_1} \tag{3.3}$$

$$0 = \Delta B - \frac{1}{2}\left(\frac{q_1}{h_{1b}}\right)^2 - (h_{1b} + h_{0b}) \tag{3.4}$$

$$0 = \Delta B - \frac{1}{2}\left[\left(\frac{q_1}{a_{1s}}\right)^2 - \left(\frac{q_2}{(1 - a_{1s} - a_{0s})}\right)^2\right] - (h_{1s} + h_{0s}) \tag{3.5}$$

$$1 = \left(\frac{q_1^2}{a_{1s}^3} + \frac{q_2^2}{(1 - a_{1s} - a_{0s})^3}\right) W_1 \tag{3.6}$$

The first three equations represent the Bernoulli function (2.18) at the surface. The Bernoulli function in the Atlantic (subscript a) is given by (3.1), and (3.2) and (3.3) give the Bernoulli function at the section above the sill (subscript s) and inside the Mediterranean basin (subscript b) respectively. Equations (3.4,3.5) represent the condition of vanishing hydraulic functional (2.22), i. e. the constant difference in Bernoulli potentials between the layers, at the interface depth inside the basin and for the section above the sill. The last equation (3.6) is the condition for a control point at the sill (2.24).

To make the above equations complete, a relation between the cross-sectional areas a_{is} and the layer thicknesses h_{1s} is needed, which is determined by the strait geometry (see the discussion in section 2.3). To accommodate arbitrary cross sections in the model, this relation is not parameterised explicitly, but calculated from a lookup-table, which contains width-depth pairs defining the cross-section at the sill. In the following equations it is therefore implied that the h_{is} and the a_{is} are equivalent and can be calculated from each other.

These equations have to be solved for q_1, q_2, h_{0s}, h_{1s}, B and ΔB. Unfortunately, an analytic solution does not exist. On the other hand, it is unwise to solve the full set using an standard multidimensional iterative scheme, e. g. a 6-dimensional Newton-Raphson iteration. This is not only computationally inefficient, but can also lead to wrong solutions, as the system is nonlinear with possibly several disjunct roots, the

number of which is not obvious from the set of equations. For this model, the equations are therefore reduced analytically as far as possible, and iteration is used only for the equations for which explicit solutions are not possible. This approach also leads to a clearer intuitive understanding of the relation between the different variables.

HYCOBOX calculates the unknown quantities from these equations in the following order:

- From (3.1, 3.3, 3.4) the following quantities are calculated:

$$B = -\frac{\rho_1 h_{0a}}{\rho_2 - \rho_1} \tag{3.7}$$

$$q_1 = h_{1b}\sqrt{2\left(B + \frac{\rho_1 h_{0b}}{\rho_2 - \rho_1}\right)} \tag{3.8}$$

$$\Delta B = \frac{1}{2}\left(\frac{q_1}{h_{1b}}\right)^2 + (h_{1b} + h_{0b}) \tag{3.9}$$

- As it is not possible to derive an expression for h_{1s} or a_{1s} in closed form, (3.5) and (3.6) are used to give

$$\begin{aligned} 0 &= a_{1s}^4 \cdot \frac{1}{W_1(h_{1s})} \\ &+ a_{1s}^3 \cdot \left(2h_{1s} + 2h_{0s} - 2\Delta B - \frac{a_{\text{tot}} - a_{0s}}{W_1(h_{1s})}\right) \\ &+ (a_{\text{tot}} - a_{0s}) \cdot q_1^2 \end{aligned} \tag{3.10}$$

  which is solved for a_{1s} by a Newton-Raphson iteration. Note that some of the coefficients of a_{1s} are functions of h_{1s}. After each iteration, the lookup-table is used to calculate the value of h_{1s} from a_{1s}, and the coefficients for the next iteration are recalculated with the new value of h_{1s}. This iteration also requires the value for h_{0s}, which is taken from the last timestep. As variations in h_{0s} are small compared to h_{1s}, the error is small.

- From (3.2) the new sea surface at the sill h_{0s} is calculated

$$h_{0s} = \frac{\rho_2 - \rho_1}{\rho_1}\left[\left(\frac{q_1}{a_{1s}}\right)^2 - B\right] \tag{3.11}$$

- From (3.6) the outflow q_2 is calculated as

$$q_2 = -\sqrt{(a_{\text{tot}} - a_{1s} - a_{0s})^3\left(\frac{1}{W_1} - \frac{q_1^2}{a_{1s}^3}\right)} \tag{3.12}$$

The representation of the strait is consistent with hydraulic control theory above. In particular, as the calculation of the difference in Bernoulli potentials ΔB uses both values at the control point and at the entrance to the strait, unrealisable solutions that cannot be matched through are avoided.

3.2 Connection to the basin and hydraulic jump

The submodel for the strait assumes that the boundary conditions for the strait are given by appropriate basin values. For temperature and salinity, this means:

$$S_1 = S_A \tag{3.13}$$

$$S_2 = S_L \tag{3.14}$$

$$T_1 = T_A \tag{3.15}$$

$$T_2 = T_L \tag{3.16}$$

where S_A, T_A, S_L and T_L are salinity and temperature of the Atlantic surface (subscript A) and the lower layer in the basin (subscript L, for the definition of the basin quantities see section 3.3) respectively.

For the interface depth, however, the situation is more complicated, as hydraulic jumps can occur. If the strait regime is submaximal, the flow is subcritical from the sill towards the Mediterranean basin, so that a continuous connection of the interface from the basin into the strait without hydraulic jump is possible. In this case, the interface at the strait entrance h_{1b} is equal to the interface in the basin $h_{U'}$. If the strait is in the maximal regime, however, the flow is supercritical from the virtual control towards the basin, and has to revert back to the subcritical flow inside the basin in a hydraulic jump or smoother hydraulic transition. In this case, the interface in the strait is decoupled from the interface in the basin, and the interface depth at the strait entrance is determined by the fully controlled maximal solution of the strait equations $h_{1b}^{\max}$. The transition between submaximal and maximal regime occurs when the interface in the basin gets shallower than this threshold value, i. e. $h_{U'} < h_{1b}^{\max}$

Therefore, the interface depth at the entrance to the strait h_{1b} is given by

$$h_{1b} := \max(h_{U'}, h_{1b}^{\max}) \tag{3.17}$$

For later use, the height of the hydraulic jump is defined as

$$h_{\mathrm{HJ}} := h_{1b} - h_{U'} \tag{3.18}$$

To get $h_{1b}^{\max}$, the maximal solution is continuously being calculated in HYCOBOX. Although the net exchange Q is small compared to the total transport q, the limiting case of $Q = 0$ as in (2.4) is not good enough for this purpose and leads to discontinuities when the hydraulic jump is switched on. For the calculation of the maximal exchange we can assume that Q is given by $E - P$, so that $q_2 = (E - P) - q_1$, and that $h_0 \ll h_1$.

For the maximal solution, the existence of a virtual control leads to the additional criticality condition (2.28) at the basinside strait entrance

$$1 = \frac{q_1^2}{h_1^3} \tag{3.19}$$

The solution for maximal exchange is calculated iteratively using the following steps, starting with an estimate for $h_{1s}^{\max} = 0.62544$:

- From (3.6), an estimate for $q_1^{\max}$ can be obtained as the (positive) root of the quadratic

$$\begin{aligned} 0 &= (q_1^{\max})^2 \left[(a_{1s}^{\max})^3 - (a_{\mathrm{tot}} - a_{1s}^{\max})^3\right] \\ &- q_1^{\max} \left[2(E-P)(a_{1s}^{\max})^3\right] \\ &+ \left((E-P)^2 - W_1(a_{\mathrm{tot}} - a_{1s}^{\max})^3\right)(a_{1s}^{\max})^3 \end{aligned} \tag{3.20}$$

- From (3.19), an estimate for $h_{1b}^{\max}$ is

$$h_{1b}^{\max} = (q_1^{\max})^{2/3} \tag{3.21}$$

- An estimate for $\Delta B_{\max}$ is calculated from (3.4)

$$\Delta B_{\max} = \frac{1}{2}\left(\frac{q_1^{\max}}{h_{1b}^{\max}}\right)^2 + h_{1b}^{\max} \tag{3.22}$$

- A new estimate for $a_{1s}^{\max}$ and is given by the roots of (3.10), which are calculated by a Newton-Raphson iteration

$$\begin{aligned} 0 &= (a_{1s}^{\max})^4 \\ &+ (a_{1s}^{\max})^3 \left[W_1(2h_{1s}^{\max} - 2\Delta B_{\max}) - a_{\mathrm{tot}}\right] \\ &+ a_{\mathrm{tot}}\,(q_1^{\max})^2 \end{aligned} \tag{3.23}$$

- From the lookup table, a new value for $h_{1s}^{\max}$ is calculated from $a_{1s}^{\max}$.

The new estimate of $h_{1s}^{\max}$ is then used for the next iteration. As $h_{1s}^{\max}$ is expected to change only very slowly (on the timescale relevant for density changes, which affect the dimensionalisation of $(E-P)$), only one iteration per timestep is performed.

3.3 Representation of the basin

The basin submodel calculates the state of basin as a response to air-sea fluxes (net evaporation $E-P$ and atmospheric heat loss H_{Atm}) and to the strait transport q_i, given by the strait submodel. The basin in HYCOBOX consists of three boxes of variable volume (see also figure 3.1). Two boxes represent the upper layer of comparatively fresh water (box U) and the lower, more saline layer (box L). The third box (box F) represents a water mass that is subject to air-sea fluxes and is being transformed, so it can – depending on the choice of the water formation parameterisation – alternatively be interpreted as a separate geographical region, e. g. the Levantine, as a thin surface layer, or as a sinking water mass before it mixes into the surrounding. Only the water formation box F exchanges fluxes with the atmosphere, while the boxes U and L are not in direct contact with the atmosphere. Water from the Atlantic flows into the upper box, is mixed into box F and then converted to deep water, and subsequently flows out through the strait, with the flow rates being determined by the submodel for the strait. The model allows exchange between all three boxes with a strength set by predefined parameters. Each of the boxes is characterised by its volume, its salinity and temperature.

This model design was strongly influenced by Tziperman and Speer (1994), who uses a similar 3 box model with an lower layer, upper layer and surface layer interacting with the atmosphere. However, the exchange between the boxes in Tziperman's model was set such that the volume of each box is forced towards a predefined volume, and the representation of the strait uses only the analytical solution for maximal exchange. Therefore the feedback between strait and basin is very limited in Tziperman's model, which was mainly designed for studying water formation in the basin. In the HYCOBOX model, on the other hand, the volume of the boxes U and L is allowed to

change freely, only the water formation box F is subject to forced relaxation towards a specified volume.

For the sake of intuitiveness, all volumes are expressed as layer thicknesses[3] h_i by dividing them through the total basin area A. The mass budget equations for the three boxes are

$$A\frac{dh_F}{dt} = -(E-P) + c_{UF} - c_{FU} - c_{FL} \tag{3.24}$$

$$A\frac{dh_U}{dt} = q_1 - c_{UF} + c_{FU} - c_{UL} + c_{LU} \tag{3.25}$$

$$A\frac{dh_L}{dt} = q_2 + c_{FL} + c_{UL} - c_{LU} \tag{3.26}$$

$$h_{U'} = h_F + h_U \tag{3.27}$$

$$h_0 = H - h_F - h_U - h_L \tag{3.28}$$

Here, the constant H is the total depth of the basin. The actual value of H is not important for the water budget, but has implications for the salt budget, as it determines the thickness of the lower layer and therefore the timescale for salinity changes (see chapter 4 below).

The parameters c_{XY} are transport rates between the different boxes, and depending on their parameterisation different processes in the basin can be modelled. The transport rates between upper and lower box c_{UL} and c_{LU} determine the mixing and diffusion across the interface (=pycnocline) in the basin, and depending on whether mixing in the basin is the focus of an experiment, they are set to

$$c_{UL} = c_{LU} = 0 \qquad \text{no mixing} \tag{3.29}$$

$$c_{UL} = c_{LU} = \frac{\kappa}{d} \qquad \text{mixing} \tag{3.30}$$

where $\kappa = 0.5 \times 10^{-4}\,\mathrm{m^2 s^{-1}}$ is the background diffusion coefficient, and d the effective diffusion length.

The transport rate c_{FL} describes the water mass formation, i. e. the rate with which water from the water formation box F is transformed into water of the lower layer box L. Its interpretation and different parameterisations are described below in section 3.4.

[3] If the water formation box F is interpreted as a surface layer, h_F is its thickness, however if it is interpreted as a geographical region, h_F has no intuitive interpretation.

The model assumes that no water is brought back from the lower layer into the water formation box. The water formation box F is refilled from the upper layer box. As we are not interested in the evolution of volume of the water formation box – for the feedback only the sum $h_{U'} = h_U + h_F$ is relevant –, c_{UF} is parameterised such that the volume of box F is forced back to a specified volume $h_{F\,\mathrm{set}}$ within a reasonable relaxation time $t_{\mathrm{relax}} = 0.1\,\mathrm{year}$. Therefore

$$c_{UF} = A \cdot \frac{h_{F\,\mathrm{set}} - h_F}{t_{\mathrm{relax}}} \tag{3.31}$$

In most experiments, the specified volume for the water formation box F was assumed to be 30% of the volume of box U, i. e. $h_{F\,\mathrm{set}} = 0.3 \cdot h_U$. This choice is somewhat arbitrary, but the system is not sensitive to the value of $h_{F\,\mathrm{set}}$.

Furthermore, c_{UF} and c_{FU} can also contain terms that describe the mixing and diffusion between upper layer and the water formation box similar to the transport between upper and lower layer.

The transport between the boxes affects the salinity and temperature of each box, as the water is mixed into the box volume. The water properties of the upper layer box U are also influenced by the inflowing Atlantic water with $S_{1\,\mathrm{strait}}$ and $T_{1\,\mathrm{strait}}$, and the water mass formation box F is subject to air-sea-fluxes, namely the excess evaporation $E - P$ and the atmospheric heat loss H_{Atm}. This leads to equations for the salinities

$$Ah_F \frac{dS_F}{dt} = (S_U - S_F) \cdot c_{UF} + S_F \cdot (E - P) \tag{3.32}$$

$$Ah_U \frac{dS_U}{dt} = (S_1 - S_U) \cdot q_1 + (S_L - S_U) \cdot c_{LU} + (S_F - S_U) \cdot c_{FU} \tag{3.33}$$

$$Ah_L \frac{dS_L}{dt} = (S_U - S_L) \cdot c_{UL} + (S_F - S_L) \cdot c_{FL} \tag{3.34}$$

and for the temperatures

$$Ah_F \frac{dT_F}{dt} = (T_U - T_F) \cdot c_{UF} - \frac{H_{\mathrm{Atm}}}{c_{\mathrm{water}}\,\rho_F} \tag{3.35}$$

$$Ah_U \frac{dT_U}{dt} = (T_1 - T_U) \cdot q_1 + (T_L - T_U) \cdot c_{LU} + (T_F - T_U) \cdot c_{FU} \tag{3.36}$$

$$Ah_L \frac{dT_L}{dt} = (T_U - T_L) \cdot c_{UL} + (T_F - T_L) \cdot c_{FL} \tag{3.37}$$

where the last terms in (3.32) and (3.35) are the changes due to air-sea interaction in the water formation box. c_{water} is the specific heat capacity of water.

3.4 The water formation rate c_{FL}

The transport rate c_{FL} from the water formation box F to the lower layer box L describes the water formation processes in the basin and has to be parameterised in terms of the air-sea fluxes $E-P$ and H_{Atm}, and in terms of the water properties h_i, S_i and T_i. Given the complexity of the water formation processes in nature, there is no obvious parameterisation that naturally describes the system. Furthermore, as c_{FL} is supposed to describe water formation over the whole basin, water formation schemes derived from local observations are of very limited use. Therefore, this study attempts not to restrict the possible water formation parameterisations too much, but – where necessary – uses a number of different parameterisations, motivated by physical considerations. The considerable uncertainty about the best parameterisation is probably the largest source of errors and uncertainties in the HYCOBOX model, and a considerable shortcoming.

The water formation is influenced by several physical mechanisms and depends on the following quantities:

Upper layer thickness: As the upper layer is the reservoir from which deep/intermediate water is produced, it can be assumed that the water formation rate decreases when the volume of the upper layer decreases. A possible parameterisation assumes that the water formation rate is a linearly increasing function of the upper layer thickness

$$c_{FL} = \alpha \cdot h_{U'} + \beta \tag{3.38}$$

If β is small, then c_{FL} is essentially proportional to the upper layer thickness. This may be a good approximation if the upper layer is well mixed, so that it is involved in the water formation in its entirety. If the upper layer is not well mixed, and only the surface is affected by air-sea-interaction, the water formation will not depend strongly on the upper layer thickness but be essentially constant. In this case, β is large compared to the first term. Clearly many others factors like wind stress determine how strongly the water formation depends on the thickness, but the benefits of a more complex parameterisation would be dubious for the purpose of this model.

Density difference between the layers: Primarily only the surface water, represented by box F, is affected by air-sea-interaction, and its density changes according to the atmospheric fluxes. However, deep/intermediate water is formed only when the surface water is dense enough to sink down into the lower layer. Therefore water formation takes place only when $\rho_F > \rho_L$. The larger the density difference between a water parcel and its environment, the faster it sinks, leading to a water formation parameterisation of

$$c_{FL} = \begin{cases} \mu(\rho_F - \rho_L) & \text{for} \quad \rho_F > \rho_L \\ 0 & \text{for} \quad \rho_F \leq \rho_L \end{cases} \tag{3.39}$$

However, a water formation parameterisation proportional to the density difference necessarily leads to a salinity or temperature catastrophe, unless mixing between boxes L and U is included, i. e. unless $c_{LU} \neq 0$ (see (3.30)). Without mixing of fresher water into L, its density changes only as a result of water formation. With this parameterisation of c_{FL}, the density of the water in box L therefore can only increase but never decrease, leading to very high salinity in the lower layer and very low water formation rates – a clearly unphysical situation. Mixing of fresher water from box U into box L maintains a density difference between the water formation box F and the deep water L and a nonzero water formation rate[4]. Figure 3.3 demonstrates this density catastrophe in two HYCOBOX model experiments[5]. The top figure shows an experiment with a density dependent water formation rate, but without mixing, with infinitely increasing density. The bottom figure includes a non-zero mixing and leads to a steady state.

Alternatively, a salinity catastrophe can be avoided if c_{FL} contains an additional term not proportional to the density difference. In this study however, the preferred approach is to include the mixing terms whenever a density dependent water formation parameterisation was used.

[4]The importance of mixing for water formation processes was also noted by Tziperman and Speer (1994), albeit in different context.

[5]For the parameters used in the experiment, see Appendix C.

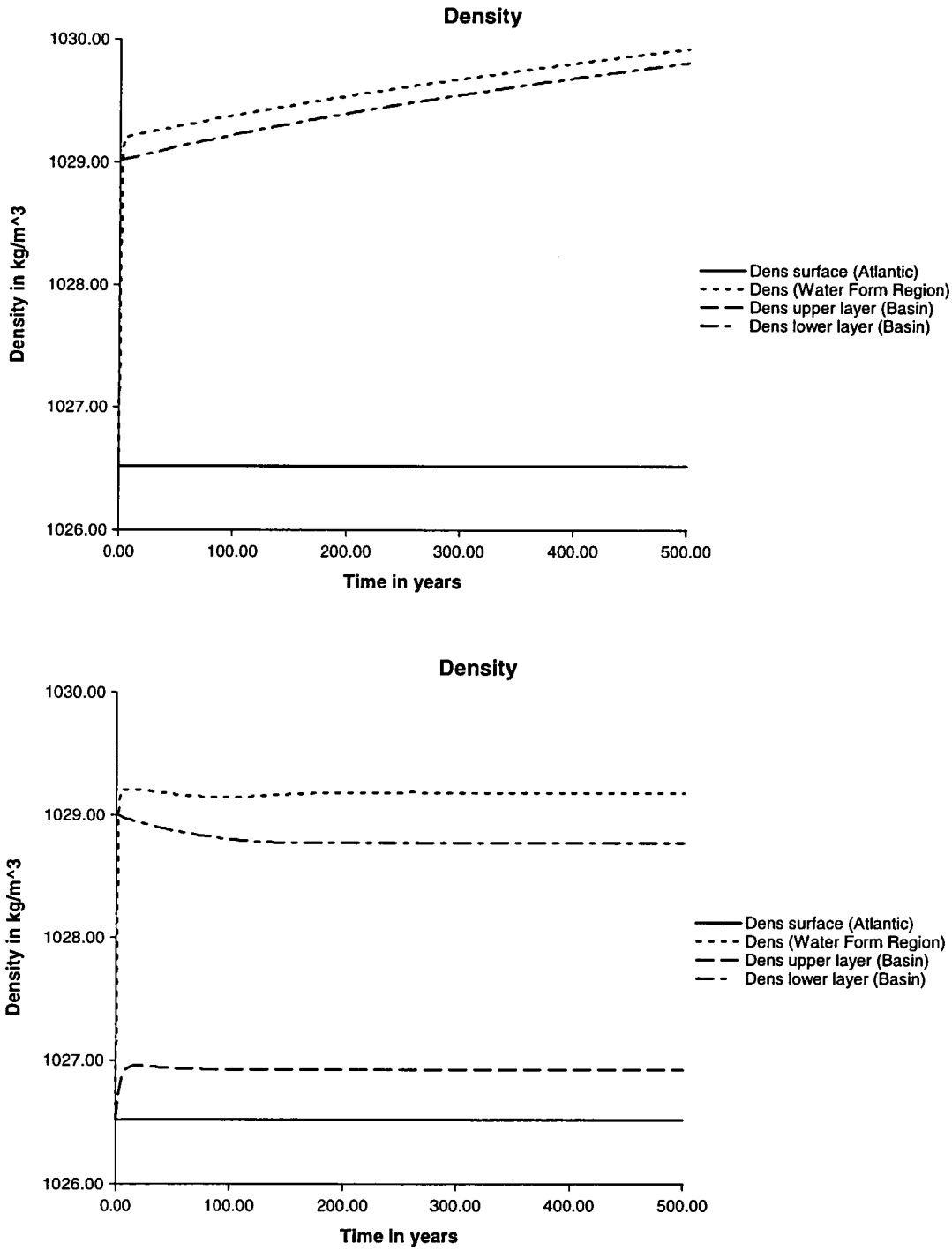

Figure 3.3: The importance of mixing for a stratification dependent water formation rate. Top: If the mixing term c_{UL} is not included, the density of the lower layer can only increase. Bottom: Mixing maintains a density difference between water formation box and lower layer.

Net evaporation: The water formation rate can also depend on the net evaporation $E - P$ over the basin:

$$c_{FL} = \zeta(E - P) + \eta \tag{3.40}$$

If the water formation rate is proportional to $E - P$ (i. e. $\eta = 0$), then changes in evaporation will affect the water formation rate very strongly. On the other hand, if $\zeta = 0$, changes in net evaporation mainly change the density of the water formation box F according to (3.32), and the water formation rate changes only indirectly if the water formation rate depends on the density difference. The relative size of ζ and η therefore determines whether changes in net evaporation lead to changes in the water formation *rate* or the *density* of the newly formed water.

These parameterisations for the fundamental physical mechanisms can be combined to construct more realistic parameterisations. For reasons of stability, it is advisable to always include a term proportional to the upper layer thickness, so that the water formation rate is reduced when the upper layer thickness gets too thin. Therefore the water formation parameterisation used in this study include a term proportional to the upper layer thickness. Three parameterisations (labelled (I), (D) and (E)) are generally used[6]:

$$\text{(I)} \quad \text{interface} \quad c_{FL} = \alpha \cdot h_{U'} \tag{3.41}$$

$$\text{(D)} \quad \text{density} \quad c_{FL} = \begin{cases} \mu \cdot h_{U'} \cdot (\rho_F - \rho_L) & \text{for} \quad \rho_F > \rho_L \\ 0 & \text{for} \quad \rho_F \leq \rho_L \end{cases} \tag{3.42}$$

$$\text{(E)} \quad \text{evaporation} \quad c_{FL} = \zeta \cdot h_{U'} \cdot (E - P) \tag{3.43}$$

Among the range of possible water formation parameterisations in this model, (D) is the most realistic parameterisation, as it reflects directly the physical mechanism of water sinking due to buoyancy loss. Although not explicitly dependent on the evaporation, both evaporation and atmospheric heat loss indirectly influence the water formation, as they increase the density ρ_F of the water formation box.

[6]For some more technical aspects and the units of the parameters α, μ and ζ see appendix C.1

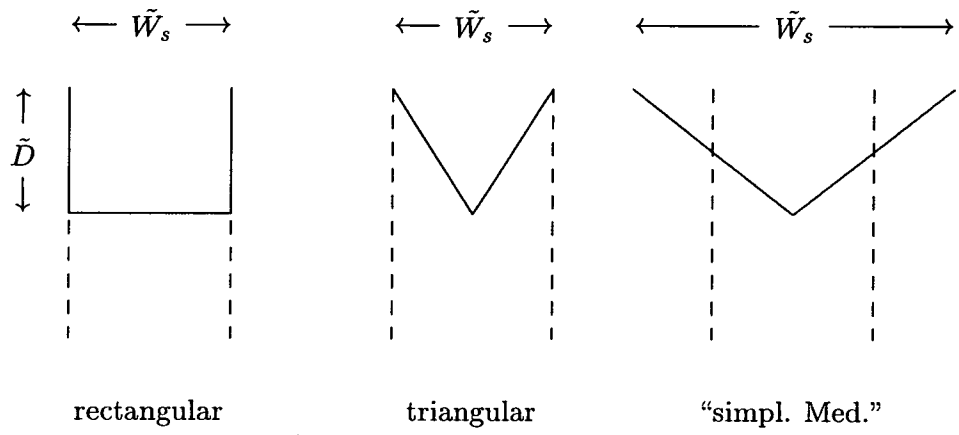

Figure 3.4: The different cross sections used in this study. The nondimensional width at the narrows (dashed lines) is defined as $\tilde{W} = 1$. At the sill, the rectangular and the simple triangular cross-section have $\tilde{W}_s = 1$, while the so-called "simplified Mediterranean" cross-section is twice as wide ($\tilde{W}_s = 2$).

3.5 Different cross-sections in comparison

The HYCOBOX model allows a wide variety of strait cross-sections to be used. At the entrances to the strait, the cross-section is effectively rectangular, as the depth is assumed to be infinite, but at the sill the cross-section can freely be chosen and is specified in lookup tables containing depth-width pairs (see section 3.1). In this section, results from the basin submodel for some important cross-sections are compared.

Although cross-sections in the model are not restricted to simple forms, here we only use three different cross-sections (see figure 3.4): A rectangular cross-section with a constant channel width, and triangular cross-sections with different widths at the sill $\tilde{W}_s$ (the width at the basinside entrance is defined to be $\tilde{W} = 1$). Of particular relevance is a triangular cross section with a width at the sill twice the width at the basinside entrance, i. e. $\tilde{W}_s = 2$. As Bryden and Kinder (1991) discuss, the Camarinal Sill in the Strait of Gibraltar has a depth-width-profile that is close to a triangle with 284 m depth and 22.3 km width, approximately twice as wide as the Tarifa Narrows. Therefore the HYCOBOX cross-section with $\tilde{W}_s = 2$ can be regarded as a "simplified Mediterranean" cross-section. This "simplified Mediterranean" cross-section will be used for all experiments from chapter 5 onwards.

For most practical purposes, the strait response can be characterised by the func-

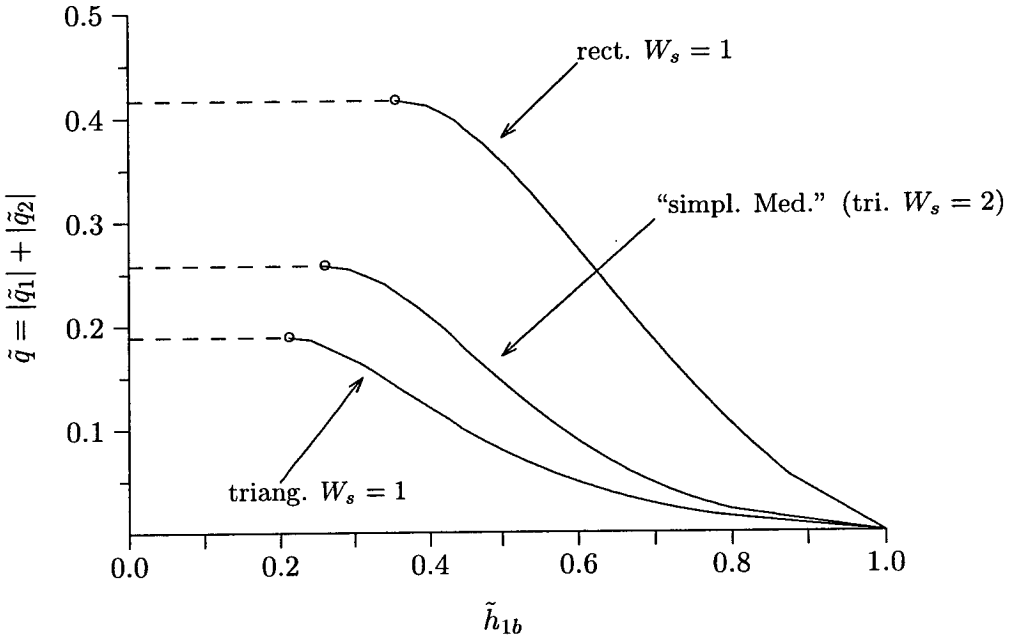

Strait geometry	$\tilde{W}_s$	$\tilde{h}_{1b}^{\max}$	$\tilde{q} = \lvert\tilde{q}_1\rvert + \lvert\tilde{q}_2\rvert$
rectangular	1.0	0.355	0.416
triangular	1.0	0.212	0.189
triangular ("simplified Med.")	2.0	0.260	0.258

Figure 3.5: Top: The nondimensional flow $\tilde{q}$ as a function of the nondimensional interface depth in the basin $\tilde{h}_{1b}$ for different cross-sections. The switchover between submaximal and maximal regime is indicated by a circle. Bottom: The maximal transport and the interface depth for the transition between maximal and submaximal regime for three important cross-sections.

tion $\tilde{q}(\tilde{h}_{1b})$ (see figure 2.4), i. e. the nondimensional transport as a function of the interface position in the basin. Figure 3.5 compares the result for three important cross-sections, namely the simple rectangular cross-section with constant channel width, a triangular cross-section with constant channel width ($\tilde{W}_s = 1$), and the "simplified Mediterranean" (triangular with $\tilde{W}_s = 2$).

Compared to the rectangular cross-section, the triangular cross-sections differ in two aspects: They have a considerably smaller transport, and the interface depth for the transition between the maximal and the submaximal regime is at shallower depths (see figure 3.5). The values for the maximal transports obtained by HYCOBOX compare well to the literature values: For the rectangular geometry, several researchers (Armi 1986, Armi and Farmer 1985, 1986, 1987, 1988, Farmer 1981, Farmer and Armi 1986, 1988, Farmer and Denton 1985) have found that $\tilde{q} = 0.416$ (see also section 2.2 and in particular equation 2.5). For triangular cross-sections, Bormans and Garrett (1989b) used a triangular channel with separate sill and narrows not unlike the HYCOBOX "simplified Mediterranean" geometry, and obtain a maximal transport of $q_1 = 1.2\,\mathrm{Sv}$, equivalent to $\tilde{q} = 0.22$ with the dimensionalisation used here[7], while HYCOBOX obtains $\tilde{q} = 0.258$. The slightly higher transport in HYCOBOX can be explained by the fact that Bormans and Garrett (1989b) use a finite depth at the narrows, whereas HYCOBOX assumes that the bottom layer is infinite.

It is useful to note that the lower transport of triangular cross-sections is not a result of the different cross-sectional *area*: In fact, the double-width triangular cross-section with $\tilde{W}_s = 2$ ("'simplified Mediterranean") has the same cross-sectional area as the rectangular cross section, but the maximal transport is only about 60% of the maximal transport of the rectangular strait.

As a spin-off, it may be possible that these results can be used to improve the performance of General Circulation Models (GCMs), where narrow channels can sometimes only be represented by a few gridpoints and therefore have essentially a rectangular

[7]Note that the width here has been nondimensionalised with respect to the the width at the narrows, while e. g. Bryden and Kinder (1991) quotes the above result from Bormans and Garrett (1989b) using the width at the sill. However, while Bryden and Kinder (1991) quote the value of $q = 0.149 W_s D\sqrt{Dg'}$, the original values in Bormans and Garrett (1989b) ($W = 15\,\mathrm{km}$, $W_s = 25\,\mathrm{km}$, $D = 300\,\mathrm{m}$, $g' = 0.02\,\mathrm{m/s^2}$, $q_1 = 1.2\,\mathrm{Sv}$) lead to $W_s D\sqrt{Dg'} = 18\,\mathrm{Sv}$ and therefore $q = 0.13 W_s D\sqrt{Dg'}$.

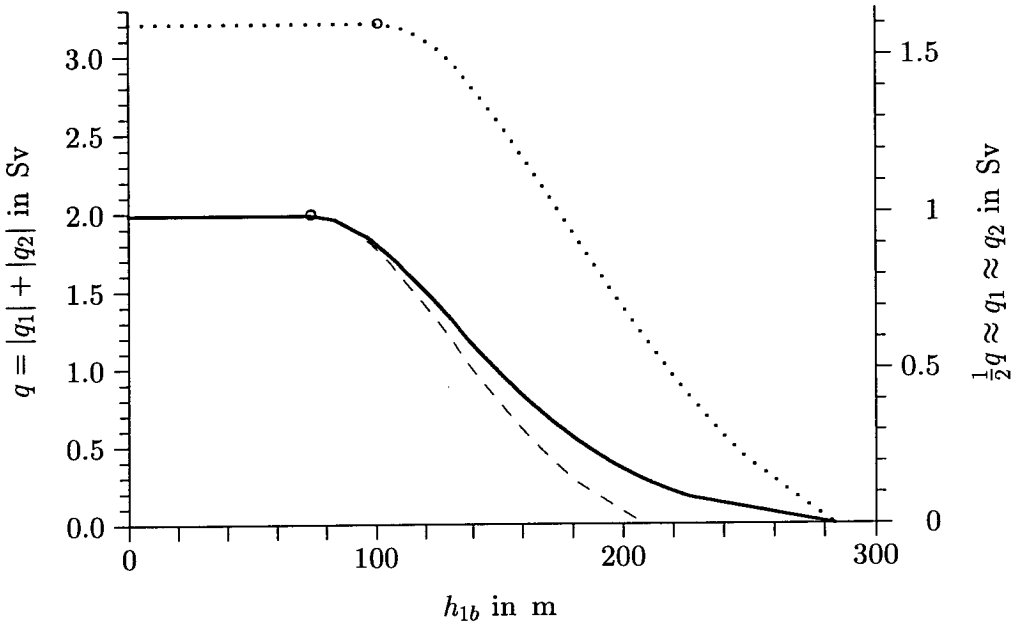

	Description	W	W_s	D	$\frac{1}{2}\,q^{\max}$	$h_{1b}^{\max}$
solid line	"simp. Mediterranean"	12.0 km	24.0 km	284 m	0.993 Sv	73.8 m
dotted line	rect., same area as Med	12.0 km	12.0 km	284 m	1.604 Sv	100.9 m
dashed line	rect., same q and h	11.9 km	11.9 km	208 m	0.997 Sv	73.9 m

Figure 3.6: Comparison between the triangular Mediterranean cross-section (solid line) and two rectangular cross-sections. The dashed line shows the best representation discussed in the text; the dotted line shows a rectangular cross-section of the same cross-sectional area. The dimensionalisation uses $g' = 0.018\,\mathrm{ms}^{-22}$ (equivalent to a salinity difference of approximately 2.5 psu).

cross-section. However, if the rectangular channel is chosen to be of comparable width and depth to the real triangular channel, the strait in the GCM will enable transports that are too high by a factor of almost 2. For a strait that is maximal or close to maximal, the best rectangular representation of a triangular channel should have the same maximal transport $q^{\max}$ and the same switchover depth between maximal and submaximal regime $h_{1b}^{\max}$. For the Strait of Gibraltar, using the values from figure 3.5, this leads to the conditions

$$0.260 \cdot D_{\text{Gib}} = 0.355 \cdot D_{\text{GCM}} \tag{3.44}$$

$$0.258 \cdot W_{\text{Gib}} D_{\text{Gib}}^{(3/2)} = 0.416 \cdot W_{\text{GCM}} D_{\text{GCM}}^{(3/2)} \tag{3.45}$$

where D_{Gib} and W_{Gib} are depth and width of the real Strait of Gibraltar, whereas D_{GCM} and W_{GCM} are the depth and width of channel in the GCM. Therefore

$$D_{\text{GCM}} = 0.732 \cdot D_{\text{Gib}} = 208\,\text{m} \tag{3.46}$$

$$W_{\text{GCM}} = 0.989 \cdot W_{\text{Gib}} = 11.9\,\text{km} \tag{3.47}$$

The best rectangular representation should therefore have a width similar to the width at the narrows, but with a sill depth considerably shallower. Figure 3.6 shows the dimensionalised function $q(h_{1b})$ for these two cross-sections. It is obvious that these two very different straits give similar results if the system is not too far away from the maximal regime. For comparison the figure also shows a rectangular cross-section with $D_{\text{GCM}} = D_{\text{Gib}}$ and $W_{\text{GCM}} = W_{\text{Gib}}$, i. e. the naive choice which overestimates the transport considerably.

Unfortunately, GCMs pose the further constraint that the channel width has to be a multiple of the grid size. Furthermore, it should be noted that this method is only applicable if it is established a priori that the strait exhibits a pure 2-layer exchange. In the case of Gibraltar however, in addition to the LIW which forms the bulk of the outflowing water, there is also a thin layer of denser WMDW (Western Mediterranean Deep Water) at the bottom (Bryden and Stommel 1982). Obviously, the outflow of this water mass would not be modelled correctly if the sill depth is reduced considerably. Finally, in a GCM the viscosity in straits is often modified for numerical reasons, so that this calculation may not be directly applicable. The usefulness of this

approach therefore still has to be established, but it is suggested that appropriate GCM experiments be performed in future.

Chapter 4

Feedback between basin and strait

In this chapter, the feedback between basin and strait is discussed with the aim of clarifying the physical mechanism that determine the state of the system. First, the relevant budget constraints for salt, heat and volume are considered in more detail. For small perturbations, the mechanisms that lead the system back to the steady state are discussed and their characteristic timescales derived. There is a hierarchy of timescales: Sea-level adjustments to balance the water budget within a few days, adjustments of the interface depth between the upper and the lower layer which occur on timescales of the order of years or a few decades, and changes in salinity and/or temperature which take place on timescales of decades or centuries.

This discussion forms the basis of the experiments discussed in subsequent chapters, where the more abstract ideas presented here are applied to realistic situations.

4.1 The steady state

Before discussing the feedback mechanisms and the dynamical aspects of the system, it is useful to characterise the steady state.

4.1.1 Water, salt and heat budget

The steady state is characterised by balanced water, salt and heat budgets (note that $q_2 < 0$)

$$q_1 + q_2 = Q = E - P \tag{4.1}$$

$$S_1 \cdot q_1 + S_2 \cdot q_2 = 0 \tag{4.2}$$

$$[(T_1 - T_1) \cdot q_1] + (T_2 - T_1) \cdot q_2 = \frac{H_{\mathrm{Atm}}}{c_{\mathrm{water}}\,\rho} \tag{4.3}$$

where H_{Atm} is the total heat loss to the atmosphere, and the temperature of the inflow T_1 has been taken as the reference value for temperature changes, so that the inflow term in the heat budget (in square brackets) is identically zero.

For the discussion in this section, a simplified form of the model equations (3.24, 3.25, 3.26) is sufficient. As the focus of this chapter is the global budget, mixing between the boxes can be ignored for the moment, so that all exchange rates between the boxes c_{XY} are set to zero except for c_{FL}, which parameterises the water formation rate. Furthermore, the discussion is easier if the water formation box F and the upper layer box U are combined to an effective upper layer $U' = U + F$, leading to equations

$$A\frac{dh_{U'}}{dt} = q_1 - (E - P) - c_{FL} \tag{4.4}$$

$$A\frac{dh_L}{dt} = q_2 + c_{FL} \tag{4.5}$$

$$h_0 = H - h_L - h_{U'} \tag{4.6}$$

Previous researchers (e. g. Bryden and Stommel 1984) have viewed the feedback mainly from the point of view of the strait, assuming that the water properties inside the basin are constrained by the limiting effects of the strait. Under this paradigm, the salinity and temperature difference between in- and outflow can be said to be determined by the strait flow. Rewriting the salt and water budgets (4.1, 4.2), the total transport in the strait is

$$q = q_1 - q_2 = \frac{S_1 + S_2}{S_2 - S_1}(E - P) \tag{4.7}$$

so that the salinity difference is inversely related to the strait transport:

$$\Delta S = S_2 - S_1 = \frac{(S_1 + S_2)(E - P)}{q} \tag{4.8}$$

Similarly, the temperature difference is given by (4.3)

$$\Delta T = T_2 - T_1 = -\frac{H_{\text{Atm}}}{q_2\, c_{\text{water}}\, \rho} \tag{4.9}$$

As the flow rate in the strait is limited by the maximal solution, the salinity difference and the temperature difference must be minimal. For submaximal situations, the salinity and temperature difference between in- and outflow are always greater.

However, it is useful to also view the system from a different perspective and take the basin processes as the starting point. These two paradigms are not contradictory but rather supplement each other. We can regard $E - P > 0$ and H_{Atm} as given, and c_{FL} as determined by the water formation process in the basin (possibly c_{FL} may be a function of the air sea fluxes or water properties). Then – assuming that the water properties of the inflow S_1 and T_1 are given – the steady state is

$$|q_2| = c_{FL} \tag{4.10}$$

$$|q_1| = c_{FL} + (E - P) \tag{4.11}$$

$$S_2 = S_1 + S_1 \frac{E - P}{c_{FL}} \tag{4.12}$$

$$T_2 = T_1 - \frac{H_{\text{Atm}}}{c_{FL} \cdot c_{\text{water}}\, \rho} \tag{4.13}$$

The first two equations (4.10, 4.11) state the obvious fact that the same amount of intermediate/deep water flows out of the basin as is being formed, while the inflow balances the water formation and evaporation.

In the salinity equation (4.12), the second term is positive for net evaporation over the basin, so that the salinity of the outflowing water exceeds the salinity of the inflowing water. For the temperature equation (4.13), the last term describes the temperature decrease due to heat loss to the atmosphere, including both sensible and latent heat. It should be noted that in general H_{Atm} also depends on the evaporation, so that a change in evaporation changes both the salinity and the temperature. With no heat loss, (4.13) reduces to the trivial statement $T_2 = T_1$.

It is obvious that the water formation rate c_{FL} plays the most important role in determining the steady state of the system. The strait and budget equations give only one constraint limiting the range of c_{FL}. As the strait dynamics limits the outflow q_2 when the maximal regime is reached, the water formation cannot exceed this limit in

the steady state. While the precise nature of the feedback mechanism that reduces c_{FL} in the case of $c_{FL} > q_2^{\max}$ depends on the details of the water formation mechanism, it is obvious that the water formation in the long run is limited by the supply of fresh water from the Atlantic and therefore cannot exceed $|q_1|$.

However, this is the only constraint that the strait and budget equations place on the range of c_{FL}. There are no lower limits to the water formation rate, and no constraints in the submaximal case. In particular, this means that there is no fundamental mechanism in the basin-strait feedback that determines whether the strait is in the maximal or submaximal regime[1].

4.1.2 Maximal and submaximal states in HYCOBOX experiments

A series of HYCOBOX experiments were performed to illustrate how the steady state depends on the water formation rate. As only the rate of water formation is relevant here, but not details of the water formation process, the simplest water formation parameterisation (3.38) was chosen, in which the water formation rate is assumed to be proportional to the thickness of the (effective) upper layer U' only

$$c_{FL} = \alpha \cdot h_{U'} \tag{4.14}$$

With this parameterisation, the choice of the parameter α effectively determines the water formation rate, and in particular, it determines whether the strait can reach maximal exchange.

Using a rectangular cross-section, a number of HYCOBOX experiments with different values for α were performed. Figures 4.1, 4.2, 4.3 and 4.4 illustrate two of these runs. In the first run, for a choice of $\alpha = 0.25$ (figures 4.1 and 4.2), the water formation rate is high enough to reach the maximal regime in the steady state. The run starts with a submaximal situation, in which the interface in the basin is at 170 m well below the threshold for maximal exchange. In the course of approximately 5 years, the basin is filled with deep/intermediate water, so that the interface gets shallower (figure 4.1 top). The interface continues to rise over the maximal threshold, but as the water

[1]Note, however, that there may be additional feedbacks involving changes in the water formation rate. These will be discussed later.

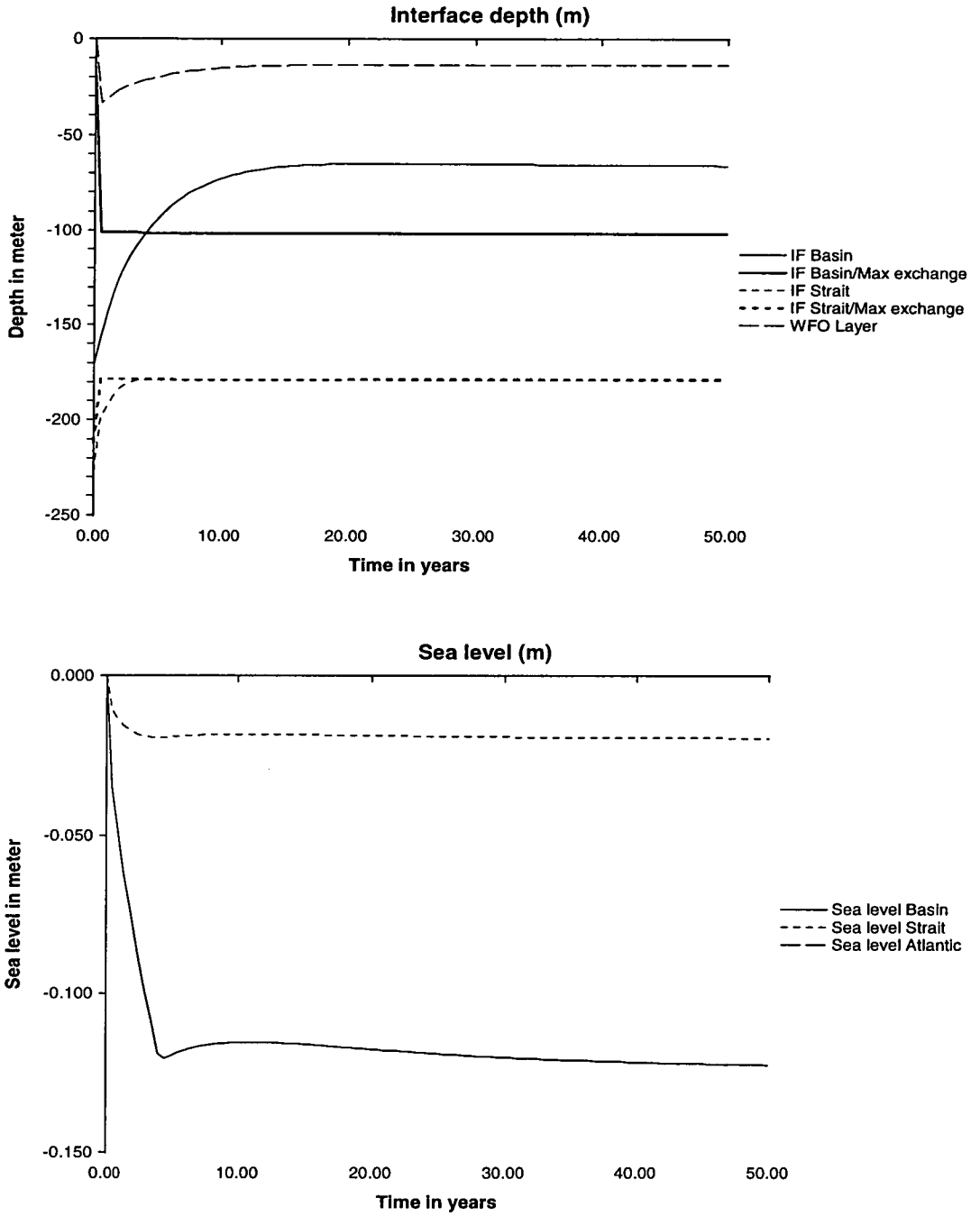

Figure 4.1: A HYCOBOX run with $\alpha = 0.25$, reaching maximal exchange after about 5 years. The graphs show the time evolution of the interface depth (top) and the sea level in the basin (solid lines) and in the Strait (dashed lines). The thick lines show the solution for maximal exchange.

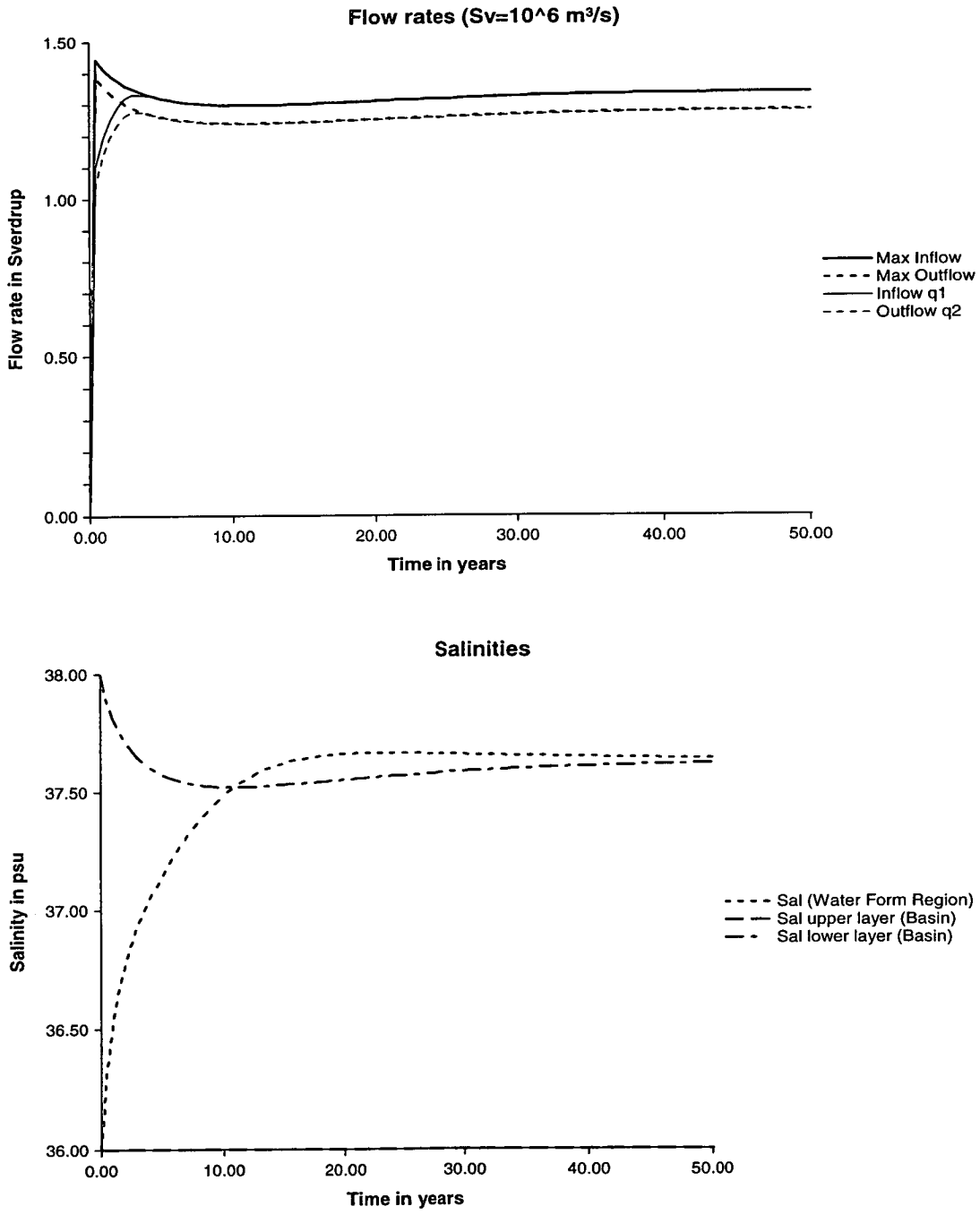

Figure 4.2: The same HYCOBOX run as in figure 4.1 leading to maximal exchange after about 5 years. The top graph shows the actual flow rates q_1 (solid line) and q_2 (dashed line), the thick lines show the solution for maximal exchange. The difference between in- and outflow is the net evaporation. The bottom graph shows the salinities S_L (dash-dotted line) and S_F (dashed line).

formation decreases with decreasing upper layer thickness, it finally reaches a level at which the water formation c_{FL} is equal to the maximal $q_2^{\max}$. The flow rates (figure 4.2 top) increase during the first five years until they reach the maximal solution (thick lines in figure 4.2 top). Note that the value of the maximal transport is not constant, but depends on the density difference between in- and outflow ($q \propto \sqrt{\rho_2 - \rho_1}$, as can be seen from the dimensionalisation in table 2.1). The density difference, however, changes as the basin salinity adjusts to the steady state (figure 4.2 bottom). The sea level difference between Atlantic and Mediterranean (figure 4.1 bottom) also increases, thus increasing the inflow q_1. Note that the slope of the sea level curve has a discontinuity when the exchange reaches maximal. The reason for this discontinuity is the intimate relation between inflow and sea level difference, and the fact that the inflow increases rapidly before it reaches the maximal regime, whereas it changes only slowly in the maximal regime following salinity changes.

The flow rates in figure 4.2 also illustrate that the concept of "maximal exchange" is an ambiguous one. "Maximal exchange" should not be misunderstood to imply that there is a uniquely defined or universal maximal value for the possible flow through the strait (see also section 2.4). Instead, the maximal flow allowed by the strait dynamics always depends on the density difference, which is not constant.

The second HYCOBOX run (figure 4.3 and 4.4) illustrates a situation ($\alpha = 0.12$) in which the maximal regime is not reached. Figure 4.3 (top) shows that the interface stays below the threshold necessary for the maximal regime, and the flow rate does not reach the maximal value (figure 4.4 top).

In both cases, the final state does not depend on the initial state, i. e. the parameter α determines uniquely whether the system will evolve into a maximal or submaximal regime, independent of the initial conditions. Figure 4.5 summarises the final state for a series of experiments with different α. For $\alpha < 0.18$ (submaximal regime), the flow rate q_1 and the salinity difference $S_2 - S_1$ show the expected inverse relationship (4.8).

4.2 Feedback mechanisms and their relevant timescales

While the steady state is easy to characterise by global budget constraints, it is important to note that the system need not be in the steady state at all times. Neither does

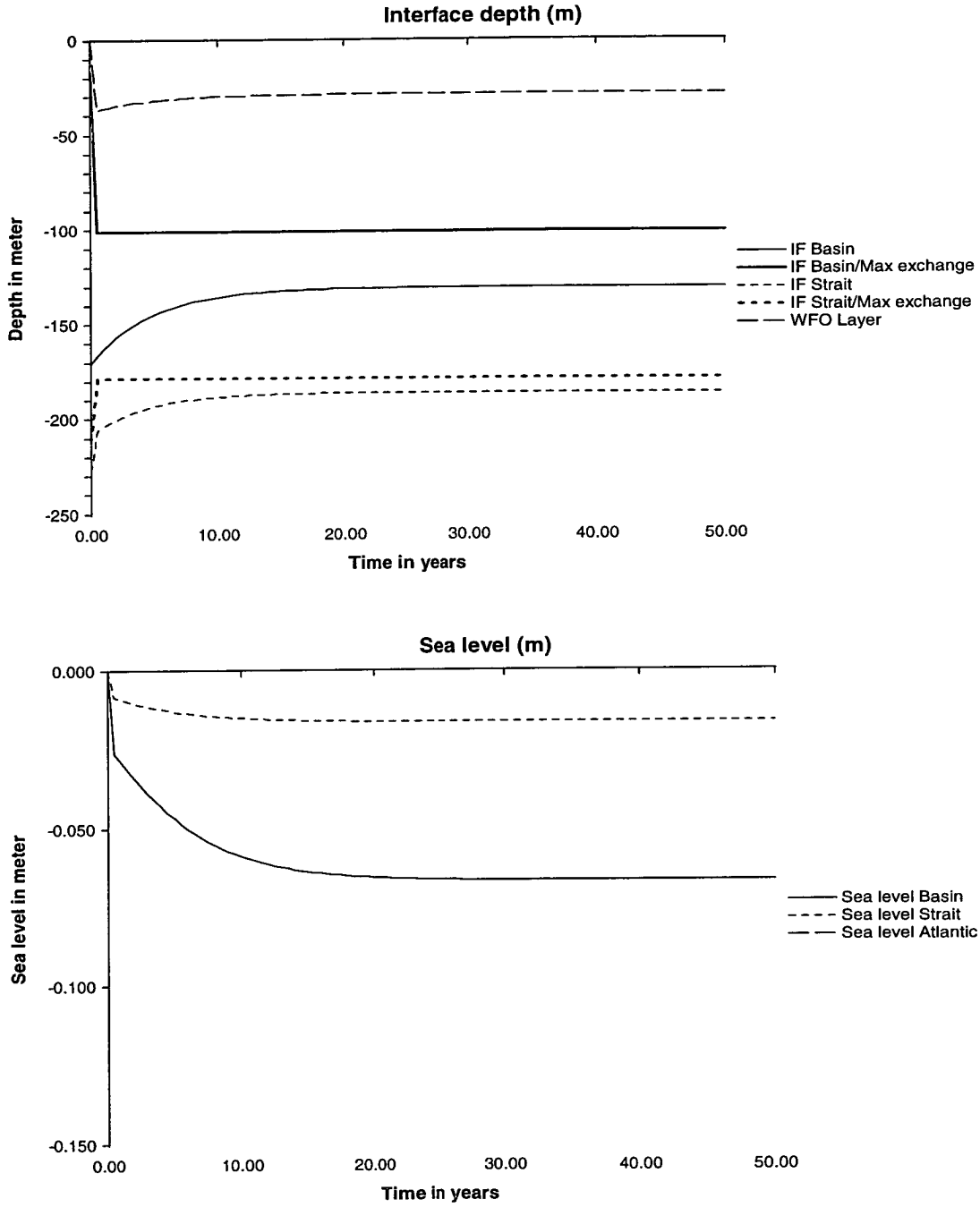

Figure 4.3: A HYCOBOX run with $\alpha = 0.12$. The maximal exchange is never reached. For a description of the different lines, see the caption to figure 4.1

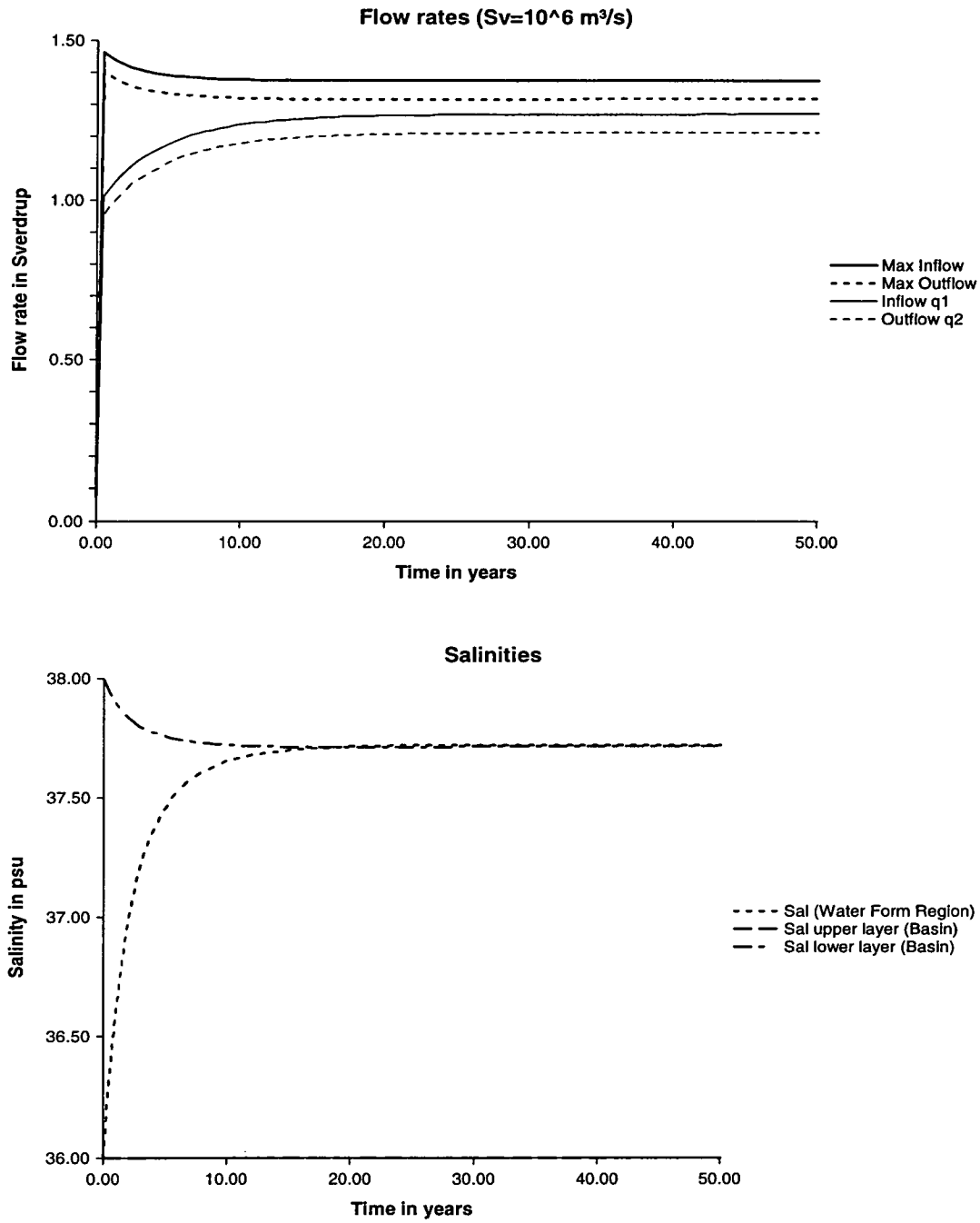

Figure 4.4: The same HYCOBOX run as in figure 4.3 in which maximal exchange is not reached. Details as in figure 4.2.

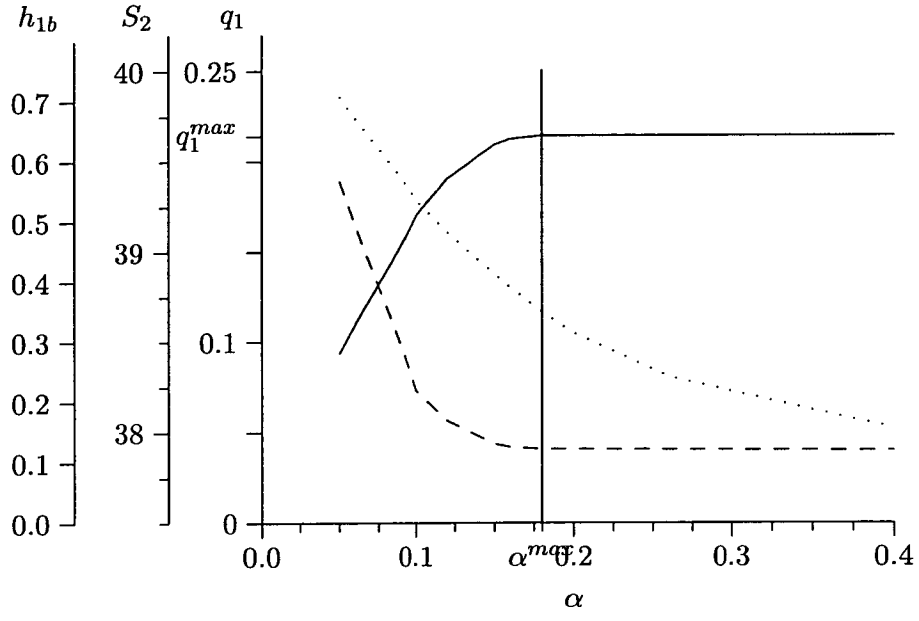

Figure 4.5: Values for h_{1b} (dotted line), S_2 (dashed line) and q_1 (solid line) in a steady state for different values of the parameter α. For $\alpha > 0.18$, the system reaches maximal exchange. For the upper layer salinity a value of $S_1 = 36$ psu was chosen.

HYCOBOX assume balanced budgets a priori, as was obvious in the HYCOBOX runs shown in figures 4.1, 4.2, 4.3, 4.4. One of the aims of this study is to investigate the transient features of the system and its reaction to changing boundary conditions. In this section, the adjustment timescales for different feedback mechanisms are discussed and illustrated with HYCOBOX experiments.

There are a number of negative feedback mechanisms that lead the system back to the steady state. Their characteristic timescales are calculated here assuming a small perturbation from the steady state. In this section, these perturbations are mainly used as mathematical tools and do not necessarily represent physical situations. A more physical approach follows in the next chapter 5, where the system response to changing external conditions is investigated.

4.2.1 Water budget

In the steady state, the net evaporation over the basin $E - P$ balances the net strait exchange Q

$$Q = q_1 + q_2 = E - P \tag{4.15}$$

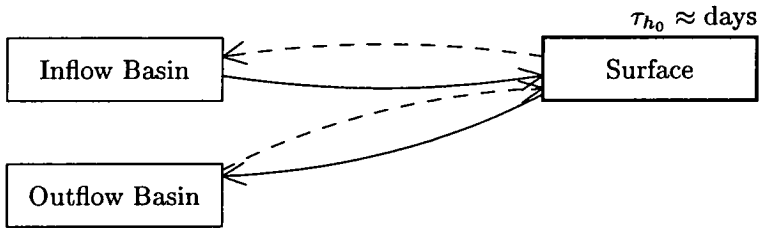

Figure 4.6: The feedback balancing the water budget. Positive influences (e. g. inflow increases → sea surface goes up) are represented by solid lines, negative influences by dashed lines. Each loop has an overall negative sign, i. e. the feedback is stable. The change in sea level dominates the time scale (thick box).

A balanced water budget is achieved by a simple negative feedback. If the excess evaporation over the basin is higher than the net exchange Q, then the sea level in the basin will drop, i. e. the sea level difference between basin and Atlantic will increase. From (3.7) and (3.8) the inflow q_1 is proportional to the square root of the sea level difference

$$q_1 = k \cdot \sqrt{h_{0b} - h_{0a}} \qquad \text{with} \quad k = h_{1b}\sqrt{\frac{2\rho_1}{\rho_2 - \rho_1}} \tag{4.16}$$

where h_{1b} and the densities ρ_i change only on timescales considerably longer than h_{0b} (see below).

On the other hand, the outflow q_2 reacts on the sea level as follows. From (3.6)

$$1 = \left(\frac{q_1^2}{a_{1s}^3} + \frac{q_2^2}{(1 - a_{1s} - a_{0s})^3}\right) W_1 \tag{4.17}$$

follows that $q_1^2 + q_2^2 \approx$ const, as a_{0s} is smaller than a_{tot} by a factor of 1000, and all the other parameters change only on much longer timescales. Therefore, if the sea level difference increases, q_1 will increase too, whereas q_2 decreases by a comparable amount. The net inflow into the basin goes up, and the sea level in the basin rises again, balancing the water budget. This feedback system is graphically represented in figure 4.6, where positive feedbacks (e. g. "inflow goes up → sea surface goes up") are shown as solid arrows and negative feedback as dashed arrows.

To estimate the timescale for this feedback, a small perturbation around the steady state is assumed. The sea level in the basin is

$$h_{0b} = h_{0b}^{\text{steady}} + h_{0b}^{\text{pert}} \qquad \text{with} \quad \frac{dh_{0b}^{\text{steady}}}{dt} = 0 \tag{4.18}$$

with all other quantities in the basin staying in the steady state. The only quantities that reacts to the changing sea level is $q_1 = q_1(h_{0b})$ and $q_2 = q_2(h_{0b})$, with the assumption (justified above) that $\frac{\partial q_1}{\partial h_{0b}} \approx \frac{\partial q_2}{\partial h_{0b}}$ (note that $q_2 < 0$). An expansion of (4.6), using also (4.4) and (4.5), leads to

$$\begin{aligned}
\frac{dh_{0b}^{\text{pert}}}{dt} &= \frac{1}{A}\left((E-P) - q_2(h_{0b}^{\text{steady}}) - \frac{\partial q_2}{\partial h_{0b}} \cdot h_{0b}^{\text{pert}} - q_1(h_{0b}^{\text{steady}}) - \frac{\partial q_1}{\partial h_{0b}} \cdot h_{0b}^{\text{pert}}\right) \\
&= -\frac{2}{A} \cdot \frac{\partial q_1}{\partial h_{0b}} \cdot h_{0b}^{\text{pert}} \\
&= -\frac{1}{\tau_{h_0}} \cdot h_{0b}^{\text{pert}} \qquad \text{with} \quad \tau_{h_0} := \frac{A}{2\frac{\partial q_1}{\partial h_{0b}}}
\end{aligned} \tag{4.19}$$

so that the system moves back to the steady state exponentially with a characteristic timescale of τ_{h0}. The characteristic timescale can be obtained from (4.16), leading to

$$\tau_{h_0} = \frac{A}{2\frac{\partial q_1}{\partial h_{0b}}} = \frac{A(h_{0b}^{\text{steady}} - h_{0a})}{q_1} \tag{4.20}$$

Therefore, the characteristic timescale (e-folding time) is the time that would be needed to fill the basin to the same sea level as the Atlantic with the current inflow, assuming that all outflow stopped. For the Mediterranean, realistic values are $q_1 = 1\,\text{Sv}$ and a sea level difference of 10 cm, leading to a characteristic timescale of

$$\tau_{h_0} = 2.4 \times 10^5\,\text{s} = 3\,\text{days} \tag{4.21}$$

This typical timescale is illustrated by an HYCOBOX experiment (figure 4.7). In this experiment, the sea level in the basin is artificially lowered from the steady state value of -16 cm to -41 cm relative to the Atlantic. After about three weeks (0.06 years), the sea level has again reached the steady state value. The e-folding time in this experiment is 4 days.

As the timescale for changes in sea level is of the order of days, the water budget can be assumed to be essentially balanced when changes on a seasonal scale or longer term trends are considered. As an aside, however, note that atmospheric pressure changes occur on similar timescales, leading to important implications for the inverse barometer effect, which links sea levels to atmospheric pressure changes. The Mediterranean reacts to pressure changes neither like the free ocean nor like an enclosed basin, but complicated corrections to the inverse barometer effects are necessary (see e. g. Le Traon and Gauzelin 1997, Candela 1991).

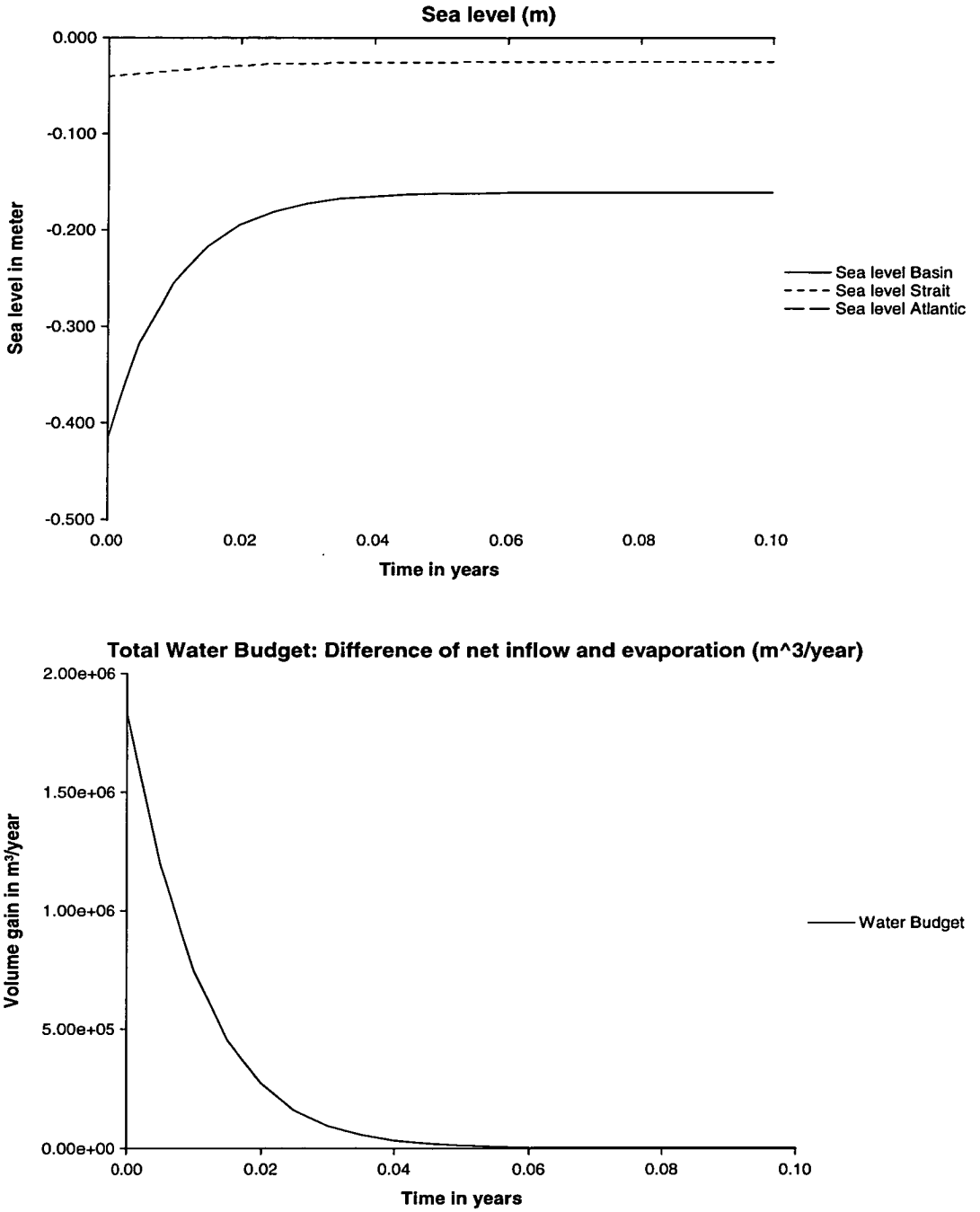

Figure 4.7: The characteristic timescale for changes in sea level. Top graph: The sea level in the basin. Bottom: The water budget, i. e. the net inflow into the basin. At $t = 0$, the sea level is artificially changed from the steady state value. The characteristic timescale (e-folding time) is ≈ 0.011 years ≈ 4 days.

4.2.2 Salt budget

Knudsen's relation holds for a steady state, in which there is no net exchange of salt:

$$S_1 q_1 + S_2 q_2 = 0 \tag{4.22}$$

or

$$q = \frac{S_1 + S_2}{S_2 - S_1} Q = \frac{S_1 + S_2}{S_2 - S_1} (E - P) \tag{4.23}$$

The feedback system regulating the salt budget is more complex than the one for the water budget, as there are several possible ways for the basin to react to an unbalanced salt budget, depending on details of the water formation processes.

The salt budget can be discussed in (at least) two different ways, namely in terms of absolute salt content of the basin, or in terms of salt transport rates. In the first case, an unbalanced salt budget is seen as an excess or lack of salt in the basin compared to the steady state. In the second case, an unbalanced salt budget is seen as a net in- or outflow of salt, without reference to the total salt content. The two perspectives are linked by noting that an excess salt content in the basin in general means a net outflow of salt through the strait. While the first perspective may be more intuitive, it should be kept in mind that it is also possibly more misleading, because the total salt content in the steady state is not uniquely determined by the budget equations. In particular, in the maximal regime only the salinity difference between the layers is determined, but not the volume of each layer[2].

Assume the salt budget is unbalanced after some perturbation of the system, e. g. there is an excess of salt in the basin compared to the steady state, leading to a net outflow of salt. Excessive salt can either mean a higher salinity of the lower layer, or a larger volume of the lower layer, i. e. a shallower interface. This leads two basic mechanisms through which the salt budget can be balanced:

Salinity: A net outflow of salt can lead to a salinity decrease in the lower layer. As S_2 – and subsequently to a lesser extent $q_2 \propto \sqrt{\Delta\rho}$ – increases, more salt is

[2]For the water formation parameterisations used in the HYCOBOX model runs, there is a feedback between water formation rate and interface, so that the interface is effectively fixed too. However, as this is a somewhat artificial feature of the HYCOBOX model, it is not advisable to unnecessarily include it into a general discussion of the feedback.

transported out of the basin. The reverse happens for a negative salt budget.

Interface depth: Instead of changing the salinity of the deep water, an unbalanced salt budget could change the amount of high salinity water in the basin. A net outflow of salt would lower the interface between deep and surface layers, and (3.9, 3.10, 3.12) show that a change in interface depth affects the outflow q_2. The inflow q_1 then adjusts as a secondary effect through the sea level feedback described above. A decrease in q_2 therefore leads the system back to a balanced salt budget.

For net inflow of salt and rising interface, the outflow can only increase as long as the system is submaximal. Once the maximal exchange is reached, the system can only balance excess inflow of salt by increasing the salinity of the lower layer.

Therefore there is an asymmetry between maximal and submaximal regime: In the submaximal regime, both changes in salinity and interface depth affect the salt budget, whereas in the maximal regime changes in interface depth have no effect on the salt budget.

The interface feedback

The two mechanisms have different characteristic timescales. For the change in interface depth (see figure 4.8), the calculation of the characteristic timescale is similar to the calculation for changing sea level. Assuming a perturbation around the steady state

$$h_{U'} = h_{U'}^{\text{steady}} + h_{U'}^{\text{pert}} \qquad \text{with} \quad \frac{dh_{U'}^{\text{steady}}}{dt} = 0 \tag{4.24}$$

Inserting this in (4.4), where both the inflow q_1 and the water formation rate c_{FL} are functions of $h_{U'}$, yields

$$\begin{aligned} A\frac{dh_{U'}}{dt} &= -(E-P) + \left(q_1(h_{U'}^{\text{steady}}) + \frac{dq_1}{dh_{U'}}h_{U'}^{\text{pert}}\right) \\ &\quad - \left(c_{FL}(h_{U'}^{\text{steady}}) + \frac{dc_{FL}}{dh_{U'}}h_{U'}^{\text{pert}}\right) \\ \frac{dh_{U'}^{\text{pert}}}{dt} &= -\frac{1}{A}\left(\frac{dc_{FL}}{dh_{U'}} - \frac{dq_1}{dh_{U'}}\right)h_{U'}^{\text{pert}} \end{aligned} \tag{4.25}$$

Therefore

$$\tau_{h_U} := \frac{A}{\frac{dc_{FL}}{dh_{U'}} - \frac{dq_1}{dh_{U'}}} \tag{4.26}$$

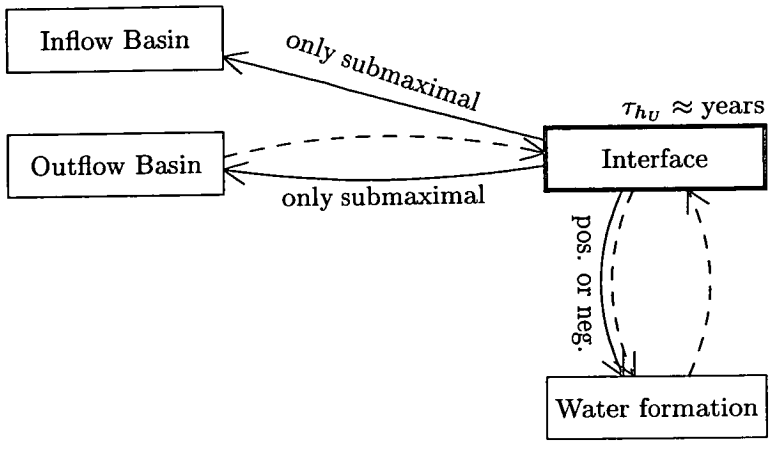

Figure 4.8: The interface feedback. The movement of the interface depth is the dominant timescale (thick box) $\tau_{h_{U'}}$. The strait transport depends on the interface only in the submaximal regime. The stability of the feedback between interface depth and water formation depends on the details of the water formation parameterisation, in particular the sign of $\frac{dc_{FL}}{dh_{U'}}$ (see table 4.1 below).

The first term in the denominator characterises the response of the basin to changing interface depth, the second term characterises the response of the strait. The term $\frac{dq_1}{dh_{U'}}$ vanishes for maximal exchange. For submaximal exchange, its value cannot be calculated explicitly from the strait equations, but an estimate from figure 2.4 (noting that $h_{1b} = h_{U'}$ for submaximal exchange) gives approximate values of -0.5 in nondimensional units. Therefore

$$\frac{dq_1}{dh_{U'}} = \begin{cases} 0 & \text{maximal regime} \\ -0.8 \ldots 1.4 \times 10^4\,\mathrm{m^2/s} & \text{submaximal regime} \end{cases} \tag{4.27}$$

where the value for the submaximal regime depends on the density difference and the depth of the interface.

The term describing the basin response depends on the parameterisation of the water formation rate. For a rough estimate of the order of magnitude of τ_{h_U}, the water formation rate can be assumed to be proportional to the thickness of the upper layer $c_{FL} = \alpha h_{U'}$ (see also (3.38)), leading to

$$\frac{dc_{FL}}{dh_{U'}} = \alpha = \frac{c_{FL}}{h_{U'}} \tag{4.28}$$

As numerical examples, the values from the two experiments shown above (figure 4.1,

case	regime	$\frac{dq_1}{dh_{U'}}$	$\frac{dc_{FL}}{dh_{U'}}$	stability
(i)	maximal	$\frac{dq_1}{dh_{U'}} = 0$	$\frac{dc_{FL}}{dh_{U'}} > 0$	stable
(ii)			$\frac{dc_{FL}}{dh_{U'}} < 0$	unstable
(iii)	submaximal	$\frac{dq_1}{dh_{U'}} < 0$	$\frac{dc_{FL}}{dh_{U'}} > 0$	stable
(iv)			$\frac{dq_1}{dh_{U'}} < \frac{dc_{FL}}{dh_{U'}} < 0$	stable
(v)			$\frac{dc_{FL}}{dh_{U'}} < \frac{dq_1}{dh_{U'}} < 0$	unstable

Table 4.1: Stability of the steady solution for the interface depth.

4.2, 4.3, 4.4) give

$$A\frac{dc_{FL}}{dh_{U'}} = \begin{cases} 0.25\,\text{year}^{-1} \cdot \text{A} = 1.9 \times 10^4\,\text{m}^2/\text{s} & \text{maximal regime} \\ 0.12\,\text{year}^{-1} \cdot \text{A} = 0.9 \times 10^4\,\text{m}^2/\text{s} & \text{submaximal regime} \end{cases} \tag{4.29}$$

Therefore the characteristic timescale for changes in interface depth in both the maximal and the submaximal situation is

$$\tau_{h_U} \approx 1.2 \approx 10^8\,\text{s} \approx 4\,\text{years} \tag{4.30}$$

The interface feedback is illustrated with a HYCOBOX experiment shown in figure 4.9. In this experiment, the interface depth was changed artificially from its steady state value of 76 m to 56 m. After approximately 20 years, it has returned to the steady state. The e-folding time in this experiment is 4.2 years, well in agreement with the above calculation.

As the water formation parameterisation $c_{FL}(h_{U'})$ in general cannot be further specified at this point, there is the possibility that $\tau_{h_{U'}}$ is negative. In this case, (4.25) is an exponentially growing function, i. e. the steady state is unstable. This is in contrast to the sea level feedback above and the salinity feedback below, which are always stable feedback mechanisms.

The sign of $\tau_{h_{U'}}$ depends on the sign and relative size of the derivative of the water formation rate $\frac{dc_{FL}}{dh_{U'}}$. The different possible cases are summarised in table 4.1. Note that the steady state is stable if $\frac{dc_{FL}}{dh_{U'}} > 0$ (situations (i) and (iii) in table 4.1), i. e. the water formation rate increases with increasing upper layer thickness.

In the two situations (ii) and (v) the steady state is unstable. In the maximal case (ii), it is sufficient that $\frac{dc_{FL}}{dh_{U'}} < 0$, whereas in the submaximal case (v) the stronger

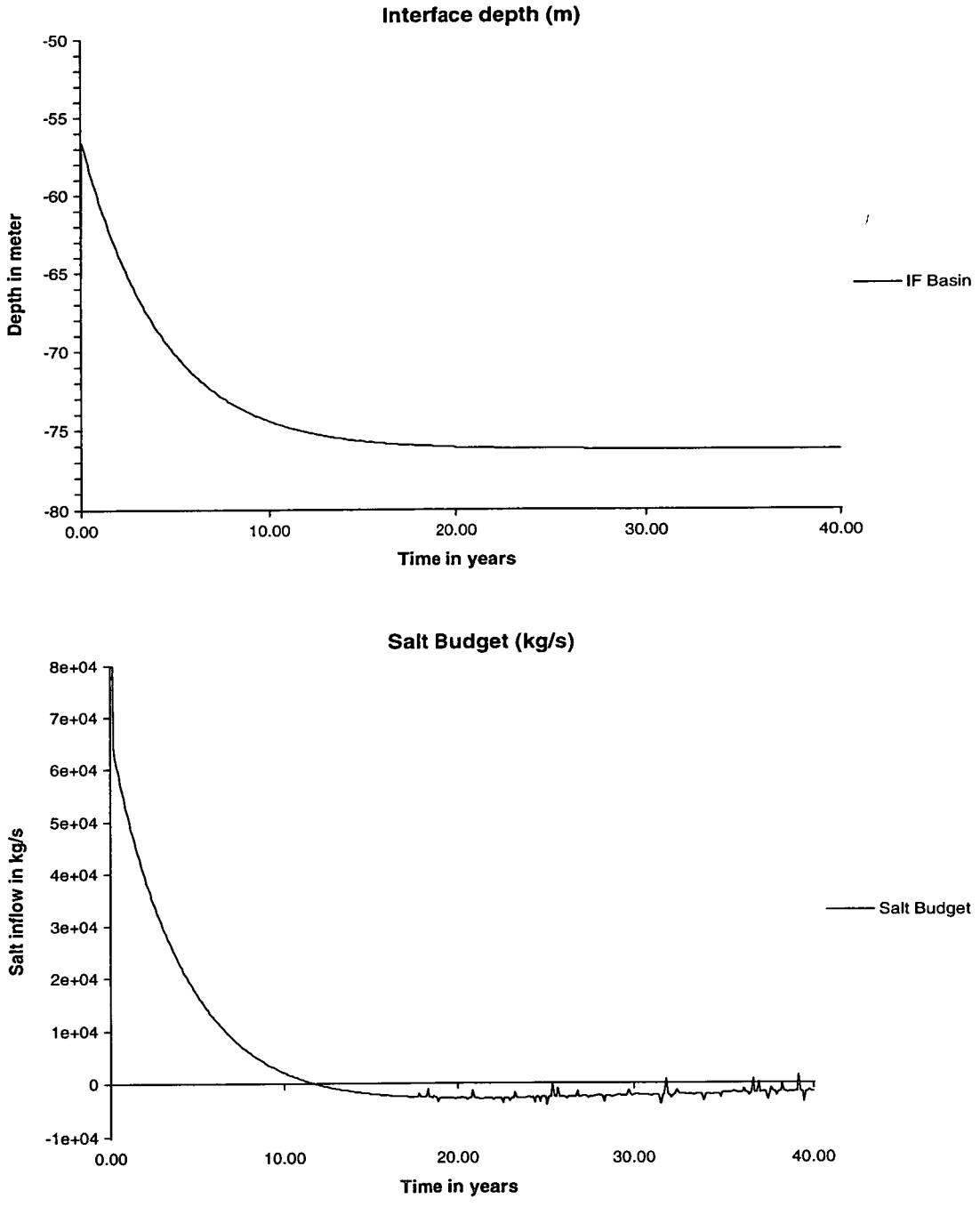

Figure 4.9: The characteristic timescale for the adjustment of the interface depth in the basin. Top: The interface depth in the basin. Bottom: The salt budget, i. e. the net salt inflow into the basin. At $t = 0$, the interface is artificially changed from 76 m to 56 m. The characteristic timescale is ≈ 4.2 years. Note that the salt budget is still slightly unbalanced at $t = 40$. This is due to a salinity change and reflects the longer salinity timescale (see section 4.2.2).

condition $\frac{dc_{FL}}{dh_{U'}} < \frac{dq_1}{dh_{U'}}$ applies, where it should be noted that $\frac{dq_1}{dh_{U'}}$ approaches zero when the interface depth approaches the switchover depth (see figure 2.4). Is the possibility of an unstable situation realistic, or can it be assumed that the feedback is always stable? In particular, is there a possibility for a mechanism that leads the system necessarily from the submaximal to the maximal regime, or vice versa?

Firstly, it should be noted that three water formation parameterisations used in HYCOBOX (see section 3.4) have $\frac{\partial c_{FL}}{\partial h_{U'}} > 0$. However, this does not imply that the total derivative is positive, if other parameters change in the parameterisation of c_{FL} change with $h_{U'}$.

For very small $h_{U'}$, i. e. very thin upper layer, the water formation necessarily has to decrease with decreasing layer thickness, making $\frac{dc_{FL}}{dh_{U'}} > 0$, which ensures that an exponentially fast movement of the interface is certainly stopped when reaching the sea surface. On the other hand, for a deep interface it is difficult to imagine that the water formation rate shows any strong dependence on the interface depth, as water formation will mostly take place in the upper part, i. e. $\frac{dc_{FL}}{dh_{U'}} \approx 0$ for a deep interface. This makes it very unlikely that the submaximal unstable situation (v) is possible in the regime far from the switchover point.

However, there is a possibility that unstable situations arise with intermediate interface depths above or closely below the switchover point, where a small excursion of $\frac{dc_{FL}}{dh_{U'}}$ into the negative is sufficient. A physical mechanism for this instability can be imagined if the water formation is assumed to be monotonically increasing with the density difference, as the HYCOBOX parameterisation (D). In this case, if the interface drops and the volume of the upper layer increases, the density difference will tend to decrease, because the air-sea-fluxes now act on a larger volume. With decreasing density difference, the water formation rate decreases. However, as will be seen in section 5.2, this is only a temporary effect, as the density difference then increases as an secondary adjustment to the lowered interface depth and the decreased strait transport.

The salinity feedback

The second mechanism that restores a balanced salt budgets acts through changing the salinity of the lower layer. To estimate its characteristic timescale τ_{S_2}, again a

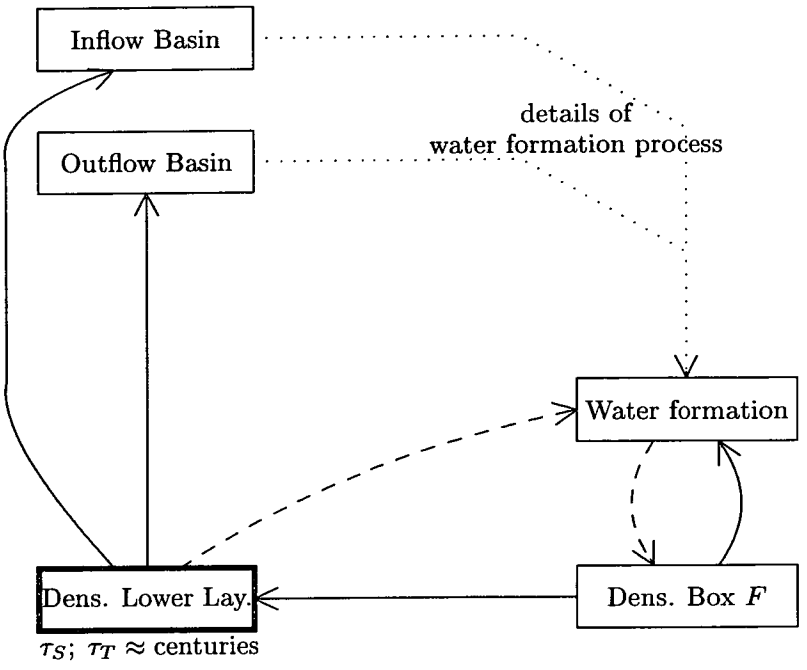

Figure 4.10: The density feedback, with a timescale of τ_S or τ_T respectively, dominated by slow reaction of the density in the lower layer.

perturbation around the steady state is assumed.

$$S_2 = S_2^{\text{steady}} + S_2^{\text{pert}} \tag{4.31}$$

For the simplified system (4.4, 4.5, 4.6), the equation for the lower layer salinity (3.34) is

$$Ah_L \frac{dS_2}{dt} = (E - P)S_1 + c_{FL}(S_1 - S_2) \tag{4.32}$$

Therefore

$$\frac{dS_2^{\text{pert}}}{dt} = -\frac{1}{\tau_S} \cdot S_2^{\text{pert}} \qquad \text{with} \qquad \tau_S := \frac{Ah_L}{c_{FL}} \tag{4.33}$$

For basin depth with an average depth of $h_L = 1000\,\text{m}$ and an area of $2.4 \times 10^{12}\,\text{m}^2$, and a water formation rate of $c_{FL} = 1.5\,\text{Sv}$, we find that

$$\tau_S \approx 1.6 \times 10^9\,\text{s} = 50\,\text{years} \tag{4.34}$$

The salinity feedback is illustrated with a HYCOBOX experiment shown in figure 4.11. The interface depth was changed artificially from its steady state value of 76 m to 56 m. The return to the steady state takes approximately 200 years, and follows an exponentially decaying curve with an e-folding time of 44 years.

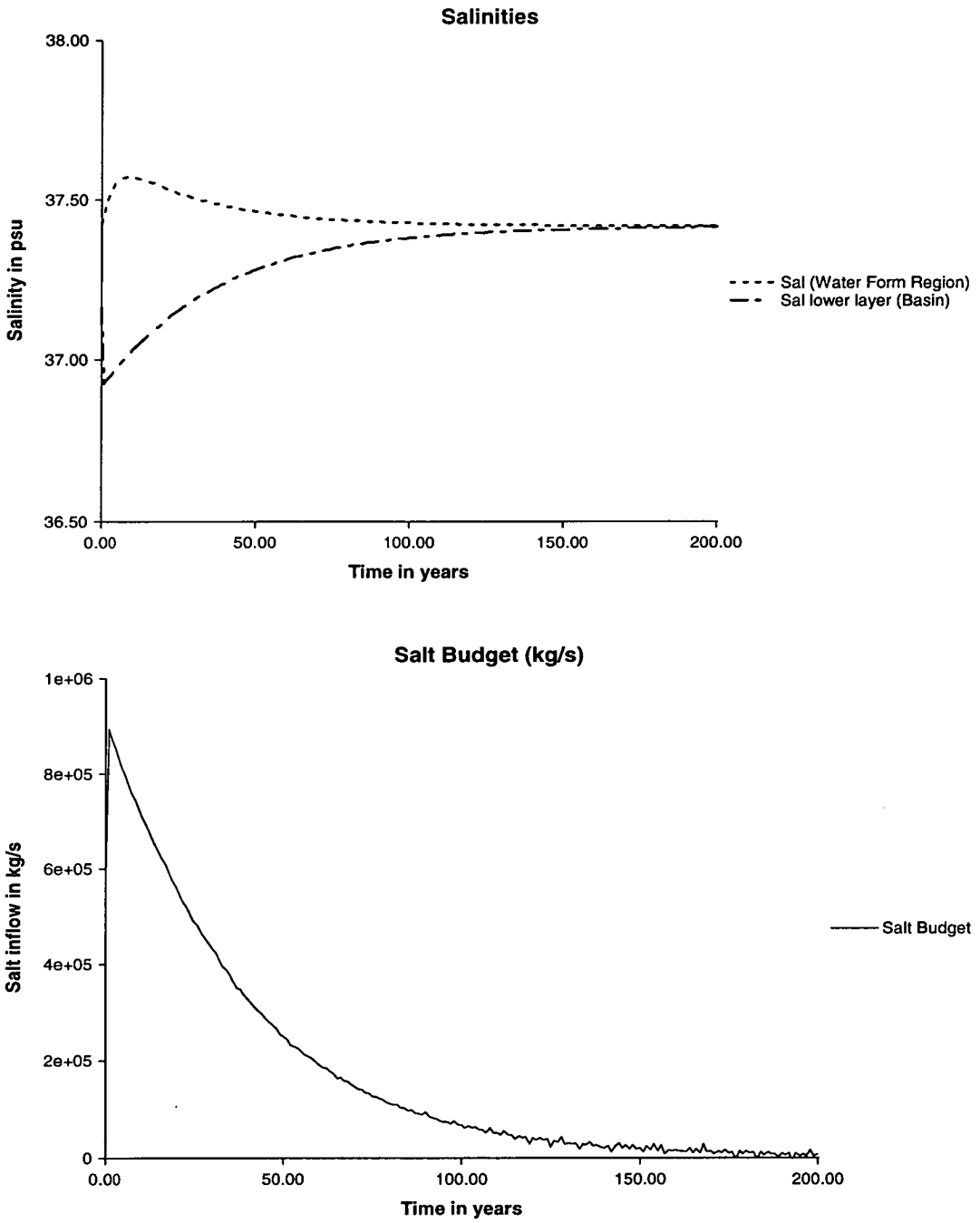

Figure 4.11: The characteristic timescale for the adjustment of the salinity. Top: The salinity of the lower layer and the water formation box. Bottom: The salt budget, i. e. the net salt inflow into the basin. At $t = 0$, the lower layer salinity is artificially changed from 37.4 psu to 36.9 psu. The characteristic timescale is ≈ 44 years.

4.2.3 Heat budget

The mechanisms restoring the heat budget (4.3) are similar to the mechanisms restoring the salt budget.

Temperature If the heat loss over the basin is not balanced by a net inward heat transport through the strait, the system can react by decreasing the temperature of the intermediate and deep water, thus increasing the net heat transport into the basin.

Interface depth Instead of decreasing the temperature of the intermediate water, a larger amount can be formed, thus raising the interface. If the system is in the submaximal regime, this will increase the strait transport and therefore balance the heat budget.

Similar to the salt budget, the interface mechanism can only act in the submaximal case. The characteristic timescales $\tau_T = \tau_S$ and τ_{h_U} are the same as for the salt budget.

Figure 4.11 shows a HYCOBOX experiment, in which the temperature of the lower layer was artificially changed from its steady state value of 13.4 °C to 14.4 °C. Similar to the experiment for the salinity feedback (figure 4.12), the exponential return to the steady state takes approximately 200 years, and the e-folding time is 44 years, in agreement with the calculation for $\tau_T = \tau_S$ (4.34).

4.2.4 The different timescales in perspective

The previous discussion shows that there are three distinct timescales with which the system reacts to perturbations or changes in the boundary conditions:

Days: The sea level and therefore the water budget adjusts within a few days.

Years: The interface feedback reacts on timescales of a few years.

Decades to centuries: The salinity and temperature of the basin have characteristic timescales of several decades or even centuries, depending on the depth of the water that is affected.

Figure 4.13 summarises the different feedback mechanisms and timescales.

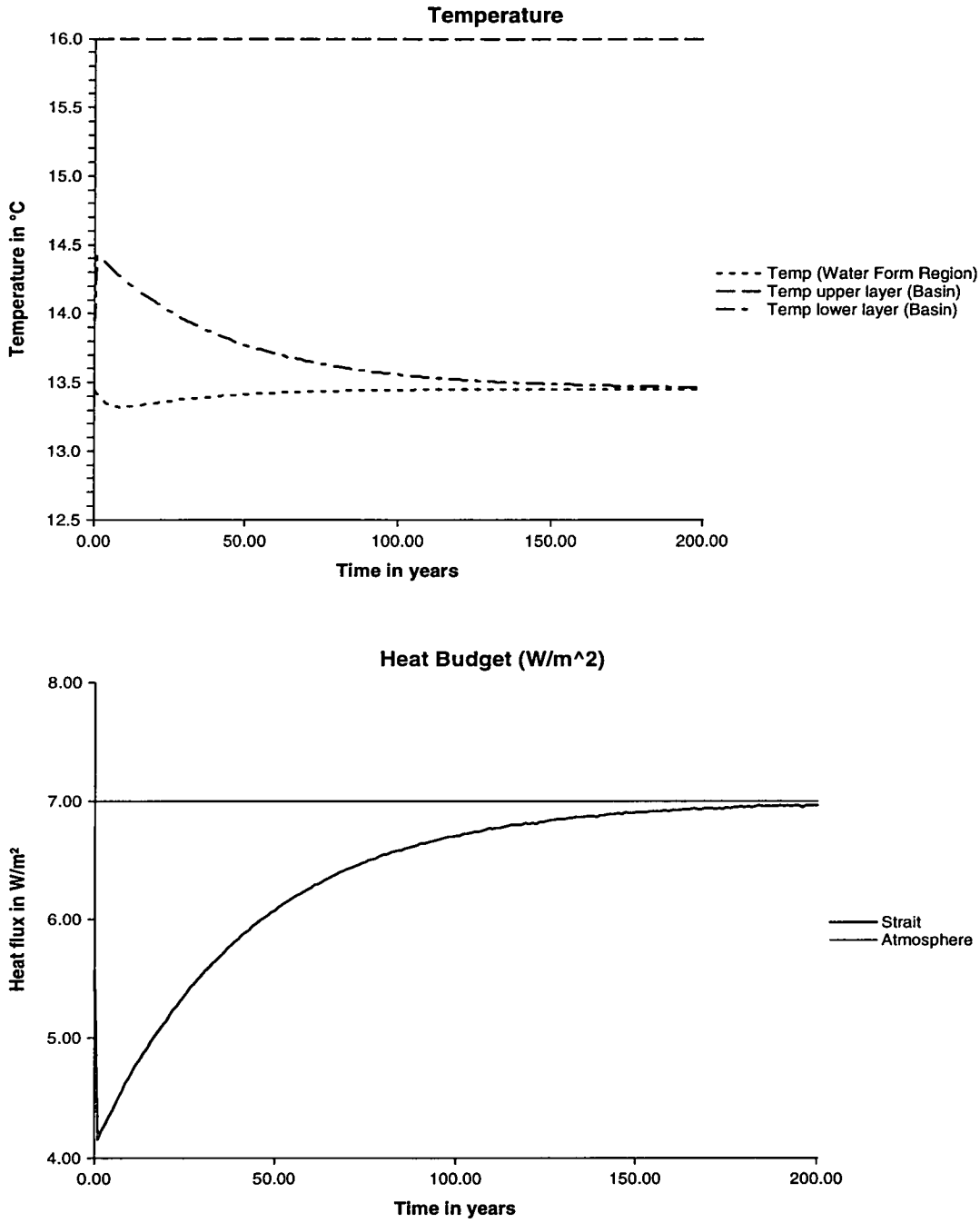

Figure 4.12: The characteristic timescale for the adjustment of the temperature. Top: The temperature of the lower layer and the water formation box. Bottom: The heat budget, i. e. the net transport of heat into the basin, and the heat loss to the atmosphere. At $t = 0$, the lower layer temperature is artificially changed from 13.4 °C to 14.4 °C. The characteristic timescale is ≈ 44 years.

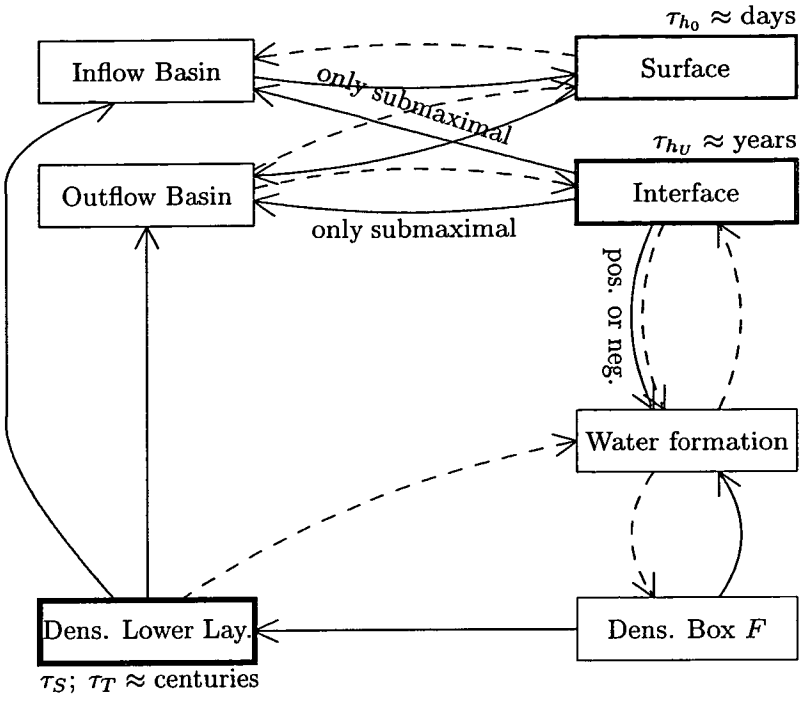

Figure 4.13: The feedback mechanisms between basin and strait. The three dominant timescales are indicated by increasingly thick boxes with $\tau_S > \tau_{h_U} > \tau_{h_0}$.

The clear hierarchy of timescales can also be seen in the HYCOBOX runs in figures 4.1-4.4. The long term behaviour is dominated by the slow change of lower layer salinity (figure 4.2 and 4.4 bottom). The interface depth (figure 4.1 and 4.3 top) changes strongly within the first 10 years, but then changes only slowly following the salinity changes. On the timescales shown on these figures, the sea level (figure 4.1 and 4.3 bottom) does not exhibit an independent dynamic, but mirrors the timescales given by the interface adjustment during the first 10 years and the slower salinity adjustment thereafter. The two mechanism affecting the salt and heat budgets have timescales considerably longer than a year. Therefore they cannot follow seasonal cycles, so that the heat and salt budgets will in general be out of balance.

All mechanisms, with the possible exception of the interface mechanism, are stable feedback mechanisms, pushing the system towards the steady state discussed in section 4.1. This also means that there is no intrinsic mechanism that favours the maximal regime over the submaximal regime. Whether the steady state is submaximal or maximal is determined by the water formation rate: If the water formation mechanism is

such that a small amount of highly saline water is formed (as in the experiment shown in figure 4.3 and 4.4), then the steady state will be in the submaximal regime with comparatively small strait transport and higher salinity difference between in- and outflow, whereas a water formation mechanism that produces larger amounts of less saline water will lead to a maximal situation (e. g. the experiment in figure 4.1 and 4.2). There are no obvious fundamental constraints on the water formation process that determine its nature.

However, it seems plausible that mixing between the layers in the basin makes it more likely that the system is in the maximal regime or close to it. Mixing tends to reduce the stratification and therefore favours the formation of larger amounts of less dense water, and it also tends to reduce the density of the lower layer. The mixing therefore might be seen as contributing to the total effective water formation. The contribution of mixing is more pronounced in the submaximal regime, where the primary water formation rate and the strait transport are low. Therefore there has to be a considerable and – for a large basin – unlikely reduction in the water formation rate for the system to maintain a submaximal steady state.

Although this so-called overmixing argument (Bryden and Stommel 1984) is a plausible physical mechanism, and gains some support from the fact that the observed values for the salinity difference and strait transport in the Mediterranean Sea are indeed the expected values for a maximal or close-to-maximal regime, it does not provide a fundamental constraint that guarantees maximal exchange in all circumstances. In terms of the HYCOBOX model, the choice of the water formation parameters α, μ or ζ (depending on the type of water formation parameterisation used – see chapter 3.4) still determines the regime, although the overmixing mechanism reduces the parameter space that leads to the submaximal regime.

While this chapter investigated the feedback mechanisms from an abstract point of view, the next chapter uses HYCOBOX experiments to discuss how these different mechanisms interact in more realistic cases where the system is subject to changing air-sea-fluxes.

Chapter 5

Effect of changing boundary conditions

To understand changes occurring in the Mediterranean, both now and in past times, the response of the system to changing boundary conditions has to be investigated. For example, the damming of large rivers systems in the 20th century reduced the freshwater input into the Eastern Mediterranean, and the salinity should be expected to increase with an appropriate time-lag. Changing atmospheric conditions, e. g. due to global warming, also change the freshwater and heat budgets. This section discusses a series of HYCOBOX experiments in which the excess evaporation $E - P$ and/or the heat loss H_{Atm} were changed, looking particularly at the transition between the old and the new steady state.

The discussion in section 4.1 made clear that the basin response is very much influenced by the parameterisation of the water formation process c_{FL}, so that definite results are not possible without a clearer definition of c_{FL}. However, while some restrictions on c_{FL} come from general physical ideas, there is no good parameterisation that can be said to be well supported by theory or observation. Therefore, instead of presenting one parameterisation, the three different simple but fundamental parameterisations that were introduced in section 3.4 is used and the response of the respective systems to changing boundary conditions compared. It may be possible in future to compare this work with observations and thus obtain further information about the water formation process.

For changes in the net evaporation $E - P$, the appropriate change in the steady state of the system can be described by a comparatively simple mathematical relation (the "SQE equation") between the salinity difference ΔS, the strait transport q and the evaporation $E - P$. While the steady states generally change in an easily predictable way with changing air-sea-fluxes (and show only small differences between the different water formation parameterisations), the transition to the new steady state as a result of air-sea-flux changes can develop an interesting behaviour. In particular, for the most realistic density dependent water formation parameterisation (D), the system reacts to a sudden change in air-sea-fluxes with a significant excursion away from the steady state, even if the final steady state is not too different from the initial steady state. Furthermore, the different feedback mechanisms interact in interesting ways, so that e. g. a change in the net evaporation does not only influence the salinities of the layers in the basin, but also the temperatures, even when – somewhat artificially – the heat loss is kept constant while the excess evaporation changes.

The last section of this chapter discusses the relevance of these experiments for observed recent changes in the Mediterranean Sea.

5.1 The SQE equation

Before describing the experiments in detail, it is useful to derive a "rule of thumb" that can be used to estimate the expected shift of the steady state as a response to changing conditions, i. e. a relation for changes in q and ΔS as a function of changes in $E - P$. In the following, the original steady state is denoted by a subscript $\cdot_{\text{old}}$ (e. g. $(E-P)_{\text{old}}$), the new state with a subscript $\cdot_{\text{new}}$.

For the following calculation, it is initially assumed that the system is in the maximal regime throughout, so that the strait exchange is clearly defined. Modifications for submaximal situations are discussed subsequently. In the maximal regime, the strait transport is

$$q = \tilde{q}\sqrt{g'D}DW = k_1\sqrt{\Delta\rho} \tag{5.1}$$

where $\tilde{q}$ is the non-dimensional strait transport (as has been discussed in section 3.5, this is a geometry-dependent quantity with a maximal value of $\tilde{q}^{\max}$), and k_1 contains

everything that is not of interest here. For a first approximation, it is assumed that the density difference is mainly produced by salinity differences, whereas temperature differences play a smaller role – an assumption often made for the Strait of Gibraltar (see e. g. Bryden and Stommel 1984). Therefore $\Delta\rho = \beta\Delta S$ from (B.4), and (5.1) simplifies to

$$q = k_2\sqrt{\Delta S} \tag{5.2}$$

On the other hand, the salt budget equation (4.7) leads to

$$q = \frac{S_2 + S_1}{\Delta S}(E - P) =: k_3\frac{E - P}{\Delta S} \tag{5.3}$$

where $k_3 = S_1 + S_2$ will – for the moment – be assumed to be constant and not affected by relatively small changes in salinity. Eliminating ΔS from (5.2) and (5.3) yields

$$q = \left(k_2^2 k_3 (E - P)\right)^{1/3} \tag{5.4}$$

Inserting this in (5.3) gives another relationship

$$\Delta S = \left(\frac{k_3}{k_2}(E - P)\right)^{2/3} \tag{5.5}$$

Therefore, when comparing old and new steady states after a change in $E - P$ there is a simple mutual relation:

$$\left(\frac{\Delta S_{\text{new}}}{\Delta S_{\text{old}}}\right)^{3/2} = \left(\frac{q_{\text{new}}}{q_{\text{old}}}\right)^3 = \frac{(E - P)_{\text{new}}}{(E - P)_{\text{old}}} \tag{5.6}$$

Note that this result corrects the relation $q^2 \propto (E - P)$ used by Rohling (1991a).

In the following, this simple but useful equation will be referred to as the "SQE equation". In the derivation of this relation the assumption was made that the density difference is mainly produced by the salinity difference. This follows Bryden and Stommel (1984), who note that the temperature contributes about 3 % to the density difference. However, more recent observations (Baringer and Price 1997) indicate that the temperature difference may play a larger role. At the Camarinal Sill, the temperature of the outflow is 12.9 °C, while the inflow ranges between 13 °C and 20 °C, leading to an average temperature difference of approximately 3 °C. The salinity of the inflow is 36 psu, the salinity of most of the outflow approximately 38 psu. With these values, the salinity difference contributes 1.5 $\frac{\text{kg}}{\text{m}^3}$ to the total density difference, while

the temperature difference contributes 0.7 $\frac{\text{kg}}{\text{m}^3}$. In the HYCOBOX runs shown below the temperature contribution is comparable to these observations, if a heat loss of 7 $\frac{\text{W}}{\text{m}^2}$ over the basin is assumed.

Therefore, caution is warranted when using (5.6). When temperature effects are included, (5.2) is not an appropriate approximation of (5.1). Instead, the following ansatz can be used

$$q = k_4(\Delta S)^x \qquad \text{with} \quad x < 0.5 \tag{5.7}$$

where k_4 and x are determined by the function value and first derivative of $q(\Delta S)$ around the initial value of the salinity difference ΔS. Therefore,

$$x = \frac{\Delta S}{q} \cdot \frac{dq}{d\Delta S} \tag{5.8}$$

and, using (5.1) and (B.4)

$$x = \frac{1}{2} \cdot \frac{1}{1 - \frac{\alpha \Delta T}{\beta \Delta S}} \tag{5.9}$$

In the calculation of x any change in the salinity and temperature difference between the layers ΔS and ΔT is ignored and the assumption made that x can be calculated from the initial values of ΔS and ΔT. Obviously, if temperature is ignored ($\Delta T = 0$), then $x = \frac{1}{2}$, leading back to (5.2).

With the ansatz (5.7), the same calculation as above is possible, leading to a more general form of the SQE equation

$$\left(\frac{\Delta S_{\text{new}}}{\Delta S_{\text{old}}}\right)^{(1+x)} = \left(\frac{q_{\text{new}}}{q_{\text{old}}}\right)^{(1+1/x)} = \frac{(E-P)_{\text{new}}}{(E-P)_{\text{old}}} \tag{5.10}$$

where x is given by (5.9). For the values in the Strait of Gibraltar with $\Delta S \approx 2\,\text{psu}$ and $\Delta T \approx -3\,^\circ\text{C}$, this leads to $x \approx 1/3$, so that the appropriate SQE equation becomes

$$\left(\frac{\Delta S_{\text{new}}}{\Delta S_{\text{old}}}\right)^{4/3} = \left(\frac{q_{\text{new}}}{q_{\text{old}}}\right)^{4} = \frac{(E-P)_{\text{new}}}{(E-P)_{\text{old}}} \tag{5.11}$$

This form of the SQE relation holds when the changes in $E - P$ are such that the system remains in the maximal regime.

For the submaximal regime, further modifications are necessary. The budget equation (5.3) still holds. In the strait equation (5.1) and subsequently (5.2) and (5.7), however, the proportionality factors k_1, k_2 and k_4 incorporate the non-dimensional flow rate in the strait, which is a known constant in the maximal regime, but depends

on the interface depth in the submaximal case. Unfortunately, the interface depth cannot be assumed to have a definite known value, because its response to changing net evaporation $E - P$ depends on the water formation process. Two possible cases have to be considered:

Interface rises with $E - P$ An increase in $E - P$ may raise the interface by forming more lower layer water thus making k_1, k_2, k_4 larger. In this case, k_4 is a monotonically increasing functions of $E - P$.

Interface drops with $E - P$ Alternatively, if the water formation rate does not increase with increasing $E - P$, the interface will tend to drop, as the resulting higher salinity difference drives more water through the strait. In this case, k_4 is a monotonically decreasing functions of $E - P$.

As k_4 is no longer constant when $E - P$ changes, it cannot be cancelled in the derivation of (5.10). Making the ansatz

$$k_4 = k_5(E-P)^a \qquad \text{with} \quad \begin{cases} a > 0 & \text{if interface rises with } E-P \\ a < 0 & \text{if interface drops with } E-P \end{cases} \tag{5.12}$$

it is again possible to derive a more general form of the SQE relation

$$\left(\frac{\Delta S_{\text{new}}}{\Delta S_{\text{old}}}\right)^{\frac{1+x}{1-a}} = \left(\frac{q_{\text{new}}}{q_{\text{old}}}\right)^{\frac{1+x}{x+a}} = \frac{(E-P)_{\text{new}}}{(E-P)_{\text{old}}} \tag{5.13}$$

Therefore, if the interface rises with rising $E - P$, i. e. $a > 0$, the total transport q increases more strongly in the submaximal regime than in the maximal regime. Part of the increase is due to an increase in density difference – this is the only factor in the maximal case –, part is due to the fact that a rising interface leads the system closer to the maximal solution. The salinity difference, on the other hand, increases less than in the maximal case. The reverse happens if the interface drops with increasing $E - P$. As a final note, if the water formation is such that the interface does not change significantly (as is the case in the maximal regime), then $a = 0$, and (5.13) collapses to the maximal SQE equation (5.10).

Parameter	Symbol	Value
Strait geometry		triangular
Sill depth	D	284 m
Width of Narrows	W	12 km
Width of Sill	W_S	$2 \cdot W$
Basin Area	A	2.4×10^{12} m^2
Effective Basin Depth	H	1000 m
Salinity of the Atlantic inflow	S_A	36 psu
Temperature of the Atlantic inflow	T_A	16 °C

Table 5.1: The model parameters used for the series of experiments to investigate the effect of changes in air-sea flux. The values were chosen to be realistic for the Mediterranean Sea.

5.2 Experiments

To investigate the effect of changing air-sea fluxes for different water formation parameterisations, a series of HYCOBOX experiments were performed. Each of the experiments runs for 1000 years. The air-sea-fluxes are constant during the first 500 years, then change to new constant values for years 500-1000. The long timescale ensures that the system is in a steady state before the change occurs. The other model parameters that were kept constant between the runs are summarised in table 5.1 and are based on Mediterranean values.

For the different runs, the three water formation parameterisations (I), (D) and (E) (see section 3.4) were used. The free parameters in the different parameterisations were chosen such that the steady states for the first 500 years are the same for each of the parameterisations. Two different sets of parameters were used, one leading to a submaximal situation, and one leading to a maximal situation before the change in air-sea-flux. The characterisation of these states and the appropriate parameters are shown in table 5.2.

At $t = 500$ years, the air-sea-fluxes change. For each of the experiments in this set, either the net evaporation $E-P$ or the atmospheric heat flux H_{Atm} increase or decrease by 20 %, whereas the other remains constant. This choice is certainly artificial: The

Maximal regime	
Steady state	$E - P = 75\,\text{cm/year} \cdot A = 0.058\,\text{Sv}$
	$H_{\text{Atm}} = 7\,\text{W/m}^2 \cdot A = 17 \times 10^{12}\,\text{W}$
	$h_{U'} = 60\,\text{m}$
	$q_2 = 1.057\,\text{Sv}$
	$\Delta S = 1.97\,\text{psu}$
	$\Delta T = -3.49\,^\circ\text{C}$
Water form. param.	$\alpha = 1.77 \times 10^4\,\text{m}^2/\text{s} = 0.229\,\text{year}^{-1} \cdot A$
	$\mu = 4.28 \times 10^4\,\text{m}^5\,\text{kg}^{-1}\,\text{s}^{-1} = 0.555\,\text{m}^3\,\text{kg}^{-1}\,\text{year}^{-1} \cdot A$
	$\zeta = 0.305\,\text{m}^{-1}$
Submaximal regime	
Steady state	$E - P = 75\,\text{cm/year} \cdot A = 0.058\,\text{Sv}$
	$H_{\text{Atm}} = 7\,\text{W/m}^2 \cdot A = 17 \times 10^{12}\,\text{W}$
	$h_{U'} = 100\,\text{m}$
	$q_2 = 0.989\,\text{Sv}$
	$\Delta S = 2.11\,\text{psu}$
	$\Delta T = -3.68\,^\circ\text{C}$
Water form. param.	$\alpha = 1.14 \times 10^4\,\text{m}^2/\text{s} = 0.128\,\text{year}^{-1} \cdot A$
	$\mu = 2.14 \times 10^4\,\text{m}^5\,\text{kg}^{-1}\,\text{s}^{-1} = 0.278\,\text{m}^3\,\text{kg}^{-1}\,\text{year}^{-1} \cdot A$
	$\zeta = 0.171\,\text{m}^{-1}$

Table 5.2: The characterisation of the two steady states that were used as the basis for the experiments testing the sensitivity to changing air-sea-fluxes. The parameters α, μ and ζ were chosen such that the required steady state is reached for the respective parameterisation.

heat flux H_{Atm} includes the latent heat loss, and in realistic situations both evaporation and heat loss change simultaneously[1]. However, it is preferable to treat heat and water fluxes independently here, as the purpose of these experiments is to investigate the basic responses of the system.

With the three water formation parameterisations, in-/decrease in evaporation and heat, each for maximal and submaximal situations, a total of 24 experiments were performed. The experiments are labelled mnemonically as e. g. $\mathrm{D}_{\mathrm{m}}^{+E}$ for the experiment with the density dependent water formation parameterisation (D), maximal initial state and increasing $E - P$.

5.2.1 Experiments with changing net evaporation

The results for the twelve experiments for changes in net evaporation are summarised in table 5.3. We first discuss how the change in net evaporation changes the steady state of the system for each of the experiments. After that, the transitional effects following the onset of the sudden change in flux and the interaction between changes in temperature and salinity are described.

Table 5.3 lists the final steady state for each of the experiments. Furthermore, the individual parts of the SQE equation (5.10) are calculated for each experiment to facilitate the comparison of the model result with the theoretical expectations. The expected values for the SQE terms are 1.20 or 0.80 respectively, however the assumptions made in deriving the SQE equation together with the fact that the parameter x changes during the experiments leads to an estimated error of 0.02.

The main results of this set of experiments may be summarised as follows:

- All experiments with increasing evaporation, for all water formation parameterisations, show the expected increase in the salinity difference and in strait transport, the experiments with decreasing evaporation show a decrease in strait transport and salinity difference.

- The different water formation parameterisations lead to different final states. For increasing evaporation, the parameterisation (I) lowers the interface by a very

[1]However, one important recent change may affect only $E - P$: The damming of rives around the Mediterranean reduces the freshwater input, but not the heat loss.

Experiment	Evaporation/Heat Flux in-/decrease	Water form. param.	$h_{U'}$	q_2	ΔS	ΔT	x	$\left(\frac{q_{new}}{q_{old}}\right)^{(1+1/x)}$	$\left(\frac{\Delta S_{new}}{\Delta S_{old}}\right)^{(1+x)}$
Initial state maximal			60.0	1.057	1.97	-3.49	0.320		
I_m^{+E}	$E-P$ +20 %	(I)	62.3	1.100	2.27	-3.29	0.342	1.17	1.21
D_m^{+E}		(D)	58.7	1.100	2.27	-3.29	0.342	1.17	1.21
E_m^{+E}		(E)	51.9	1.100	2.27	-3.29	0.342	1.17	1.21
I_m^{-E}	$E-P$ −20 %	(I)	57.2	1.011	1.65	-3.65	0.293	0.82	0.80
D_m^{-E}		(D)	61.5	1.011	1.65	-3.65	0.293	0.82	0.80
E_m^{-E}		(E)	71.6	1.011	1.65	-3.65	0.293	0.82	0.80
Initial state submaximal			100.0	0.989	2.11	-3.68	0.321		
I_s^{+E}	$E-P$ +20 %	(I)	102.8	1.016	2.46	-3.56	0.342	1.11	1.23
D_s^{+E}		(D)	98.9	1.035	2.41	-3.48	0.342	1.20	1.20
E_s^{+E}		(E)	90.2	1.071	2.33	-3.36	0.342	1.37	1.14
I_s^{-E}	$E-P$ −20 %	(I)	97.0	0.958	1.74	-3.84	0.294	0.78	0.78
D_s^{-E}		(D)	101.1	0.940	1.78	-3.91	0.294	0.80	0.80
E_s^{-E}		(E)	111.5	0.883	1.89	-4.14	0.295	0.61	0.87

Table 5.3: HYCOBOX experiments to investigate the effect of changing net evaporation on the final steady state for different water formation parameterisations. Each row lists the final state at $t = 1000$ years. At the top, the initial state before the change is listed. For a discussion of the main features, see section 5.2.1.

small amount ($< 3\,\mathrm{m}$), the density-dependent parameterisation (D) raises the interface slightly ($< 2\,\mathrm{m}$), whereas the evaporation-dependent parameterisation (E) leads to a considerable rise of $\approx 10\,\mathrm{m}$. For decreasing evaporation, the reverse is true. In the submaximal experiments this difference in the final interface depth also leads to appropriate differences in strait transport and salinity difference between the experiments. For the experiments in the maximal regime, the salinity difference and strait transport are constrained by the strait and therefore are independent of the water formation parameterisation.

- All experiments in the maximal state show results that are in reasonable agreement with the SQE equation.

- For the experiments in the submaximal state, the SQE equation is only satisfied for experiments $\mathrm{D_s^{+E}}$, $\mathrm{I_s^{-E}}$ and $\mathrm{D_s^{-E}}$, in which the interface of the final steady state is not very different from the initial steady state. For experiments $\mathrm{E_s^{+E}}$ and $\mathrm{E_s^{-E}}$, in which the interface depth changes considerably, the SQE equation underestimates the change in strait transport, but overestimates the change in salinity difference. This result is consistent with the modified SQE relation (5.13).

- Even though the heat loss H_{Atm} was kept constant, the temperature difference showed a response that is inverse to the response of the salinity difference: Experiments with increasing salinity show a decrease in the temperature difference. For a salinity change of approximately 0.3 psu in each of the experiments, the temperature changes by $0.2\,^{\circ}\mathrm{C}$. This is a secondary effect: For increasing evaporation, the water formation rate increases, but the heat loss remains the same, so that the newly formed water experiences a smaller temperature change.

Comparing the three different water formation parameterisations, the main difference in the final steady state is the interface depth, but the differences are not extreme. However, the adjustment processes and transitional states show significant and qualitative differences. In the following, transitional effects in the three experiments with decreasing $E - P$ and initial maximal state ($\mathrm{I_m^{-E}}$, $\mathrm{E_m^{-E}}$ and $\mathrm{D_m^{-E}}$) are discussed. The other cases show qualitatively similar behaviour.

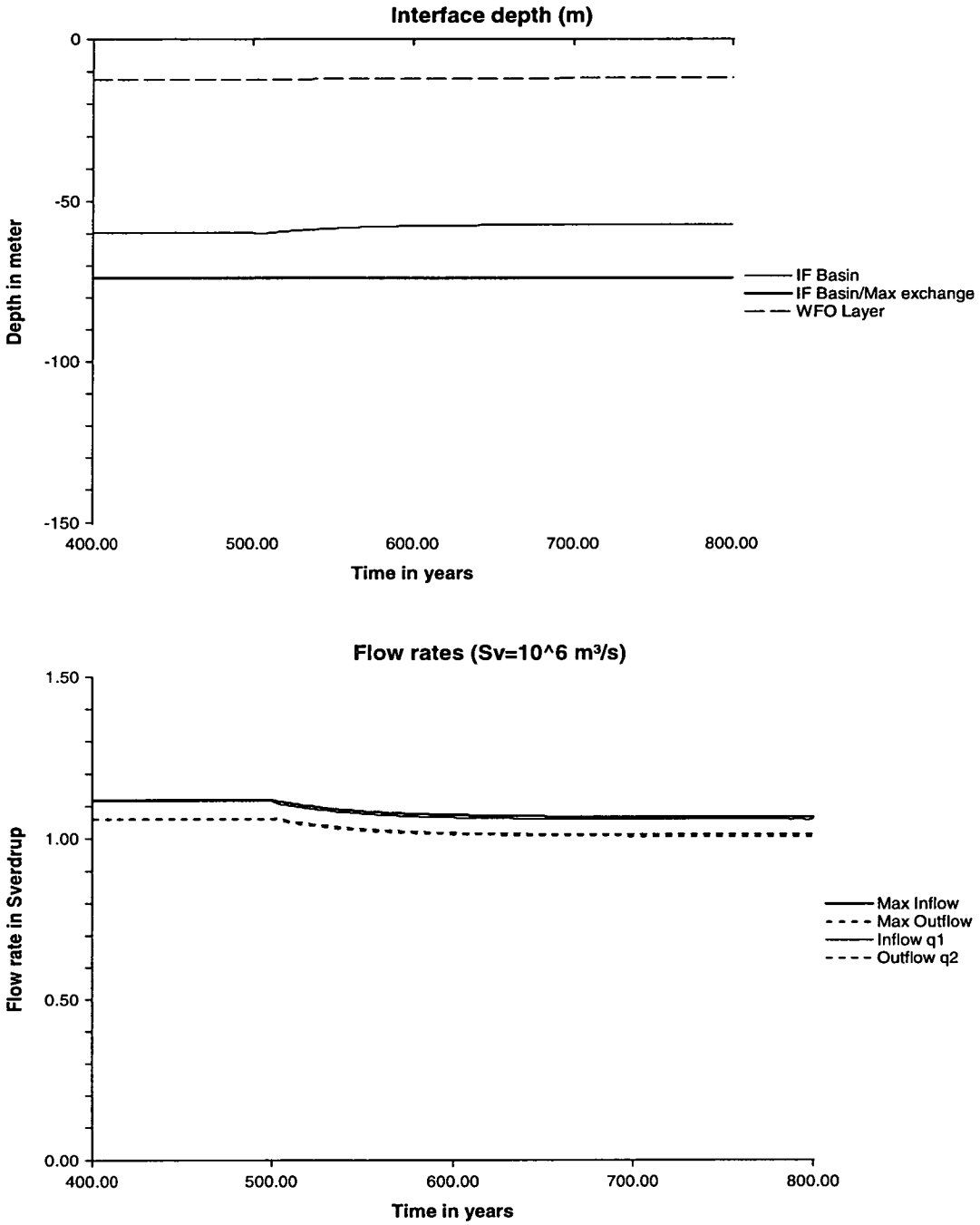

Figure 5.1: Interface depth and strait transport in experiment I_m^{-E}. After the decrease in evaporation at t=500 years, the strait transport (bottom) slowly decreases following the density changes (figure 5.2). The interface starts to rise (top), until the water formation rate again balances the strait transport.

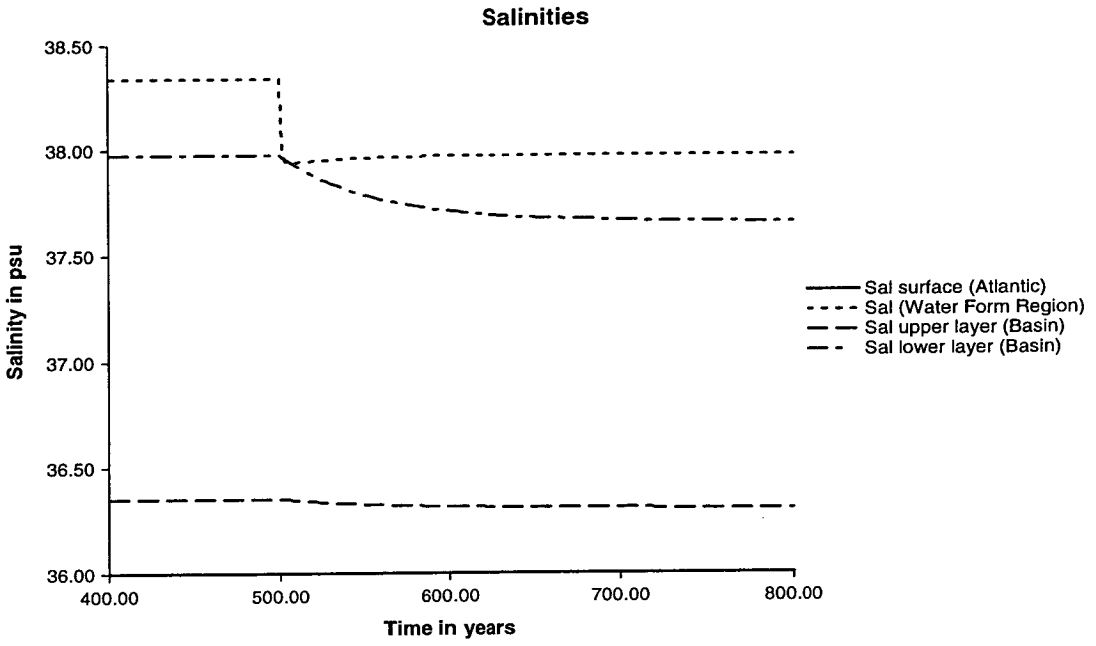

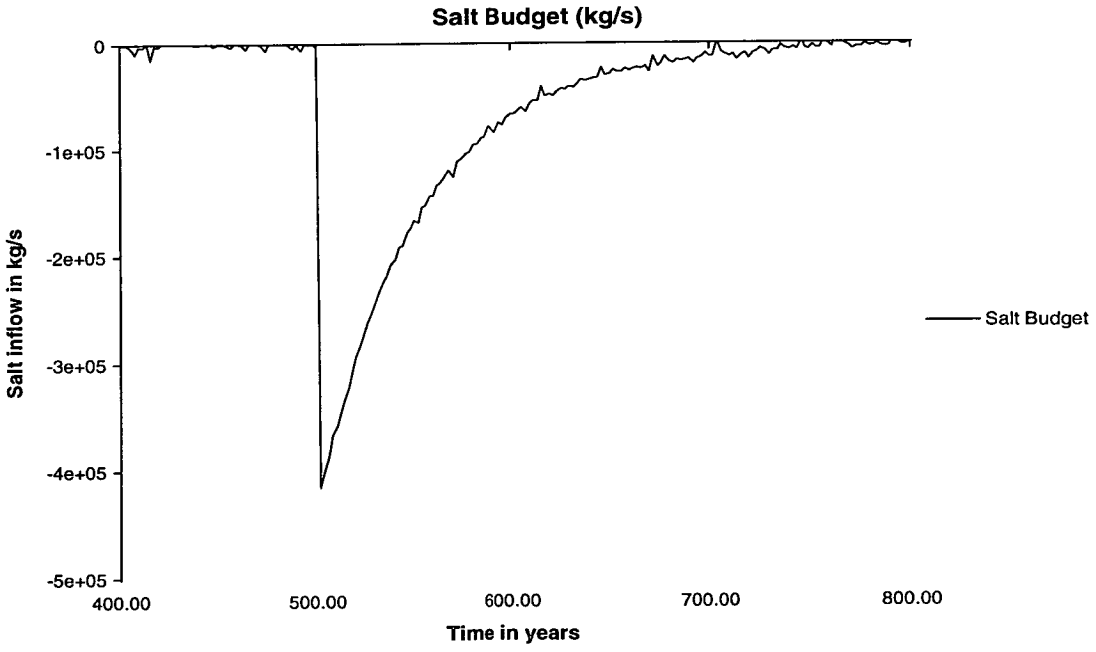

Figure 5.2: The salt budget in experiment I_m^{-E}. The e-folding time for the salt budget is $\tau_S = 60$ years.

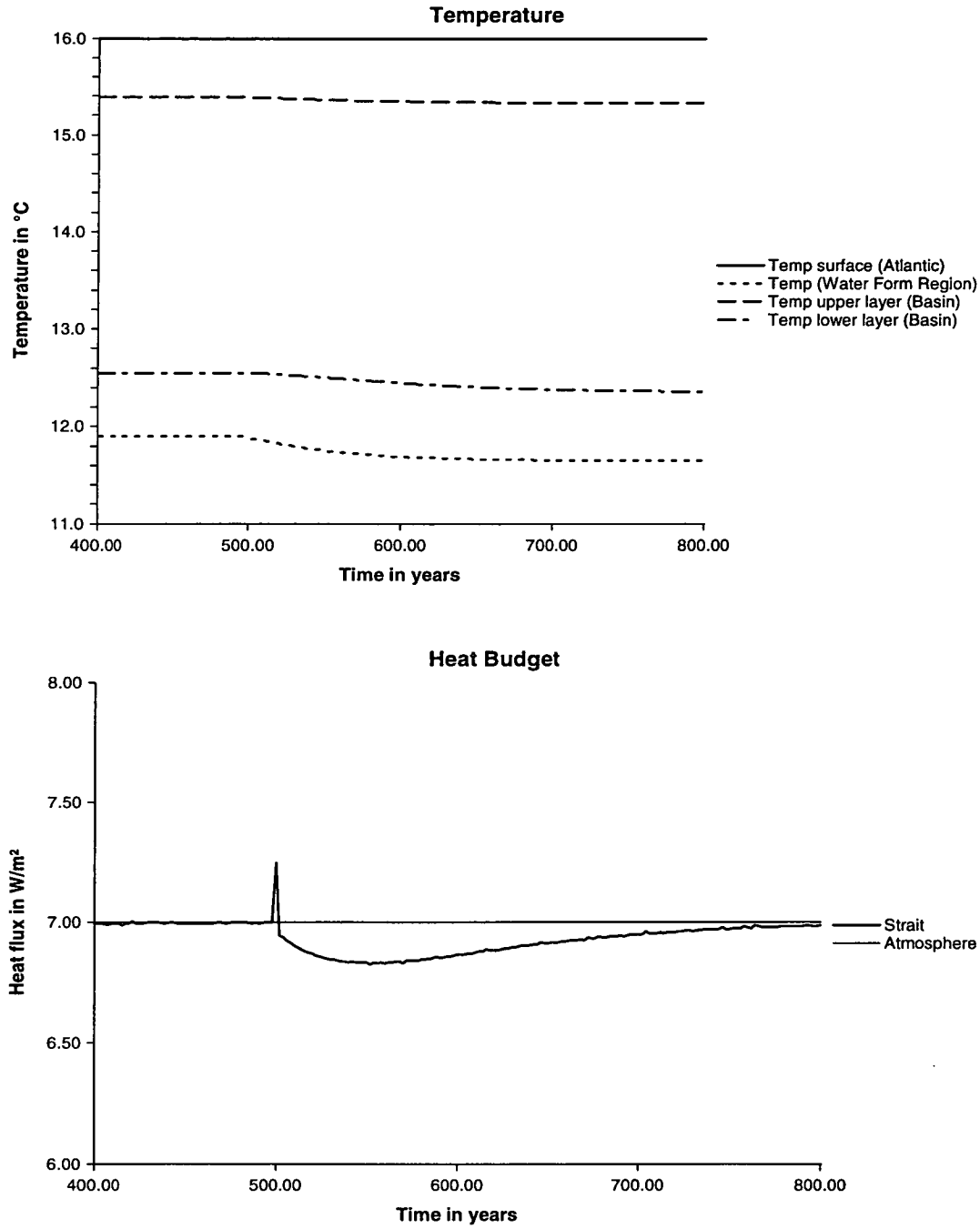

Figure 5.3: The heat budget in experiment I_m^{-E}. Although the heat loss was kept constant in this experiment, the temperature changes due to an interaction between heat and salt budgets. The positive spike in the heat budget at $t = 500$ is a numerical artefact.

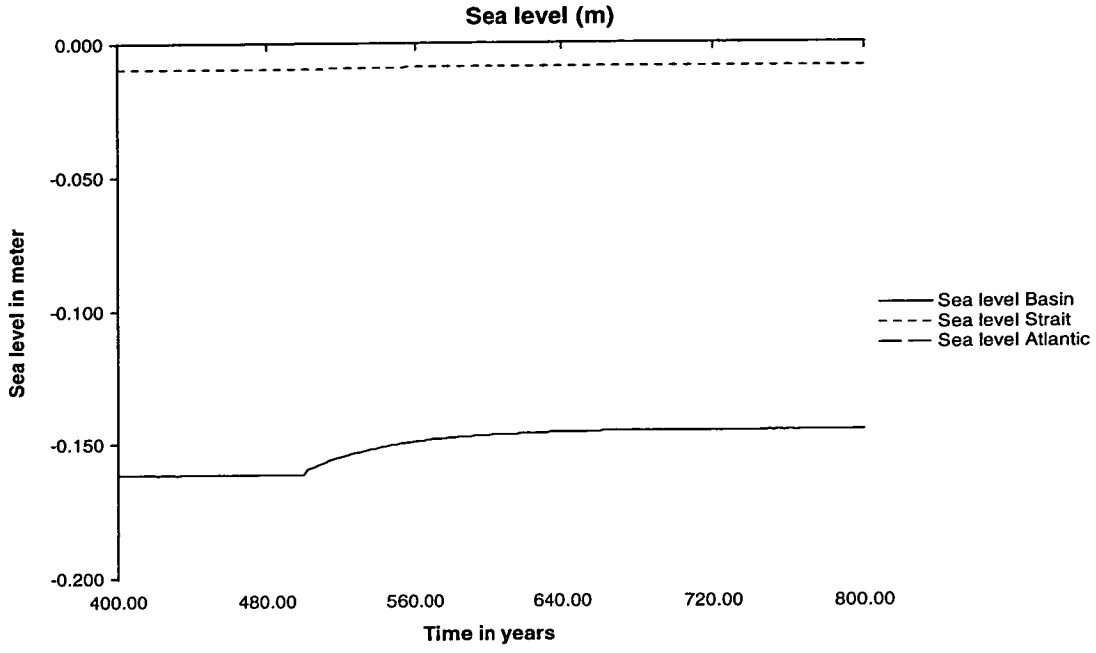

Figure 5.4: The sea level in experiment I_m^{-E} rises inside the basin, as the strait transport goes down.

Water formation parameterisation (I). Figures 5.1, 5.2, 5.3 and 5.4 show the transition between initial and final state for experiment I_m^{-E}, in which the water formation depends only on the interface depth $h_{U'}$. The transition between the initial and the final state is smooth and takes approximately 200 years, suggesting that it is dominated by the slow salinity feedback discussed in section 4.2.2.

The immediate effect of the sudden drop in net evaporation is an imbalance in the water budget, which is balanced within days by a small reduction of the inflow q_1. The short term adjustment of the water budget takes place in the same way as described above in section 4.2.1 and needs no further discussion here.

This reduction in inflow leads to an negative salt and heat budgets, as now less salt and heat are transported into the basin. Initially, the basin looses 4.5×10^5 kg/s salt (see figure 5.2 bottom), and the heat transport in the strait drops from an equivalent of $7.00\,\mathrm{W/m^2}$ to $6.94\,\mathrm{W/m^2}$ (figure 5.3 bottom.

The water formation rate, which only depends on the interface depth, does not change immediately, whereas the salinity of the water formation box (figure 5.2 top, dotted line) shows a sharp drop as a result of the reduced evaporation. As this less

dense water sinks and is mixed into the lower layer, the salinity of the lower layer (figure 5.2 top, dot-dashed line) slowly decreases too. This takes place on a timescale of a century (see the discussion in section 4.2.2).

With decreasing salinity and therefore density difference, the strait transport (figure 5.1 bottom) is reduced. The basin starts to fill up with lower layer water, i. e. the interface rises (figure 5.1 top), but this rise is limited by the fact that the water formation rate decreases with a shallower interface, so that the overall change in interface depth is small. In terms of the feedback mechanisms described in section 4.2, the water formation parameterisation (I) therefore leads to an almost pure salinity feedback.

Although the heat loss to the atmosphere H_{Atm} remains constant throughout the experiment, the temperature changes. As the water formation rate decreases slowly, the temperature of the water formation box T_F and consequently the temperature of the lower layer T_L (figure 5.3 top, dotted line and dot-dashed line) decreases. Therefore, the net heat transport through the strait increases, which eventually leads the heat budget (figure 5.3 bottom) back to a balanced state. However, initially this mechanism is offset by the decreasing strait transport, so that the net heat transport in the strait continues to *decrease* between $t = 500$ years and $t = 550$ years, and only then starts to return to a balanced situation.

The sea level in the basin (figure 5.4) rises by a small amount (≈ 2 cm). As the density difference goes down, the outflow is reduced, and to balance the water budget a smaller sea level difference is sufficient to drive the required inflow.

Water formation parameterisation (E). Figures 5.5, 5.6, 5.7 and 5.8 show the transition between initial and final state for experiment $\mathrm{E}_{\mathrm{m}}^{-E}$, in which the water formation parameterisation is proportional to the net evaporation $E-P$ and the interface depth $h_{U'}$. Unlike experiment $\mathrm{I}_{\mathrm{m}}^{-E}$, this experiment shows a considerable movement of the interface depth (figure 5.5 top graph) within the first 20 years. Therefore, the interface feedback (section 4.2.2) plays a major role in the adjustment.

With the evaporation-dependent water formation parameterisation (E), the water formation rate responds immediately to a change in net evaporation. The sharp decrease in net evaporation leads to a similarly sharp decrease in the water formation rate.

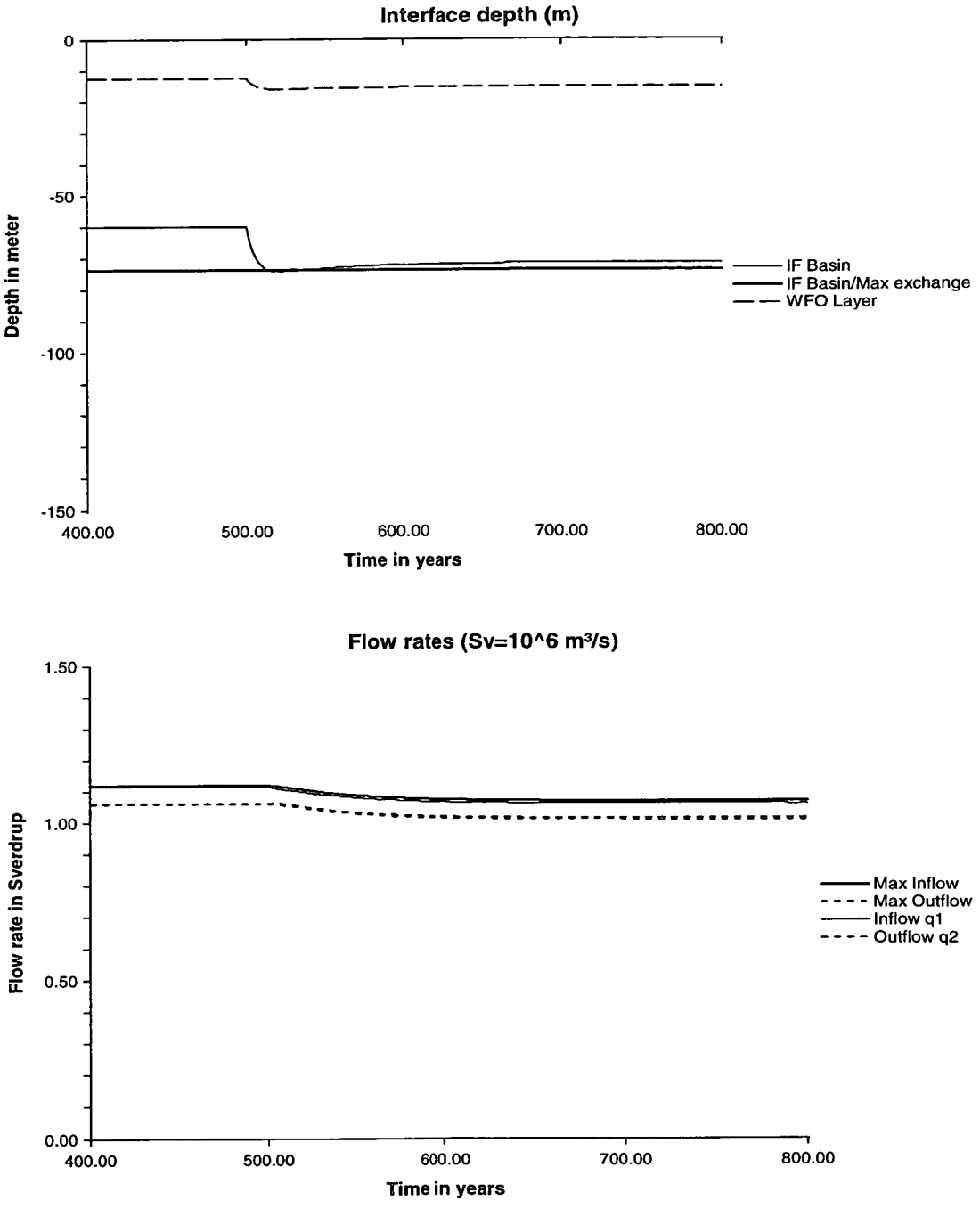

Figure 5.5: Interface depth and strait transport in experiment E_m^{-E}. The interface drops within a few years (top), the strait transport (bottom) follows the slower salinity adjustment.

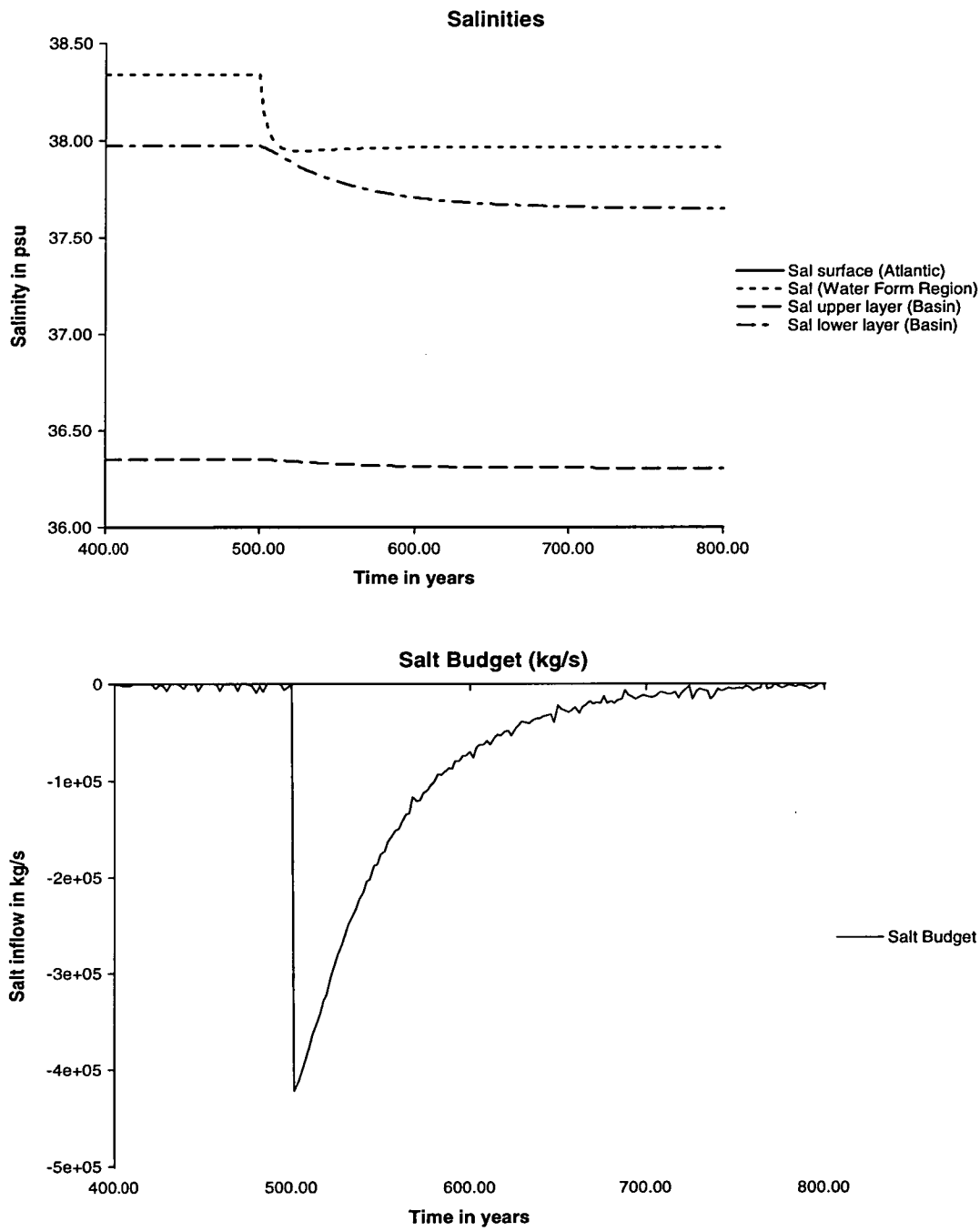

Figure 5.6: The salt budget in experiment $\mathrm{E}_{\mathrm{m}}^{-E}$. The e-folding time is $\tau_S = 60$ years.

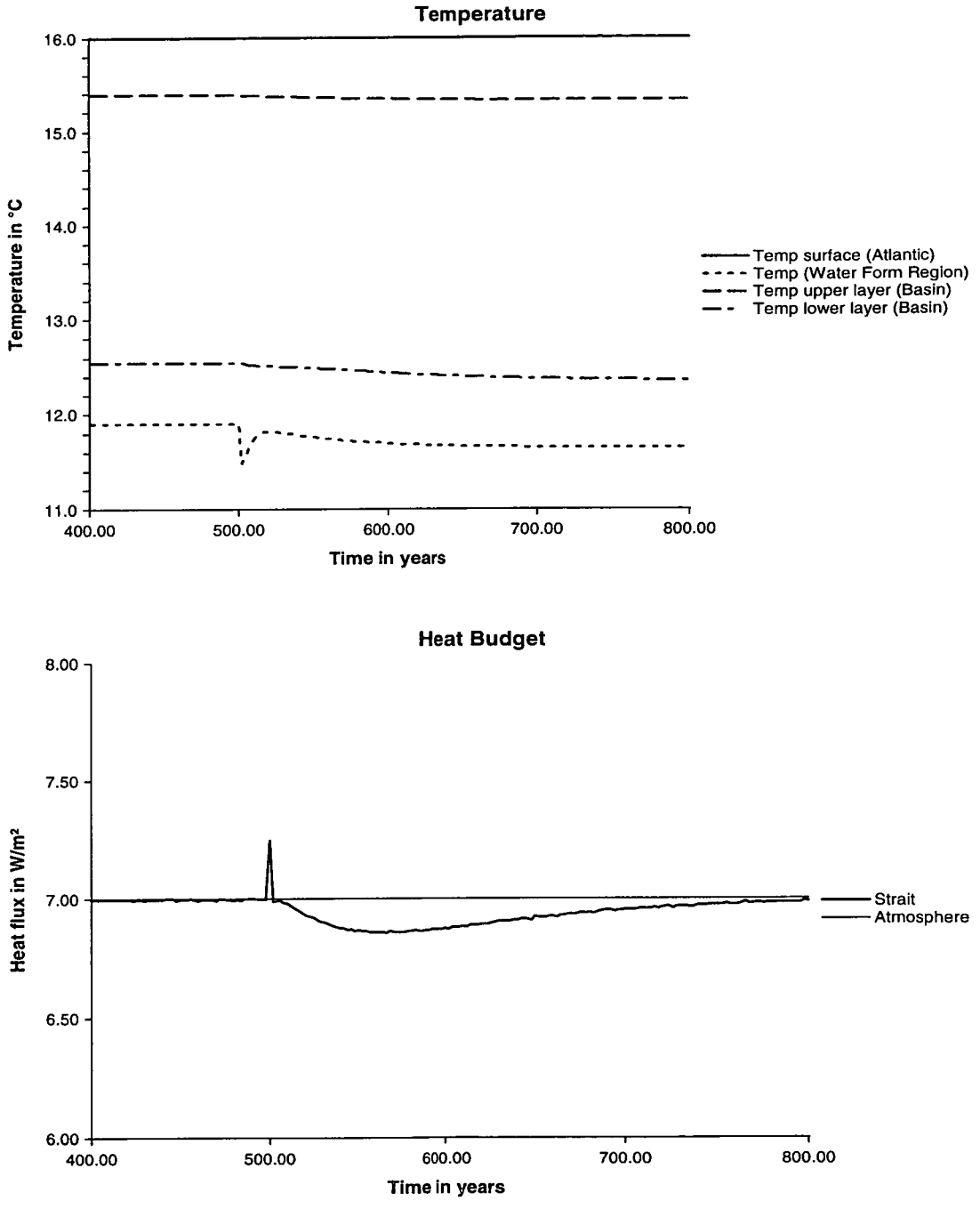

Figure 5.7: The heat budget in experiment E_m^{-E}. The main features are similar to experiment I_m^{-E} (figure 5.3), but the temperature of the water formation region (top, dotted line) shows a sudden drop as result of the drop in water formation rate. The positive spike in the heat budget (bottom) at $t = 500$ is a numerical artefact.

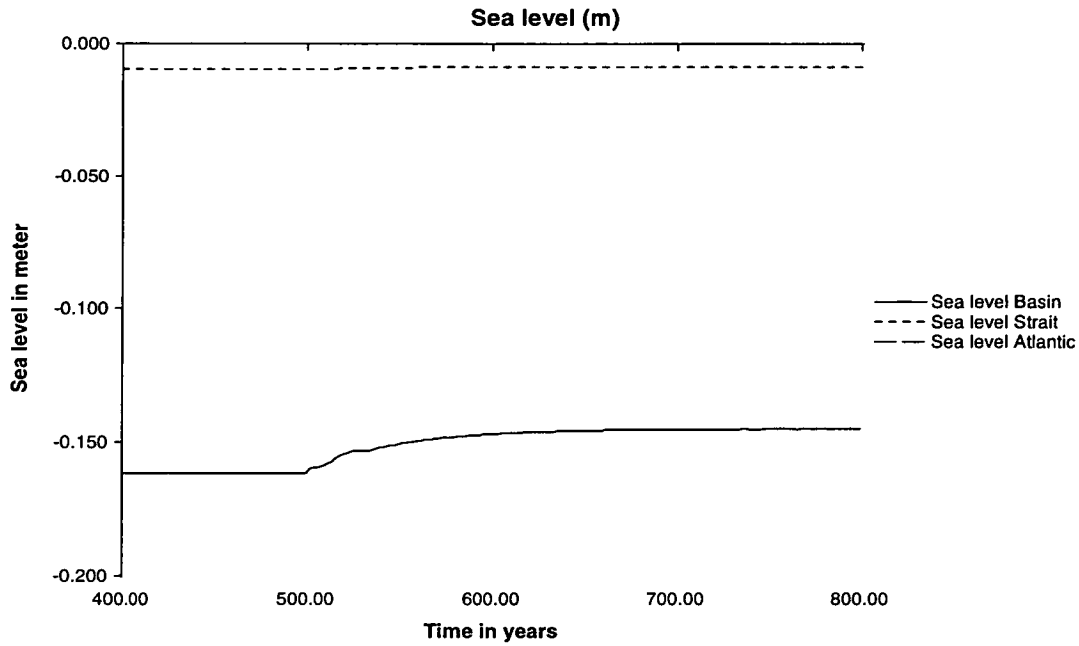

Figure 5.8: The sea level in experiment E_m^{-E} shows the same behaviour as in experiment I_m^{-E} (figure 5.4).

As the strait transport (figure 5.5 bottom) changes only slowly, the basin is emptied of lower layer water, and the interface drops with the characteristic timescale of a few years as discussed in section 4.2.2.

On the other hand, the salinity of the water formation box (figure 5.6 top, dotted line) does not exhibit the same discontinuous change as in experiment I_m^{-E} (figure 5.2). Initially, as the water formation rate is proportional to the evaporation, the change in evaporation leads only to a change in water formation *rate*, while the salinity of the newly formed water remains the same, whereas in experiment I_m^{-E} the change in evaporation leads to change in the *salinity*, while the water formation rate remains constant. Therefore the water formation parameterisation (E) leads to interface feedback mechanism, in contrast to the pure salinity feedback of parameterisation (I).

As the interface drops, the water formation rate increases again, leading to a slowly decreasing salinity of the newly formed water. Therefore, after the adjustment time of the interface feedback of 20 years, the system is again dominated by a salinity feedback very similar to the adjustment seen in experiment I_m^{-E}.

The temperature (figure 5.7) also shows a significant transitional effect. As the water

formation rate goes down, the temperature of the water formation box also shows a significant drop, because the constant heat loss is now distributed over a smaller amount of water. This negative spike in the temperature persists until the interface has settled at its new value, and the water formation rate has returned to higher values.

Water formation parameterisation (D). Finally, figures 5.9, 5.10, 5.11 and 5.12 show experiment D_m^{-E}. In this experiment the most realistic water formation parameterisation (D) is used, in which the water formation rate depends on the density difference between the water formation box and the lower layer. It is obvious – particularly in the evolution of the interface (figure 5.9 top) and the heat budget (figure 5.11 bottom) – that the transition is more complex than for the other two water formation parameterisations. In general, while in experiments I_m^{-E} and E_m^{-E} the transition from the initial to the final state occurred essentially smoothly through intermediate states, in experiment D_m^{-E} the transition involves situations which are considerably different from both the initial and the final state (which are in fact very similar to each other). In particular, there is an excursion well into the submaximal regime for more than 100 years.

The reason for this strong transitional signal is the development of an instability. The change in evaporation does not change the water formation directly, but – as in experiment I_m^{-E} – the salinity of the water formation layer decreases (figure 5.10 top). As the water formation is proportional to the density difference between boxes F and L, the water formation rate decreases sharply, and the interface deepens (figure 5.9 top). However, as the volume of the upper layer increases, its salinity decreases, further reducing the water formation rate. In total the water formation rate decreases with increasing $h_{U'}$, i. e. $\frac{dc_{FL}}{dh_{U'}} < 0$, as can also be seen in the plot of the water formation rate c_{FL} versus the interface depth $h_{U'}$ (figure 5.13). As was discussed in section 4.2.2, this indicates an unstable exponential growth away from the steady state. Therefore, although the new state (which is reached at the end of the experiment) is in the maximal regime not far from the initial steady state, a strong excursion into the submaximal regime is possible during the transition.

The instability is stopped by several factors. After 8 years, the system leaves the

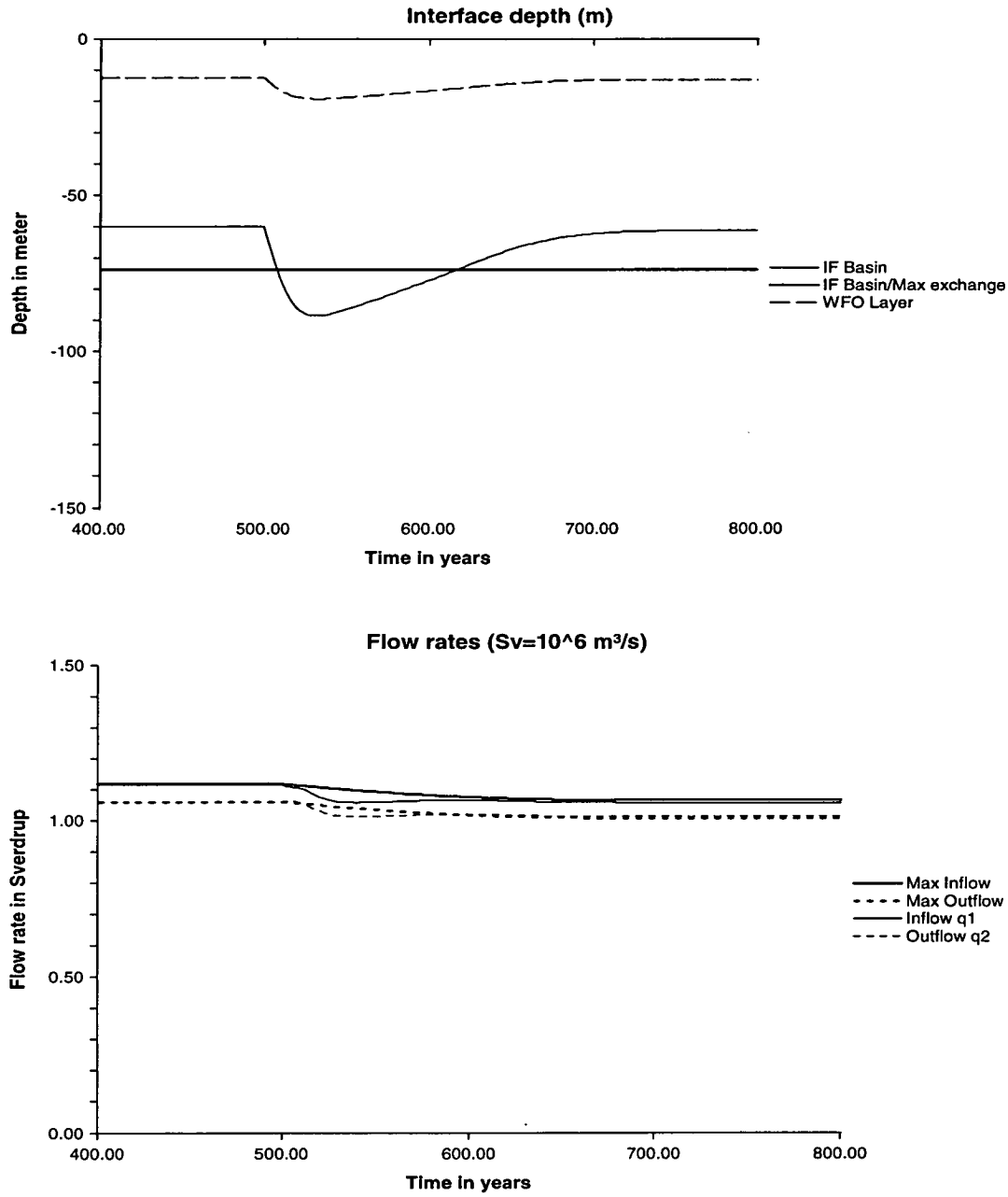

Figure 5.9: Interface depth and strait transport in experiment D_m^{-E}. Although initial and final state are not too different, there is a significant deviation during the transition, and the interface depth moves into the submaximal regime (top). The strait transport (bottom) falls below the maximal value (thick lines), which also decreases slowly due to density changes.

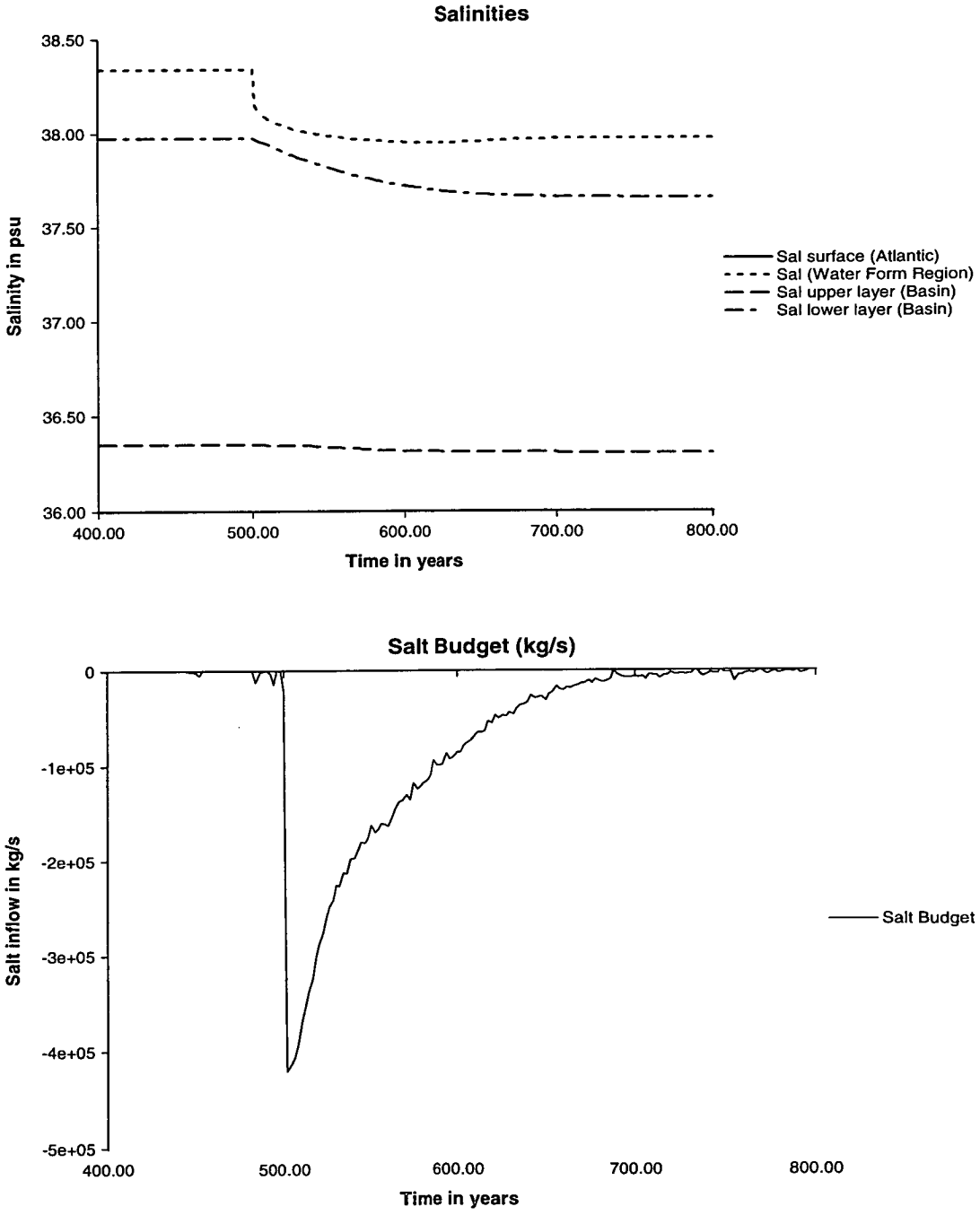

Figure 5.10: The salt budget in experiment D_m^{-E}.

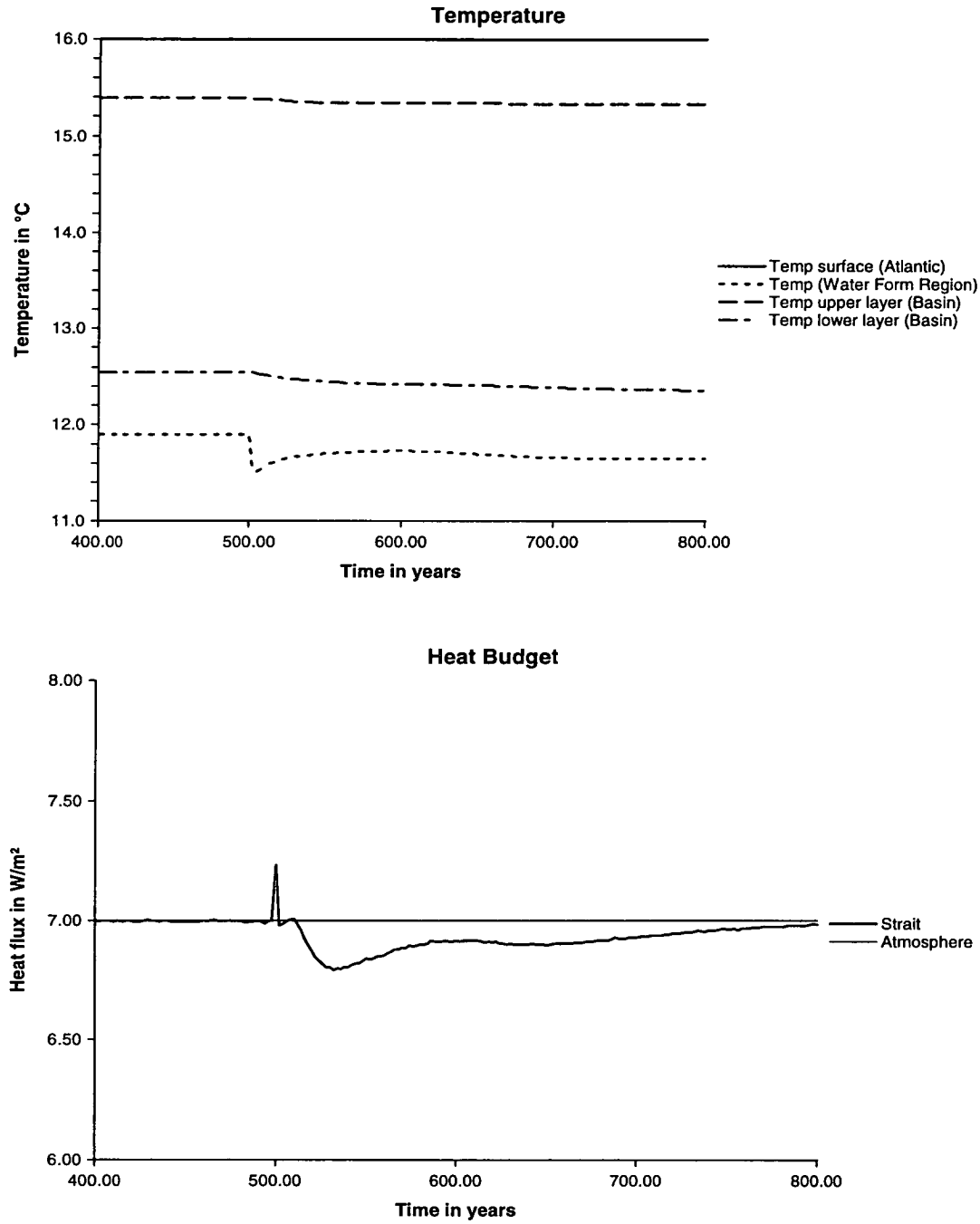

Figure 5.11: The heat budget in experiment D_m^{-E}. Again, the temperature responds to changes in the evaporation even though the heat loss was kept constant. the response is more complex than in experiments I_m^{-E} and E_m^{-E} (see text for details). The sharp positive spike in the heat budget (bottom) at $t = 500$ is a numerical artefact.

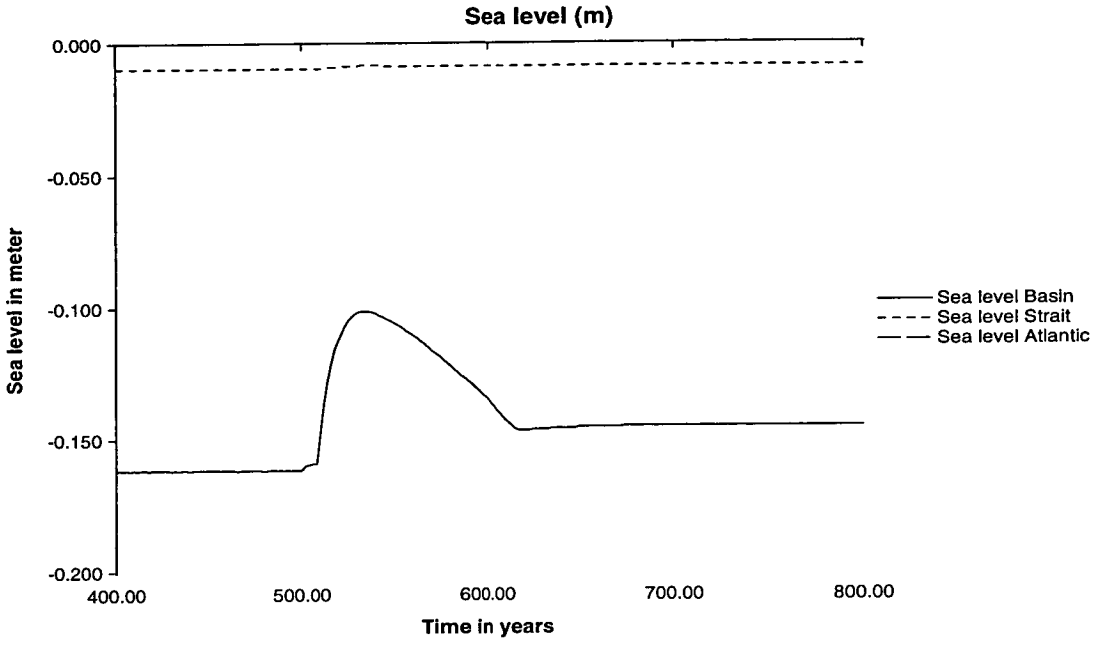

Figure 5.12: The sea level in experiment D_m^{-E} shows a strong transitional signal.

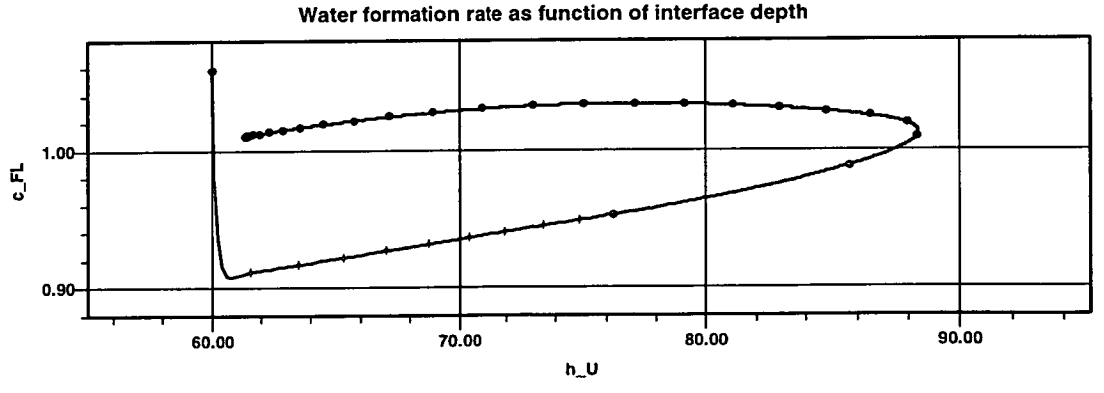

Figure 5.13: The water formation rate c_{FL} versus the interface depth $h_{U'}$ in experiment D_m^{-E}, from year 500 (top left end of the graph) to year 800. The crosses are set in distances of 1 year, the bullets at distances of 10 years. In the first year, the slope is strongly negative, indicating an unstable situation.

maximal regime and becomes submaximal. Therefore the strait transport decreases, so that the movement of the interface is slowed down. The second factor is the slow decrease in the lower layer salinity, which tends to increase the density difference between boxes F and L, thus increasing the water formation again. These two factors effectively act on the timescale of the interface mechanism (several years) and the salinity mechanism (several decades) respectively, and the interplay between the different timescales leads to a complex pattern of the evolution:

Years 500-508: The system is still in the maximal regime, but the salinity of the water formation box drops quickly, reducing the water formation considerably, while the strait transport remains almost constant, thus lowering the interface. With less water formation, the surface water experiences stronger cooling (figure 5.11 top, dotted line). The heat budget (figure 5.11 bottom), starting at a small negative value, moves back towards a balanced state. The sea level in the basin rises by a small amount (2 mm).

Years 508-531: The interface has dropped into the submaximal regime, the strait transport decreases, slowing down and eventually stopping the lowering of the interface. The strait transport also decreases slowly because the lower layer salinity decreases. As the strait transport decreases, the heat budget becomes strongly negative. At the same time, the water formation rate increases again, because the density difference between boxes F and L increases. In order to maintain the water budget with decreasing strait transport, the sea level in the basin rises by 6 cm.

Years 531-616: The water formation rate continues to increase, and the interface starts to rise again. The strait transport, however, shows only a very small increase, because the rise in interface depth (which tends to increase strait transport) is counteracted by a decrease in density difference (which tends to decrease the strait transport). The heat budget moves towards the balanced situation as a result of decreasing temperatures in the lower layer, and the sea level is lowered again.

Years 616-645: The interface has risen above the maximal/submaximal threshold,

and the system is back in the maximal regime. Therefore, from this point onwards the interface change does not influence the strait transport. However, as the salinity in the lower layer still continues to fall, the strait transports begins to decrease again, albeit by a small amount. This is particularly visible in the heat budget (figure 5.11 bottom).

Years 645-end: The decrease in lower layer salinity is now so slow that it is balanced by the decrease in temperature, so that the density difference remains constant, and the strait transport ceases to decrease. The heat budget is now only influenced by the temperature of the lower layer, and is moving back to the balanced situation.

In summary, the most realistic water formation parameterisation (D) can lead to a situation in which a sudden change in air-sea fluxes – even if they are small and hardly affect the steady state – can lead to a crisis in which the deep water formation in the basin is considerably reduced, and this situation can persist for periods of the order of a century.

Submaximal experiments. For comparison, figures 5.14, 5.15, 5.16 show the interface depth and the salinities for experiments I_s^{+E}, D_s^{+E} and E_s^{+E} in which the system started in a submaximal situation, and the net evaporation was increased by 20 %. The features are generally similar to the three experiments discussed above. Again, the water formation parameterisation (I) in experiment I_s^{+E} leads to an almost pure salinity feedback, whereas in experiment E_s^{+E} the interface mechanism plays a large role, and the salinity adjustment is considerably weaker. In contrast to the maximal experiments, in the submaximal experiments the strait dynamics does not constrain the steady state, so that the the predominance of the respective feedback leads to noticeable differences in the salinities of the final steady states: S_L changes by 0.35 psu for I_s^{+E} (pure salinity feedback), but only 0.22 psu for experiment E_s^{+E}. Experiment D_s^{+E} with the density dependent water formation parameterisation (D) again shows a strong excursion away from the steady state.

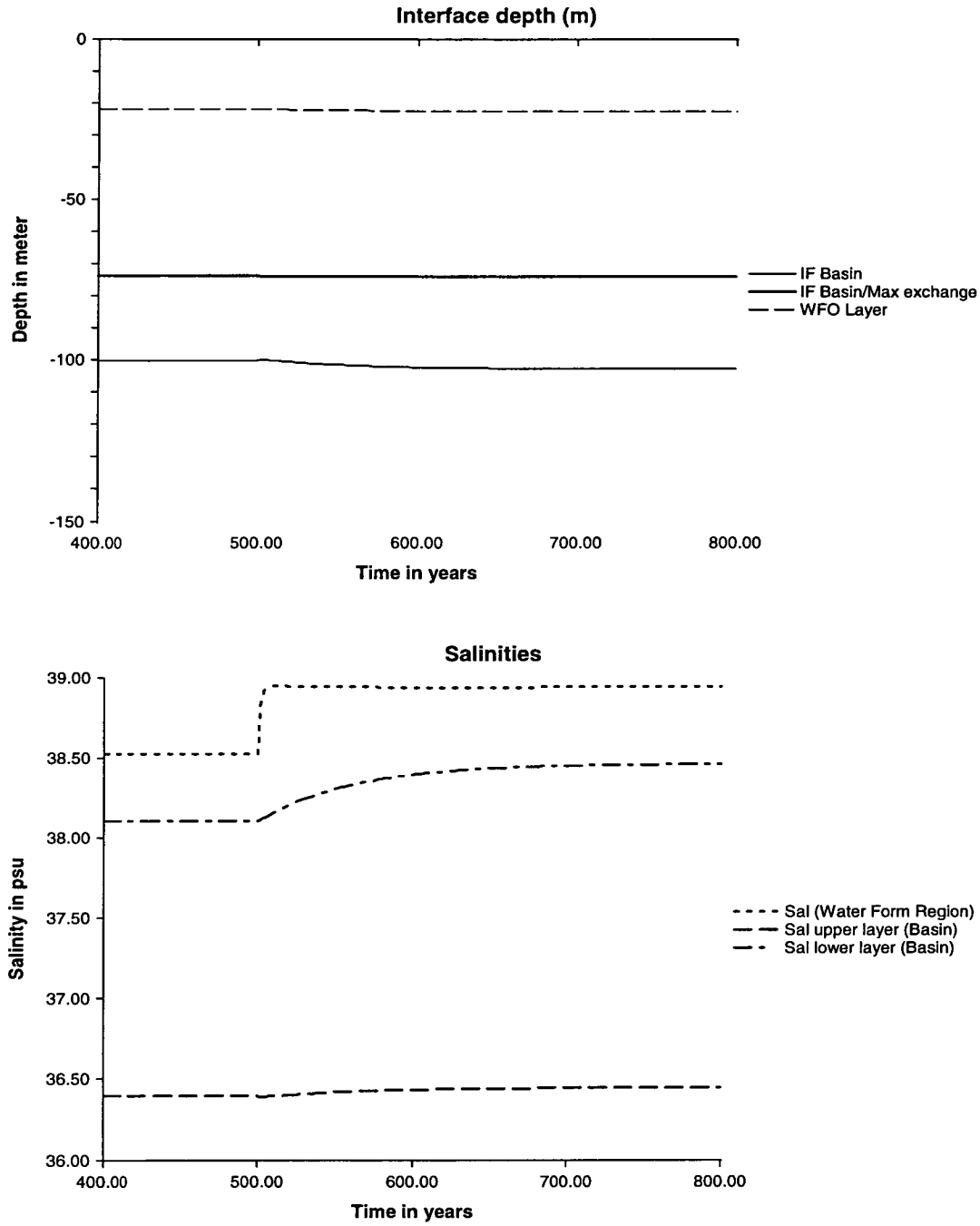

Figure 5.14: The interface depth (top) and the salinity (bottom) in experiment I_S^{+E}. It shows a pure salinity feedback: the interface changes little, while the salinity increases. Compare with figure 5.15.

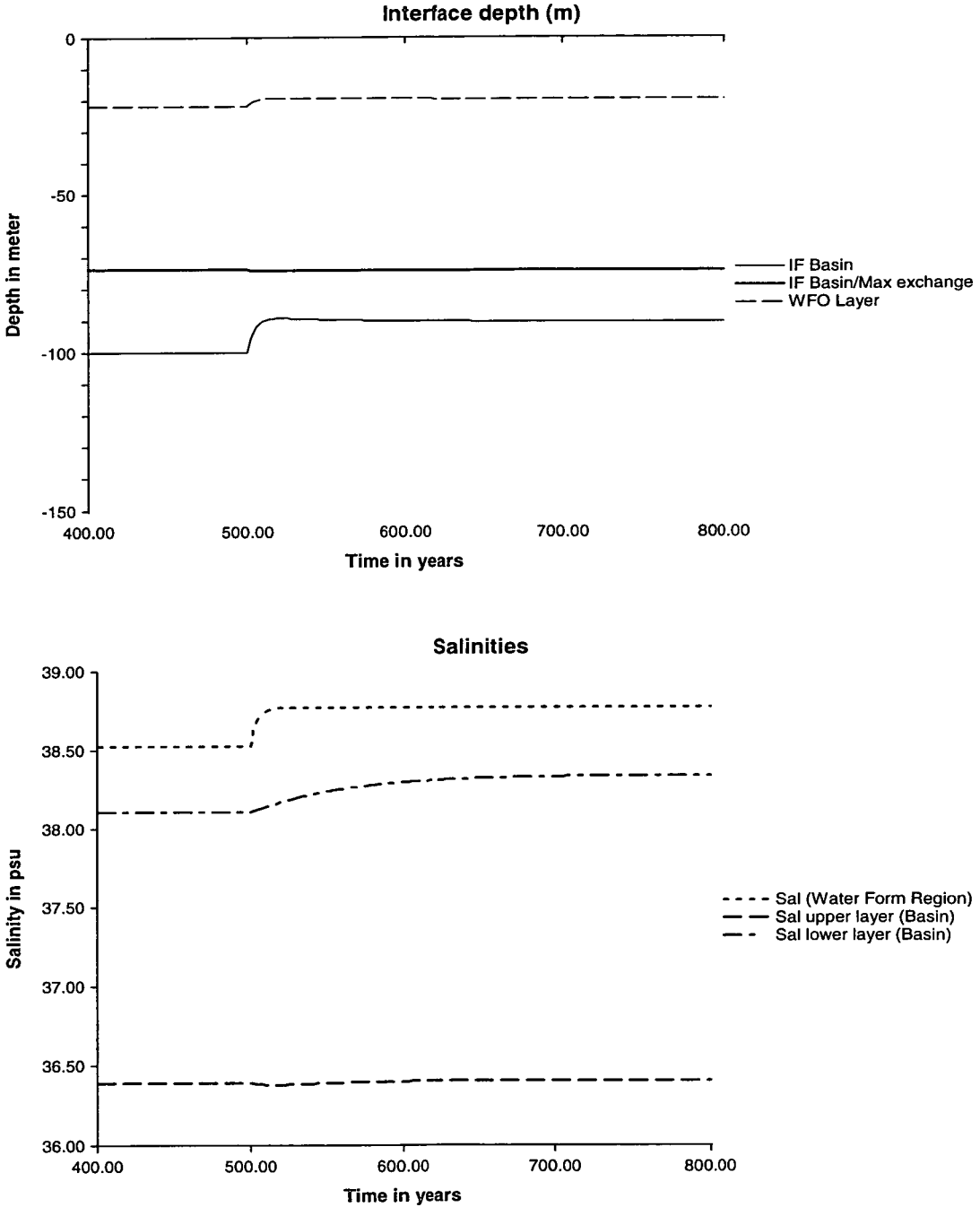

Figure 5.15: The interface depth (top) and the salinity (bottom) in experiment E_s^{+E}. Compared to experiment I_s^{+E} (figure 5.14), the salinity adjustment is considerably weaker (S_L changes by 0.22 psu for f, but 0.35 psu for d), and the interface mechanism plays a large role.

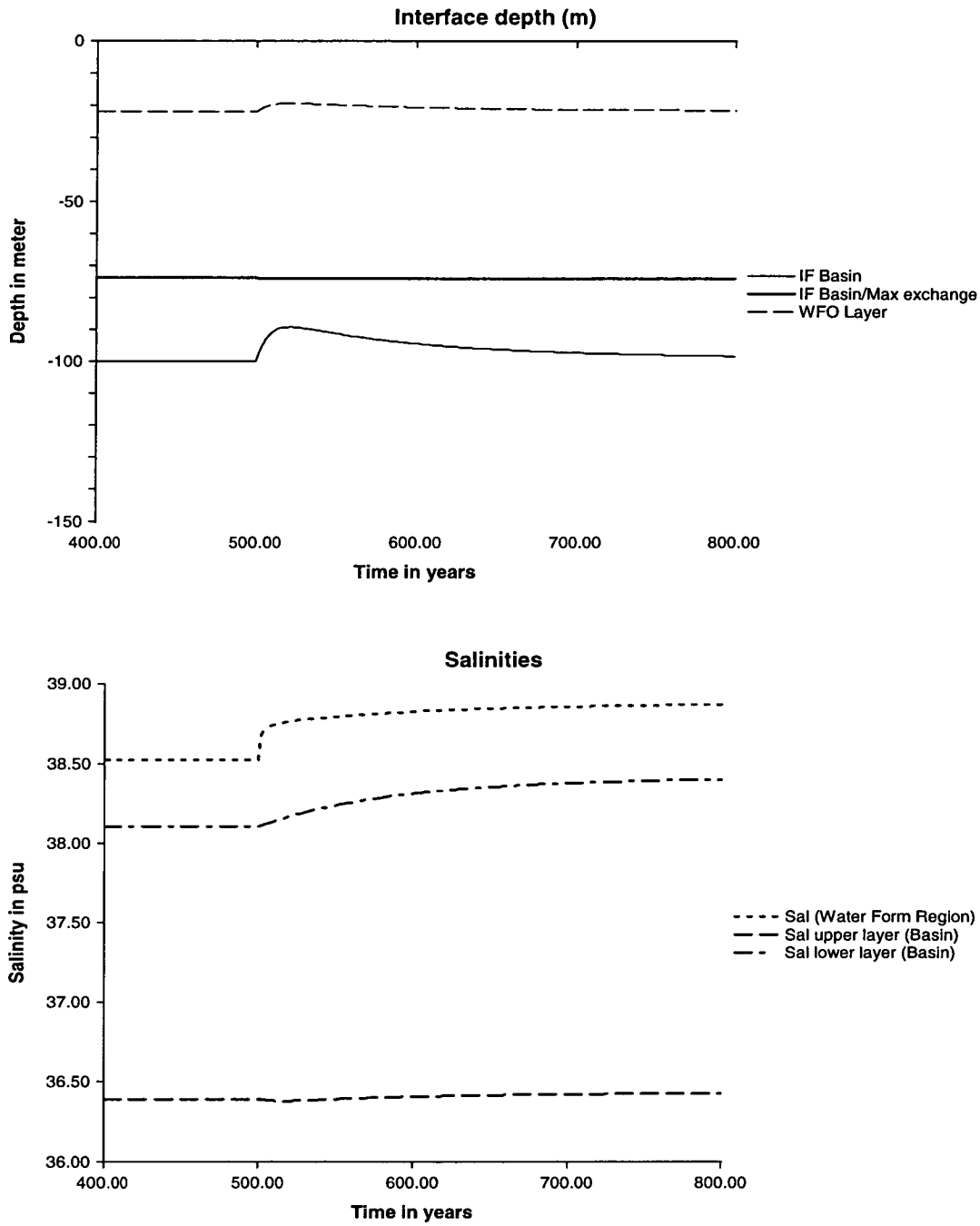

Figure 5.16: The interface depth (top) and the salinity (bottom) in experiment D_s^{+E}. As in experiment D_m^{+E} (figures 5.9, 5.10, 5.11 and 5.12) there is a complex interplay between the mechanisms, with a strong excursion away from the steady state.

Experiment	Evaporation/Heat Flux in-/decrease	Water form. param.	$h_{V'}$	q_2	ΔS	ΔT
Initial state maximal			60.0	1.057	1.97	-3.49
I_m^{+H}		(I)	61.0	1.079	1.93	-4.07
D_m^{+H}	H_{Atm} +20%	(D)	60.4	1.079	1.93	-4.07
E_m^{+H}		(E)	61.1	1.079	1.93	-4.07
I_m^{-H}		(I)	58.6	1.035	2.01	-2.82
D_m^{-H}	H_{Atm} −20%	(D)	59.4	1.035	2.01	-2.82
E_m^{-H}		(E)	58.6	1.035	2.01	-2.82
Initial state submaximal			100.0	0.989	2.11	-3.68
I_s^{+H}		(I)	101.4	1.002	2.08	-4.36
D_s^{+H}	H_{Atm} +20%	(D)	100.1	1.008	2.07	-4.32
E_s^{+H}		(E)	101.3	1.002	2.08	-4.36
I_s^{-H}		(I)	98.7	0.975	2.14	-2.98
D_s^{-H}	H_{Atm} −20%	(D)	99.7	0.970	2.15	-2.99
E_s^{-H}		(E)	98.5	0.975	2.14	-2.98

Table 5.4: HYCOBOX experiments to investigate the effect of changing atmospheric heat los on the steady state for different water formation parameterisations. Each row lists the final state at $t = 1000$ years. As $E - P$ was not varied, the water formation parameterisation (E) is equivalent to (I) and experiments E_m^{+H}, E_s^{+H}, E_m^{-H} and E_s^{-H} only repeat I_m^{+H}, I_s^{+H}, I_m^{-H} and I_s^{-H} (except for possibly small differences due to the fact that the initial state was not replicated perfectly). For a discussion of the main features, see section 5.2.2.

5.2.2 Experiments with changing heat loss

Table 5.4 summarises the final states of the system in each of the experiments for changing heat loss. It should be noted that in this set of experiments the evaporation dependent water formation parameterisations (E) is equivalent to the "interface only" parameterisation (I), as the net evaporation $E - P$ was kept constant.

To changing heat loss, the system reacts as follows (see also table 5.4):

- The final steady states are independent of the water formation parameterisation, i. e. for each set of conditions, the three runs for the different parameterisations show approximately the same final steady state.

- Changes in the heat loss do not significantly affect the depth of the interface, and therefore do not significantly influence how far away the system is from the switchover between maximal and submaximal regime. In other words, of the two feedback mechanism (interface feedback and temperature feedback, see section 4.2.3), only the the temperature feedback is active, independent of the water formation parameterisation.

- As expected, an increase/decrease in the heat loss increases/decreases the temperature difference by a similar proportion ($18 - 20\,\%$ for a change in heat flux of $20\,\%$). The strait transport also increases/decreases as a result of the change in density difference.

- The salinity difference shows an inverse response: An increase in heat loss decreases the salinity difference, although the change is very small – the salinity changes by $2\,\%$ for a change in heat flux of $20\,\%$. In more practical terms, while the temperature changes by approximately $0.6 - 0.7\,^{\circ}\mathrm{C}$, the salinity changes only by $0.04\,\mathrm{psu}$ in each of the experiments.

However, although the final steady states do not differ significantly between the different water formation parameterisations, the transitions from the initial to the final states again show qualitatively different behaviour. In the following, experiments $\mathrm{I}_{\mathrm{m}}^{-H}$ and $\mathrm{D}_{\mathrm{m}}^{-H}$ (maximal state, heat loss decreases by $20\,\%$, water formation parameterisations (I) and (D)) are shown in detail. As $E - P$ is constant, water formation

parameterisation (E) is equivalent to (I), and experiment E_m^{-H} needs not be shown in detail.

Water formation parameterisation (I). Figures 5.17, 5.19, 5.18 and 5.20 show the evolution of experiment I_m^{-H}, in which the water formation rate depends only on the interface depth. Similar to experiment I_m^{-E} (adjustment to reduced evaporation), the adjustment to the reduced heat loss does not involve the interface feedback mechanism, as can be seen from the plot of the interface depth (figure 5.17 top). The interface depth remains approximately constant, and the heat budget is balanced through an adjustment of the temperature (figure 5.18). The temperature of the water formation layer (figure 5.18 top, dotted line) increases immediately due to the reduced heat loss, and the temperature of the lower layer follows with the characteristic timescale of $\tau_T = 60$ years until the heat budget is balanced figure 5.18 bottom).

Similar to the experiments with changing evaporation, there is an interaction between the heat budget and the salt budget: The salinity changes even though the evaporation remains unchanged (figure 5.19). The reduced temperature and therefore density difference reduces the volume transport (figure 5.17 bottom). Although the change is comparatively small, it leads to an imbalance in the salt budget (figure 5.19 bottom), as the total outward salt transport in the lower layer $S_2 \cdot q_2$ is reduced more than the inward salt transport $S_1 \cdot q_1$. Consequently, the salinities of the layers inside the basin increase, until the salt budget is again balanced.

As expected, the sea level (figure 5.20) also responds: A smaller sea level difference across the strait is sufficient to drive the reduced inflow through the strait. However, the change in sea level is less than 1 cm and would therefore be essentially undetectable.

Water formation parameterisation (D). Figures 5.21, 5.23, 5.22 and 5.24 show the evolution of experiment D_m^{-H}, in which the water formation rate depends on the density difference and the interface depth. Similar to the experiments with varying evaporation, this water formation parameterisation exhibits a transitional state that is drastically different from both the initial and the final state. The system, starting well within the maximal regime, approaches the submaximal threshold, although – in this particular experiment – does not venture into the submaximal state (figure 5.21 top).

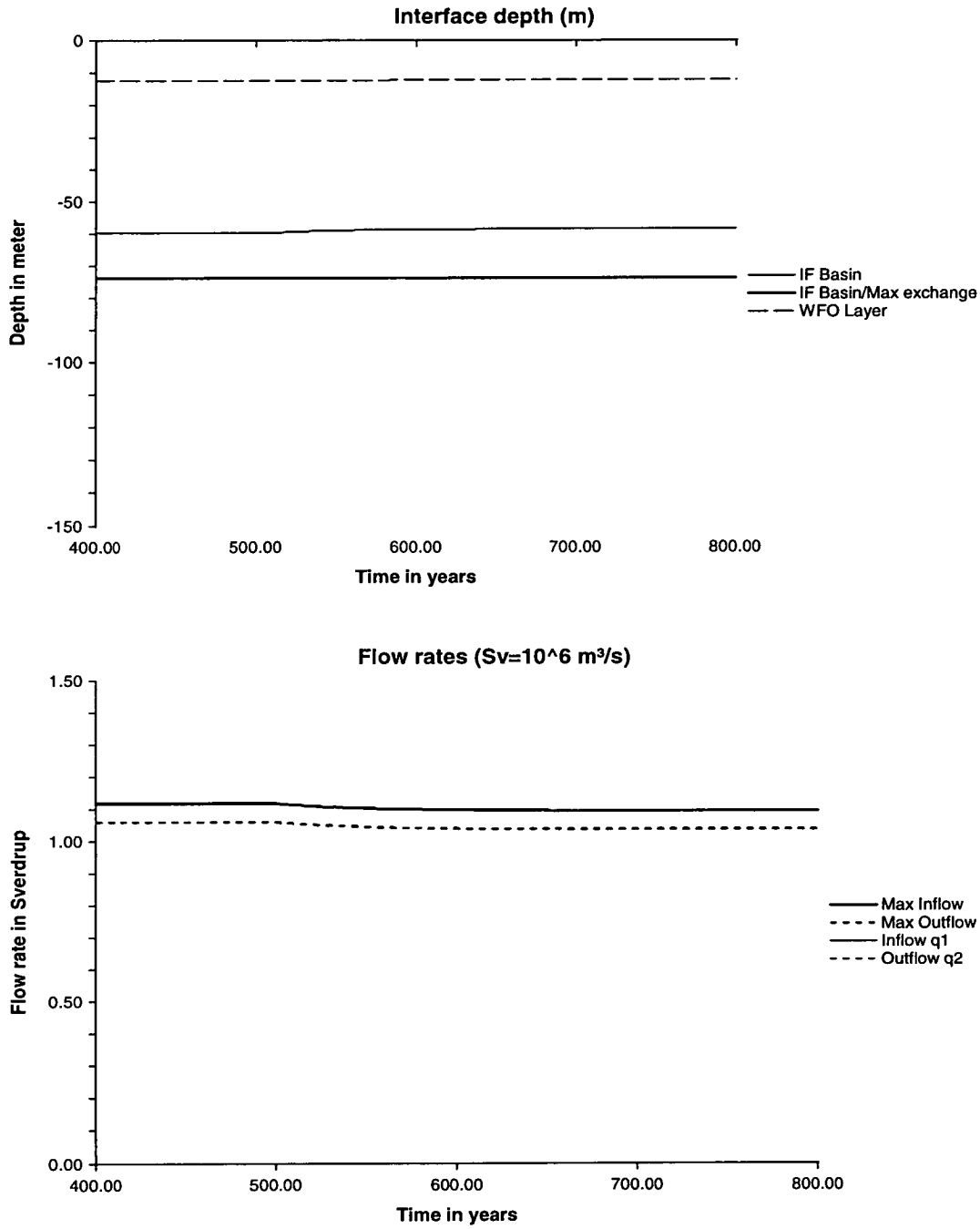

Figure 5.17: Interface depth and strait transport in experiment I_m^{-H}. The interface depth (top) is not significantly affected. The strait transport (bottom), however, goes down following the changes in density difference between the layers (see figure 5.18).

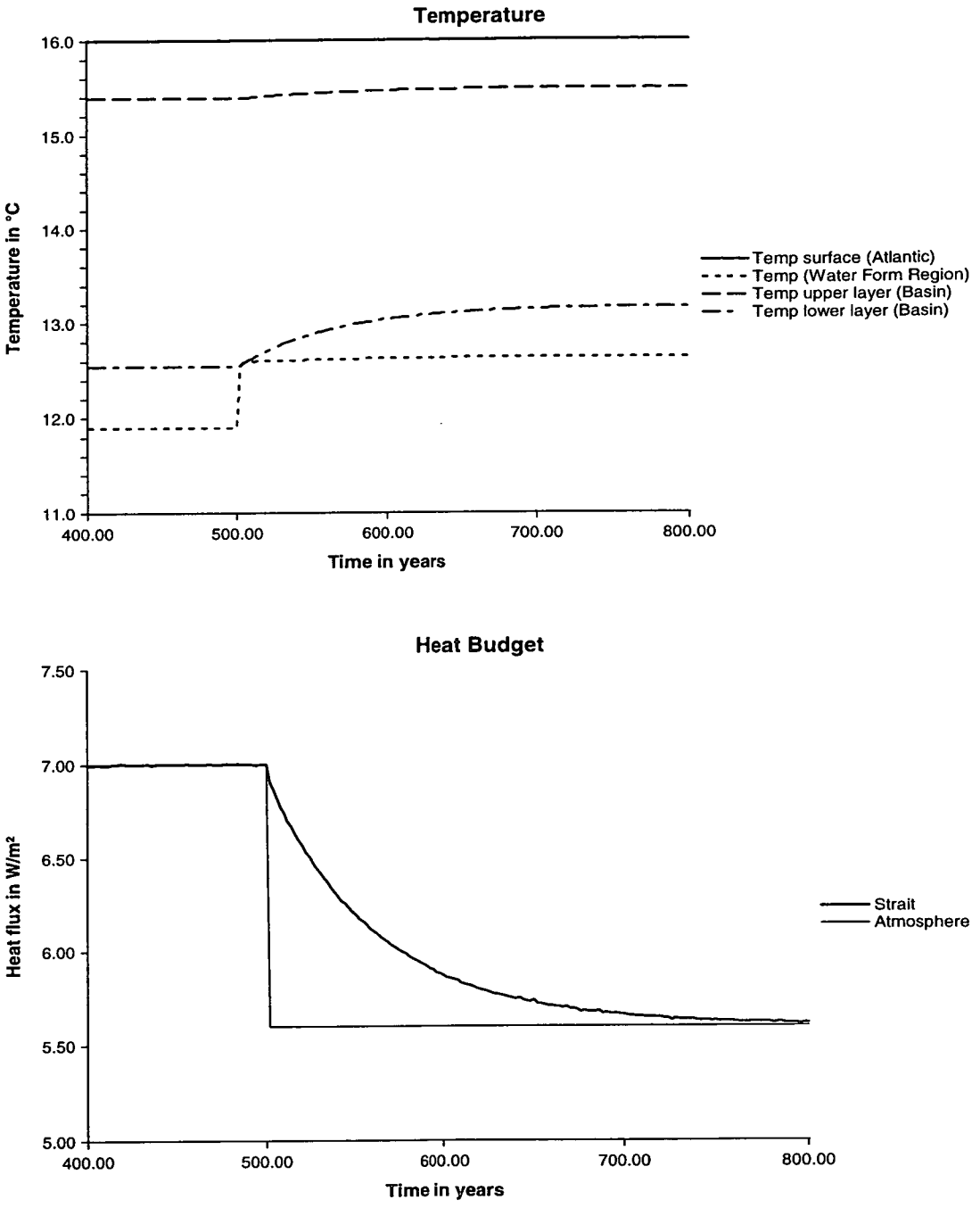

Figure 5.18: The heat budget in experiment I_m^{-H}. The heat transport through the strait (bottom, thick line) approaches the atmospheric value with an e-folding time of $\tau_T = 60$ years. The adjustment is achieved through a change in temperature of the lower layer (top, dash-dotted line).

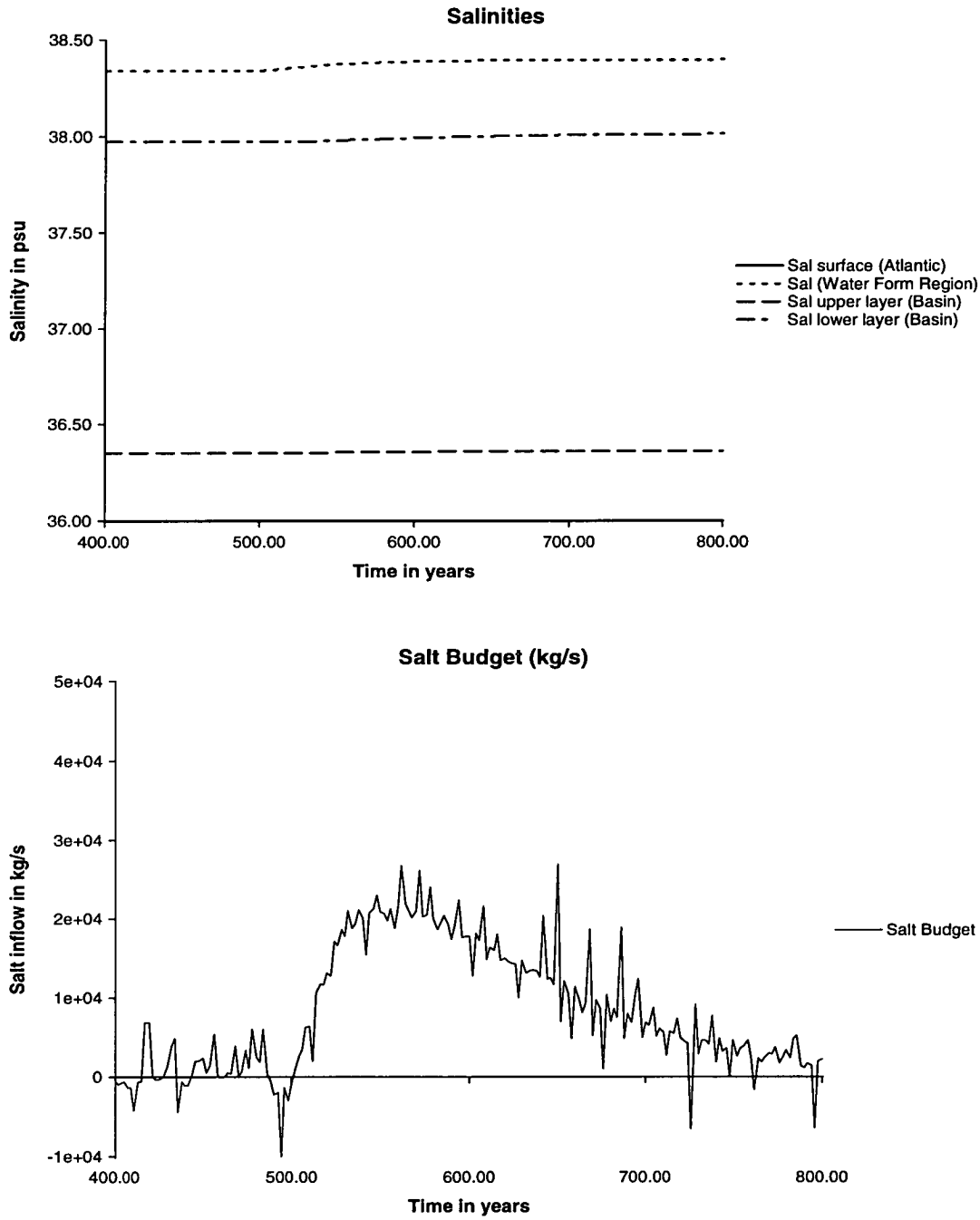

Figure 5.19: The salt budget in experiment I_m^{-H}. Although the evaporative air-sea-fluxes are not varied in this experiment, the salt budget becomes unbalanced as a result of adjustment processes of the heat budget (bottom, note that the units on the y-axis are smaller by one order of magnitude compared to the figures from the experiments shown above). Therefore, the salinities in the basin change (top).

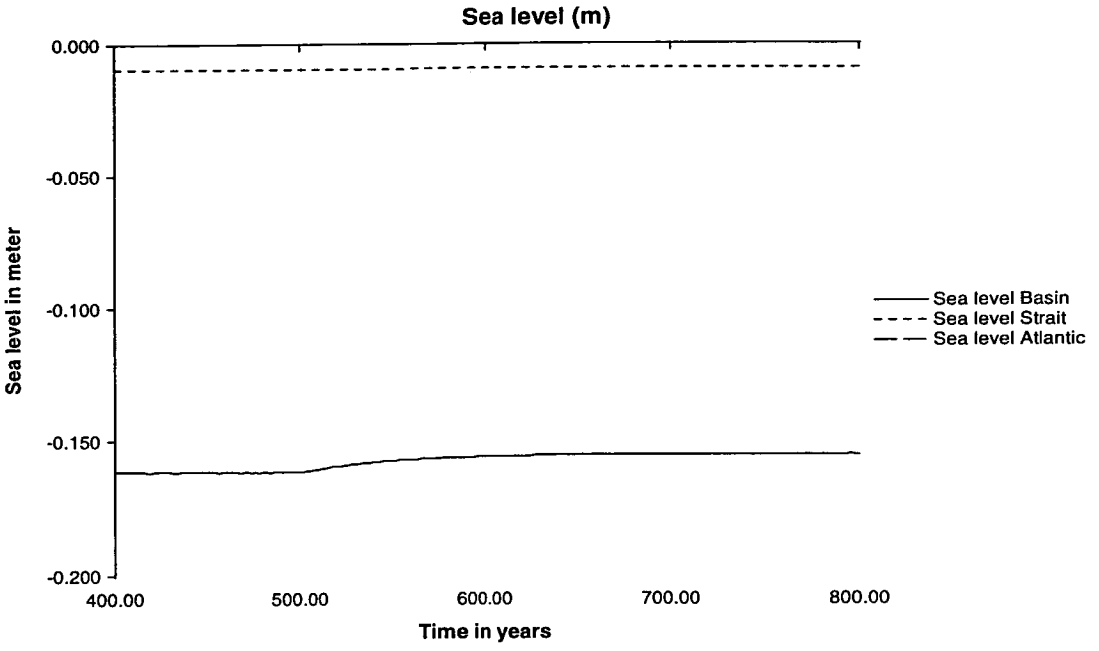

Figure 5.20: The sea level in experiment I_m^{-H}. As the strait transport goes down (driven by the reduction in density difference), a smaller sea level difference across the strait is sufficient to drive the required inflow.

The mechanism for this strong transitional signal is similar to the one discussed above in relation to experiment D_m^{-E}. Immediately after the change, the temperature and therefore the density of the water formation box goes up (figure 5.22 top, dotted line), so that the water formation collapses, and the interface goes down with the characteristic timescale for interface adjustments τ_{h_U}. The water formation rate only recovers on the longer temperature adjustment timescales τ_T as the temperature of the lower layer T_L increases due to newly formed water being mixed into it (figure 5.22 top, dash-dotted line). This leads to the characteristic kink in the evolution of the interface depth (figure 5.21 top) with the sharp initial drop and the slower recovery.

As the system remains in the maximal regime, the heat budget is only affected by the temperature feedback mechanism, and the adjustment of the heat budget (figure 5.22) is similar to experiment I_m^{-H} (figure 5.22). Again, there is an interaction between heat and salt budget (figure 5.23), which is similar to experiment I_m^{-H} in the long run, but shows differences on a shorter timescale as a result to the transitional state. In particular, the salinity of the water formation box S_F (figure 5.23 top, dotted line) increases immediately as the water formation rate collapses. Therefore, initially the

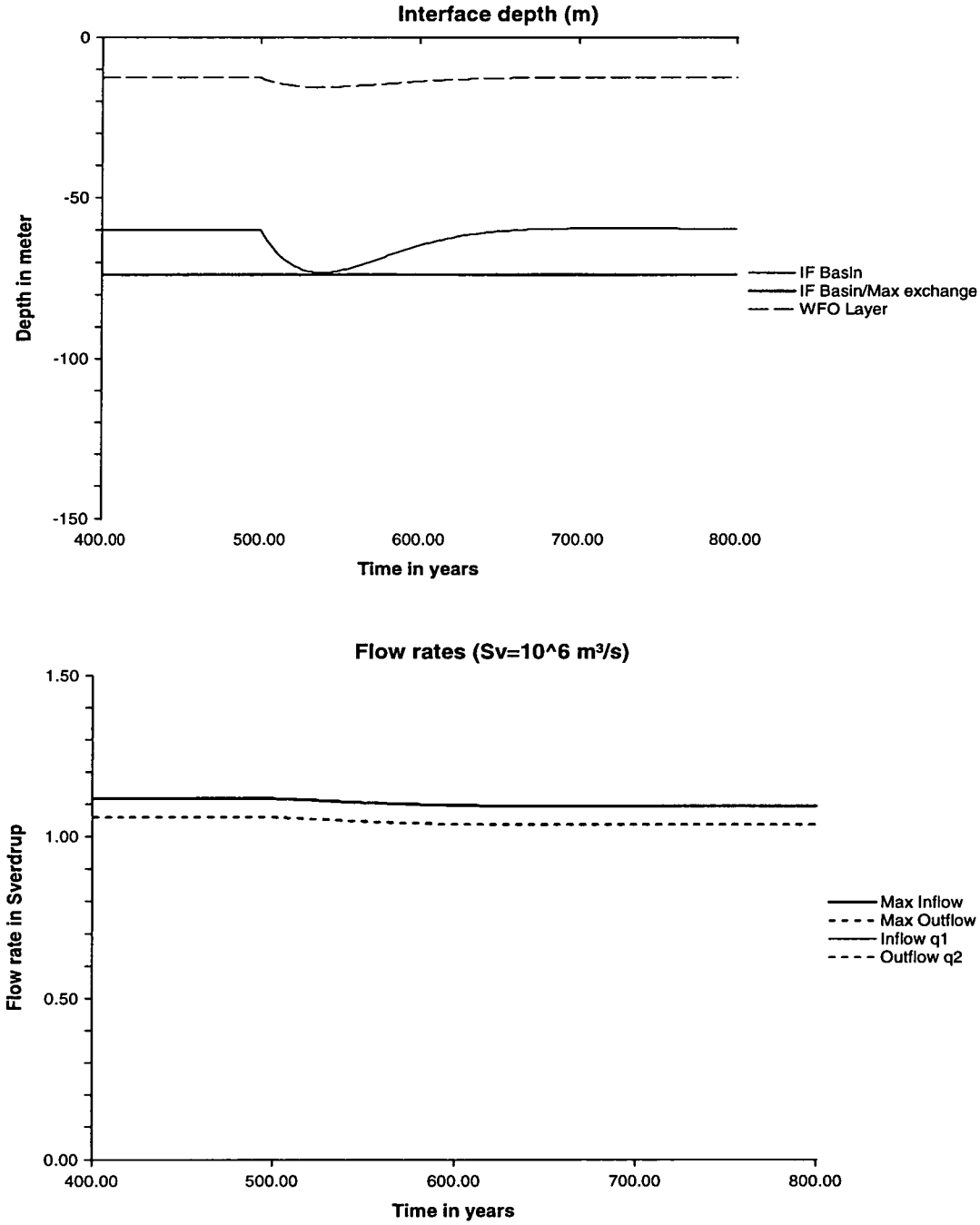

Figure 5.21: Interface depth and strait transport in experiment D_m^{-H}. Although initial and final steady state have similar interface depths, the transitional state is considerably different (top). The strait transport (bottom) shows a slow decrease due to density changes.

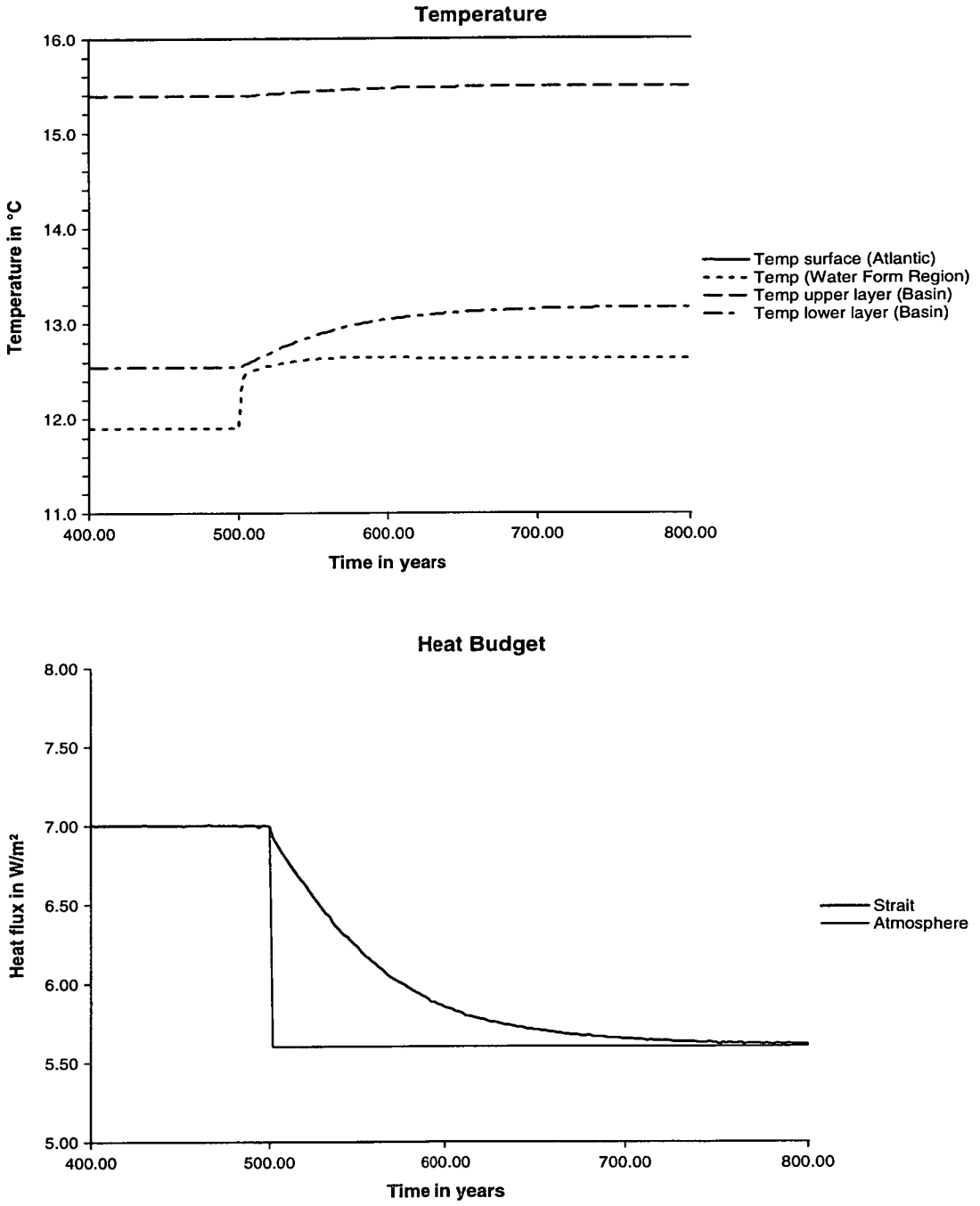

Figure 5.22: The heat budget in experiment D_m^{-H}. The heat transport through the strait (bottom, thick line) approaches the atmospheric value with an e-folding time of 50 years. The adjustment is achieved through a change in temperature of the lower layer (top, dash-dotted line).

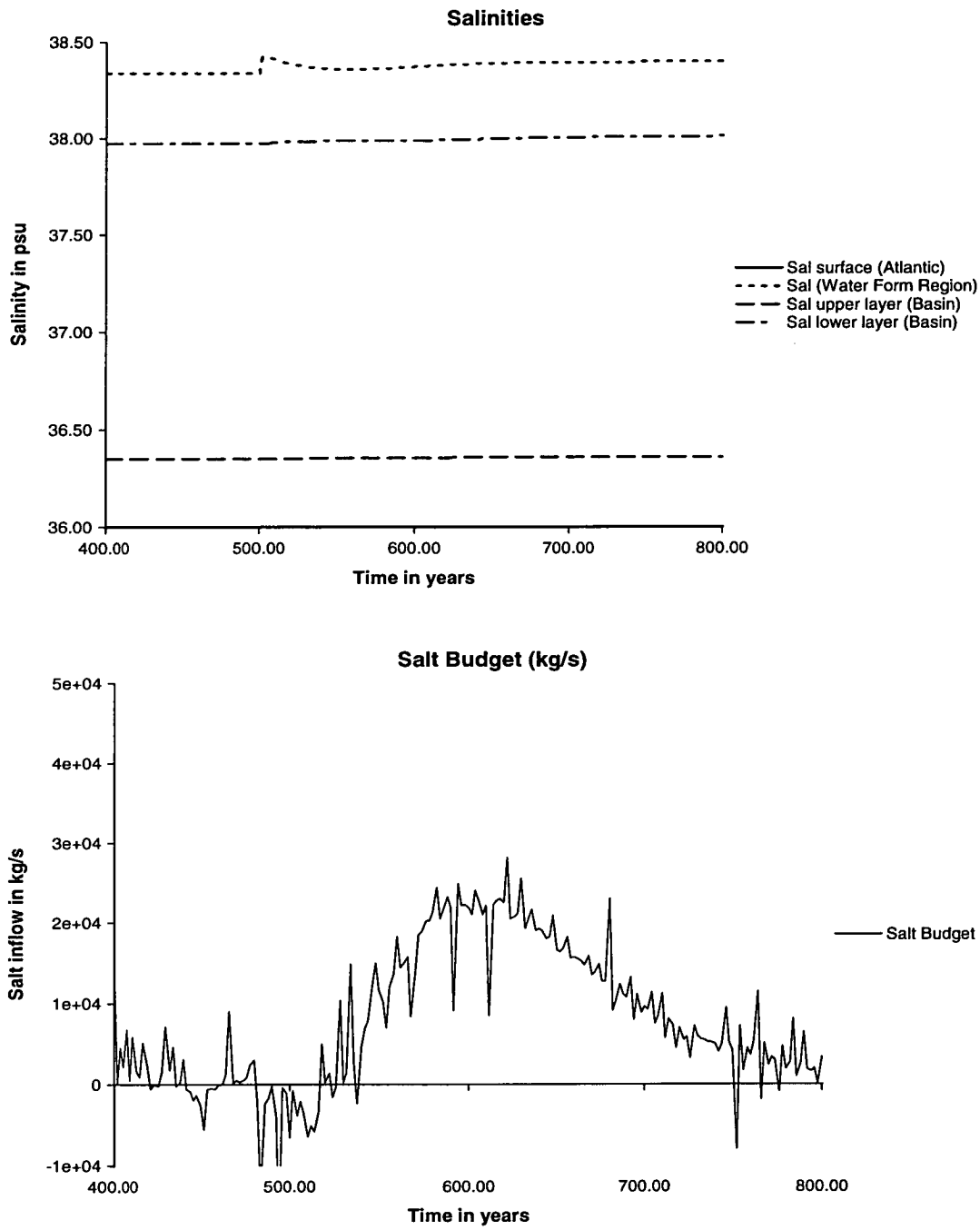

Figure 5.23: The salt budget in experiment D_m^{-H}. Again, the salinity is indirectly affected by changes in the heat budget.

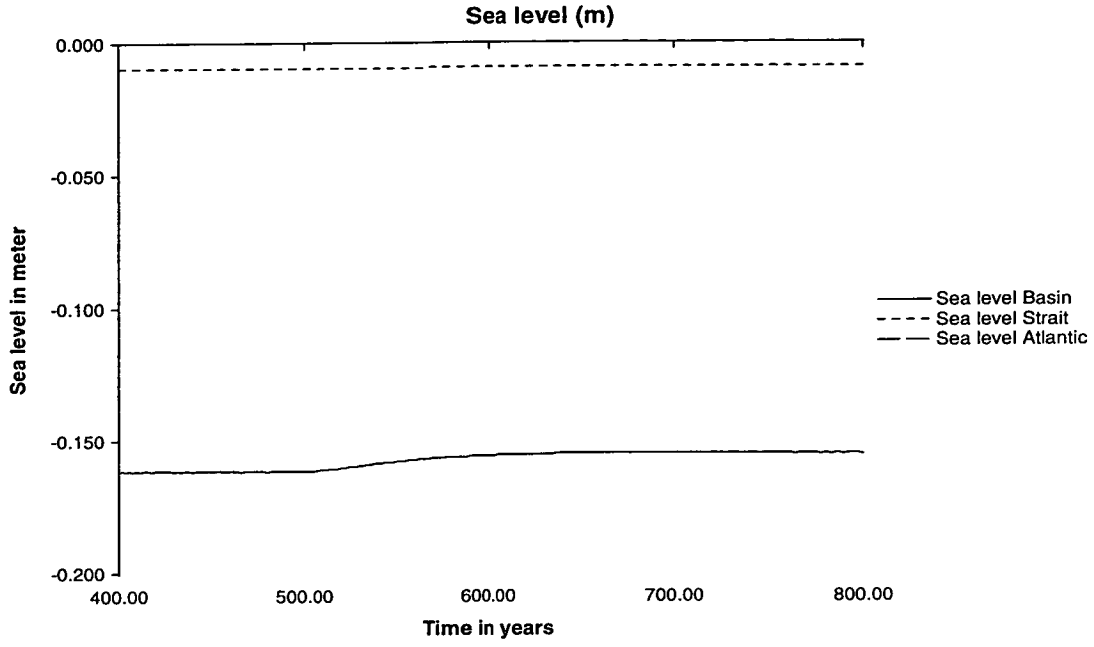

Figure 5.24: The sea level in experiment D_m^{-H}.

salinity of the lower layer increases faster than in experiment I_m^{-H}, and the salt budget shows a slight negative excursion (figure 5.23 bottom) before the reduction in flow rate leads to a net inflow of salt as discussed above for experiment I_m^{-H}.

5.3 The experiments in perspective

The experiments shown in the previous sections form a basis for the understanding of changes in the Mediterranean. Changing the budgets leads to both a shift in the steady state and to transitional effects. The bottom layer properties S_L and T_L respond on very long timescales and therefore reflect mainly shifts in the steady state of the system, whereas shorter term transitional effects are visible in the properties of the newly formed water S_F and T_F and in the interface depth, i. e. all the quantities that can change on shorter timescales. The transitional effects are also rather sensitive to the water formation parameterisation, whereas the steady state, and therefore the average basin salinity and temperature, are more robust.

These experiments can help to interpret observational evidence of changing conditions, both at the present day and on geological timescales. A number of studies

analysing measurements in the Mediterranean Sea indicate that the average salinity and temperature of the deep waters have risen noticeably in the 20th century. Bethoux et al. (1990) find that the average basin temperature is rising by 0.12 °C per century, while the average salinity increases by 0.03 psu per century, with most of the increase in the second half of the century. Rohling and Bryden (1992) find a somewhat higher increase in salinity of the Western Mediterranean Deep Water (WMDW) of 0.05 psu between 1955 and 1989, and a temperature increase of 0.07 °C.

Although there is some doubt whether these changes are statistically significant (Martin and Milliman 1997), it has been suggested that the warming of the Mediterranean reflects the global warming trend. On the other hand, Rohling and Bryden (1992) argue that the main factor causing this trend was the damming of large rivers around the Mediterranean in the second half of the 20th century, reducing the freshwater input into the Eastern Mediterranean by $13.5 \times 10^{10}\,\mathrm{m}^3$/year (equivalent to an increase in net evaporation over the whole basin of 5 cm/year) and making the Mediterranean saltier.

The two possibilities – atmospheric warming or reduced river runoff – can be discussed in the light of the experiments shown above. The change is detected mainly in the average properties of the deep water, which are insensitive to the water formation parameterisation used in the model and to transitional effects. Although the HYCOBOX experiments used abrupt changes in air-sea-fluxes while the relevant changes in nature occur over longer times, the use of the HYCOBOX results is justified because the transitional, short-term effects are ignored here.

We first discuss the hypothesis that the the main factor triggering the recent changes is the damming of river systems in the borderlands of the Eastern Mediterranean. While river runoff affects the freshwater budget, rivers contribute little to the heat budget, as heat is predominantly lost through air-sea-interaction. Therefore the damming of river systems has a qualitatively similar long term effect as the experiments in section 5.2.1, where only the net evaporation changed but the heat loss remained constant. Assuming an e-folding time of 60 years, the observed change in salinity of 0.03 to 0.05 psu within 35 years indicates that the total shift in the steady state will be around 0.1 to 0.15 psu over a period of 150 to 200 years, i. e. an increase by 5 % to 7.5 %. Using the SQE

equation (5.11), this can be caused by an increase in net evaporation by 7 to 10 %. Therefore, the known increase of the excess evaporation of 5 cm/year or 7 % due to the damming of rivers is sufficient to explain an increase in the salinity of 0.1 psu.

However, the results of the experiments listed in table 5.3 and the discussion on page 86 indicate that the observed increase in steady-state salinity of 0.10 to 0.15 psu will lead to a secondary increase in steady state temperature of 0.08 to 0.1 °C. On the other hand, with the observed warming of 0.07 to 0.12 °C over the second half of the 20th century, the total expected temperature adjustment can be assumed to be 0.2 to 0.3 °C. Therefore, the secondary temperature adjustment is not of sufficient size to explain the observed warming trend of 0.2 to 0.3 °C per century, and the observed warming must partly be a direct effect of reduced atmospheric heat loss.

Atmospheric warming, on the other hand, modifies both the net evaporation and the heat loss. The evaporation and the latent heat loss increase, but the sensible heat loss decreases. Following the discussion on page 107 and the information in table 5.4, reducing the heat loss by 20 % with constant net evaporation leads to an increase in temperature of 0.7 °C and a secondary increase of salinity of 0.04 psu. The relative size of the temperature and salinity signals can therefore be used to estimate the relative changes in $E-P$ and H_{Atm}. If S_E is the change in salinity due to changes in evaporation, and S_H is the (secondary) change in salinity due to heat loss, the following set of equations holds:

$$\begin{array}{rcrcrcl} S_E & + & S_H & = & S_{\mathrm{tot}} & = & 0.12\,\mathrm{psu}(\pm 0.02\,\mathrm{psu}) \\ \frac{0.2\,^\circ\mathrm{C}}{0.3\,\mathrm{psu}} \cdot S_E & + & \frac{0.7\,^\circ\mathrm{C}}{0.04\,\mathrm{psu}} \cdot S_H & = & T_{\mathrm{tot}} & = & 0.25\,^\circ\mathrm{C}(\pm 0.05\,^\circ\mathrm{C}) \end{array} \tag{5.14}$$

Solving this set of equations yields $S_E = 0.11\,\mathrm{psu}$ and $S_H = 0.010\,\mathrm{psu}$. $S_E = 0.11\,\mathrm{psu}$ is equivalent to an increase in excess evaporation by 7 %, while $S_H = 0.010\,\mathrm{psu}$ indicates a reduction in total atmospheric heat loss by approximately 5 %, leading to the conjecture that both the change in river runoff and a change in atmospheric conditions are necessary to explain the observed changes in deep water properties. However, the precise role of atmospheric changes remains unclear, as the relation between evaporation and (sensible and latent) heat loss cannot be well defined here, and a more detailed study of the observations would be beyond the scope of this thesis. Future work may also identify some of the transitional patterns in the observations.

Summing up, the results in this chapter provide estimates for the correlation between air-sea-flux changes and resulting changes in water properties. The next chapter 6 uses these results for a case study of changes at the beginning of the holocene.

Chapter 6

Changes in the Holocene

In this chapter, the HYCOBOX model is used to investigate the conditions in the Mediterranean Sea since the Last Glacial Maximum, approximately 18000 years BP[1]. In geological terms (see figure 6.1), this covers the second half of the Late Weichselian (22 kyr BP to 10 kyr BP, the last glacial in the Pleistocene) and the Holocene (10 kyr BP to present). Of particular interest is a period in the Early Holocene during which sediment cores reveal significant changes in the Mediterranean circulation, as carbon rich organic sediments (sapropels) were deposited. The first section of this chapter reviews the geological evidence from sediment cores, and the climatological changes that have been suggested to account for them, most of which involve an additional influx of fresh water directly into the Eastern Mediterranean, most prominently through the opening of the Black Sea.

The subsequent sections focus on one mechanism that has hitherto received little attention. During the last 18000 years, the global sea level rose by approximately 120 m (Fairbanks 1989). With lower sea level, the average salinity in the Mediterranean was considerably higher in the Last Glacial Maximum (LGM, 18000 yr BP) than at present, and strait transport considerably lower. In times of rapid sea level rise the influx of (fresher) Atlantic water increased, but due to long residence times the salinity of the deep and intermediate waters would have decreased more slowly, so that the basin was

[1] As the ^{14}C-calibration is not well established before 9 kyrBP (Stuiver et al. 1986), all dates here are given in uncalibrated radiocarbon dates. The calender age is approximately 1000 years higher than the radiocarbon age (see also figure 6.1).

more stably stratified, and convection was reduced.

The HYCOBOX model is used to quantify the effect, and compare it to the effect of additional fresh water influx. The results show that the reservoir effect is likely to have a smaller effect than increased freshwater influx, but remains a potentially siginificant factor at the onset of sapropel formation.

6.1 Sapropel formation in the Mediterranean

Due to its anti-estuarine circulation, the present day Mediterranean is well ventilated throughout the water column, and the photic zone is nutrient-depleted, resulting in low primary productivity, particularly in the east. However, sediment cores have revealed more than 150 sapropel layers in sediments since the middle miocene. A sapropel is defined as a discrete sediment bed containing at least 2 % organic carbon by weight, while sapropelitic layers contain between 0.5 % and 2 % organic carbon (Aksu et al. 1995). Generally, sapropels indicate that the production of organic carbon exceeded the oxidation of dead organic matter, so that part of the carbon could be deposited, thus suggesting very different conditions to those of the present day.

Two principal mechanisms can lead to sapropel formation. In euxinic conditions, i. e. when convection is reduced, parts of the water column have low oxygen content or become anoxic, and organic carbon cannot be oxidised (stagnation theory), leading to the deposition of black and organic rich euxinic sediments. Alternatively, if primary productivity is very high, the rate of carbon sedimentation can be too large for the carbon to be oxidised completely even in waters that are not oxygen-depleted (productivity theory). However, these principal mechanisms are not mutually exclusive, but rather interlinked: reduced convection may well lead to upwelling of nutrient rich waters and increased productivity (Kemp et al. 1999).

The youngest sapropel layer S1 was deposited 9600-6400 yr BP during the holocene (Aksu et al. 1995). A number of mechanisms have been proposed to explain the occurrence of S1, mainly invoking stagnation through the influx of large amounts of comparatively fresh water at the surface. Examples include increased freshwater input from the Nile due to monsoon intensification (Rossignol-Strick 1985) and increased rainfall in the northern borderlands of the Eastern Mediterranean (Rohling and Hilgen

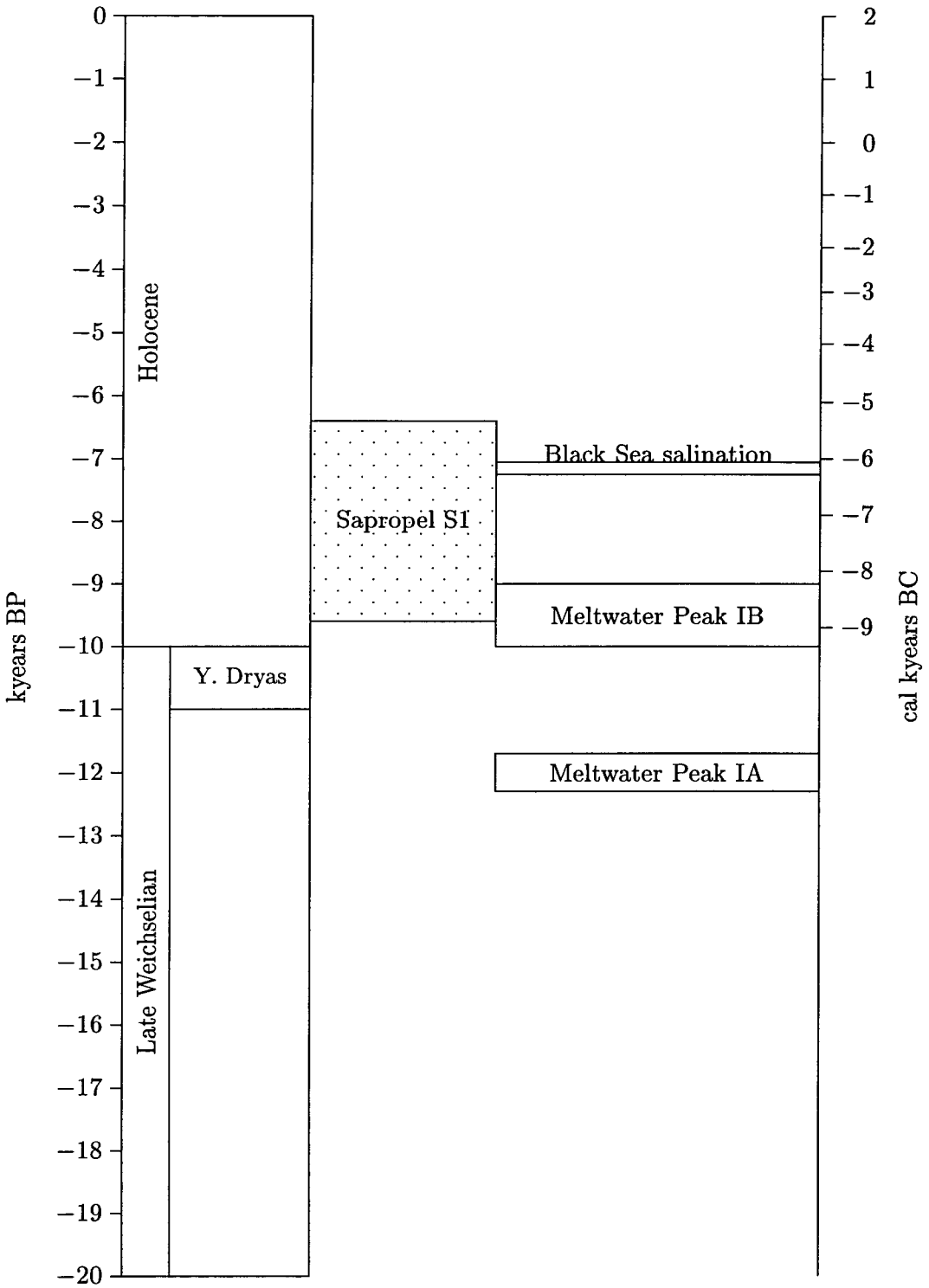

Figure 6.1: Stratigraphy from the Last Glacial Maximum to the present.

1991). However, although the freshwater inflow may have been somewhat higher 9000-7000 years BP (Bethoux 1993), it is generally thought that the freshwater budget has remained similar to the present day. Estimates of the present net freshwater gain of the Aegean mainly through the Bosphorus range from 5400 to 12400 m^3/s (Lane-Serff et al. 1997). It seems unlikely that a change in precipitation has occurred that was large enough to alter the circulation significantly.

An event that has been suggested as a cause for sapropel formation was the opening of the connection at the Strait of Bosphorus between the Mediterranean Sea and the Black Sea, which was a freshwater lake ("Black Lake") in the late pleistocene. At present, there is a two layer estuarine exchange in the Bosphorus, in which Mediterranean water flows into the Black Sea at the bottom of the Bosphorus[2] and less saline ($\approx$ 20 psu) Black Sea water flows out at the surface. For the transition between the freshwater Black Lake and the present two layer exchange, there are currently two competing scenarios. The gradual inflow scenario (e. g. Lane-Serff et al. 1997, and references therein) assumes that the Black Lake always had an outflow to the Mediterranean through the the Bosphorus Strait. When the Mediterranean Sea level had risen sufficiently above sill depth (40-60 m below present sea level), Mediterranean water started to flow in at the bottom, converting the Black Lake into a brackish Black Sea and establishing the present two layer system. For the following two or three millennia, the Aegean experienced an additional freshwater influx as the fresh water in the Black Sea was replaced by saline water. Lane-Serff et al. (1997) calculated that – depending on the conditions – the additional freshwater influx may have been between 10000 m^3/s and 30000 m^3/s, starting between 10300 years BP and 7900 years BP. This would have been a significant inflow of fresh surface water (equivalent to an increase in net precipitation over the whole Mediterranean of 13 to 40 cm/year), leading to stronger stratification and stagnation.

[2]Since early hellenistic times, this was known to be a useful feature for the sea trade with the North: One could travel against the southward surface current by lowering a stone filled bucket into the northward bottom current (Pitman and Ryan 1998). Pitman and Ryan (1998) also report the speculation that this bottom current was the underworld river Acheron described in the Argonaut saga. This saga is possibly a mythical account of sea faring into the Black Sea in the Middle Bronze Age.

In an alternative scenario for the opening of the Black Sea, presented by Ryan et al. (1997), the connection between the Black Lake and the Mediterranean was lost completely in the late pleistocene, and the lake level dropped to approximately 120 m below the present level. When the sea level in the Mediterranean rose to sill depth, this resulted in a catastrophic waterfall and subsequent drowning of the Black Sea shelf[3]. In support of this theory an unconformity in the Black Sea has been found at the base of a sapropel layer, and AMS-^{14}C-dating of the euryhaline gastropods at this horizon leads to a date of 7150 $\pm$ 100 years BP for the salination of the Black Sea. In this scenario, the freshwater input at the Bosphorus is negligible before 7150 years BP, and increases quickly to the present value afterwards. As in the gradual scenario, there is also an additional input of fresh water into the Mediterranean Sea in the centuries or millennia following the opening, as the outflowing Black Sea water was initially fresher than today. However, compared to the gradual scenario this effect was less prominent in the catastrophic scenario, as a large part of the salination happened in the very short time when the Black Sea was flooded with salty Mediterranean water, increasing its volume by approximately 15 %.

Although recent discoveries[4] of objects that might be interpreted as remains of Neolithic settlements north of Sinop at a depth of 100 m lend further support to the catastrophic flooding scenario, at present there are still open questions, and it cannot be decided with certainty which scenario is correct. For this study, both scenarios are used.

6.2 The effect of sea level change

The end of the pleistocene and the early part of the holocene is characterised by a retreat of glaciers and melting of the ice caps, leading to a sea level rise of 120 m. A detailed

[3]This scenario was speculatively linked by Pitman and Ryan (1998) to presumed patterns migration of protoindoeuropean (PIE) speakers, predynastic Egyptians, Semites and Ubaids, whose origin is speculated to be on the drowned banks of the Black Lake, and whose memories of the devastating event are preserved in the legend of Noah's flood.

[4]See the press coverage on September 15, 2000, in all major newspapers. The finds have not been published yet and should therefore be interpreted with care.

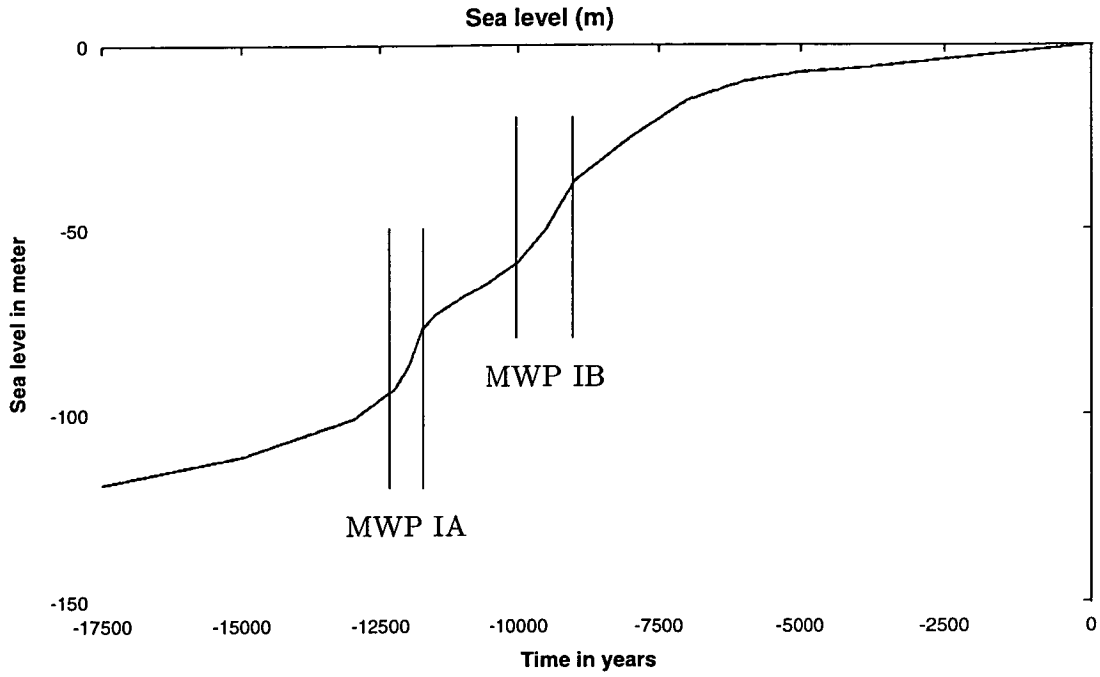

Figure 6.2: Sea level change during the holocene, showing the two meltwater peaks IA and IB (after Fairbanks (1989)).

record of the sea level rise for the last 17000 years has been obtained by Fairbanks (1989) (see figure 6.2). He found that the sea level rise was most rapid in two periods: The first meltwater peak ("Meltwater peak IA") is centred around 12000 years BP and ends at the beginning of the colder Younger Dryas chronozone, while the second ("Meltwater peak IB") occurs after the Younger Dryas, centred around 9500 years BP.

In the following, two effects of the sea level rise are relevant. Firstly, as the Strait was shallower and narrower at times of lower sea level, the exchange with the Atlantic was reduced and the conditions in the Mediterranean were more extreme than today. This has been investigated by Rohling and Bryden (1994) using a steady state hydraulic model with a triangular strait cross section. At times when the sea level rises quickly, however, a more dynamic aspect of the system becomes relevant: With residence times of centuries or millennia, the conditions in the basin lag behind the steady state situation during the meltwater peaks, in particular as the residence times were considerably longer than at the present day due to the smaller strait cross section. Therefore, while larger amounts of Atlantic water enter at the surface, the intermediate and deep water still have a comparatively higher density, leading to stronger stratification in the basin

Parameter	Value
Effective Basin Depth	$H = 2000\,\mathrm{m}$
Net evaporation	$E - P = 75\,\mathrm{cm/year}$
Heat Loss	$H_{\mathrm{Atm}} = 7\,\mathrm{W/m^2}$
Water formation parameterisation	(D)
WFO parameter	$\mu = 0.4$
Basin Mixing	yes
Strait Mixing	no
Sea level	figure 6.2
Variation in net evaporation	
Experiment (CONST)	no
Experiment (GRAD)	8500-6750 BP: linear decrease by 20 cm/year
	6750-5000 BP: linear increase by 20 cm/year
Experiment (CATA)	before 7150 BP: 20 % higher

Table 6.1: Parameters for the Holocene experiments. Experiment (CONST) uses a constant freshwater budget, experiment (GRAD) models the gradual opening of the Black Sea with increases freshwater inflow during the transition, and (CATA) models the catastrophic opening of the Black Sea after Ryan et al. (1997).

and reduced circulation. This effect may provide a new explanation for the formation of sapropels and will be discussed in the next section.

The HYCOBOX model was used to investigate the effects of sea level change. Three experiments were performed. In each of them, the sea level curve from figure 6.2 was used, but they differ in the freshwater budget (see table 6.1 and figure 6.3). In the first experiment (CONST), the freshwater budget remains constant throughout with a present-day value for the net evaporation of 75 cm/year. The second experiment (GRAD) tries to model the gradual opening of the Black Sea, based on the scenario in Lane-Serff et al. (1997): Between 8500 year BP and 5000 year BP, an additional influx of fresh water reduces the net evaporation. The influx increases linearly from 8500 year BP, reaching a peak of 15000 $\mathrm{m^3/s}$ (equivalent to 20 cm/year reduction in net evaporation over the whole basin) at 6750 year BP, and then decreases linearly until

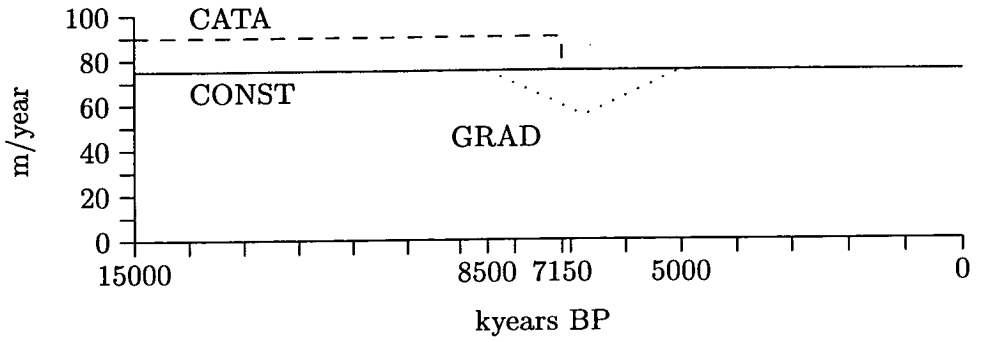

Figure 6.3: The net evaporation used for the three holocene experiments.

5000 year BP. The third experiment (CATA) models the catastrophic scenario: Before the opening of the Black Sea, the missing freshwater influx through the Bosphorus means that the excess evaporation was 20 % larger than today, and with the catastrophic event at 7150 year BP it dropped to its present-day value of 75 cm/year.

Only the water formation parameterisation (D), i. e. the density dependent parameterisation, was used in these experiments, with a parameter $\mu = 0.4$. The results are not sensitive to the value of this parameter, as a lower sea level in the past almost certainly meant that the system was in the maximal regime. The other parameters for this set of experiment are summarised in table 6.1.

Although the water formation would be the obvious variable that could indicate reduced circulation, the rather coarse parameterisation of the water formation in HYCOBOX means that it is rather insensitive in the model. Firstly, if the system is in the maximal regime, the water formation in the present parameterisation cannot deviate much from the maximal strait transport. Secondly, the water formation is a bulk property covering the whole Mediterranean, whereas a more differentiated model would be necessary to see changes in the Aegean or parts of the Eastern Mediterranean. However, some indication of changes in the circulation can be obtained from the movement of the interface depth as a result of imbalances between strait transport and water formation; and from the densities, indicating the stratification in the basin.

Figure 6.4 shows the interface depth and the salinity for experiment (CONST) with constant freshwater budget. As expected, the salinity (bottom) was considerably higher during the holocene. This essentially replicates the results obtained by Rohling and

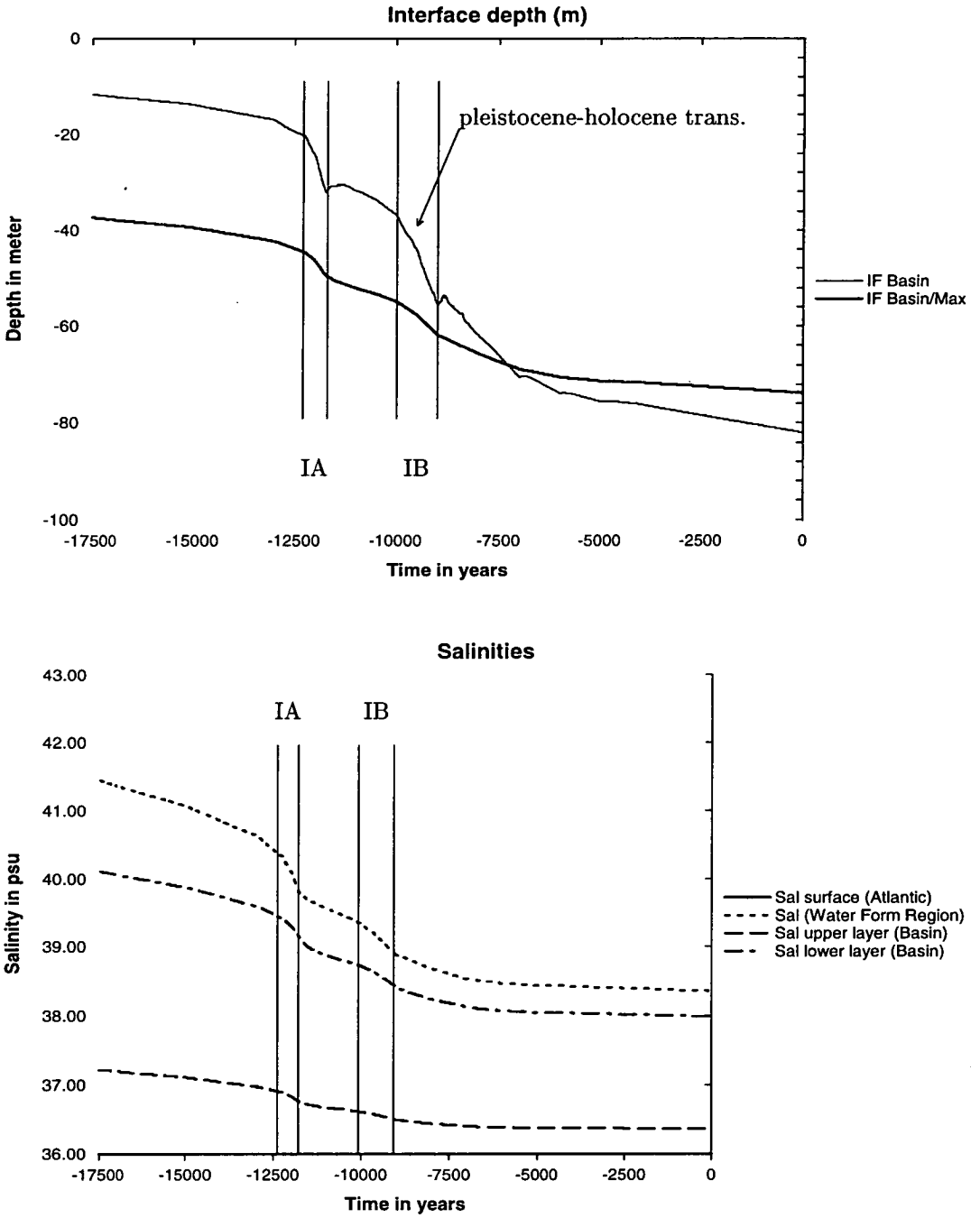

Figure 6.4: The interface depth (top) and the salinity (bottom) for the experiment with constant freshwater budget. The interface deepens considerably around the pleistocene-holocene transition.

Bryden (1994), both qualitatively and quantitatively, although the numerical values differ slightly, as they used a somewhat smaller value for the net evaporation (56 cm/year). Of particular interest is the pleistocene-holocene transition at 9600 year BP, at which the disappearance of planktonic foraminifera of the genus *Neogloboquadrina* is interpreted as an indication that the pycnocline dropped below the photic zone (Rohling and Gieskes 1989). In the HYCOBOX experiment, the interface depth deepens suddenly from 36.9 m at 10000 years BP to 55.5 m at 9000 year BP.

The experiment for the gradual scenario (GRAD), shown in figure 6.5, shows the same behaviour as (CONST) before the onset of the freshwater influx from the Black Sea. In particular, the drop of the interface depth at the beginning of the holocene is reproduced. The additional freshwater influx from the Black Sea leads to a considerable freshening of the Mediterranean in the 7th millennium BP, evident in a noticeable minimum of the salinity in the water formation layer and the lower layer (figure 6.5 bottom) centred around 6500 years BP, i. e. 200-300 years after the largest freshwater input.

The interface depth drops during the first half of the freshwater event, i. e. during the time when the net evaporation decreases (8500 – 6750 year BP), but starts to rise again in the second half of the event (6750 – 5000 year BP), leading to an interface depth shallower than in experiment (CONST). The drop in interface in the first half indicates a reduced water formation, and – as Lane-Serff et al. (1997) noted – this may have been a factor in the formation of sapropels. The timing of the event used here is rather late for the sapropel formation (9600 – 6750 year BP), but there are considerable uncertainties in the timing and scale of the additional freshwater influx, so that a link between the opening of the Black Sea and the Mediterranean sapropel layer S1 is not impossible – assuming that the gradual scenario rather than the catastrophic scenario happened.

In the experiment for the catastrophic scenario (CATA) (figure 6.6), the salinity in the basin is by approximately 0.4 psu higher than in the other two experiments prior to the event at 7150 years BP, as the freshwater influx is lower. At the time of the opening, the salinity shows a sharp drop, and the interface depth has an excursion into the submaximal regime, indicating a collapse of the circulation. As such, this transition

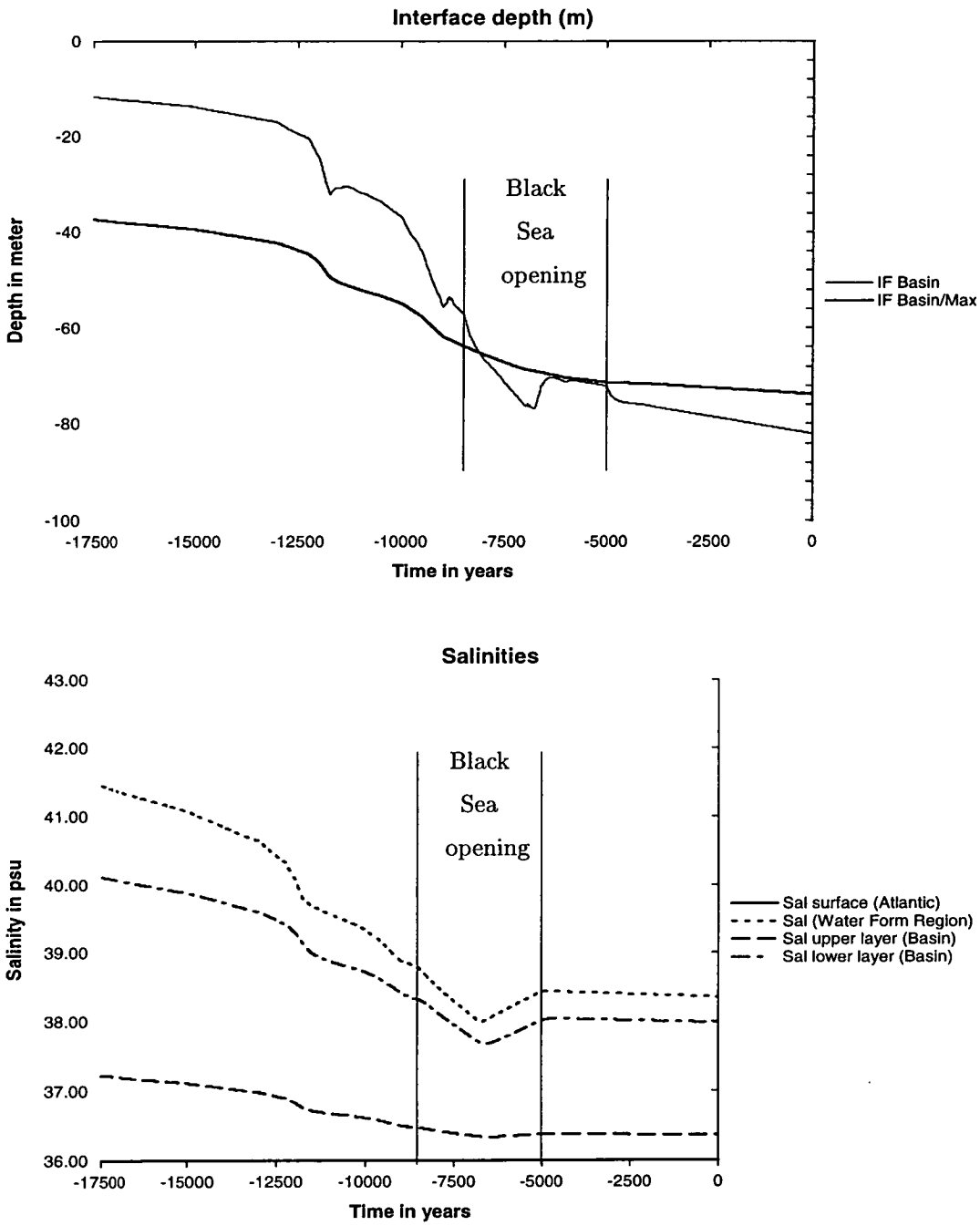

Figure 6.5: The interface depth and the salinity for experiment (GRAD) with the gradual opening of the Black Sea.

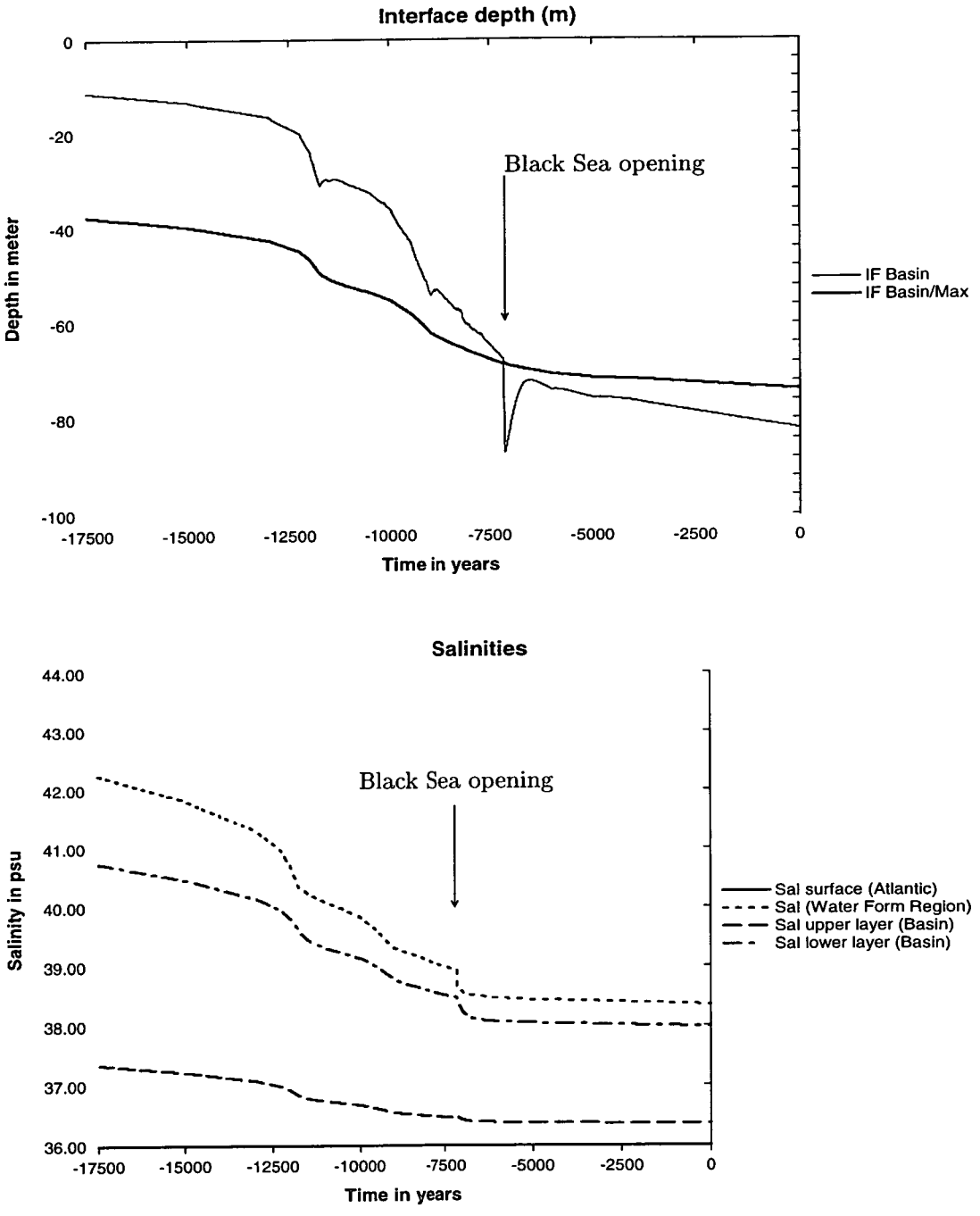

Figure 6.6: The interface depth and the salinity for experiment (CATA) with the catastrophic opening of the Black Sea.

is very similar to the one investigated in experiment D_m^{-E} in chapter 4, in which the evaporation was reduced by 20 % starting from a maximal situation. This experiment was discussed in detail in chapter 4. Both experiments show a sharp drop in interface depth below the final steady state (figure 6.6 top). In the holocene experiment, the drop in interface depth lasts for approximately 500 years with an e-folding time of 200 years, not inconsistent with the expected e-folding time for density adjustments of 160 years from (4.33) for the parameters in this experiment.

While the drop in interface depth indicates a reduced circulation for half a millennium after the catastrophic opening of the Black Sea, the timing makes it unlikely that the flooding of the Black Sea and subsequent increase in freshwater influx into the Mediterranean are a causal factor for sapropel formation, which began approximately 2500 years before the event. However, the additional freshwater may have been a factor in maintaining a low circulation towards the end of the deposition of sapropel S1, i. e. from 7150 years BP to 6400 years BP.

Comparing the two scenarios, the catastrophic scenario could lead to a shorter, but more complete collapse of the circulation than the gradual scenario. Timing of the sapropel layer and its duration favours the gradual scenario, but makes the catastrophic opening an unlikely cause for the Mediterranean sapropels, as the catastrophic flooding happened towards the end of the sapropel formation.

6.3 The reservoir effect and sapropel formation

A mechanism for sapropel formation that has not received much attention is the reservoir effect: As the sea level rises and the input of Atlantic water through the Strait of Gibraltar increases, the salinity of the deep and intermediate water changes only slowly, leading to a transient increase in stratification. The three HYCOBOX experiments can be used to compare the reservoir effect with the effect of the changing water budgets in the two experiments (GRAD) and (CATA).

Figure 6.7 shows the density difference $\Delta\rho = \rho_L - \rho_F$ between the lower layer L and the water formation box F for the three experiments. This density difference was chosen because it most directly influences the water formation rate (3.42). If this density difference is small (i. e. the graph shows a peak in the positive – upward –

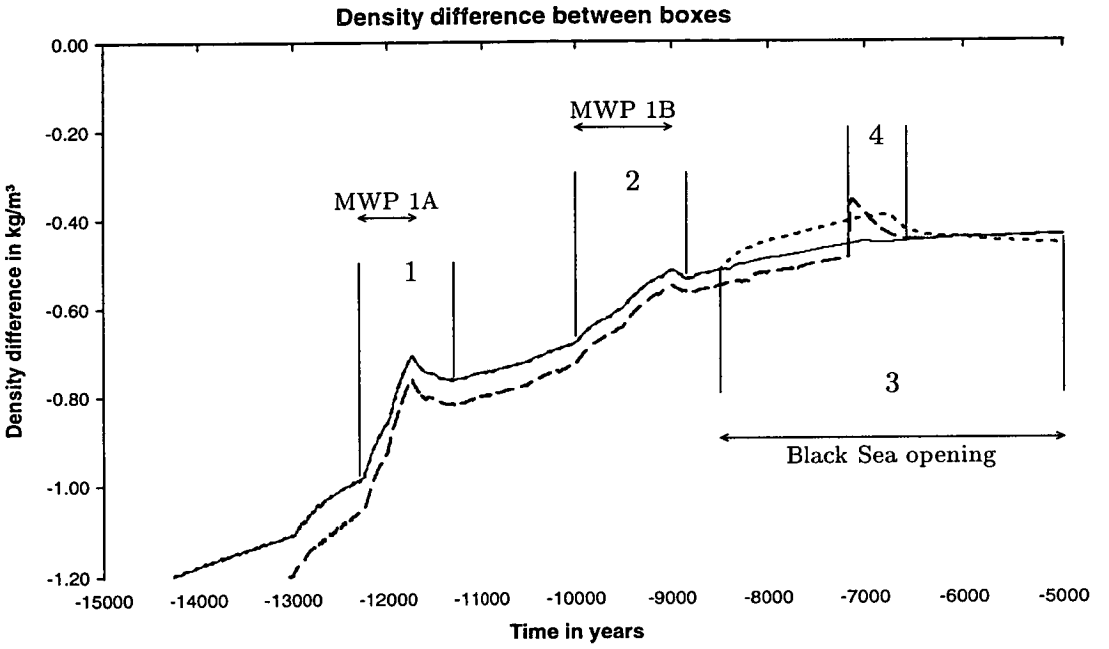

Figure 6.7: The density difference between boxes F and L for the three experiments. (CONST): solid line; (GRAD): dotted line; (CATA): dashed line. The experiment for the catastrophic opening of the black sea shows a stronger stratification before the event as the excess evaporation is lower. Vertical lines mark the beginning and end of the different peaks in stratification, see also table 6.2, and the arrows mark the duration of the meltwater peaks and the gradual Black Sea opening. The stratification shows local extrema 300-500 years after the freshwater events IA and IB.

Peak	age	peak width	$\Delta\rho$	baseline	peak height
	kyears BP	kyears	kg/m^3	kg/m^3	kg/m^3
1. Meltwater IA	11750	1000	−0.71	−0.83	0.12
2. Meltwater IB	9000	1250	−0.52	−0.56	0.04
3. Gradual	6750	3500	−0.39	−0.45	0.06
4. Catastrophic	7150	600	−0.35	−0.46	0.11

Table 6.2: Comparison of the peaks in stratification in figures 6.7.

direction), the newly formed water is not very dense and therefore less likely to sink, so that the water formation is reduced.

For both scenarios, the curve show peaks at the respective freshwater events, confirming that this variable is a sensitive indicator of the circulation regime. In view of the reservoir mechanism, the curves show clear peaks at the two main meltwater events at 11750 years BP and 9000 years BP, three to five centuries after the strongest meltwater influx (12000 years BP and 9500 years BP). Table 6.2 shows the different peaks in comparison. In each case, the peak height is calculated from the value compared to a baseline. For the two freshwater events, the baseline is taken from the experiment with constant freshwater budget, which serves as a control run here. For the two meltwater peaks, no control run is available, and the height of the peak is estimated as the height above a hypothetical straight line connecting the bases of the peak.

Comparing the two freshwater events, the catastrophic scenario leads to a considerably higher peak of $0.11\,kg/m^3$ than the gradual scenario ($0.06\,kg/m^3$), however with 600 years it is also considerably shorter than the gradual scenario with 3500 years. Meltwater peak IA is the strongest of all three events, with a peak height of $0.12\,kg/m^3$. This would indicate that this meltwater peak could have had a stronger or at least similar impact on the circulation as the Black Sea events. On the other hand, the later meltwater peak IB leads to a peak that is $0.4\,kg/m^3$, only two thirds of the height the peak connected to the gradual opening of the Black Sea ($0.6\,kg/m^3$), but it is sufficiently high to suggest that it had non-negligible effects on the circulation of the Mediterranean.

The timing of the different events (see figure 6.1) suggests that the sapropel layers

are deposited following the meltwater peak IB, or during the gradual opening of the Black Sea. The result of these experiments show that the meltwater peak had a smaller effect than the gradual opening of the Black Sea. However, the timing of the Black Sea opening is rather late compared to the sapropel deposition, and as the salination of the Black Sea is accurately and independently dated to 7150 years BP, there is only limited scope for an earlier freshwater influx from the Black Sea. Therefore it is fair to speculate that the meltwater peak IB may have influenced the onset of the sapropel formation. Furthermore, if the catastrophic scenario is accepted over the gradual scenario, the meltwater peak IB remains as a strong cause for reduced circulation during this period.

It is unclear, however, why the much stronger meltwater peak IA did not lead to sapropel formation. Possible explanations include additional changes in the freshwater budget that were not considered here, or stronger cooling in the Younger Dryas, intensifying the deep water formation. It also seems likely that the Mediterranean circulation in general was in a less stable state at the pleistocene-holocene transition than during the late pleistocene – a question, however, that cannot be resolved with a simple box model.

Chapter 7

The hydraulic jump and mixing in the strait

For the maximal regime, the system develops a hydraulic jump between the Mediterranean and the Strait, as the supercritical flow at the strait entrance reverts to the subcritical flow inside the basin (figure 7.1). In the HYCOBOX model described so far, the hydraulic jump is nothing more than a discontinuity in the Bernoulli function, decoupling the interface depth in the strait from the interface depth in the basin as energy is lost in the jump. The water properties of the layers are not modified.

However, a sheared stratified flow and an internal hydraulic jump between two miscible layers can be expected to lead to mixing and entrainment processes, which hitherto have been neglected. It is the purpose of this chapter to explore some of the possible effects that may arise when these mechanisms are considered. The discussion here is far from a comprehensive account of mixing processes, instead the focus is on – partly speculative – aspects that may give rise to interesting dynamical behaviour and new feedback mechanisms.

The first section of this chapter introduces some basic ideas about mixing in strait related processes. With a view to finding feedback processes with interesting internal dynamics, the entrainment of upper layer water into the lower layer in the hydraulic jump on the Mediterranean side of the strait is particularly interesting, as this modifies the density of the outflowing water and therefore influences the strait transport. When this modification is applied to the model, the results suggest that this is another possible

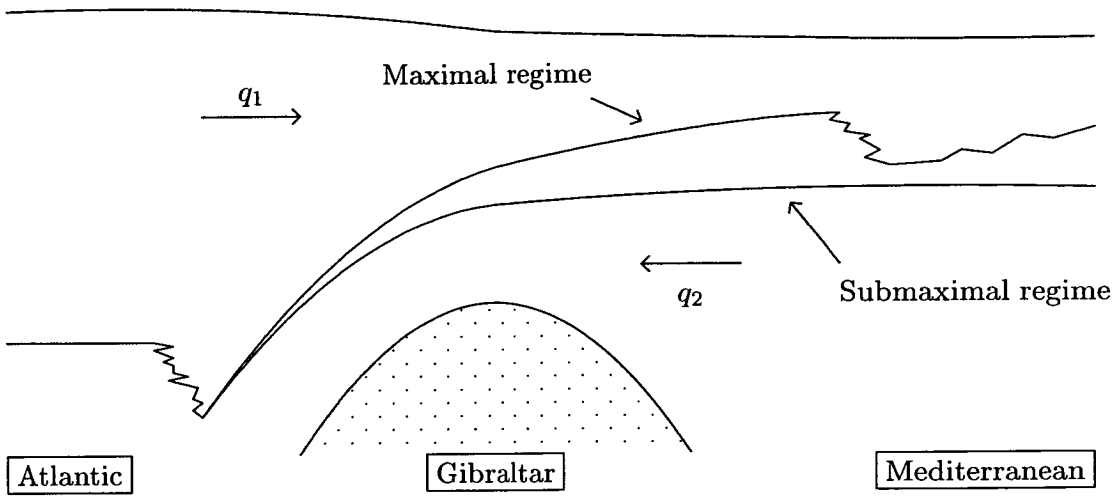

Figure 7.1: Hydraulic jumps at the strait entrances. Towards the Mediterranean, a hydraulic jump is present in the maximal regime.

mechanism that could lead to a collapse of the basin circulation for decades or centuries. A stability analysis shows that this collapse is the result of the system moving to a different (meta)stable state which is a stable fixed point of the system on timescales for which density adjustments can be neglected, but it is conjectured that it will always decay back to a more normal state on longer timescales.

Finally, the relevance of this process study is discussed. The behaviour of the HYCOBOX model is compared with results from a GCM study Myers et al. (2001) which shows a similar behaviour, leading to the conclusion that the HYCOBOX model studies can assist in the interpretation of GCM results. Whether these processes also occur in nature is the subject of the final section of this chapter.

7.1 Theoretical considerations on mixing in the strait

In the exchange flow situation shown in figure 7.1, two different mixing processes should be distinguished. Firstly, along most of the strait there is a flow with a strong shear across the interface, which leads to interfacial mixing and friction. Secondly, at the entrances to the strait, hydraulic jumps and other turbulent and dissipative processes facilitate locally enhanced entrainment and mixing between the water masses.

The stability of the stratified shear flow along the interface can be determined by calculating the Richardson number R_i. For Richardson numbers of $R_i > 1/4$ the flow is stable, while for $R_i < 1/4$ it may become unstable. The Richardson number is defined

as

$$R_i := \left(\frac{N}{\frac{du}{dz}}\right)^2 \tag{7.1}$$

where N is the Brunt-Väisälä-frequency (or buoyancy frequency), defined as

$$N^2 := -\frac{g}{\rho}\frac{d\rho}{dz} \tag{7.2}$$

(see, e.g, Baines 1995). For an estimate the non-differential form, i. e. the bulk Richardson number

$$R_i = -\frac{g}{\rho}\frac{\Delta\rho}{\Delta u^2}\Delta z \tag{7.3}$$

can be used. Using values for the Strait of Gibraltar ($\Delta\rho = 1\,\mathrm{kg/m^3}$, $\Delta u = 2\,\mathrm{m/s}$ and $\Delta z = 100\,\mathrm{m}$), this leads to

$$R_i = 1/4 \tag{7.4}$$

Therefore, the bulk Richardson number does not give a clear indication whether the shear flow is in the stable or unstable regime, and the stability may also change over time. However, in other situations (e. g. in the seasonal thermocline) it is known that the local Richardson number can be much lower than that based on mean density and velocity gradients (Fernando 1991, Padman and Jones 1985), so that the shear flow at Gibraltar may be potentially unstable. Observations in the Strait of Gibraltar (Wesson and Gregg 1994) suggest that there is strong mixing related to tidal effects which may be stronger at spring tides compared to neap tides. Using a completely different approach, Bormans and Garrett (1989b) include an estimated coefficient for interfacial friction in a steady state 2-layer numerical model and find that interfacial friction (and mixing) reduces the strait transport.

Although it is clear that mixing across the interface all along the strait is an important factor, these effects will not be considered here in detail. The aim of this study is to find new types of dynamical behaviour, but interfacial friction and mixing are little influenced by other variables discussed in this study, so that they are not expected to add any new dynamical features to the system. However, shear flow instabilities clearly have to be included in studies which aim to get as precise numeric values for characteristic quantities as possible.

A new type of dynamical behaviour, however, can be expected from mixing and entrainment in the hydraulic jumps or other turbulent transitions at the strait entrances.

The hydraulic jump in the Atlantic is not of interest here, for two reasons: As the interface slumps to great depth very quickly (Baringer and Price 1997), the inflowing water, which comes mainly from the surface, is not strongly affected, so that there is no feedback. Secondly, the hydraulic jump in the Atlantic does not depend on conditions inside the basin and – by the same argument as made above for the stratified shear flow – does not add new dynamics to the basin-strait-system.

This is not the case for the hydraulic transition between the strait and the Mediterranean basin. In the submaximal regime, there is a subcritical flow from the sill into the basin (see chapter 2), whereas in the maximal regime the supercritical flow in the strait is discontinuously connected to the subcritical basin in a turbulent and dissipative hydraulic transition. Therefore, the presence and height of the hydraulic jump depends on the interface depth in the basin, and the entrainment and mixing processes can also be expected to depend on basin conditions, opening the possibility of additional feedback mechanisms.

The mechanism proposed here assumes that fresh water from the inflowing upper layer is entrained into the lower layer in the hydraulic jump. This has two effects: Firstly, the inflow of fresh water into the basin is reduced, as parts of the inflowing water is immediately entrained into the lower layer and flows out again. Secondly, the density of the outflowing water in the strait is lower, and as the strait transport depends on the density difference between the layers, the strait transport decreases accordingly. In total, the presence of strong mixing in the hydraulic jump reduces the water exchange between the Mediterranean and the Atlantic.

7.2 HYCOBOX modifications

In the model, the hydraulic jump is present when the system reaches the maximal regime (see section 3.2). This is the case when the interface in the basin is shallower than a threshold depth which is determined by the maximal solution of the strait equations. The height of the hydraulic transition h_{HJ} is defined as the difference between the interface depth in the basin and the interface depth at the basin-side entrance of the strait (see figure 7.2):

$$h_{\mathrm{HJ}} := h_{1b} - h_{U'} \tag{7.5}$$

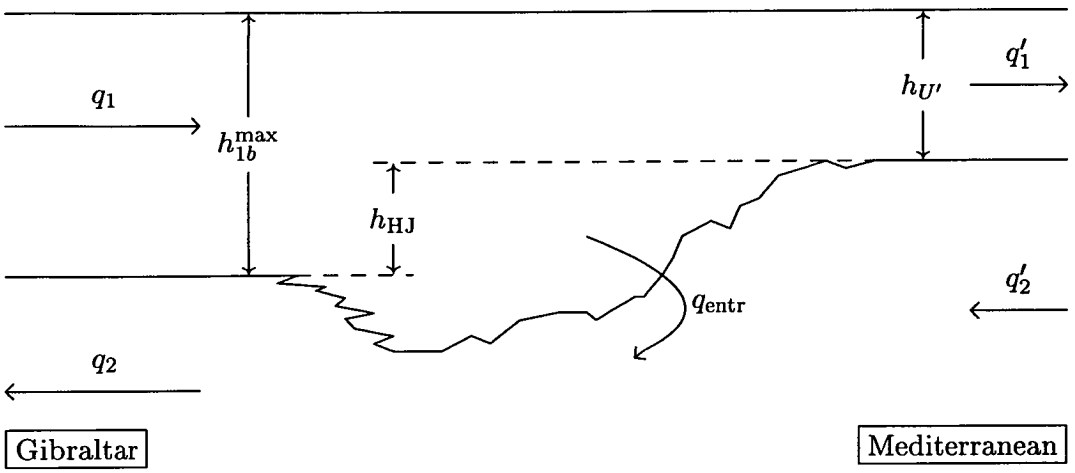

Figure 7.2: The hydraulic transition between strait and basin, and the definition of the entrainment in the HYCOBOX model

To investigate the possibility of a dynamical feedback between mixing processes and other strait and basin processes, the HYCOBOX model was modified to include mixing in the hydraulic jump. The parameterisation used here is mainly guided by practical considerations and is kept as simple as possible. Mixing in the model is characterised by the following assumptions:

- A proportion of the inflowing water is mixed into the outflowing water, decreasing the density difference in the strait and reducing the exchange with the basin.
- The amount of mixing increases with the height of the hydraulic jump. For simplicity, this increase is assumed to be linear up to a maximal value.

This leads to the following modifications. The entrainment q_{entr} is the amount of water which is entrained from the inflowing upper layer into the outflowing lower layer (see figure 7.2). It is given by

$$q_{entr} = E \cdot q_1 \tag{7.6}$$

and the entrainment rate $E = q_{entr}/q_1$ is calculated as proportional to the height of the hydraulic jump:

$$E = k_{entr} \frac{h_{HJ}}{h_{1b}^{max}} \tag{7.7}$$

This parameterisation introduces the mixing strength k_{entr} as a new nondimensional parameter. Figure 7.2 illustrates a physical interpretation for (7.7): A fraction $\frac{h_{HJ}}{h_{1b}}$ of

the inflow is directly affected by the turbulence, and parts of it – a fraction given by k_{entr} – is being entrained into the lower layer. Therefore, the mixing strength k_{entr} can have values between 0 and 1, although high values seem unlikely, as they would imply almost complete entrainment of the incoming water.

The amount q_{entr} of inflowing water that is being entrained into the lower layer reduces the effective inflow into the basin. Similarly, as part of the outflow q_2 comes from the entrained water q_{entr}, the effective outflow from the basin is smaller than the strait transport. Let q_1' and q_2' be the effective in- and outflow, i. e. the amount actually entering or leaving the basin boxes U and L. Then

$$q_1' = q_1 - q_{\text{entr}} \tag{7.8}$$

$$-q_2' = -q_2 - q_{\text{entr}} \tag{7.9}$$

where q_2 and q_2' are negative, q_1, q_1' and q_{entr} are positive. In the volume equations (3.25, 3.26) for the basin boxes U and L, the strait transports q_i are replaced by the effective basin transports q_i'.

The entrained water is being mixed into the outflow and therefore changes the salinity and temperature of the outflowing water. With S_1 and S_2 being the salinity of the layers in the strait, S_A the salinity of the Atlantic surface, and S_U the salinity of the lower layer in the basin, the boundary conditions (3.13, 3.14, 3.15, 3.16) now become

$$S_1 = S_A \tag{7.10}$$

$$S_2 = S_L - (S_L - S_1)\frac{q_{\text{entr}}}{q_2} \tag{7.11}$$

$$T_1 = T_A \tag{7.12}$$

$$T_2 = T_L - (T_L - T_1)\frac{q_{\text{entr}}}{q_2} \tag{7.13}$$

For $q_{\text{entr}} = 0$, all equations collapse to the corresponding equations in chapter 3.

Figure 7.3 shows the modification introduced through the hydraulic jump. In addition to the existing feedback loops (see also figure 4.13), two new paths are possible (shown in thick lines): Firstly, the hydraulic jump directly reduces the effective transport. A reduction in effective transport raises the interface and therefore heightens the hydraulic jump. Secondly, the entrainment in the hydraulic jump reduces the outflow

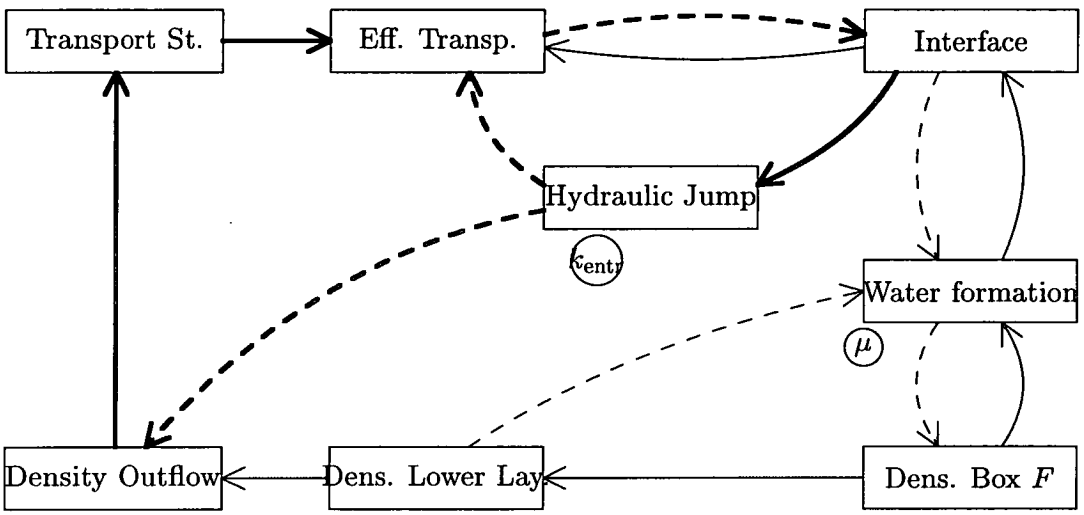

Figure 7.3: The feedback loops arising from the introduction of the hydraulic jump. There are two new paths (thick lines), both leading to an overall positive (unstable) feedback. The other influences (thin lines) were discussed in chapter 4. The strength of the feedbacks through the hydraulic jump depends on the parameter k_{entr}, the feedback through the water formation/density loop on the parameter μ. As in previous diagrams, solid lines indicate a positive influence, while dashed lines are negative influences. For simplicity, the surface feedback (see chapter 4 and figure 4.13) has been omitted, and inflow and outflow are not shown separately.

Variable	Value
Net evaporation	$E - P = 75\,\mathrm{cm/year} \cdot A = 0.058\,\mathrm{Sv}$
Heat loss	$H_{\mathrm{Atm}} = 7\,\mathrm{W/m^2} \cdot A = 17 \times 10^{12}\,\mathrm{W}$
Interface depth	$h_{U'} = 81\,\mathrm{m}$
Outflow	$q_2 = 1.051\,\mathrm{Sv}$
Salinity difference (Strait)	$\Delta S = 1.97\,\mathrm{psu}$
Temperature difference (Strait)	$\Delta T = -3.47\,^\circ\mathrm{C}$
Water formation parameter	$\mu = 3.1 \times 10^4\,\mathrm{m^5\,kg^{-1}\,s^{-1}}$
	$= 0.4\,\mathrm{m^3\,kg^{-1}\,year^{-1}} \cdot A$

Table 7.1: The characterisation of the steady state used as the basis for the experiments investigating the effect of entrainment in the hydraulic jump. Given are the values for the situation without a hydraulic jump.

of the density, which reduces the actual strait transport, and again raises the interface and the height of the hydraulic jump. The strength of these feedbacks is determined by the parameter k_{entr}. As can be seen from the diagram, both these feedback paths are positive loops which potentially lead to unstable situations.

7.3 The evolution of the system: HYCOBOX experiments

A number of HYCOBOX experiments were performed to investigate the effect of these modifications. As a proper rational for the parameter k_{entr} is unknown, the experiments were designed as a sensitivity study using several values of k_{entr} ranging from 0 to 0.5. For the water formation parameterisation, the most realistic parameterisation (D) was used, in which the water formation rate is proportional to the stratification in the basin, i. e. the density difference between the water formation box F and the lower layer L, and proportional to the interface depth (see section 3.4). Mixing between the boxes is included as described in chapter 3.3. The geometry and air-sea-fluxes were chosen to represent the present day Mediterranean situation and are listed in table 7.1.

All experiments start in the same submaximal situation and run for 100 years to reach the steady state at $t = 0$ years. To model a short dry event, in years $t = 0$ to $t = 10$ the net evaporation is 20% larger and then reduced back to its initial value for

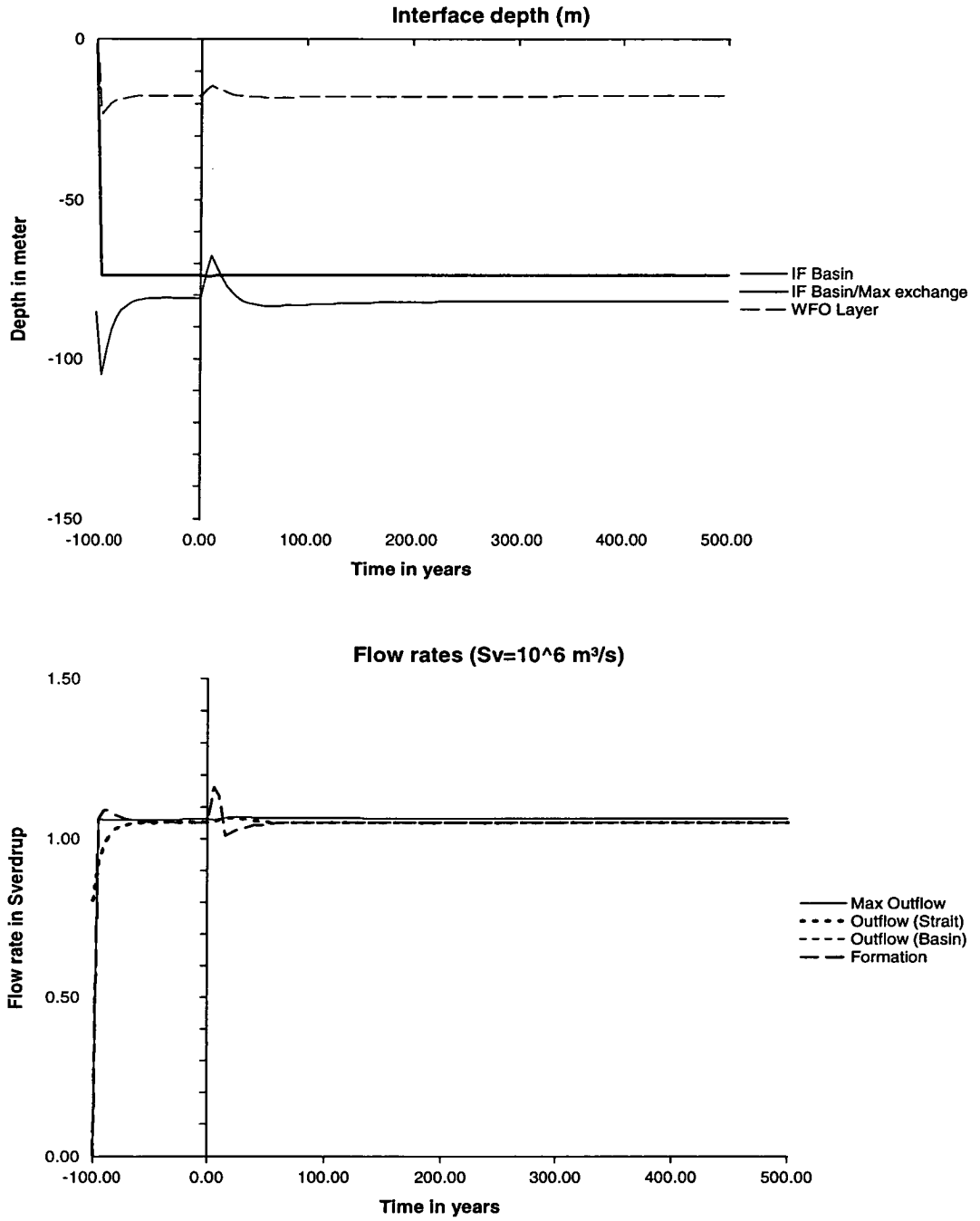

Figure 7.4: Interface (top) and strait transport for the control experiment without entrainment in the hydraulic jump. In years $t = 0$ to $t = 10$, the evaporation is 20% larger, pushing the system shortly into the maximal regime. During this time, the water formation increases.

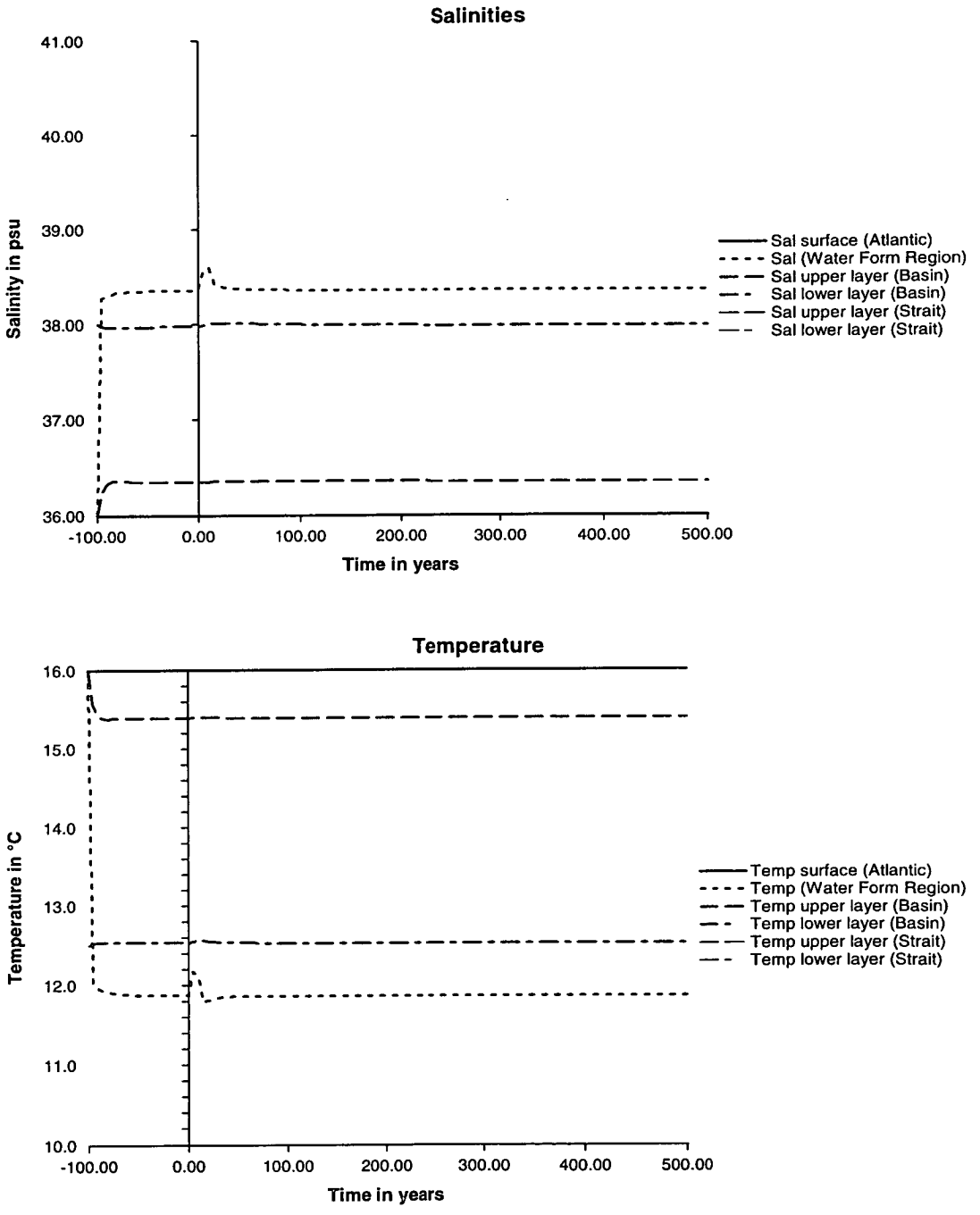

Figure 7.5: Salinity and temperature in the control experiment. The 10-year dry event leads to spikes in the properties of the water formation box (dotted lines), but is not sufficient to change the properties of the main water masses in the basin significantly.

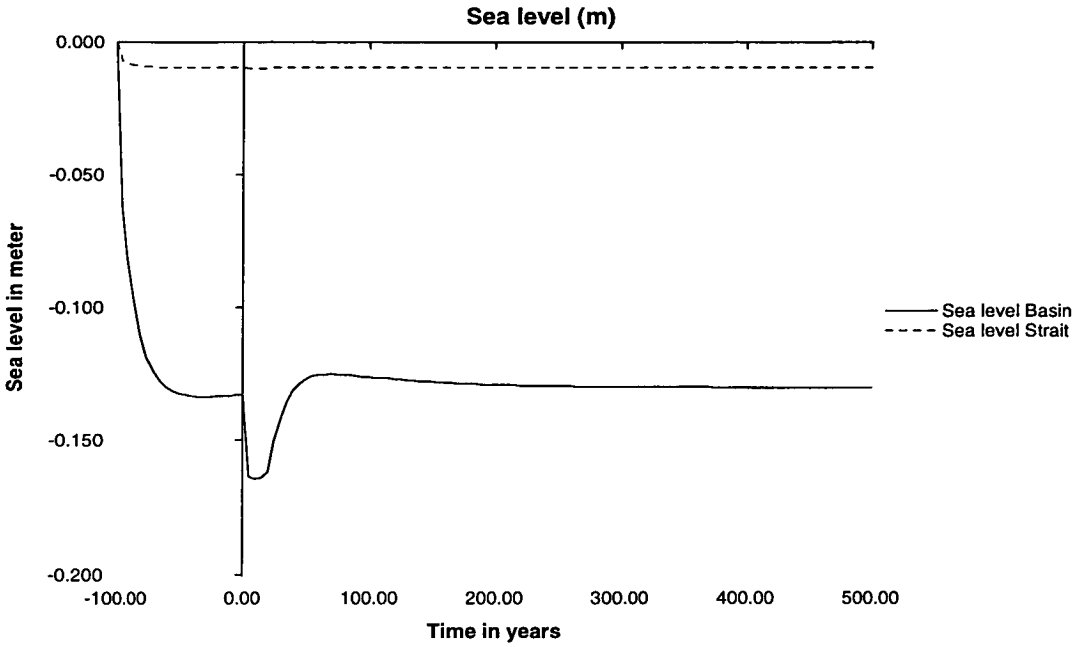

Figure 7.6: The sea level in the control experiment only shows a short change as the strait goes into the maximal regime.

the rest of the experiment. This short anomalous dry event pushes the system into the maximal regime. In the following, one experiment with entrainment in the hydraulic jump ($k_{\text{entr}} = 0.4$) is shown in detail and compared with the control experiment without entrainment ($k_{\text{entr}} = 0$), so that the qualitative features of the time evolution can be discussed. In the next section, the stability of this experiment is analysed. Using the other experiments with different values of k_{entr}, the role of this parameter is then investigated in the subsequent section.

Figures 7.4, 7.5 and 7.6 show the control experiment in which no entrainment takes place in the hydraulic jump, i. e. $k_{\text{entr}} = 0$. In accordance with results discussed in chapter 4, the water formation rate (figure 7.4 bottom, dashed line) goes up at the onset of the 10-year evaporation event, and the interface (figure 7.4 top, thin solid line) rises briefly over the threshold for the maximal regime (thick line). The sea level curve (figure 7.6) shows a corresponding change. However, as the period with anomalous net evaporation is considerably shorter than the timescale for salinity and temperature adjustments (see section 4.2), the salinity and temperature (figure 7.5) do not change significantly, although the properties of the water formation box (dotted lines) are

different during the event.

In summary, the system reacts to the 10-year evaporation event with a short excursion into the maximal regime, which is visible in the evolution of the interface depth and the sea level, but without discernible salinity and temperature signal, and returns to the steady state within approximately 30 years.

The situation is markedly different when mixing in the hydraulic jump is included. Figures 7.7, 7.8 and 7.9 show the evolution of an experiment with $k_{\text{entr}} = 0.4$, but otherwise the same conditions as the control run. The evolution of this system may roughly be divided into two significantly different phases, with transitional phases between them:

Strong mixing/weak circulation (ca. years 10-155, labels II to IV): A strong hydraulic jump (figure 7.7 top) with mixing reduces the strait transport (figure 7.7 bottom). The salinity and temperature differences in the strait are reduced compared to the basin values (see B and F in figure 7.8), which reduces the salt and heat transport through the strait and leads to extreme salinity and temperature values in the basin. Basin circulation, i. e. the formation rate and exchange with the Atlantic, is greatly reduced (figure 7.7 bottom, A and D).

Weak mixing/strong circulation (ca. from year 175 onwards, V/VI): The strait regime is submaximal, there is no hydraulic jump, the circulation is stronger, and salinity and temperature return to less extreme values.

Note the somewhat unintuitive feature that the basin circulation and the exchange with the Atlantic is higher in the first phase than in the second phase, although the strait regime is maximal.

This behaviour is the result of a complex interaction between a number of mechanisms:

I. Years 0-10: The evaporation event increases the water formation rate (figure 7.7 bottom, dashed line), so that the interface (figure 7.7 top) rises enough to push the strait into the maximal regime, and a hydraulic jump forms. The salinity and temperature of the water formation box (7.8 dotted lines) also react to the increased evaporation.

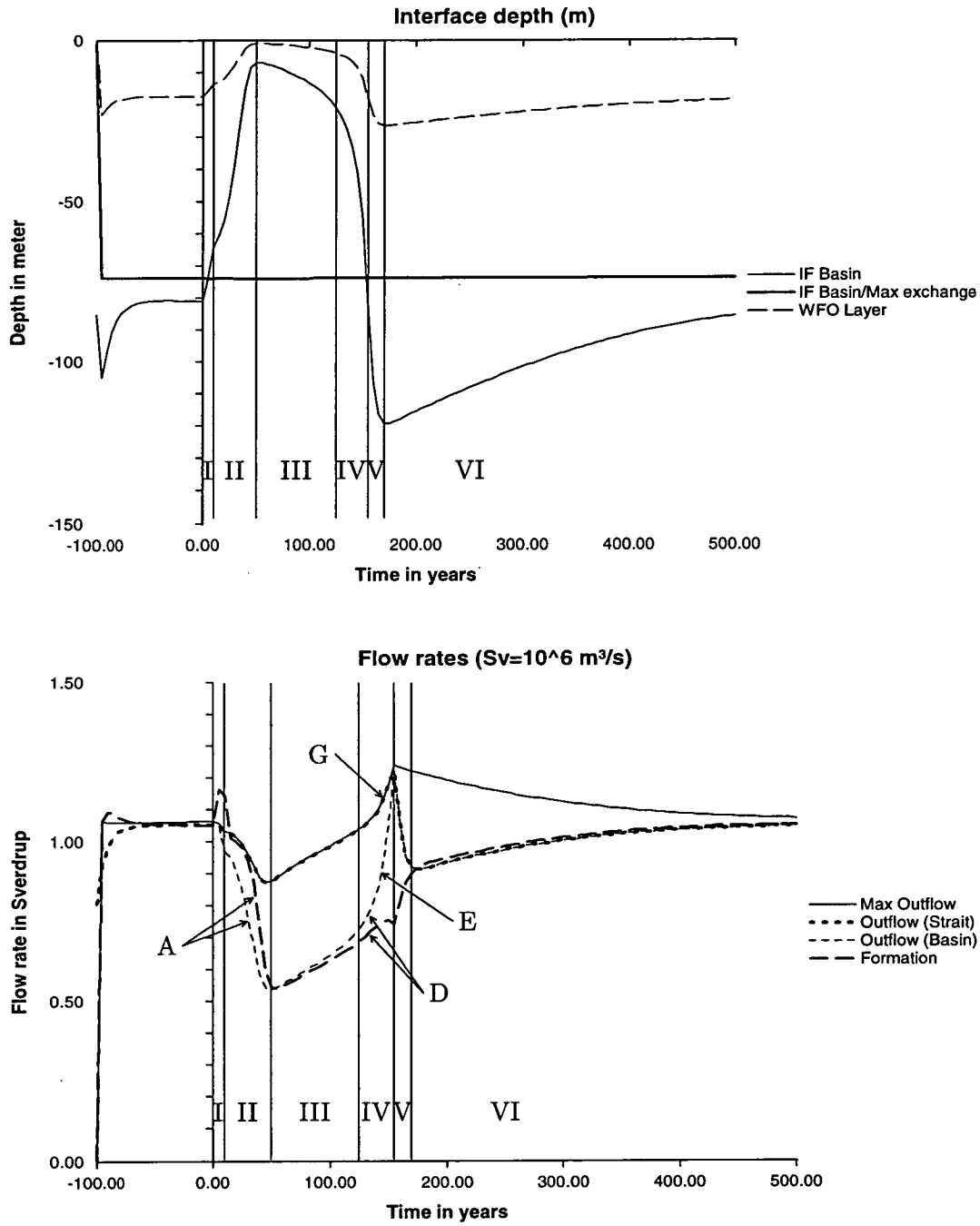

Figure 7.7: Interface (top) and transports for the experiment with entrainment in the hydraulic jump ($k_{\text{entr}} = 0.4$). In years $t = 0$ to $t = 10$, the evaporation is 20% larger, pushing the system shortly into the maximal regime. During this time, the water formation increases. The subsequent evolution of the system can be divided into 6 phases (I to VI). Details are discussed in the text.

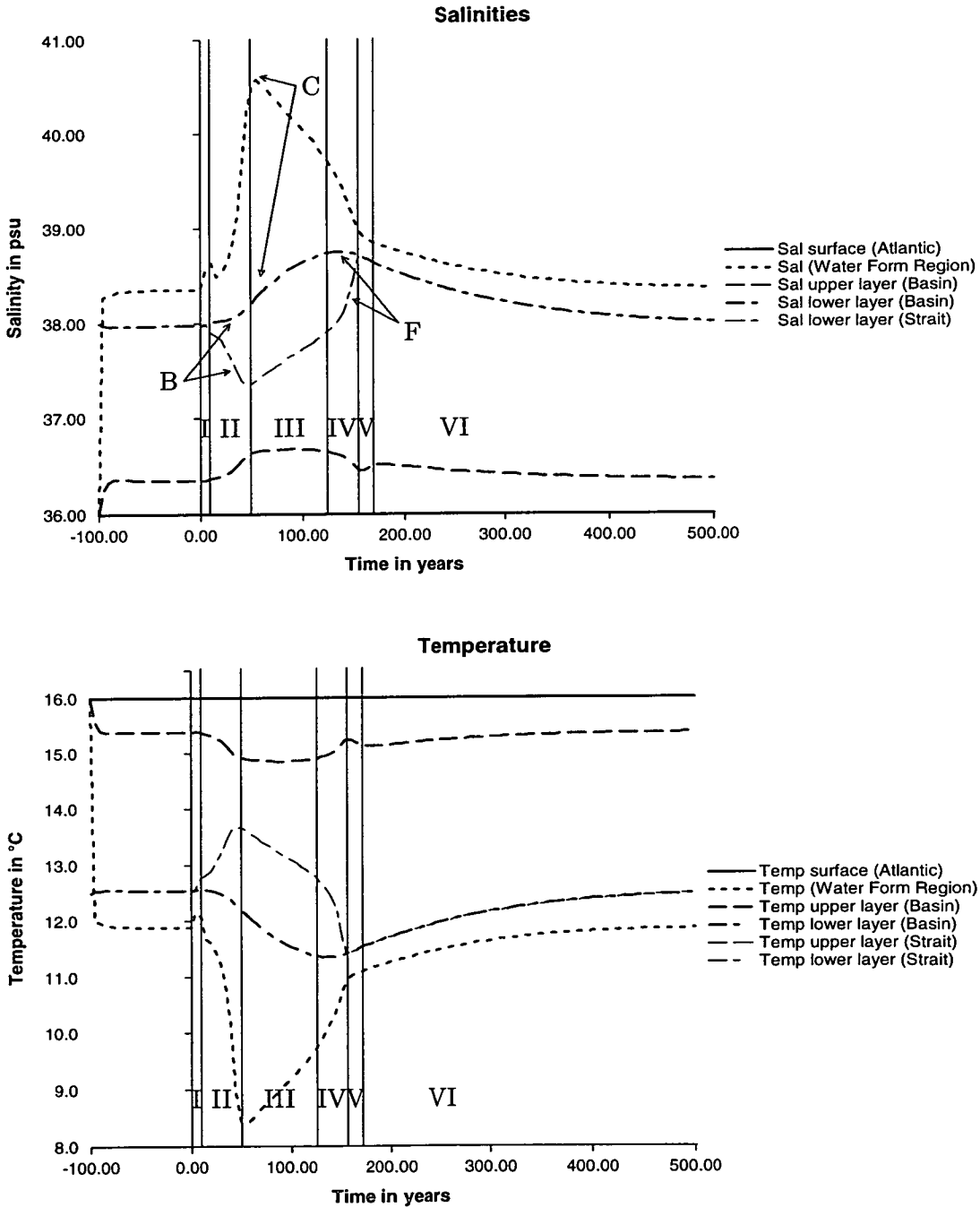

Figure 7.8: Salinity and temperature in the entrainment experiment. The 10-year evaporation event leads to spikes in the properties of the water formation box (dotted lines), but is not sufficient to change the properties of the main water masses in the basin significantly. Details are discussed in the text.

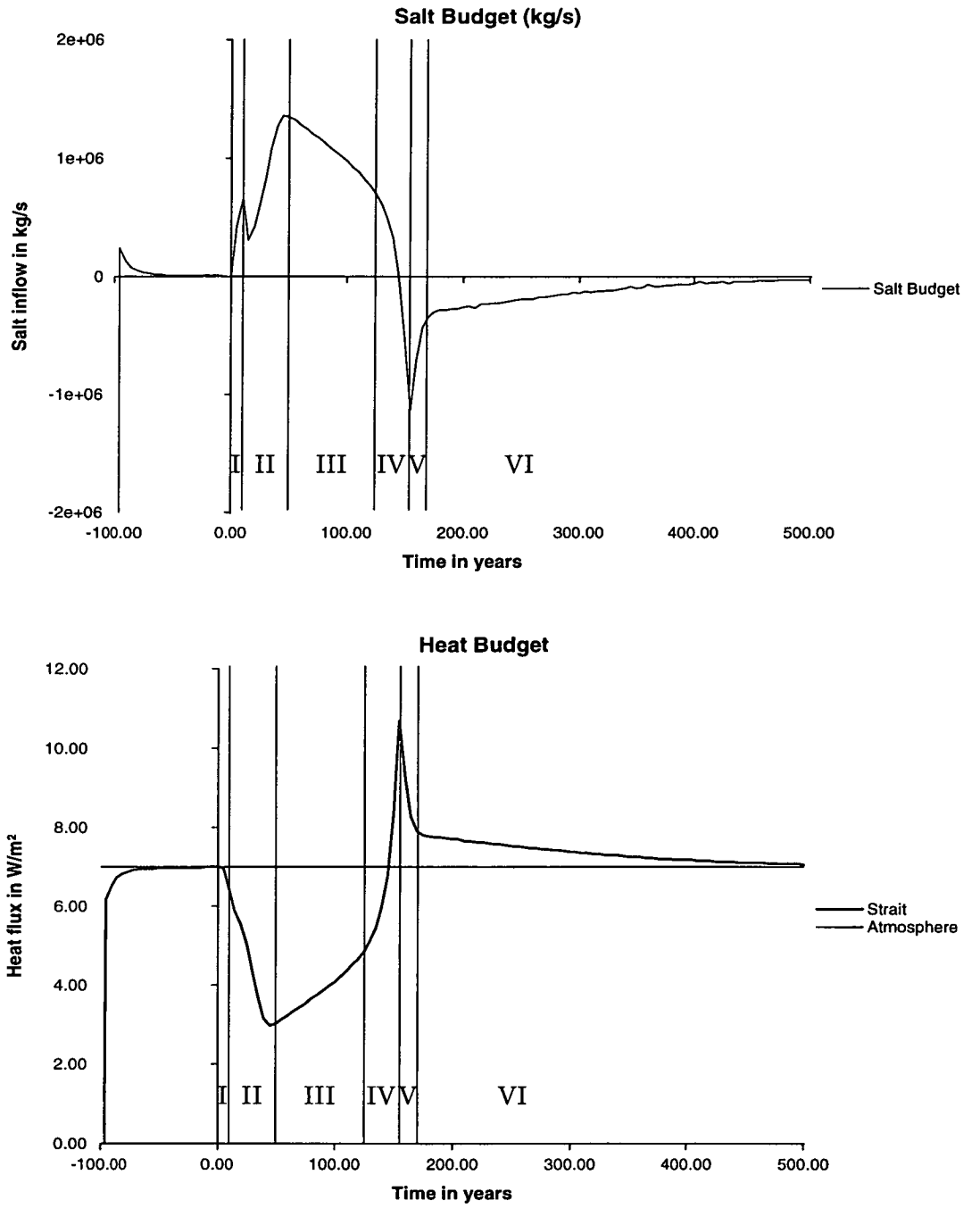

Figure 7.9: Salt and heat budget in the entrainment experiment. In the salt budget, the spike from the evaporation event is visible in years 0 to 10.

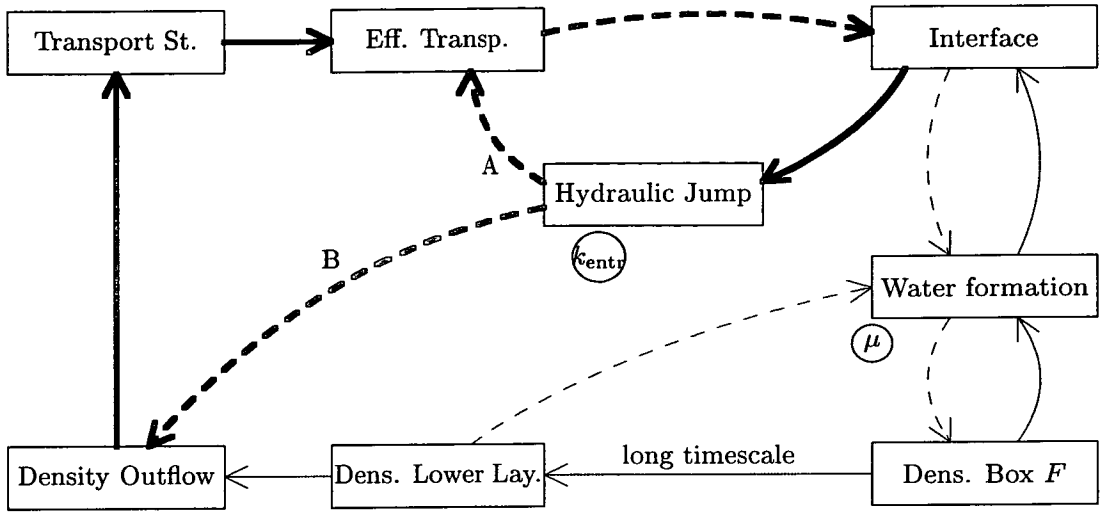

Figure 7.10: In phase II, a strong positive feedback (thick lines) reduces the effective exchange, and the interface rises. Similarly, in phase IV the positive feedback lowers the interface and leads to a collapse of the hydraulic jump.

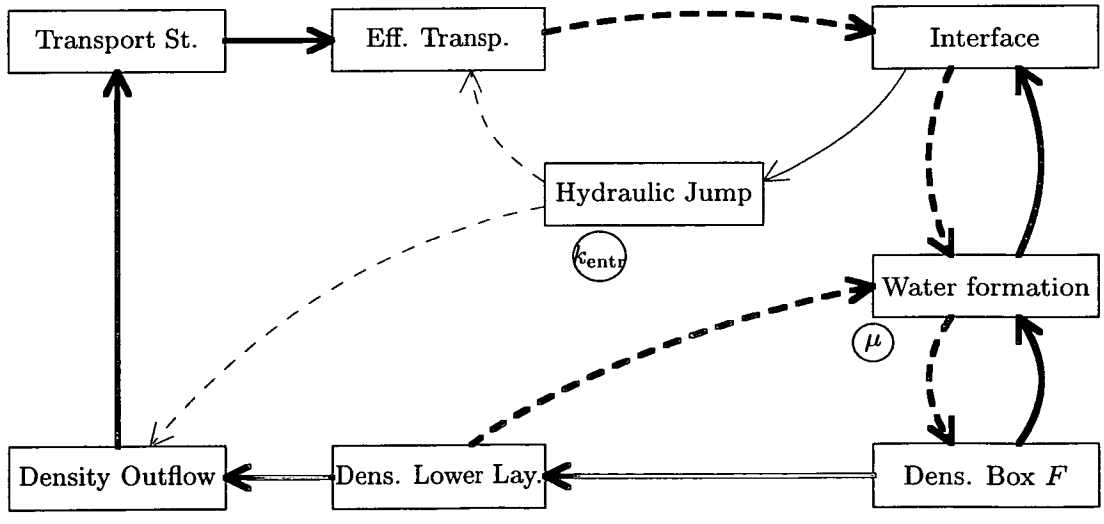

Figure 7.11: In phase III, the density changes balance the destabilising effects of the hydraulic jump.

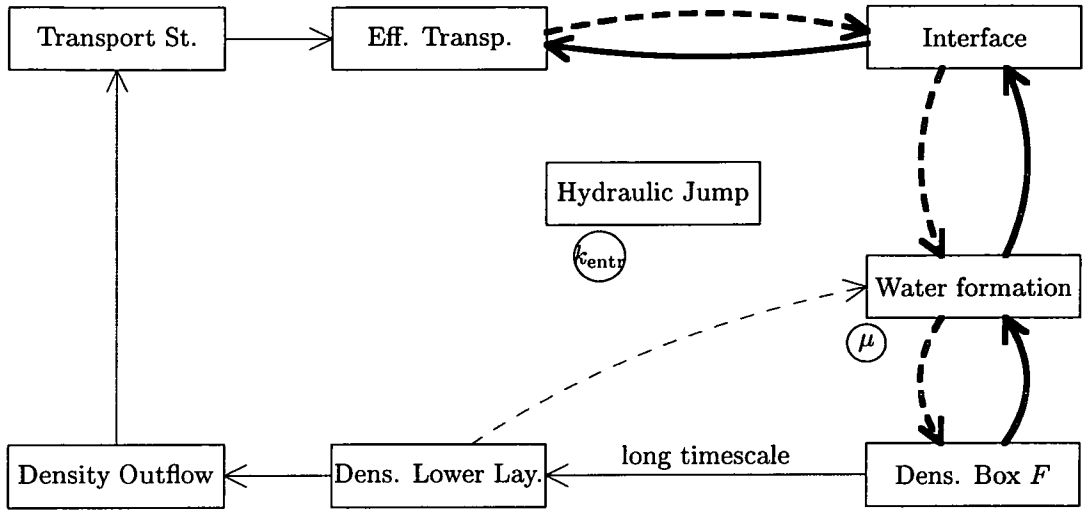

Figure 7.12: In phase V, the hydraulic jump has disappeared, leaving the stabilising feedback through the interface mechanism and the (slower) density mechanism.

II. Years 10-50: Although air-sea-fluxes are back to the original value, the system does not return to its steady state, as there is an unstable positive feedback between interface depth and strait exchange (figure 7.10). Due to mixing in the hydraulic jump, the effective transports into and out of the basin are smaller than the strait transport (A in figures 7.7 bottom and 7.10). Therefore, the water formation rate is higher than the basin outflow, and the interface continues to rise. Secondly, fresh inflowing water is mixed into the outflow, leading to a lower salinity of the outflow compared to the lower layer in the basin (B in figures 7.8 top and 7.10). With the effective transport and the salinity of the outflow reduced, the salt budget (figure 7.9 top) becomes unbalanced. Similarly, the heat budget (bottom) becomes unbalanced. At the same time, as the interface gets shallower, the water formation rate decreases and the salinity and temperature of the water formation box increases/decreases correspondingly (figure 7.8). The timescale of this phase is determined mainly by the timescale for interface changes (see section 4).

III. Years 50-125: Around $t = 50$, the water formation rate gets lower than the effective strait transport, and the interface stops rising. From this point onwards, changes take place on the longer timescales of the salinity and temperature mech-

anisms, stabilising the system (figure 7.11). The salinity started to rise from year 0 onwards, as the newly formed water gets increasingly saline. Although the salinity of the water formation box stops increasing around year 50, the lower layer salinity continues to rise (C in figure 7.8 top), and similarly the temperature continues to fall. Therefore the density difference between in- and outflow in the strait also increases, enhancing the strait transport. With increased transport and salinity and temperature difference, the salt and heat budgets (figure 7.9) move back towards the balanced state. The increased strait transport also means that the interface starts to fall again. However, the movement of the interface is slowed down, as the water formation rate increases at almost the same rate as the effective transport. In other words, the destabilising positive feedback of the hydraulic jump mechanism is stabilised by other mechanisms (figure 7.11).

IV. Years 125-155: In this (and the following) phase, the faster interface adjustment again dominates the dynamics as in phase II (figure 7.10). By approximately the year 125, the water formation rate cannot keep up with the increasing strait transport (D in figure 7.7 bottom). This leads to a runaway effect: As the interface drops, the mixing in the hydraulic jump decreases, so that the effective exchange with the basin increases strongly (E in figure 7.7 bottom). Reduced mixing also increases the density difference in the strait (F in figure 7.8), and the actual strait transport (G in figure 7.7 bottom) goes up. All these effects lead to a sharply falling interface depth in the basin, and at $t = 155$ the threshold between maximal and submaximal regime is reached. As strait transport and density difference go up, the salt and heat budgets (figure 7.9) become balanced already at $t = 145$, but as the fluxes continue to change, the budgets again become unbalanced in the opposite direction.

V. Years 155-170: In year 155, when the strait returns to the submaximal regime the strait transport is considerably larger than the water formation rate, so that the interface continues to fall well into the submaximal regime, and the hydraulic jump disappears (7.12). Although the water formation rate increases with falling interface (except for a small negative spike around $t = 155$ as a result of the strong

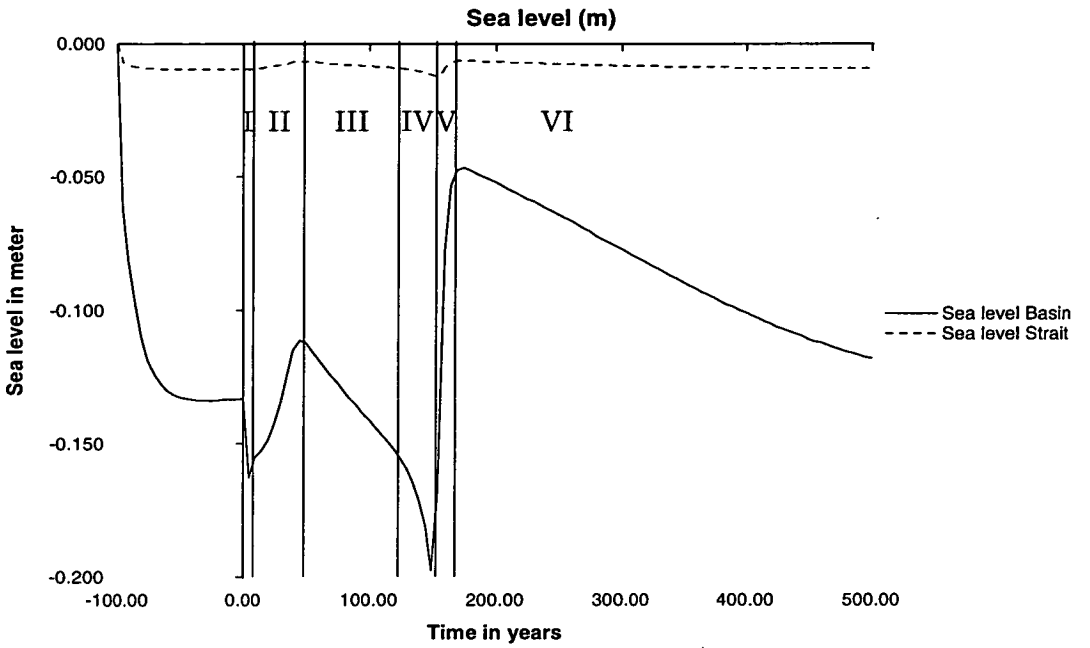

Figure 7.13: The sea level in the entrainment experiment shows a complex behaviour related to the strait transports.

inflow of fresh surface water), it balances the outflow only after the interface has fallen well into the submaximal regime with very low strait transport. During this period of decreasing strait transport, the salt and heat flux through the straits are reduced too, and the budgets move closer to the balanced state.

VI. Years 170 onwards: From year 170 onwards, the system slowly returns to the steady state, starting from a situation with very deep interface, very high basin salinity, very low basin temperature and unbalanced salt and heat budgets. This adjustment takes place in the way described in chapter 4 on the long timescales of salinity and temperature changes with an e-folding time of 180 years. At the end of the experiments ($t = 500$ years) the system is almost back at the original state before the evaporation event.

The complex behaviour is also visible in the strong sawtooth pattern in the evolution of sea level (figure 7.13). As was discussed in chapter 4, the evolution of the sea level mirrors the evolution of the strait transport (figure 7.7 bottom, thick dotted line), slightly modified by the changing densities.

In summary, the entrainment in the hydraulic jump leads to a complicated evo-

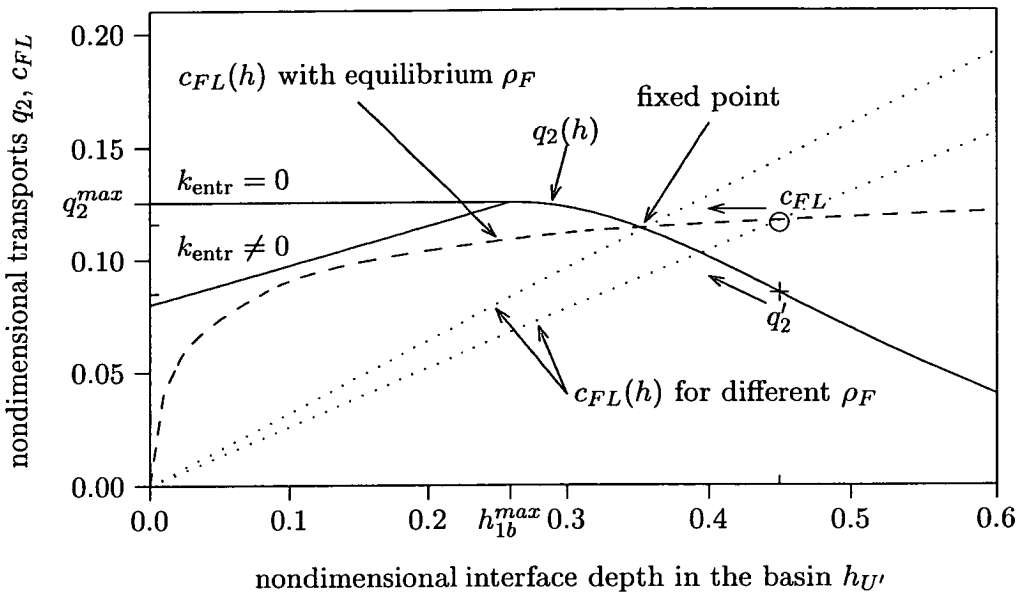

Figure 7.14: Definition of the curves in the $h_{U'}$-q-diagram. The q_2'-curve (solid) is fixed by the geometry and (for the maximal part) the choice of the entrainment parameter k_{entr}. The water formation rate c_{FL} is a linear function of the interface depth (dotted lines). If the changing density of the newly formed water ρ_F is taken into account, the water formation rate lies on the dashed line. The steady state ($c_{FL} = q_2'$) is given by the intersection between the solid and the dashed curve. This fixed point is stable: For deeper interfaces, $c_{FL} > q_2'$ (circle and cross), and the basin is filled with lower layer water, making the interface shallower.

lution of the system in which the different feedback mechanisms interact on different timescales. Of particular interest is the fact that a relatively small, short event like an increase in evaporation by 20% for a period of 10 years leads to a cascade of changes which significantly alter the state of the system for several centuries, and also produce secondary quick changes after a relatively constant situation for almost two centuries.

7.4 Stability analysis

The experiments in the previous section show that the system can move to a significantly different state after a comparatively small perturbation. This section investigates the stability of the system, while the next section discusses the role of the entrainment parameter k_{entr}.

For the stability analysis, it is useful to separate the relevant timescales. First the

focus is on the stability of all the mechanisms that act on the timescale of the interface adjustment, while changes on the much longer salinity and temperature adjustment timescales are discussed later. For the analysis of the interface adjustments the density in the basin can therefore be regarded as constant. However, it is important to note that the density of the outflowing layer ρ_2 is modified by the mixing processes and can therefore change on timescales determined by interface adjustments. The density of the newly formed water in the water formation box ρ_F changes on timescales of days, set by the relaxation time t_{relax} in (3.31), and must also be included in the analysis.

The interface adjustment works through a balance between the water formation rate c_{FL} and the effective exchange q'. The evolution and stability of the system can easily be visualised by plotting the effective exchange and the water formation rate in a nondimensional $h_{U'}$-q-diagram (see figure 7.14), where the transports are divided by the dimensionalisation constant $c(q) = WD\sqrt{Dg(\rho_2 - \rho_1)/\rho}$, and the interface depth by $c(h) = D$ (see chapter 2 and table 2.1). However, to remove the inconvenience that the nondimensional water formation rate then depends on the strait density ρ_2, which may change quickly due to mixing, rather than the slowly changing ρ_L, all transports are also multiplied by

$$\sqrt{1-E} = \sqrt{\frac{\rho_2 - \rho_1}{\rho_L - \rho_1}} \tag{7.14}$$

The strait transport $q_2(h_{U'})$ in nondimensional units is a known functional of the strait geometry only (though the submaximal part cannot be expressed algebraically in explicit form) and therefore defines a fixed line in the $h_{U'}$-q-diagram (see also figure 2.2 in section 2.4). For the submaximal regime, the effective exchange q_2' is equal to the strait transport q_2. For the maximal regime, the effective exchange is reduced if entrainment in the hydraulic jump is considered. With the linear parameterisation (7.6, 7.7) described in section 7.2, the the effective transport q_2' therefore increases linearly with $h_{U'}$ for the maximal regime:

$$q_2' = q_2^{\max} \cdot (1-E) = q_2^{\max} \cdot \left(1 - k_{\text{entr}} + k_{\text{entr}} \cdot \frac{h_{U'}}{h_{1b}^{\max}}\right) \tag{7.15}$$

In the $h_{U'}$-q-diagram, the maximal part of the curve then follows

$$q_2' \cdot \sqrt{1-E} = q_2^{\max} \cdot \left(1 - k_{\text{entr}} + k_{\text{entr}} \cdot \frac{h_{U'}}{h_{1b}^{\max}}\right)^{3/2} \tag{7.16}$$

For the sake of notational simplicity, in the following the factor $\sqrt{1-E}$ is assumed to be included in the dimensionalisation constants and therefore does not appear explicitly in the equations.

In the $h_{U'}$-q-diagram (figure 7.14) the effective exchange q_2' forms a curve (solid line) with a maximum at $h_{1b}^{\max}$, which is monotonically decreasing in the submaximal part and monotonically increasing (or constant for $k_{\text{entr}} = 0$) in the maximal part[1].

On the other hand, the water formation rate (3.41) is a linear function whose slope depends on the densities in the basin

$$c_{FL} = h_{U'} \cdot \frac{\rho_F - \rho_L}{\sqrt{\rho_L - \rho_1}} \cdot \frac{\mu\sqrt{\rho}}{W\sqrt{Dg}} \tag{7.17}$$

In the $h_{U'}$-q-diagram (figure 7.14) the water formation rate forms a straight line (dotted lines). While the last factor in (7.17) is a constant for any given system, the second factor involves the densities of different water masses. The density of the inflow ρ_1 is assumed constant, and the lower layer density ρ_L changes on much longer timescales than the interface and can therefore be regarded as constant for this stability analysis. However, the density of the water formation box ρ_F adjusts on timescales of the order of days to changes in air-sea-fluxes, but more importantly also to changes in the water formation rate. As this adjustment is much faster than the interface adjustments, ρ_F can be assumed to always have the equilibrium value for the actual values of the air-sea-fluxes and water formation rate. From (3.32) and (3.35), a realistic ansatz for the relation between ρ_F and c_{FL} is

$$\rho_F - \rho_U = \frac{f_{\text{flux}}}{c_{FL}} \tag{7.18}$$

where f_{flux} is some function of the air-sea-fluxes alone[2]. Inserting (7.18) into (7.17) leads to an equation that is quadratic in c_{FL} and linear in $h_{U'}$:

$$c_{FL}^2 + \frac{\mu\sqrt{\rho}}{W\sqrt{Dg}} \cdot \frac{1}{\sqrt{\rho_L - \rho_1}} \cdot ((\rho_L - \rho_U) \cdot c_{FL} - f_{\text{flux}}) \cdot h_{U'} = 0 \tag{7.19}$$

[1]For the range of values used here, the deviation of the maximal part of the curve from a straight line is almost unnoticeable in the plots.

[2]It would be unnecessarily complicated to derive this function f_{flux} explicitly from (3.32) and (3.35). For any given situation, it is easier to calculate the value of f_{flux} from the actual water formation rate and densities.

This equation defines a manifold in $h_{U'}$-q-space. The function $c_{FL}(h_{U'})$ is monotonically increasing from $c_{FL}(0) = 0$, and for large $h_{U'}$ it approaches the limit

$$\lim_{h_{U'} \to \infty} c_{FL} = \frac{f_{\text{flux}}}{\rho_L - \rho_U} \tag{7.20}$$

With these definitions, the water formation rate c_{FL} and the effective exchange q_2' can be plotted in the $h_{U'}$-q-diagram (dashed line and solid line in figure 7.14). Fixpoints are given by the intersection of the two curves. The stability of the fixed points can easily be established: If the slope of the c_{FL} is larger than the slope of the q_2'-curve, a perturbation away from the fixed point in e. g. positive $h_{U'}$-direction leads to a situation in which the water formation rate (open circle in figure 7.14) is higher than the effective exchange (cross), thus filling the basin and decreasing $h_{U'}$. Therefore, if the slope of the c_{FL}-curve is larger than the slope of the q_2'- curve at the fixed point, the fixed point is stable; if it is smaller, then the fixed point is unstable. This is essentially an equivalent requirement to the stability condition discussed in chapter 4.2.2

$$\frac{\partial c_{FL}}{\partial h_{U'}} > \frac{\partial q}{\partial h_{U'}} \tag{7.21}$$

It now is possible to plot the $h_{U'}$-q-diagrams for the experiments shown in the previous section. Figure 7.15 compares the steady state (at $t = -5$ years) for the control experiment ($k_{\text{entr}} = 0$) and the experiment with $k_{\text{entr}} = 0.4$ which evolves into a strong mixing/weak circulation regime.

In the control experiment there is only one fixed point at $h_{U'} = 0.285D = 81\,\text{m}$ for the initial net evaporation (lower curve). When the net evaporation is increased by 20%, the c_{FL}-curve moves upwards (upper curve), and this fixed point is shifted to $h_{U'} = 0.243D = 69\,\text{m}$ in the maximal regime. Therefore, during the evaporation event the interface rises (in the experiment: $h_{U'} = 67\,\text{m}$ at the end of the evaporation event at $t = 10$), but then quickly moves back to the original value after the evaporation event.

For the experiment with $k_{\text{entr}} = 0.4$, however, there are three fixed points for the initial evaporation, two of which are stable, at $h_{U'} = 0.285D = 81\,\text{m}$ and $h_{U'} = 0.0235D = 7\,\text{m}$, and one unstable at $h_{U'} = 0.245D = 70\,\text{m}$. During the evaporation event the submaximal stable fixed point disappears, and the system is pushed towards the remaining fixed point in the maximal regime. When the evaporation goes back to

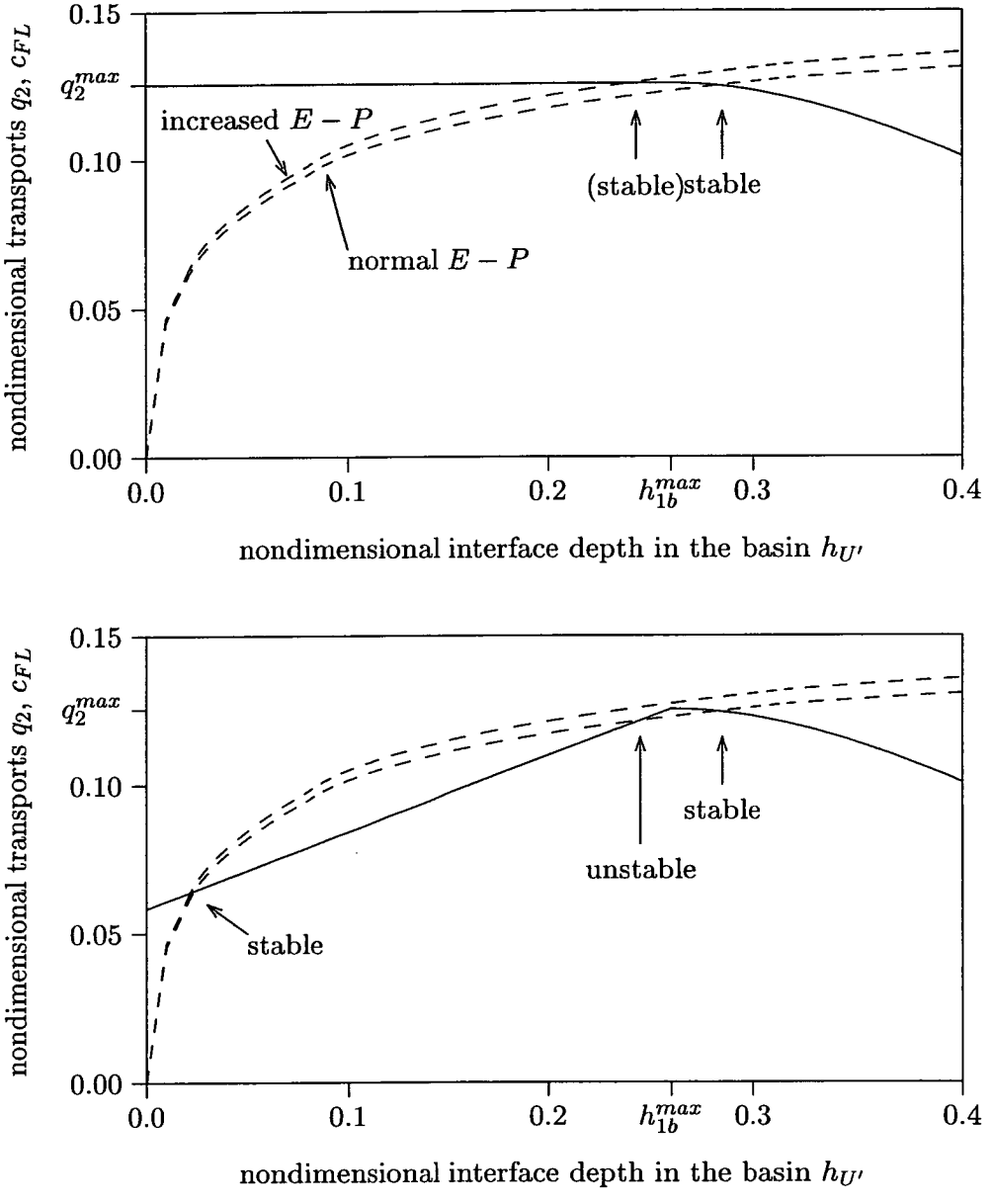

Figure 7.15: $h_{U'}$-q-diagrams for the steady state of the two experiments with $k_{\text{entr}} = 0$ and $k_{\text{entr}} = 0.4$. The c_{FL}-curve is given both for the normal $E - P$ (lower dashed curves) and the increased values (upper dashed curves). For $k_{\text{entr}} = 0$, there is only one fixed point which moves to slightly shallower interface depths when the evaporation increases. For $k_{\text{entr}} = 0.4$, however, there are three fixed points. Two of these points merge and disappear with increasing evaporation, leaving only one fixed points at a very shallow interface depth.

the normal value, the interface is already shallower than the unstable fixed point, so that it does not return to the original submaximal fixed point, but to the maximal fixed point. In the model run, an the shallowest interface depth of $h_{U'} = 7\,\mathrm{m}$ is reached at $t = 50\,\mathrm{years}$.

From the geometry of the curves it is easy to show that – depending on the parameters – the system can have either one fixed point or three. In the case of one fixed point, this fixed point is always stable and can lie in the maximal or submaximal regime. In the case of three fixed points, one fixed point lies in the submaximal regime and two in the maximal regime. The submaximal fixed point is always stable. Therefore the system can show bifurcations, where each of the parameters k_{entr} and μ can act as bifurcation parameters. This will be discussed in detail in the next sections.

In the discussion so far the focus was on the adjustment of the interface, and the assumption was made that density changes in the basin can be neglected, as they change only on longer timescales. However, if the system switches between fixed points of the interface mechanism, the long term stability is affected by subsequent density adjustments. In the following, the decay of the maximal fixed point, i. e. the strong mixing/weak circulation regime discussed in section 7.3, is investigated.

Figure 7.16 shows the evolution of the experiment with $k_{\mathrm{entr}} = 0.4$ in a series of $h_{U'}$-q-diagrams, where the changing basin densities are taken into account. During the evaporation event, there is only a fixed point in the far maximal regime, and the system moves towards it, reaching it at approximately $t = 50\,\mathrm{years}$. However, now the water formation rate is much lower than in the initial steady state. Therefore, the density of the basin starts to increase. In the $h_{U'}$-q-diagram, the c_{FL}-curve moves downwards. Consequently, the stable fixed point in the maximal regime first moves to higher $h_{U'}$, but at $t = 125$ another apex of a saddle node bifurcation is reached, where now the density is the bifurcation parameter, and the two maximal fixed points merge and disappear, leaving only one fixed point in the far submaximal regime.

It seems reasonable to conjecture that a strong mixing/weak circulation state always decays in the way described here, as the bulk density of the basin increases and the c_{FL}-curve in the $h_{U'}$-q-diagram flattens. If this conjecture is true, this state is a (meta-)stable state on timescales shorter than the timescales of density changes, but not on

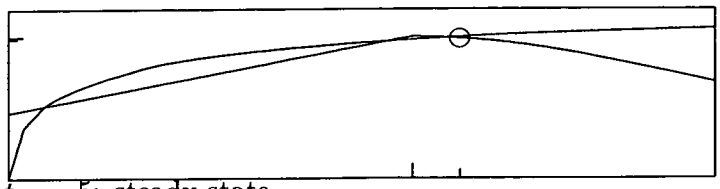

$t = -5$: steady state

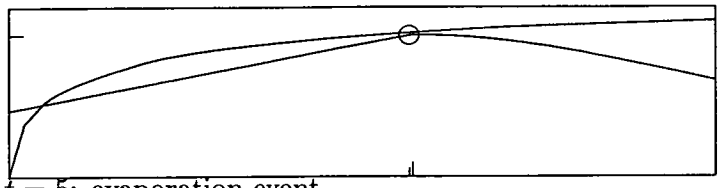

$t = 5$: evaporation event

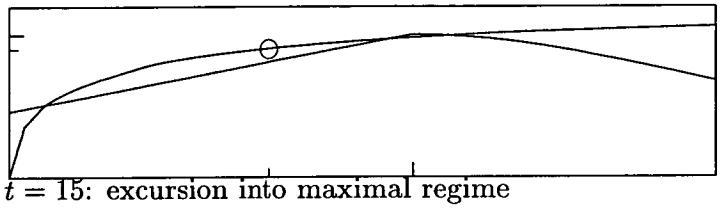

$t = 15$: excursion into maximal regime

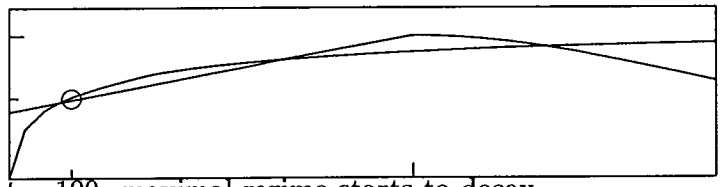

$t = 100$: maximal regime starts to decay

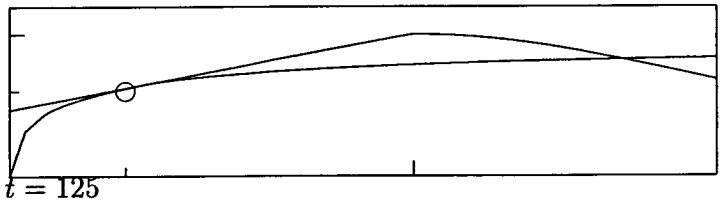

$t = 125$

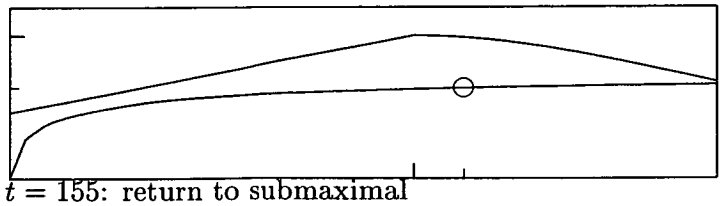

$t = 155$: return to submaximal

Figure 7.16: $h_{U'}$-q-diagrams for the evolution of the system with $k_{\text{entr}} = 0.4$. The circle is the actual water formation rate (see also figure 7.7).

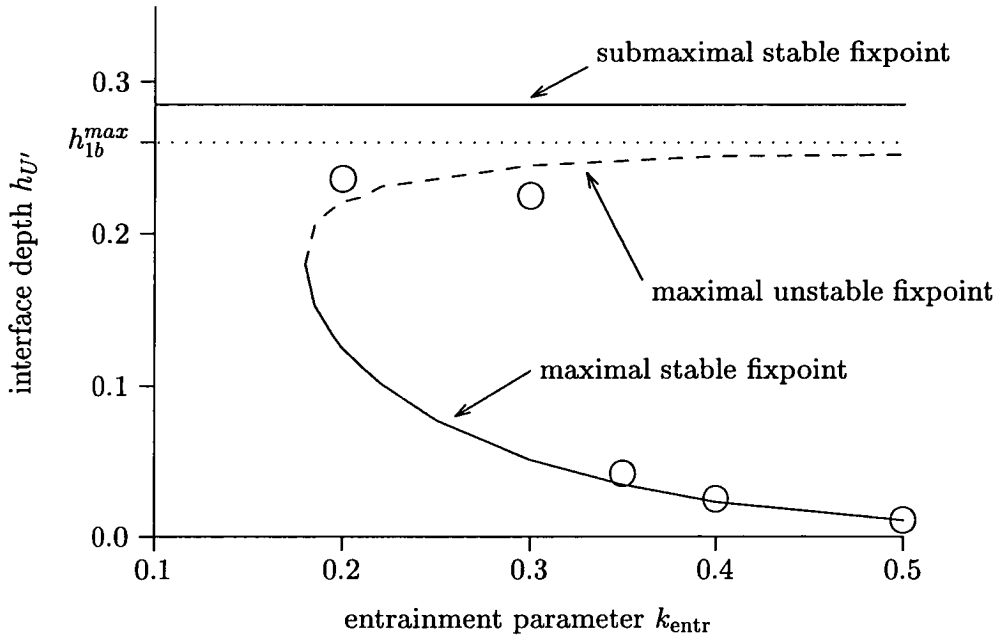

Figure 7.17: Bifurcation diagram for the system with $E - P = 75\,\mathrm{cm/year}$ and $\mu = 0.4$, where k_{entr} is used as the bifurcation parameter. Stable fixed points are shown as solid lines, unstable fixed points as dashed lines, and the dotted line is the boundary between the maximal and the submaximal regime. The fixed points were calculated from $h_{U'}$-q-diagrams for different values of k_{entr}, while the open circles are the HYCOBOX-results for the II/III transition from table 7.2. For the calculation of the bifurcation diagram, all basin densities were assumed to have the steady state values (i. e. the values at $t = -5\,\mathrm{years}$).

longer timescales, for which only the submaximal state is stable.

7.5 The entrainment parameter k_{entr}

Having established in the previous section that the system can have one or three fixed points (if slower density adjustments are ignored), this and the following section investigate how the number and position of these fixed points depend on the parameters k_{entr} and μ. First, the role of the entrainment parameter k_{entr} is investigated.

From physical considerations and from figure 7.14 it is obvious that there is only one fixed point if the entrainment parameter k_{entr} is small, whereas there are three fixed points if the parameter exceeds a threshold, so that k_{entr} can be regarded as the bifurcation parameter for this system.

Figure 7.17 shows the resulting bifurcation diagram for a given $\mu = 0.4$ and $E - P =$

75 cm/year as in the experiments above. The fixed points have been obtained from $h_{U'}$-q-diagrams for a range of values for k_{entr}, assuming that the basin densities have steady state values. There is one constant stable fixed point in the submaximal regime, and a saddle node bifurcation with an apex at $k_{\mathrm{entr}} \approx 0.18$, i. e. for $k_{\mathrm{entr}} > 0.18$ multiple states exist.

To compare these theoretical results with model experiments, a series of experiments with different k_{entr} was performed. The open circles in figure 7.17 indicate the position of the shallowest interface. The details of the experiments can be found in table 7.2. For $k_{\mathrm{entr}} > 0.3$, there is good agreement between the expected values and the model results. For $k_{\mathrm{entr}} = 0.2$, the shallowest interface – reached during the evaporation event – is deeper than the unstable fixed point, so that the maximal fixed point cannot be reached. The result for $k_{\mathrm{entr}} = 0.3$ seems somewhat contradictory: Although the interface gets (slightly) shallower than the unstable fixed point, the system nonetheless returns to the deeper submaximal fixed point. However, the position of the fixed points depends on the densities. In this case the basin density can no longer be assumed constant, and the small adjustment away from the steady state densities (on which this bifurcation diagram is based) brings the two branches of the saddle-node-bifurcation closer together, so that the unstable fixed point again is shallower than the actual interface, pushing the system back to the submaximal fixed point.

Figures 7.18 and 7.19 compare the qualitative behaviour of the experiments with values from $k_{\mathrm{entr}} = 0.3$ to $k_{\mathrm{entr}} = 0.5$. For simplicity, only the evolution of salinity is shown, as all phases are easily discernible in the salinity plot, and salinity is also the quantity that has most practical relevance. It is obvious that the experiments with $k_{\mathrm{entr}} > 0.3$ exhibit qualitatively the same behaviour as the experiment with $k_{\mathrm{entr}} = 0.4$ that was discussed in the section 7.3, not surprising in view of the bifurcation diagram (figure 7.17). The experiment with $k_{\mathrm{entr}} = 0.3$ (figure 7.18) does not develop clearly into the submaximal state, although the return to the initial state does take considerably longer than in the control experiment with $k_{\mathrm{entr}} = 0$ (figure 7.5 top) – a behaviour again consistent with the bifurcation diagram, which showed that the system does not venture far enough beyond the unstable fixed point.

Besides the differences in the position (in variable-space) of the fixed points, the

Experiment	k_{entr}		(steady state)	0	0.3	0.35	0.4	0.5
II/III transition	t	year		10	(29)	67	50	34
Interface depth	$h_{U'}$	m	80	67	64	12	7	3
Entrainment rate	E		0	0	0.04	0.30	0.36	0.48
Water formation rate	c_{FL}	Sv	1.05	1.16	1.16	0.64	0.54	0.38
Effective exchange	q_2'	Sv	1.05	1.06	1.00	0.64	0.54	0.37
Strait outflow	q_2	Sv	1.05	1.06	1.04	0.93	0.89	0.78
Sal. in Form. Box	S_F	psu	38.35	38.60	38.63	39.89	40.57	42.48
Temp. in Form. Box	T_F	°C	11.87	12.17	12.10	9.45	8.40	5.65
IV/V transition	t	year		18	62	146	153	202
Strait outflow	q_2	Sv	1.05	1.06	1.08	1.17	1.22	1.27
Sal. in Lower Layer	S_L	psu	37.98	38.02	38.02	38.54	38.75	39.38
Temp. in Lower Layer	T_L	°C	12.53	12.55	12.55	11.67	11.34	10.42
V/VI transition	t	year			(93)	167	172	220
Interface depth	$h_{U'}$	m	80		86	112	119	106
Strait outflow	q_2	Sv	1.05		1.05	0.96	0.91	0.90

Table 7.2: Summary of the entrainment experiments. The experiments can be characterised by three clearly definable times, namely the end of phases II, IV and V, and the values of quantities that have extrema at these points. For $k_{\text{entr}} = 0.3$, the transition times II/III and V/VI are not well defined.

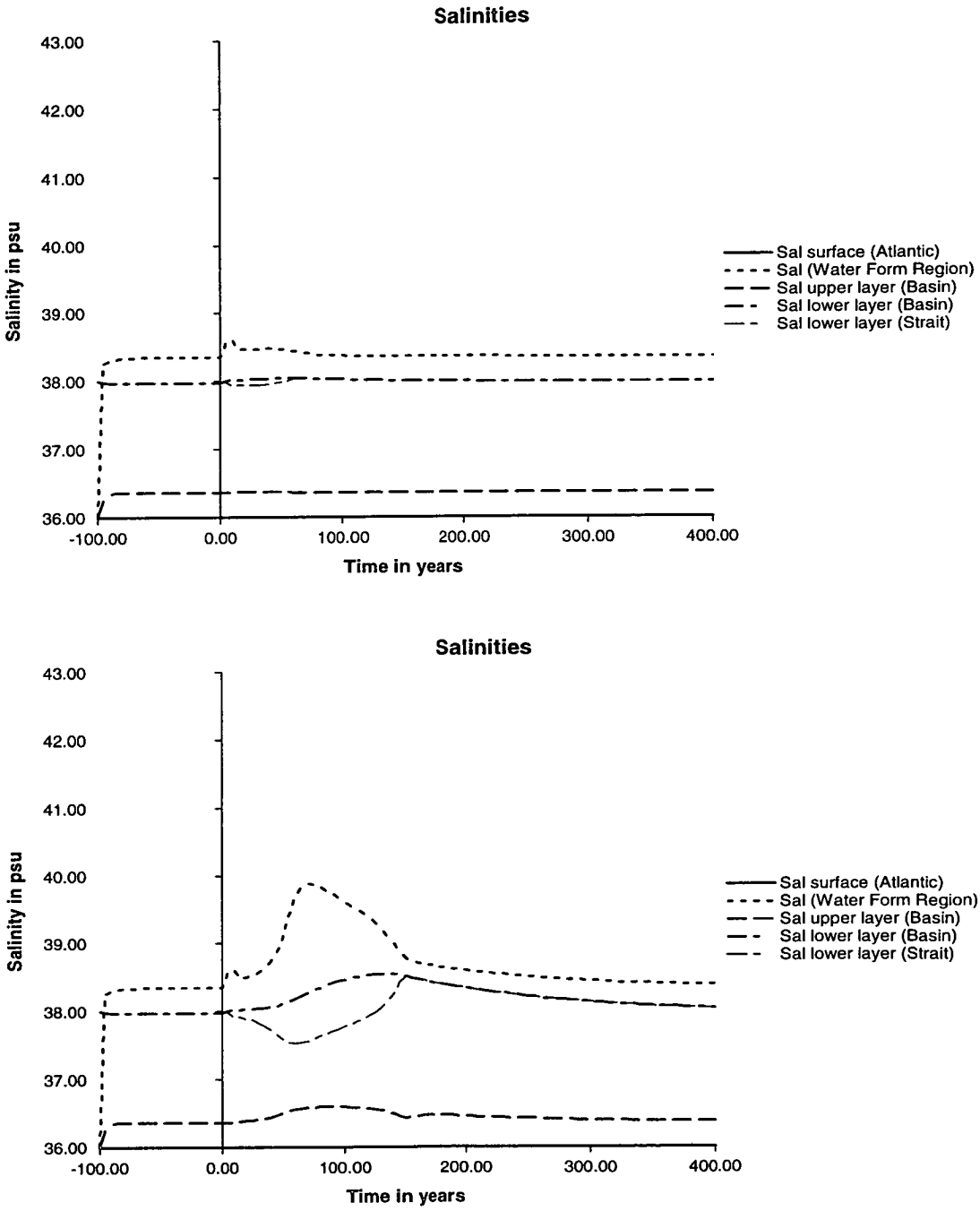

Figure 7.18: The evolution of salinity in the experiments with $k_{\text{entr}} = 0.3$ (top) and $k_{\text{entr}} = 0.35$ (bottom).

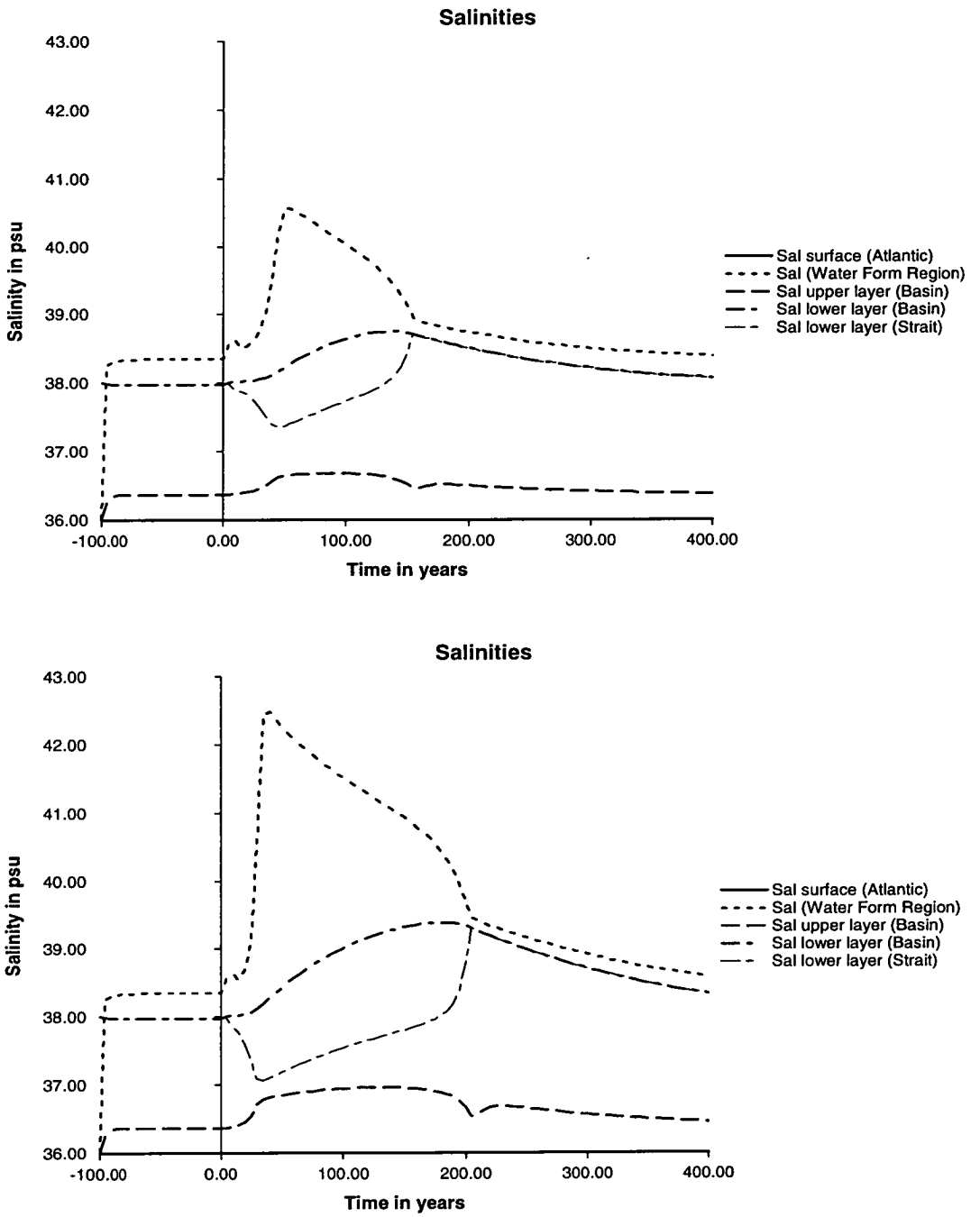

Figure 7.19: The evolution of salinity in the experiments with $k_{\text{entr}} = 0.4$ (top) and $k_{\text{entr}} = 0.5$ (bottom).

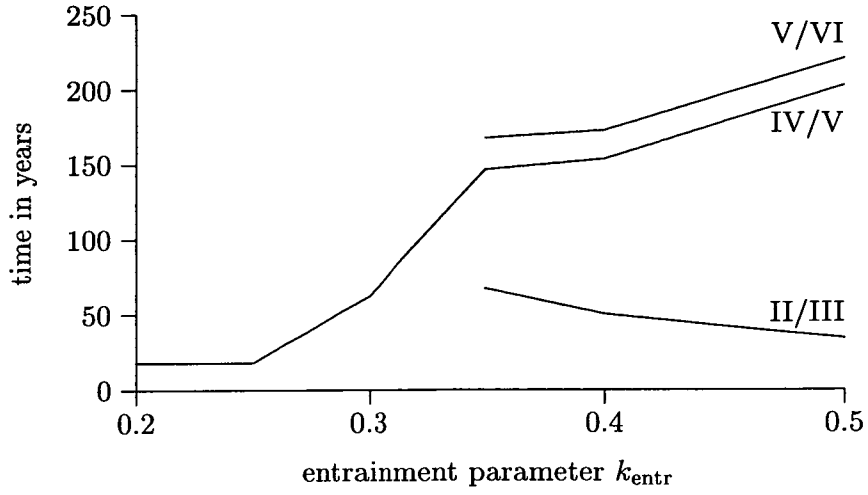

Figure 7.20: The time scale of the evolution as a function of the parameter k_{entr}. Shown are the times at which the system moves from phase II to III, from IV to V, and V to VI.

timescales of the evolution are strongly influenced by the entrainment parameter. The timescale can be characterised by three clearly definable events, namely the ends of phases II, IV and V. At the transition from II to III, the interface has its shallowest level, i. e. the hydraulic jump is strongest, the strait transport and the water formation are at a minimum, and the salinity and temperature of the water formation box are at a peak. In the experiment described in section 7.3 ($k_{\text{entr}} = 0.4$), this occurs at $t = 50$ years. At the transition IV/V, the system switches back to the submaximal regime. At this time, the salinity and the temperature of the lower layer in the basin reach their extreme values. The end of phase V is the time of deepest interface. The main variables at these times are listed in table 7.2.

Figure 7.20 shows the timescale of the evolution as a function of the entrainment parameter. An increasing k_{entr}, i. e. stronger mixing in the hydraulic jump, has two main effects:

- The transition from the original state to the low circulation regime, i. e. the length of phase II, decreases.
- The metastable low-circulation state persists longer.

This behaviour can be understood by noting that the feedback loops that pass through the hydraulic jump (see figure 7.3) are stronger with increasing k_{entr}. Therefore, the

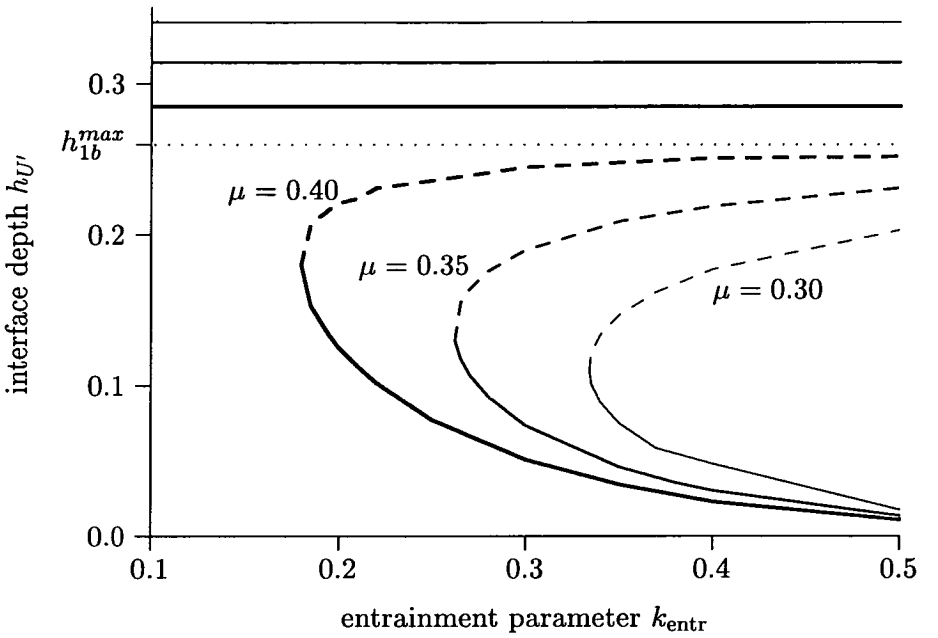

Figure 7.21: Bifurcation diagrams for different values of μ, using k_{entr} as the bifurcation parameter.

initial runaway feedback leading into the low circulation regime (figure 7.10) is faster, and the resulting state is more extreme in terms of interface depth and density (see also figures 7.18 and 7.19). On the other hand, the restoring feedbacks through the density adjustments (figure 7.11) do not increase with k_{entr} and therefore need longer to move the system out of the more extreme state.

To summarise: An increasing entrainment parameter k_{entr} has the following effect:

- The transition from the original state to the low circulation regime occurs faster.
- The metastable state persists longer.
- The hydraulic jump develops to greater height.
- The salinity and temperature also go to significantly more extreme values with higher values for k_{entr}.

7.6 The water formation parameter μ

The second important parameter influencing the evolution of the system is the water formation parameter μ. This parameter primarily determines the water formation

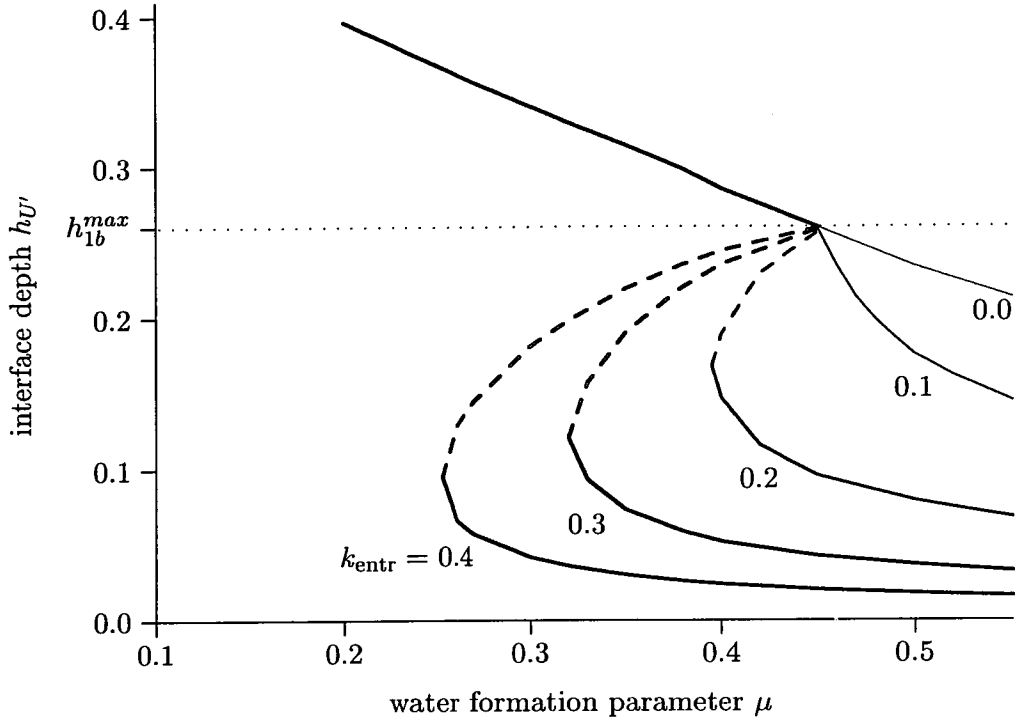

Figure 7.22: Bifurcation diagrams for different values of k_{entr}, using μ as the bifurcation parameter.

rate, and in the context of the feedbacks of the system (see figure 7.3) it influences the strength of the stabilising interface and salinity feedbacks. Therefore, it can be expected that the fixed points of the system move closer together with increasing μ, and if μ is high enough so that the steady state is in the maximal regime, there is only one fixed point (see the discussion in section 7.4).

Figure 7.21 shows the bifurcation diagram for different values of μ, where again the entrainment parameter k_{entr} has been used as the bifurcation parameter. As expected, both stable fixed points move to shallower depths with increasing water formation rate, whereas the unstable fixed point moves towards the submaximal regime.

Further insight is gained if the water formation parameterisation μ is used as the bifurcation parameter. The resulting bifurcation diagram is shown in figure 7.22. If no mixing is present in the hydraulic jump (thin line, $k_{entr} = 0$), the interface depth decreases almost linearly with higher water formation rate, and for $\mu > 0.45$ the interface is shallow enough for the system to be in the maximal regime. For entrainment parameters larger than approximately 0.15, a double saddle-node-bifurcation develops

(thicker lines), where one apex is situated at the boundary between the maximal and the submaximal regime, and the other apex at a shallower interface. Therefore, for an entrainment parameter of e. g. $k_{\text{entr}} = 0.4$, the system has one fixed point in the submaximal for $\mu < 0.25$, three fixed points for $0.25 < \mu < 0.45$, with a qualitative behaviour similar to the experiments discussed in section 7.3.

For $\mu > 0.45$, there is only one fixed point in the maximal regime. However, following the discussion at the end of section 7.4, the maximal fixed point is only stable if slower density changes are ignored, and the fixed point from the bifurcation diagram will not be the steady state of the system. The evolution of such a system is show in figures 7.23 and 7.24. The competition between the different mechanisms discussed in section 7.3 leads to an oscillatory behaviour. The system goes into a shallow interface/low circulation regime, but due to the increasing basin density the water formation collapses, the system moves into the submaximal regime, recovering to a lower basin density, but with the recovery of the water formation, the cycle starts anew. It is particularly noteworthy that this behaviour occurs for an entrainment parameter as low as $k_{\text{entr}} = 0.20$, i. e. only 20% of the water affected by the hydraulic jump (equals about 10% of the total inflow) is entrained.

If the water formation is high enough and/or the entrainment low enough, the system stays in the maximal regime for the complete cycle, and a lower basin density cannot be reestablished. In this case, the system behaves as a damped oscillator, eventually settling in a state with an interface depth somewhat shallower than the interface of corresponding non-entrainment situation, but deeper than the fixed points from the bifurcation diagram (which is calculated using the non-entrainment steady state densities). An example for this type of behaviour with $\mu = 0.60$ and $k_{\text{entr}} = 0.15$ is shown in figure 7.25.

In total, there are three qualitatively different types of behaviour depending on the parameters μ and k_{entr}. Their respective area in the μ-k_{entr}-plane is shown in figure 7.26.

One submaximal state: For small water formation and entrainment, there is essentially only one stable state in the submaximal regime, and while the system may move into the maximal regime after a perturbation, it decays back to the sub-

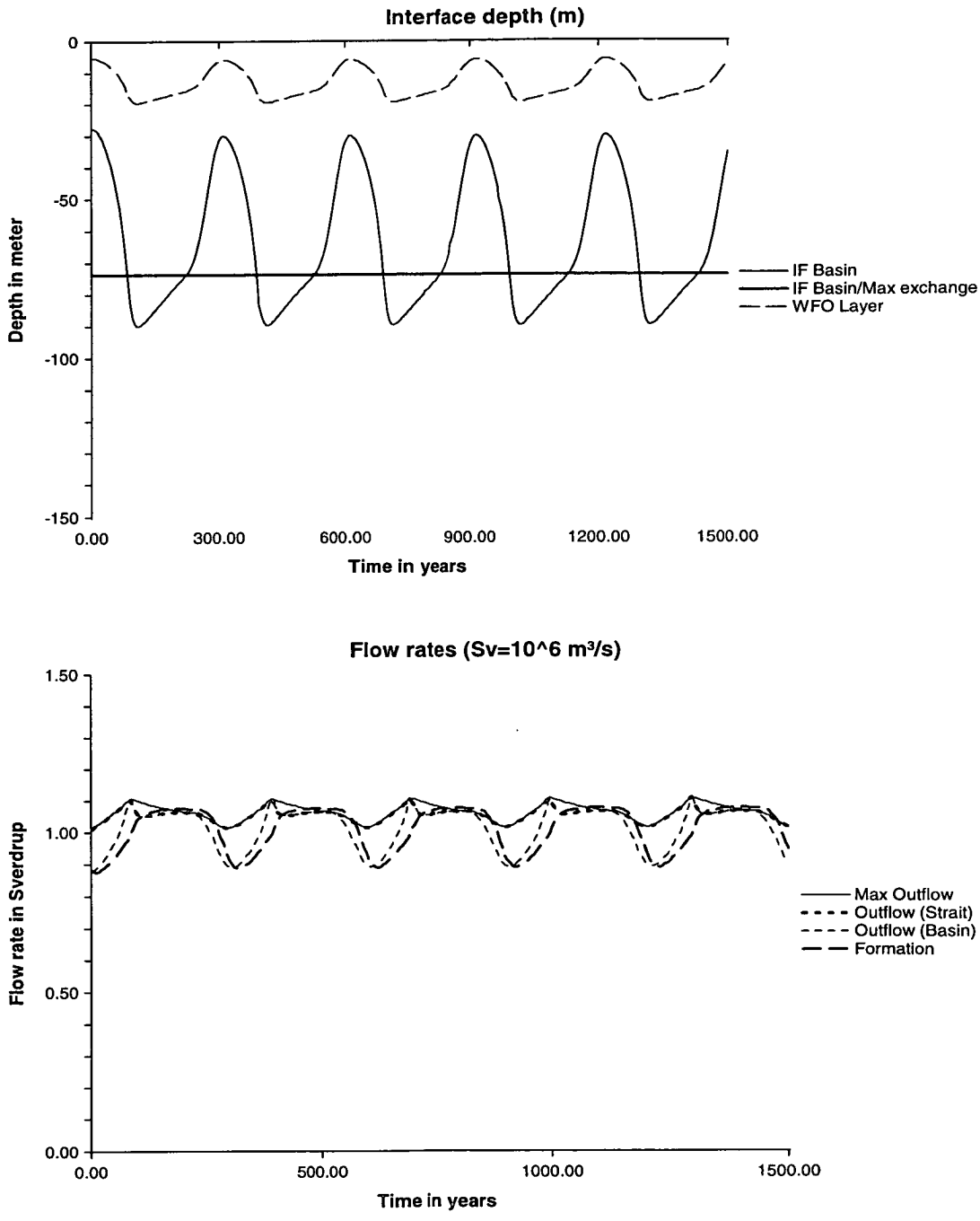

Figure 7.23: Interface depth and strait transport for an experiment with strong water formation ($\mu = 0.5$) and moderate entrainment in the hydraulic jump ($k_{\text{entr}} = 0.20$). The system oscillates.

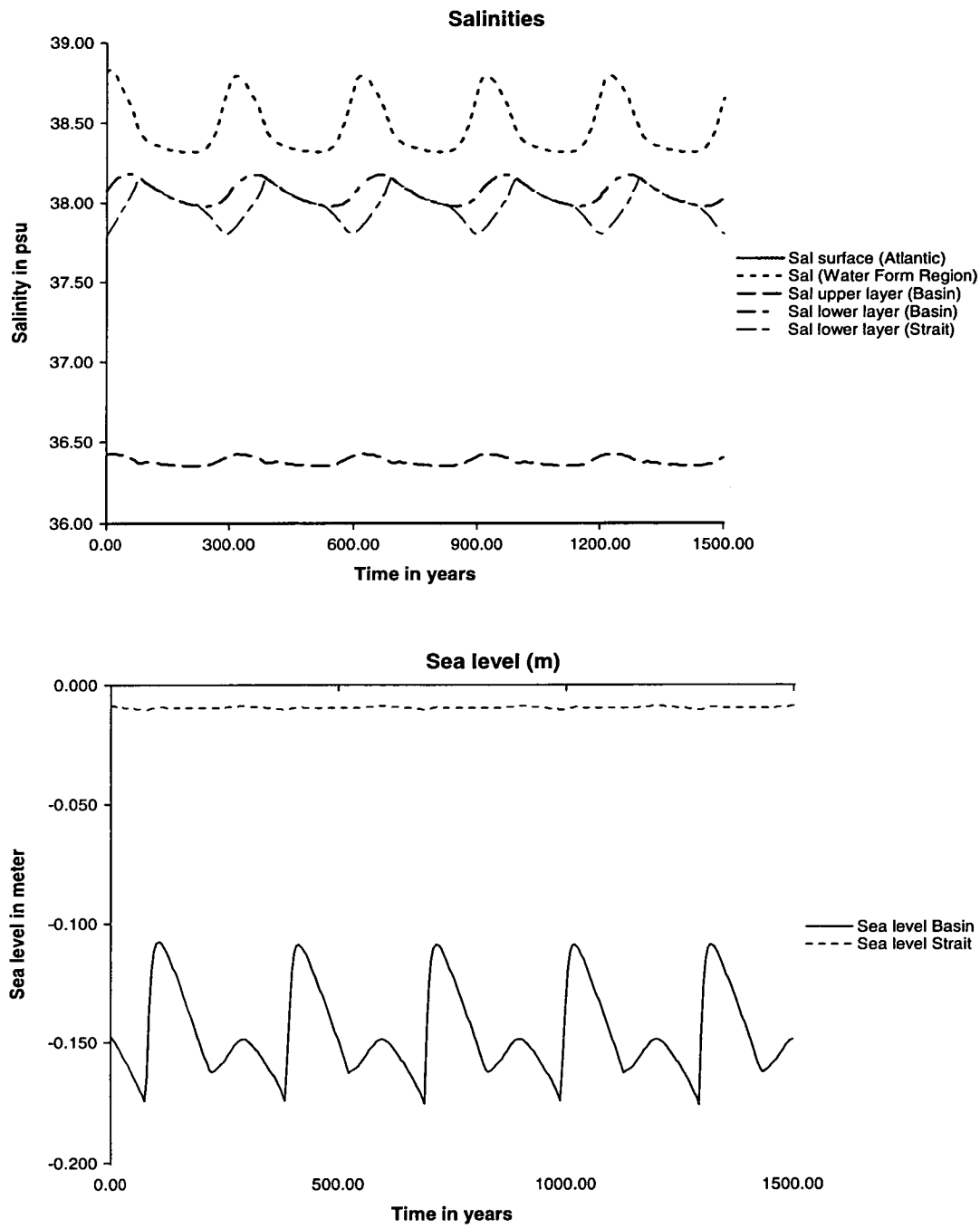

Figure 7.24: Salinity and sea level in the same experiment as figure 7.23.

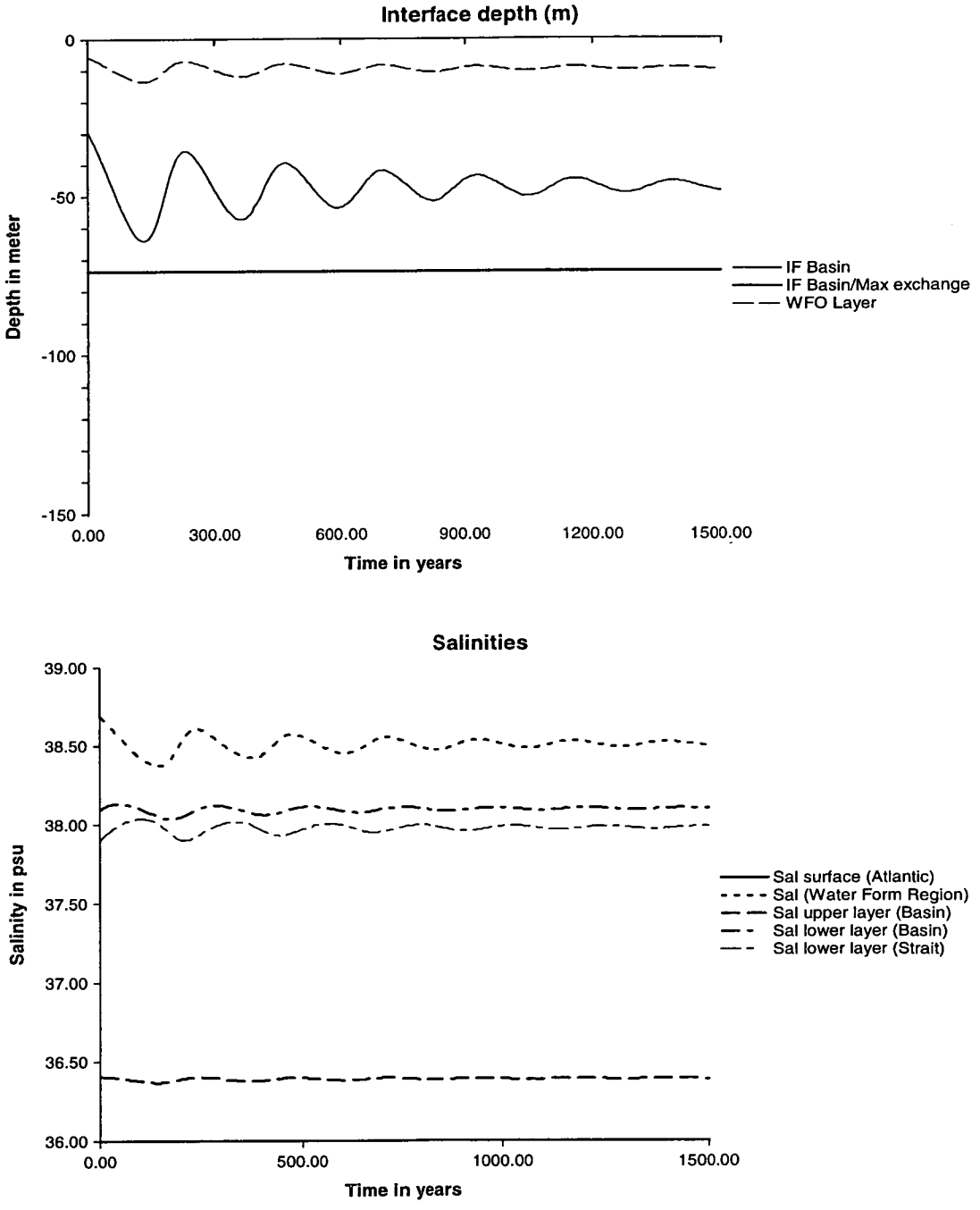

Figure 7.25: Interface depth and salinity in an experiment with higher water formation and lower entrainment than the experiment in figure 7.23. The system is a damped oscillator ($\mu = 0.60$, $k_{\text{entr}} = 0.15$)

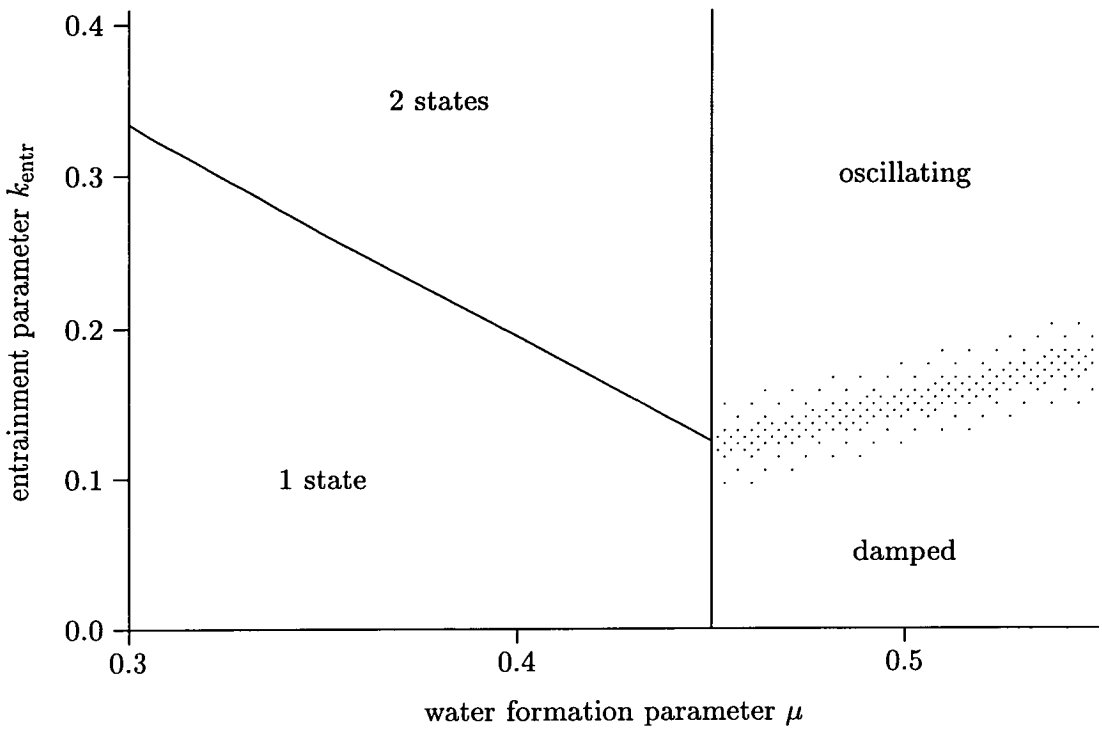

Figure 7.26: The three different types of behaviour in the μ-k_{entr}-plane. For oscillating behaviour, smaller entrainment rates tend to lead to damped oscillators.

maximal state within a few years. An example is the experiment shown in figures 7.4 ff.

One submaximal state, one metastable maximal state: For higher entrainment parameter $k$entr, but a water formation lower enough, there is a metastable state in the maximal regime in addition to the submaximal steady state. The system can move into the metastable state after a comparatively small and short perturbation and remain there for centuries. An example is the experiment shown in figures 7.7 ff.

Oscillating: If the water formation is high enough for the non-mixing steady state to be in the maximal regime, the presence of mixing leads to an oscillating behaviour. If the mixing is strong enough, no steady state exists (example: figure 7.23 ff.), whereas for smaller mixing the system approaches a steady state as a damped oscillator (example: figure 7.25).

7.7 Comparison with GCM results

In this section, the results of a GCM study by Myers et al. (2001) are reviewed in the light of the ideas discussed in the previous sections. Two experiments were performed with the MOMA ocean general circulation model of the Mediterranean Sea under flux forcing, with a basin resolution of $0.25° \times 0.25°$ with 19 vertical levels. Details of the model are described by Myers and Haines (2001), Myers et al. (2001).

The experiments were set up to reproduce modern day conditions in the Mediterranean Sea. Two experiments (I and II) were performed, using the same surface fluxes, but different initial conditions. The surface fluxes were diagnosed from an initial spin-up experiment which was run for 100 years with restoring boundary conditions. The diagnosed fluxes are then used to directly force the two experiments. The initial state of experiment I is the final state of the spin-up experiment, whereas experiment II is started from the annually averaged ocean data from the Mediterranean Oceanic Data Base (MODB) (Brasseur et al. 1996). The main difference is that the initial surface salinity in experiment II is somewhat higher than in experiment I.

The two experiments exhibit very different evolution: Experiment I remains in a state similar to the circulation of the present day Mediterranean for 100 years until the end of the experiment, whereas in experiment II, which was run for 200 years, the circulation collapses. Within a century, this leads to a salinity crisis. Figure 7.27 shows the final basin salinity of the two experiments: In experiment II (bottom), the basin average salinity is 38.85 psu, significantly higher than in experiment I (38.53 psu). After approximately 140 years the salinity goes back to more normal values, as can be seen in the basin average salinity (figure 7.28), although the previous state is not reached by the end of the experiment.

There are some indications that the mechanisms leading to the collapse of the circulation are similar to the mechanisms discussed in this chapter. Figure 7.29 shows the density cross-section through the strait during the time of the salinity crisis (at $t = 100$ years, top); and in year 200, when the circulation has started again. During the salinity crisis, the interface depth is considerably shallower towards the basin. The strong strong slope of the interface on the eastern side of the strait indicates the presence of a hydraulic jump or other hydraulic transition.

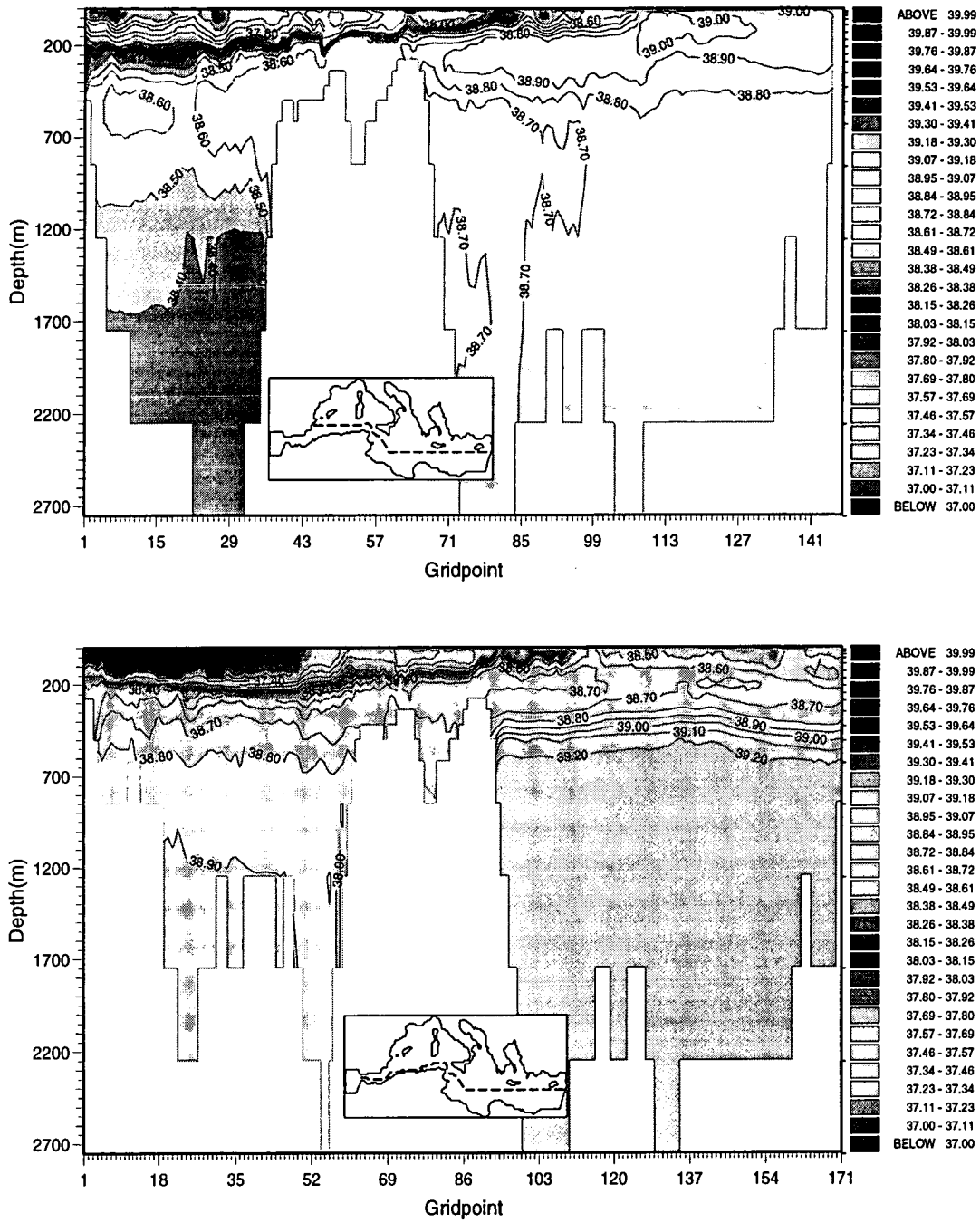

Figure 7.27: Basin salinity in the two GCM experiments at $t = 100$ years. Experiment I (top) has a circulation similar to the present day Mediterranean Sea, whereas in experiment II (bottom) the water formation collapses and the basin salinity increases to extreme values. From Myers et al. (2001).

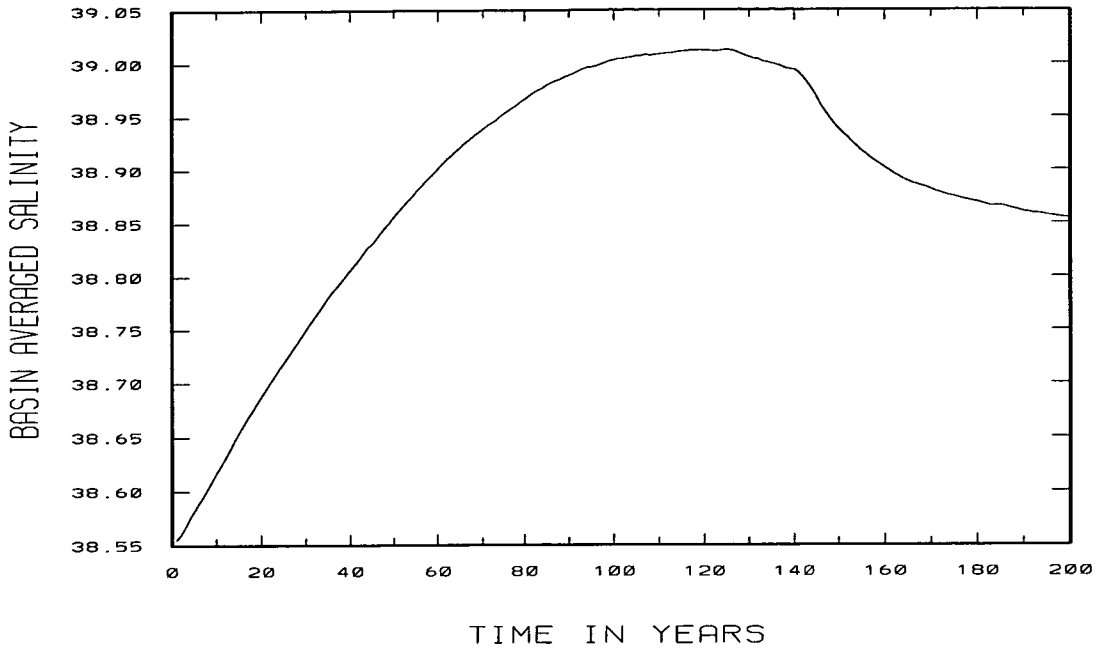

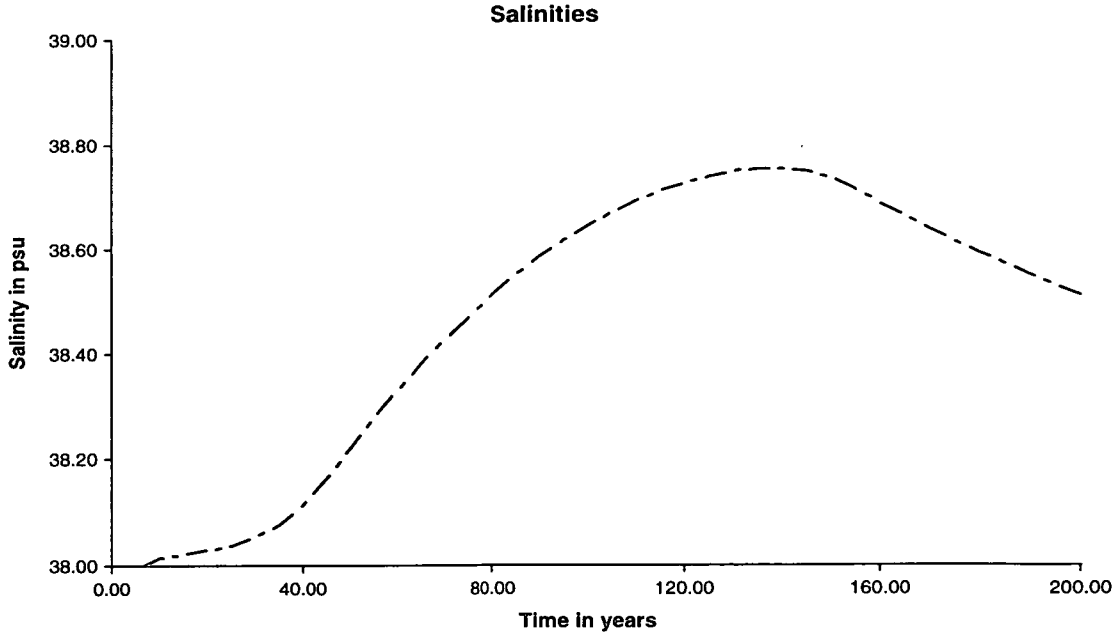

Figure 7.28: Top: Five year running mean of the basin average salinity in the GCM experiment, from Myers et al. (2001). Bottom: For comparison, the lower layer salinity of the HYCOBOX experiment from figure 7.8 ($k_{\text{entr}} = 0.4$; $\mu = 0.4$). The qualitative behaviour, timescale and size of the salinity excursion is similar in both experiments.

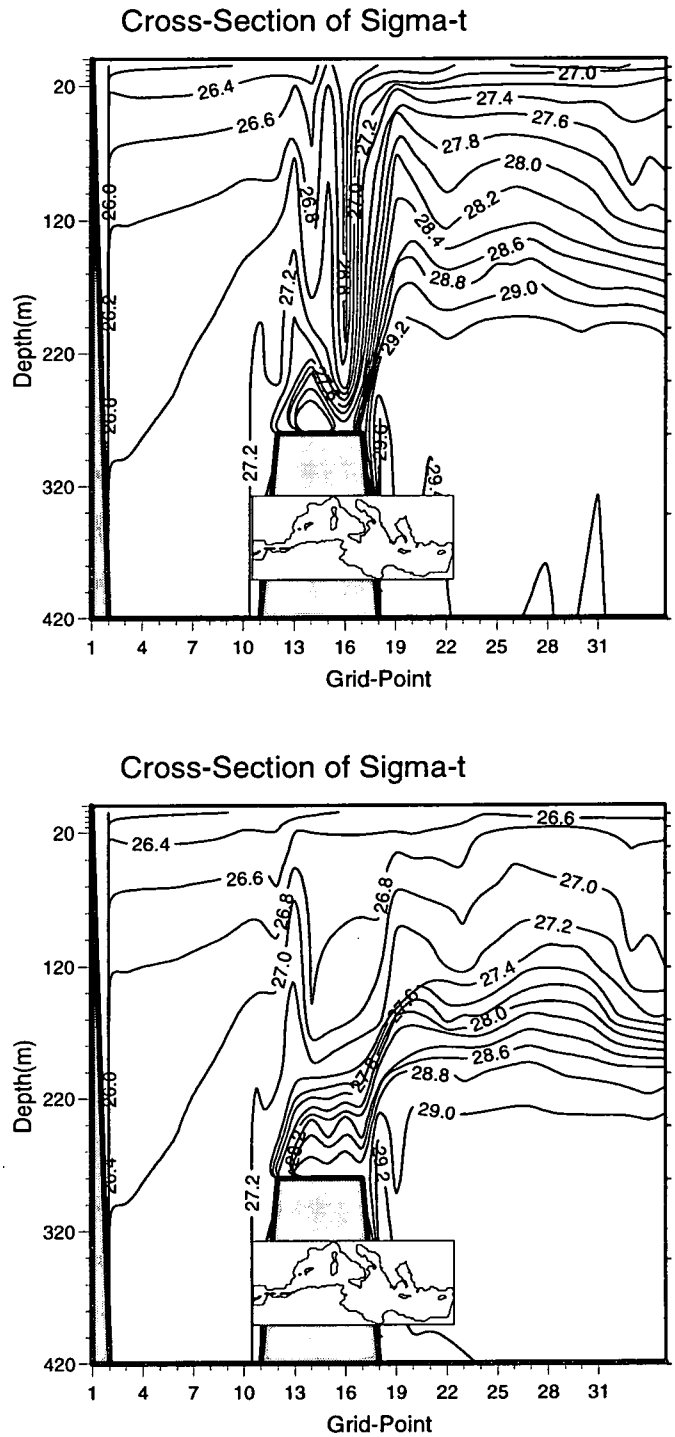

Figure 7.29: Annually averaged density cross-section through the Strait of Gibraltar at $t = 100$ years (top) and $t = 200$ years (bottom). The interface is considerably shallower towards the basin at $t = 100$ years with a strong slope towards the strait, indicating the presence of a hydraulic jump. The hydraulic jump has disappeared again in year 200. From Myers et al. (2001).

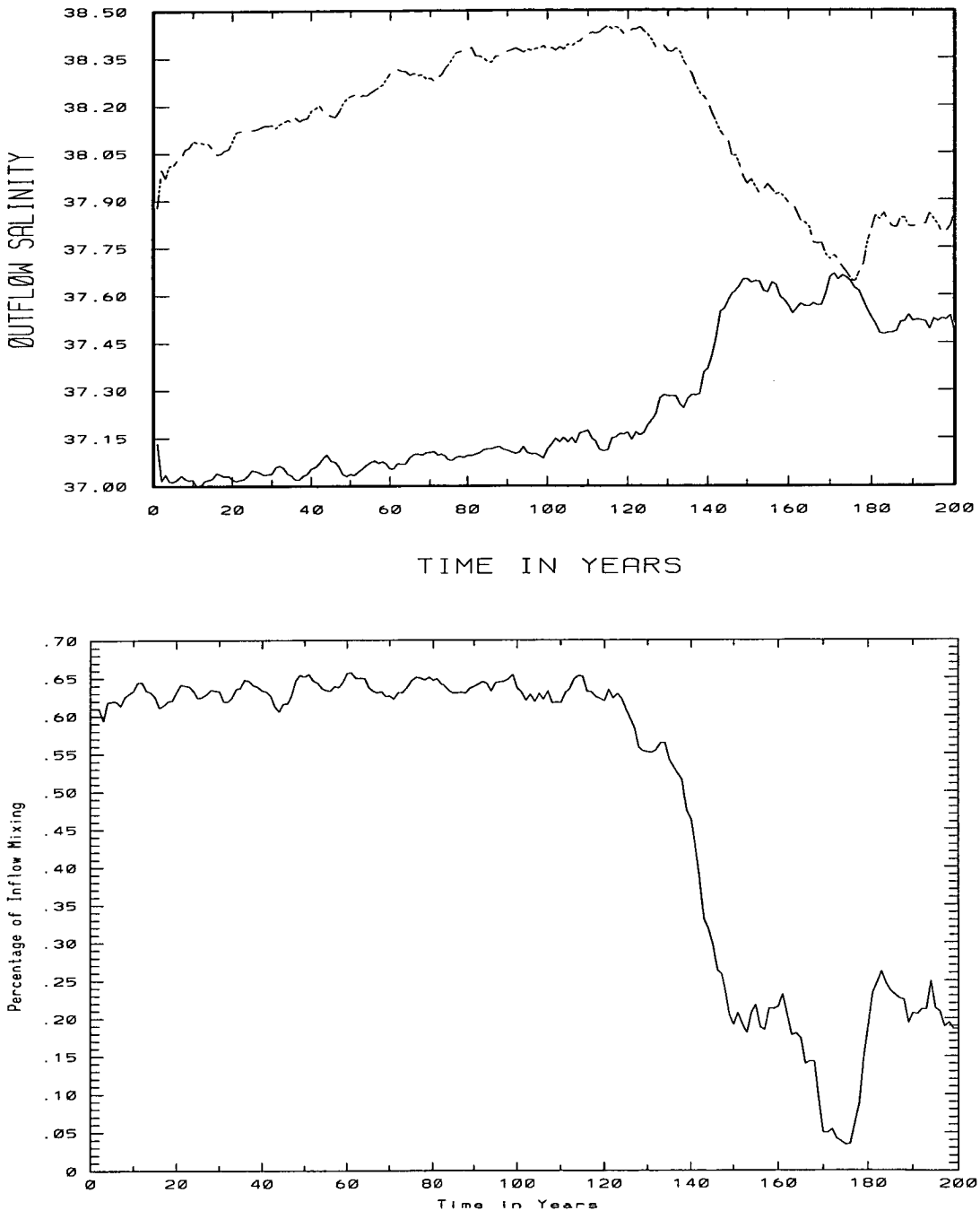

Figure 7.30: Evidence for strong, variable mixing in the hydraulic transition near the strait. Top: Five year running mean of the outflow salinity in the Strait of Gibraltar (solid line) and in the Western Alboran Sea (dashed line). During the presence of the hydraulic jump (up to approximately year 140), the outflowing water is fresher in the strait than in the basin, suggesting that inflowing water is mixed into the outflow. The bottom figure shows the five year running mean of the percentage of inflow mixed into the outflow, calculated from the salinity difference in the top figure. From Myers et al. (2001).

Mixing in the hydraulic transition can be inferred from figure 7.30. The top graph of figure 7.30 shows the salinity of the outflow as a function of time, both in the Strait of Gibraltar (solid line) and further east, in the Western Alboran Sea (dashed line). Before the year 140, the salinity is considerably (more than 1 psu) higher in the Alboran Sea than in the Strait of Gibraltar, but the difference vanishes almost completely within a few decades afterwards, coinciding with the collapse of the hydraulic jump. This can be explained by fresher surface water being entrained into the outflow when the hydraulic transition is present. The bottom graph in figure 7.30 shows the percentage of inflowing water mixed into the outflow that is necessary to produce the greatly reduced outflow salinity shown in the top graph. Before the collapse of the hydraulic jump, approximately 60 % of the inflow appears to be mixed into the outflow, while the normal mixing (reached again after $t = 140$ years) is close to 20 %. The hydraulic transition leads to an additional entrainment of $\approx$ 40 %. This would indicate that the entrainment parameter k_{entr} is large enough for the system to be in the regime in which the meta-stable state is possible (see figure 7.26), and indeed the time evolution of the salinity in the GCM experiment (figure 7.28) resembles the evolution of the salinity in the HYCOBOX experiment in figure 7.8 very closely, both qualitatively and quantitatively.

A similar behaviour is observed in a different model experiment with the same model, described in Myers and Haines (2001). This experiment was part of a series of experiments to investigate the sensitivity of the circulation to changes in air-sea-flux forcing. When the net evaporation was increased by 25 %, the model showed qualitatively similar behaviour. Myers and Haines (2001) note that the model resolution is too coarse to allow the mixing processes in the strait be represented correctly. In fact, assuming that the height of the hydraulic jump is approximately half of the sill depth, the values in figure 7.30 (bottom) suggest a very high entrainment parameter $k_{\text{entr}} \approx 0.8$, i. e. 80 % of the inflowing water that is affected by the jump is entrained into the lower layer. This may indicate that the behaviour in this particular GCM experiment is unrealistic and an artefact of the numerical mixing scheme near the strait. However, it is difficult to compare the two different mixing parameterisations, and a smaller k_{entr} is suggested by the fact that the salinity excursion in the GCM experiment

is similar in timescale and size to the HYCOBOX experiment with $k_{\text{entr}} = 0.4$.

Although it remains unclear whether this type of dynamics occurs in nature, it seems to be possible in current GCM experiments – as realistic features or as artefacts – and this possibility should be kept in mind when interpreting GCM experiments. In particular it should be noted that the presence of a metastable state may already influence the system at smaller values of the entrainment than shown in figure 7.30, which may not be obvious if it does not lead to a collapse of the circulation that is as complete as the one shown in figure 7.27.

7.8 Entrainment scenarios in nature

In this chapter, a speculative mechanism was introduced which assumes that a significant proportion of the inflowing surface water is entrained into the outflow, producing an interesting dynamical behaviour with multiple states or oscillating solutions, and it has been argued that this can influence GCM experiments. It remains to be seen, however, if this mechanism is indeed realised in nature. This section tries to scan a number of experimental and observational results in view of the proposed mechanism. It cannot, however, claim to deliver unambiguous evidence for its presence in nature - a question which would require considerably more research.

There is a range of theoretical and experimental work on hydraulic jumps, some of which also investigate the entrainment rates. However, not all aspects relevant to the problem discussed here seem to be well understood. Generally, in a gravitationally stable stratified fluid in which one layer is turbulent, entrainment is thought to take place from the non-turbulent into the turbulent layer (e. g. Fernando 1991). In the case of the hydraulic jump, if the inflowing layer is assumed to intrude turbulently into an essentially laminar or even stagnant water mass, then entrainment from the lower layer into the upper layer would be expected, whereas there is little entrainment from the upper layer into the lower layer – in contradiction to the process proposed here. However, as Baines (1995) notes (for the somewhat different situation of experiments with a stationary hydraulic jump behind an obstacle): "Mixing is evident in both layers." Furthermore, it is not unreasonable to assume that in the case of a 2-layer exchange flow both layers are turbulent, so that there is no a priori preference for

entrainment in only one direction.

Results by Klemp et al. (1997) on the energetics of internal propagating bores also suggest that classical assumptions sometimes may have to be modified. Classically, it has been assumed that energy dissipation mainly occurs in the expanding layer, whereas energy dissipation in the contracting layer is negligible (Wood and Simpson 1984, Baines 1995), although Baines (1995) notes that this cannot be strictly correct. However, Klemp et al. (1997) show that there is a slight *increase* of energy within the expanding layer, and suggest that the structure of internal bores may be "fundamentally different" from classical external bores. Li and Cummins (1998) compare the two assumptions for propagating bores and conclude that the bore speeds agree to within a few percent, making it difficult to judge which is correct. They also point out that there is a need for further laboratory experiments with detailed quantitative measurements of mixing. While these results primarily affect our understanding of propagating bores, they might also have implications for stationary hydraulic jumps, which would be relevant for the mechanism proposed here.

As for the entrainment rates, a number of studies (reviewed in Fernando 1991) have produced an entrainment law of a form

$$E \propto R_i^{-n} \tag{7.22}$$

where E is an entrainment coefficient, and the exponent n is a constant. However, even for the same types of physical systems with the same range of Richardson numbers, the results produced by different experimenters can differ by a factor of five with varying values for n (Fernando 1991), as the turbulence critically depends on many factors that are difficult to control experimentally, leading Fernando (1991) to comment that "perhaps no other specific topic has been more controversial than the entrainment law".

It would be beyond the scope of this study to take sides in these arguments and propose a definite value for the mixing and entrainment in the hydraulic jump. However, we believe that we can conclude from these studies that entrainment from the upper layer into the lower layer is a real possibility, at least in certain situations, and that it can be strong enough to be relevant for the type of behaviour proposed in this chapter.

Furthermore, it should be pointed out that the situation in the Strait of Gibraltar is far from a perfect non-rotating two layer flow with a laboratory type hydraulic jump.

Instead, the Strait of Gibraltar is for example also influenced by tidal effects, which are known to produce bores and hydraulic jumps (e. g. Lafuente and Lucaya 1994) and thus modify mixing processes. La Violette and Arnone (1988) present observations in the Strait of Gibraltar indicating the presence of internal waveforms like hydraulic jumps and waveforms which are thought to be produced by an interaction between the tidal current and the exchange flow in the Strait. These are assumed to be major mixing mechanisms. More recent observations (Pistek and La Violette 1999) found that wave packets normally emanating from the Strait into the Alboran Sea can be absent for unknown reasons, possibly as a response to temporary changes in the strait regime.

Another feature that complicates the situation is the system of cyclonic and anti-cyclonic gyres in the Alboran Sea, immediately east of the Strait of Gibraltar (Tintore et al. 1988), which certainly facilitate mixing between the layers. For example, Davies et al. (1993) observed unstable filamentary features along the Almeria-Oran front, suggesting additional mixing. On the other hand, experimental and numerical studies (Bormans and Garrett 1989c, Speich et al. 1996) indicate that the Alboran Gyres are driven by the jet of inflowing Atlantic water, suggesting that the strength of the gyres is influenced by the strait regime. Lafuente et al. (1998) present observational evidence for the variability of the Alboran Gyres. Of particular interest here are "speculative ideas" (Lafuente et al. 1998) to correlate the variability of the Alboran Gyres with the state of the hydraulic control in the Strait of Gibraltar, which suggest that the Alboran Gyres decays when the exchange regime switches from maximal to submaximal.

The possibility that the strength of the mixing processes in the Alboran Gyres depend on the state of the strait, and in particular that they increase when the strait is in the maximal regime, is of particular interest in the HYCOBOX study presented here, as its effects would essentially be equivalent to the effects of mixing in a hydraulic jump as proposed above and included in the model below.

Adding more speculations to an already speculative mechanism, one may also note the following: Once the density of the outflow is reduced due to entrainment of upper layer water into the outflowing layer, the Richardson number in the strait decreases, thus facilitating further mixing along the strait.

To sum up the situation: Theoretical, experimental and observational studies do

not give a very definite picture of the mixing processes related to a hydraulic jump or other features connecting the Strait of Gibraltar to the Mediterranean basin. However, it seems possible that considerable entrainment of upper layer water into the lower layer occurs, and that the entrainment rate depends on the hydraulic regime in the strait, or (equivalently) the height of the hydraulic jump, i. e. the difference in interface depth between the basin and the strait entrance.

The mechanism introduced here may therefore play a role in the dynamics of the Mediterranean Sea or other marginal basins, either at present or during some periods in the past, and may lead to a new explanation for sudden collapses of the circulation following comparatively small perturbations and for the occurrence of sapropel layers.

Chapter 8

The Red Sea: A 3-layer problem

In this chapter, the foundation is laid for modifying the HYCOBOX model for the investigation of the Red Sea. The Red Sea is semi-enclosed marginal basin only connected to the World Ocean by the shallow and narrow Strait of Bab al Mandab. As in the case of the Mediterranean Sea, it is an evaporation-dominated basin, but instead of a simple 2-layer anti-estuarine circulation it has developed a more complicated seasonal cycle (figure 8.3). In winter, there is a 2-layer exchange with surface water flowing in and Red Sea Deep Water (RSDW) flowing out at the bottom. In summer, the simple 2-layer exchange is modified through the intrusion of Gulf of Aden Intermediate Water (GAIW) between the layers, and the reversal of the surface layer, leading to a 3-layer exchange.

Therefore, the HYCOBOX model cannot be used directly, but has to be modified to include the 3-layer case. This chapter provides the necessary mathematical foundation for the 3-layer system with a free surface, so that future work can produce a full hydraulically controlled box model of the Red Sea.

In the first section of this chapter, the general situation in the Strait of Bab al Mandab is described and observations summarised. In the following section, the relevant equations for the 3-layer-exchange at the Strait are defined and the appropriate control condition derived. The general features of typical solutions are discussed, and it is found that there are four different 3-layer flow types relevant for the study of the exchange in the Strait of Bab al Mandab. To connect the Strait equations to the Basin, the features of hydraulic jumps are discussed, and the solution method for each of the

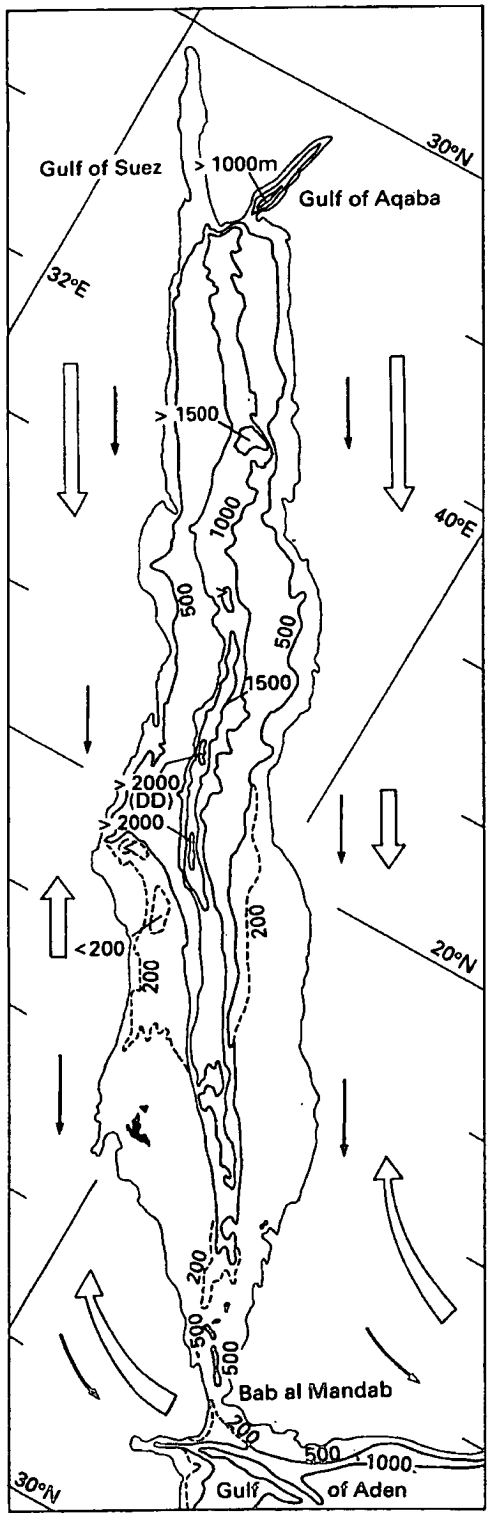

Figure 8.1: Topography of the Red Sea (from Tomczak and Godfrey 1994).

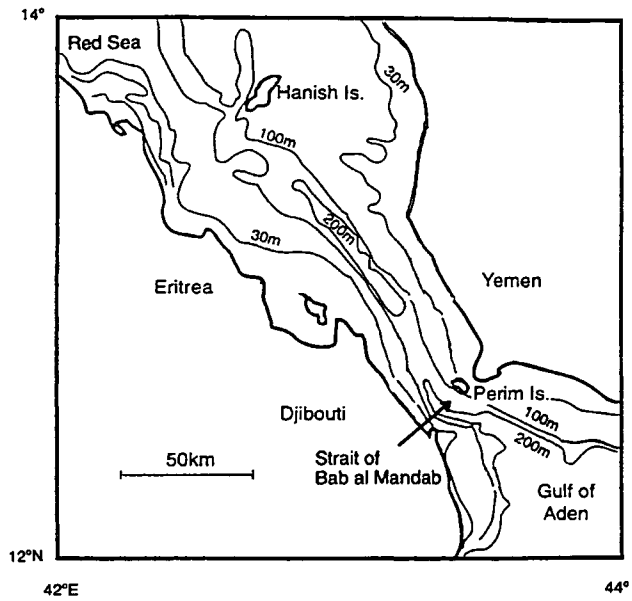

Figure 8.2: The Strait of Bab al Mandab (from Cromwell and Smeed 1998).

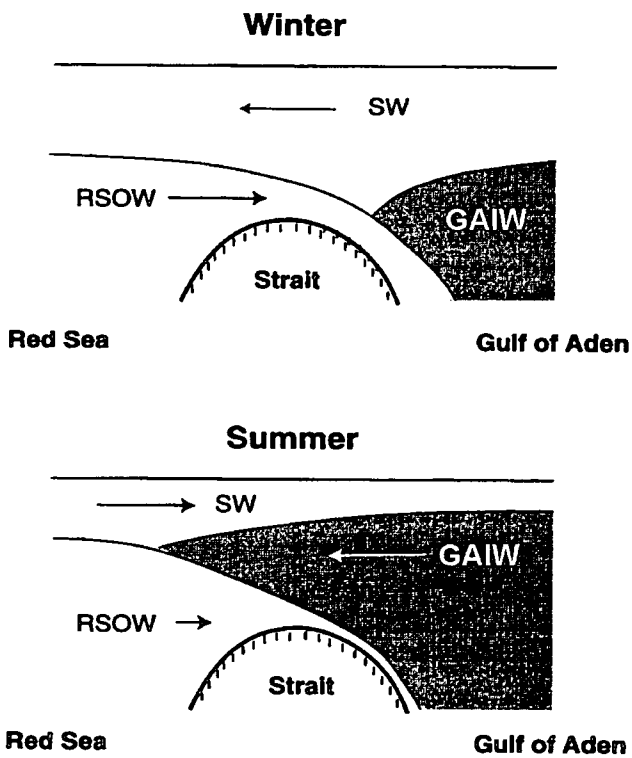

Figure 8.3: The exchange flow in winter and summer in the Strait of Bab al Mandab (from Cromwell and Smeed 1998).

four flow types is derived. With this foundation, an outlook is given of the features of a future model of the Red Sea, and a number of possible investigations are suggested.

8.1 The Red Sea and the Strait of Bab al Mandab

The Red Sea (figure 8.1) fills the rift valley formed during the separation of Africa and Arabia. It is about 2000 km long, but on average only 250 km wide, stretching south-eastwards from the Sinai peninsula in the north to the Strait of Bab al Mandab in the South. Its average depth is 560 m, with a maximum depth of 2900 m in the central trough. Before the opening of the Suez canal, the only connection to the World Ocean was through the Strait of Bab al Mandab (figure 8.2) with a sill depth of 110 m near the Hanish archipelago. Further out into the Gulf of Aden, the narrowest point (26 km) of the strait is marked by Perim Island (Tomczak and Godfrey 1994).

Situated in an extremely arid region with a precipitation of only 7 cm/year, the net water loss is near 2 m/year. Therefore, the salinity is extremely high, reaching values above 42 psu in the Northern Red Sea and the shallow Gulf of Suez, which are active centres of deep water formation. The highly saline Red Sea Deep Water (RSDW) flows out over the sill and can be traced far into the Indian ocean due to its high salinity.

Although the net circulation is anti-estuarine, the exchange at the Strait of Bab al Mandab is not a simple 2-layer flow with inflowing water at the surface and outflowing water at depth. Instead, the simple 2-layer exchange is only present in winter. During the summer months, the surface flow changes direction, and a 3-layer system develops in the strait with the top and bottom layer flowing out, and a layer of intermediate water from the Gulf of Aden flowing in between them.

This seasonal cycle is thought to be driven by the monsoon through a mechanism first proposed by Patzert (1974) (see figure 8.3). In the Gulf of Aden, a stationary layer of intermediate water, the so called Gulf of Aden Intermediate Water (GAIW) can be observed (Smeed 1997). In winter, this GAIW begins at a depth of 100 m, too deep to influence the strait exchange. With the onset of the summer monsoon around May, eastward winds induce southward Ekman transport along the coast of Yemen. This leads to upwelling in the Gulf of Aden, and the GAIW rises to a depth of about 50 m and intrudes into the strait, establishing a third layer between the outflowing RSDW

and the surface water (Smeed 1997). This mechanism is also supported by Smeed (2000), who used a 3-layer hydraulic model with rigid lid to show that the movement of the interface in the Gulf of Aden is sufficient to establish a third inflowing layer similar to the observed situation. Furthermore, assuming that the net transport through the strait balances the net evaporation, the hydraulic model also showed a reversal of the surface layer without any need for direct wind forcing of the surface layer.

On the other hand, observations suggest that wind forcing may play a role in the reversal of the surface layer. Altimetric observations (Cromwell and Smeed 1998) show an annual cycle in the sea level with an amplitude of 13 cm in the Gulf of Aden, highest in winter. The sea level in the Red Sea varies in phase with a higher amplitude of 18 cm, indicating that the sea level slope towards the Red Sea increases in summer, in apparent contradiction to the reversal of the surface flow.

The model used by Smeed (2000) does not include a free surface, and therefore does not allow direct comparison with altimetric observations. In order to clarify the causes for the reversal of the surface flow it is therefore desirable to have a hydraulic model of the strait with a free surface. This should be combined with a box model of the Red Sea to capture the basic dynamics of the system and enable a comparison with altimetric data be made.

8.2 The dynamic equations

For the 3-layer case, the relevant equations are derived in a similar way to the 2-layer case. However, while the Bernoulli functions are trivial, the Froude number condition is far from obvious and has to be derived carefully. For a straightforward derivation, the formalism based on the hydraulic functional is used. It is equivalent to a more explicit derivation by Baines (1995), but uses more abstract functional analytic concepts, and has the advantage of making the derivation considerably shorter.

We restrict the discussion to channels with rectangular cross section. Both the width and the depth are allowed to vary along the channel. The dimensionalisation of all quantities is similar to the 2-layer case (see chapter 2), except for depth-variables: Depth and layer thicknesses are dimensionalised to the actual depth at every point instead of the sill depth, so that $h_i(x) = \tilde{h}_i(x) \cdot \tilde{d}(x) \cdot D$, where $\tilde{d}(x)$ is the nondimensional

channel depth, and the tilde indicates nondimensional quantities. In the following, the tilde is omitted for simplicity.

The system is described by three equations, namely the Bernoulli difference at the two interfaces between upper and middle layer, and between middle and lower layer respectively, and a Bernoulli function at the free surface:

$$B_0 = \frac{q_1^2}{2(bdh_1)^2} - sdh_0 \tag{8.1}$$

$$\Delta B_1 = \frac{q_1^2}{2(bdh_1)^2} - \frac{q_2^2}{2(bdh_2)^2} + r(h_0 + h_1) \tag{8.2}$$

$$\Delta B_2 = \frac{q_2^2}{2(bdh_2)^2} - \frac{q_3^2}{2(bdh_3)^2} + rd(h_0 + h_1 + h_2) \tag{8.3}$$

with the additional constraint

$$h_0 + h_1 + h_2 + h_3 = 1 \tag{8.4}$$

The parameters r and s are defined as

$$r := \frac{(\rho_2 - \rho_1)(\rho_3 + \rho_2)}{2\rho_2(\rho_3 - \rho_1)} \tag{8.5}$$

$$s := \frac{(\rho_2 + \rho_1)(\rho_3 + \rho_2)}{2((\rho_2 - \rho_1)(\rho_3 + \rho_2) + (\rho_2 + \rho_1)(\rho_3 - \rho_2))} \tag{8.6}$$

and describe the density differences between the layers. The parameter r varies between 0, if the two upper layers have the same density, and 1, if the two lower layers have the same density. The parameter s is of the order of 10^3 and may roughly be interpreted as the density contrast at the surface compared to the internal interfaces.

The variables b, d, h_0, h_1, h_2 are functions in the alongchannel coordinate x. Similar to the 2-layer case, the system can be conveniently described in terms of a hydraulic functional

$$\vec{J}^{(3)}(b(x), d(x), q_i, b_i; h_i(x)) : M \to \mathbb{R}^3 \tag{8.7}$$

The same notation as in the 2-layer case is used, with the arguments before the semicolon (;) being parameters that characterise the flow, while the arguments after the semicolon are elements of the domain M on which the mapping $\vec{J}^{(3)}$ is defined. The domain M is the 3-dimensional subspace, defined by (8.4), of the 4-dimensional

product of the space of continuous real functions

$$M := \left\{ \begin{pmatrix} h_0(x) \\ h_1(x) \\ h_2(x) \\ h_3(x) \end{pmatrix} \in \mathcal{C}(\mathbb{R})^4 \quad | \quad h_0(x) + h_1(x) + h_2(x) + h_3(x) = 1 \right\} \tag{8.8}$$

The hydraulic functional has the explicit form

$$\vec{J}^{(3)}(b(x), d(x), q_i, b_i; h_i(x)) := \tag{8.9}$$
$$\begin{pmatrix} \frac{q_1^2}{2(bdh_1)^2} - sdh_0 - B_0 \\ \frac{q_1^2}{2(bdh_1)^2} - \frac{q_2^2}{2(bdh_2)^2} + r(h_0 + h_1) - \Delta B_1 \\ \frac{q_2^2}{2(bdh_2)^2} - \frac{q_3^2}{2(bdh_3)^2} + rd(h_0 + h_1 + h_2) - \Delta B_2 \end{pmatrix}$$

As in the case of two layers, the solution manifold S is the kernel of this functional, i. e.

$$S = \left\{ \begin{pmatrix} h_0(x) \\ h_1(x) \\ h_2(x) \\ h_3(x) \end{pmatrix} \in M \quad | \quad \vec{J}^{(3)} = \vec{0} \right\} \tag{8.10}$$

The control condition is given by points for which different solution sheets meet, i. e. where the Jacobian of $\vec{J}^{(3)}$ has a singularity. For the rigid lid approximation[1] ($h_0 \ll h_1$; and the net transport $q_1 + q_2 + q_3 = q$ is specified), the second and third component of (8.9) are independent of h_0, and the first component is decoupled. Therefore the explicit form of the control condition can be derived from the simplified 2-dimensional functional

$$\vec{J}_2(b(x), d(x), q_i, b_i; h_1(x), h_2(x)) :=$$
$$\begin{pmatrix} \frac{q_1^2}{2(bdh_1)^2} - \frac{q_2^2}{2(bdh_2)^2} + rh_1 - \Delta B_1 \\ \frac{q_2^2}{2(bdh_2)^2} - \frac{q_3^2}{2(bd(1 - h_1 - h_2))^2} + rd(h_1 + h_2) - \Delta B_2 \end{pmatrix} \tag{8.11}$$

[1]Note that the rigid lid approximation is introduced here only to simplify the derivation of the control condition, whereas in later calculations a free surface is used. The control condition remains valid for a free surface provided that $h_0 \ll h_1$, which is true in the cases investigated here, see (8.17).

in which the coordinates of the base space M have been transformed to eliminate h_3.

It is now straightforward to calculate the Jacobian of $\vec{J}^{(2)}$

$$\begin{aligned} D\vec{J}^{(2)} &:= \left(\frac{\partial J_i^{(2)}}{\partial h_j}\right)_{i,j=1,2} \\ &= \begin{pmatrix} rd - \frac{q_1^2}{b^2 d^2 h_1^3} & \frac{q_2^2}{b^2 d^2 h_2^3} \\ (1-r)d - \frac{q_3^2}{b^2 d^2 h_3^3} & (1-r)d - \frac{q_3^2}{b^2 d^2 h_3^3} - \frac{q_2^2}{b^2 d^2 h_2^3} \end{pmatrix} \end{aligned} \tag{8.12}$$

Control conditions are higher order solutions of $\vec{J}^2 = 0$, i. e. singularities of the Jacobian, given by

$$\det D\vec{J}^{(2)} = 0 \tag{8.13}$$

With the definition of single layer Froude numbers

$$F_i^2 := \frac{q_i^2}{b^2 d^3 h_i^3} \qquad i = 1, \ldots, 3 \tag{8.14}$$

the control condition (8.13) can be expressed as

$$0 = -r^2 + r \cdot (1 + F_1^2 - F_3^2) + F_3^2 \cdot (F_1^2 + F_2^2) + F_2^2 \cdot (F_1^2 - 1) - F_1^2 \tag{8.15}$$

The control condition (8.15) is only valid at control points. For convenience we also define a functional

$$\begin{aligned} &G(b(x), d(x), q_i; h_i(x)) := \\ &\quad -r^2 + r \cdot (1 + F_1^2 - F_3^2) + F_3^2 \cdot (F_1^2 + F_2^2) + F_2^2 \cdot (F_1^2 - 1) - F_1^2 \end{aligned} \tag{8.16}$$

As this control condition was derived assuming the rigid lid approximation, it is only an approximation to the correct condition for a free surface. However, following the same procedure for the full 3-dimensional functional $\vec{J}^{(3)}$ without rigid lid approximation, it is trivial to show that the correct control condition for the free surface is

$$\begin{aligned} 0 \;=\; & (-r^2 + r \cdot (1 + F_1^2 - F_3^2) + F_3^2 \cdot (F_1^2 + F_2^2) + F_2^2 \cdot (F_1^2 - 1) - F_1^2) \cdot s \\ & + r^2 F_1^2 - r \cdot (F_1^2 - F_1^2 \cdot F_3^2) - F_1^2 \cdot F_2^2 \cdot F_3^2 + F_1^2 \cdot F_3^2 \end{aligned} \tag{8.17}$$

All Froude numbers and r are of order of 1, while $\frac{s}{r}$ is of order of $10^3 - 10^4$, so that the equation is dominated by the first term. Therefore (8.17) is approximately equivalent to the control condition for the rigid lid approximation (8.15).

In other words, the simplified control condition (8.15) holds also when no rigid lid is assumed, if the density difference between the layers (measured by r) is small compared to the density difference between water and air (measured by s).

8.3 General solutions - rigid lid

The system is now characterised by a set of 3 equations (8.1, 8.2, 8.3), or equivalently by a 3-dimensional functional $\vec{J}^{(3)}$, which hold at every point along the channel, and an additional control condition (8.15), which holds only at control points. In this section, the general features of the solution are discussed.

Solutions to the system can be found by numerically solving the set of three equations (8.1, 8.2, 8.3). In this section, for simplicity the rigid lid approximation is used, and the free surface reintroduced in the next section. The problem is now to find solutions to

$$\vec{J}_2(h_i(x)) = 0 \tag{8.18}$$

Assuming that all parameters, i. e. the flow rates in the layer and the Bernoulli potentials, are known, the solutions for this set of equations can easily be found with a standard Newton search algorithm[2].

The solution manifold is the projection of S (8.10) onto the plane defined by $h_0 = 0$. As the domain M has three dimensions, its projection onto $h_0 = 0$ has two dimensions, and the problem and its solutions can conveniently be visualised using a 2-dimensional plot. Following Smeed (2000), the h_1-h_2-plane is used, where all allowed values lie in the triangle spanned by $(h_1 = 0, h_2 = 0)$, $(h_1 = 1, h_2 = 0)$ and $(h_1 = 0, h_2 = 1)$. Figure 8.4 shows an example for one solution, using the simple channel geometry with sill and narrows defined by

$$d(x) = 5 - 4\mathrm{e}^{-x^2} \tag{8.19}$$

$$b(x) = 5 - 4\mathrm{e}^{-x^2} \tag{8.20}$$

The solution along the channel is a two-dimensional function $(h_1, h_2)(x)$ and therefore forms a path in the h_1-h_2-plane parameterised by the alongchannel coordinate x. The figure also shows that several solution branches exist which meet in control points. The bottom diagram translates one of the paths from the h_1-h_2-plane into an alongchannel plot. It may seem that the h_1-h_2-plane is much less intuitive than the

[2]This calculation was done with the symbolic mathematics package *Macsyma*, and all programmes are listed in appendix D.3.1.

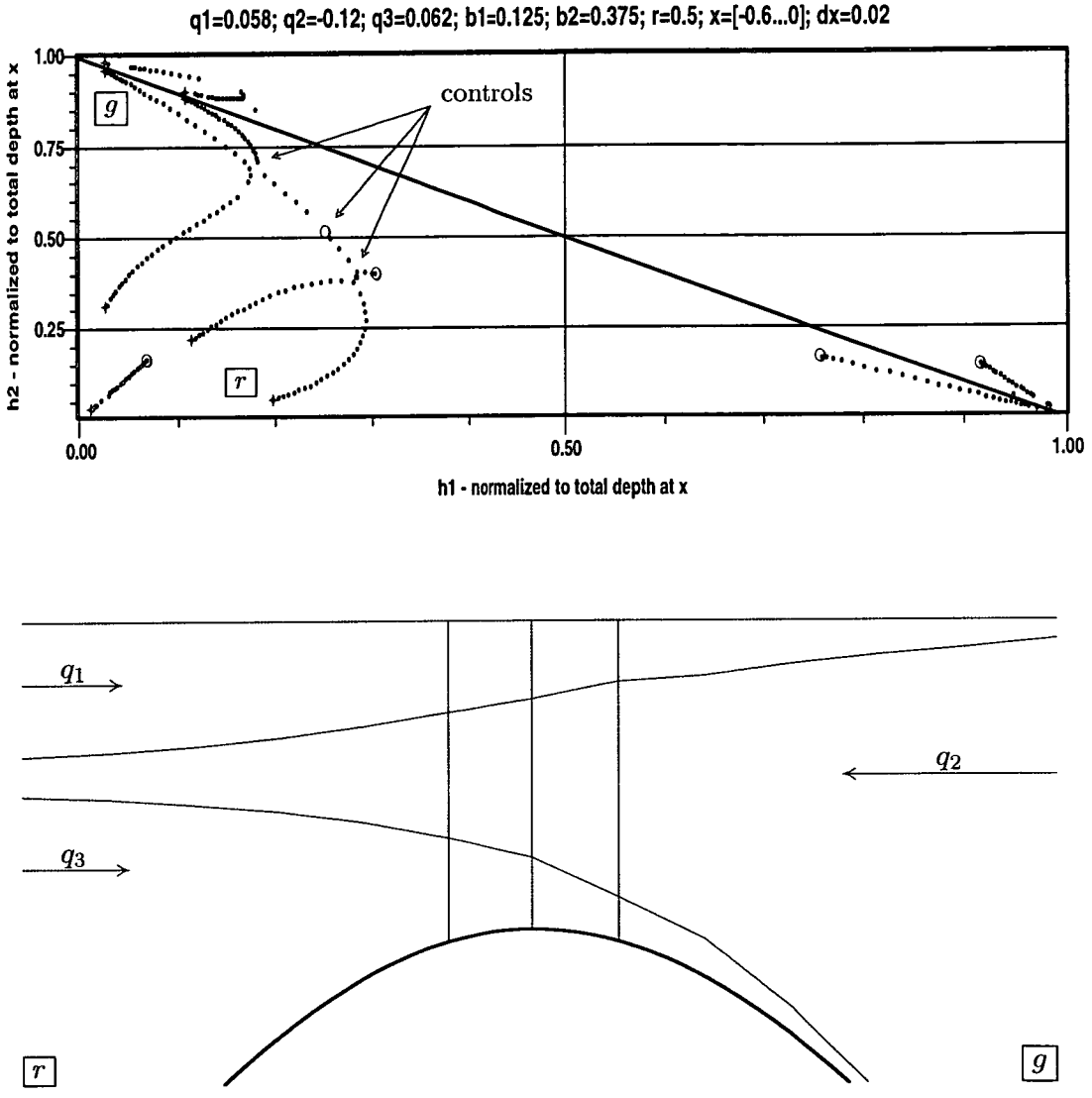

Figure 8.4: An example for a solution plotted in the h_1-h_2-plane. The parameters for this example were taken from Smeed (2000). The top graph shows the solution from $x = \pm 0.6$ (crosses) to $x = 0$ (circles) every $\Delta x = 0.02$ (dots). The solutions along the channel form paths in the h_1-h_2-plane, and different solutions branches meet in control points (arrows). The path between points r (Red Sea) and g (Gulf of Aden) is shown in the bottom diagram as an alongchannel plot, with the controls marked by vertical lines. This alongchannel plot reproduces figure 9 in Smeed (2000).

alongchannel plot, however it has the advantage that all solution branches can be plotted into one diagram, whereas a separate alongchannel plot is needed for each branch, making the h_1-h_2-plane much easier to use.

8.4 Classification of the solutions

The control points can easily be seen from the h_1-h_2-plot (figure 8.4) as the points at which different solution branches meet. Further insight is gained from the Froude number condition (8.15). Figure 8.5 shows the lines in the h_1-h_2-plane on which the Froude number condition holds for three points along the channel. This criticality condition divides the h_1-h_2-plane into seven distinct areas[3]. Following Smeed (2000), these are labelled 0, i and $-i$. Comparing the three diagrams in figure 8.5 which show the criticality condition at the sill and narrows ($x = 0$) and at two points $x = 0.1$ and $x = 0.5$ away from the sill, it can be seen that the regime 0 covers a wider area when the channel depth and width increases, whereas the other regimes are restricted to situations in which one or two of the layers are very thin. The regime 0 can be identified with an uncontrolled regime in which both modes are subcritical. The regimes $+i$ are reached by crossing the criticality condition once, whereas the regimes $-i$ are separated from 0 by two critical points. Therefore, in the regime 0 both modes are subcritical, the regimes $+i$ have one subcritical and one supercritical mode, and the regimes $-i$ have two supercritical modes.

The solutions along the channel can now be classified according to the hydraulic regimes at the two channel entrances, where a solution labelled $[i, j]$ connects regime i with regime j. For example, the solution shown in figure 8.4 connects regime 2 at $x = -0.6$ with regime -2 at $x = +0.6$, so that it is classified as $[2, -2]$ – see figure 8.6. It passes through control points at $x = -0.12$ ($2 \to 0$), at $x = 0$ ($0 \to 3$) and $x = +0.14$ ($3 \to -2$). Furthermore we use the convention that in flow type $[i, j]$ the first regime

[3]It has not been proven yet whether the saddle points of the criticality condition actually coincide with roots, or if the three areas 1, 2 and 3 are connected, as is suggested by the plots in figure 8.5. However, physical arguments suggest that the seven areas are separate – one always has to move through a criticality condition when moving from one regime to another –, but for the discussion here this technical detail is of minor relevance.

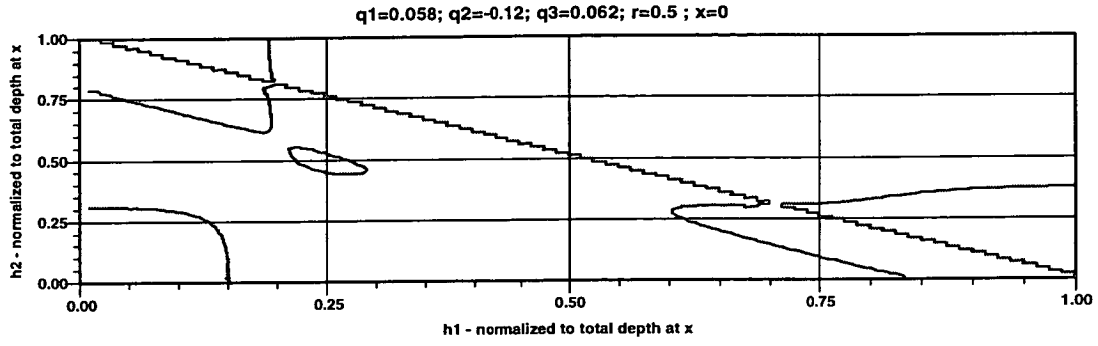

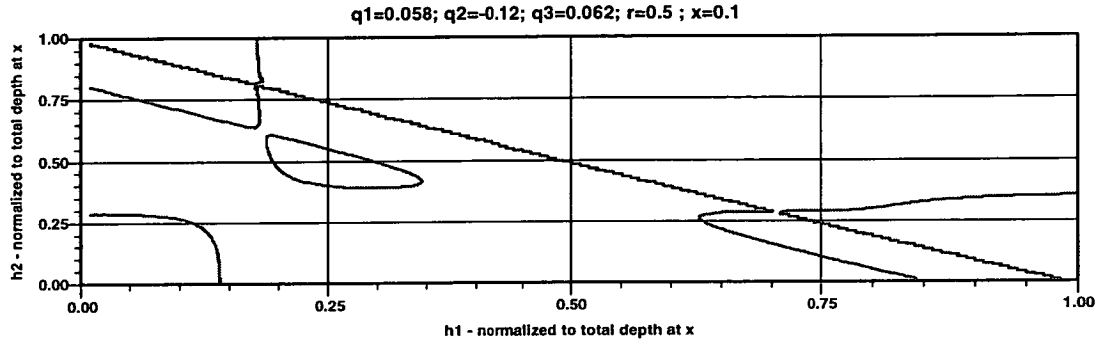

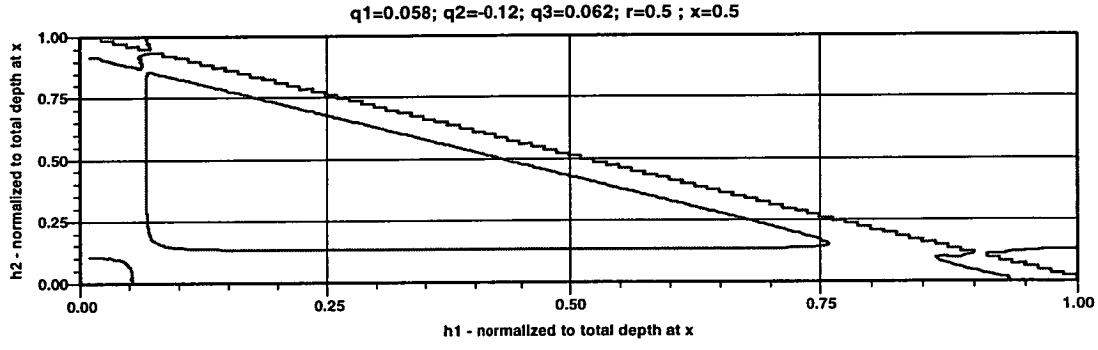

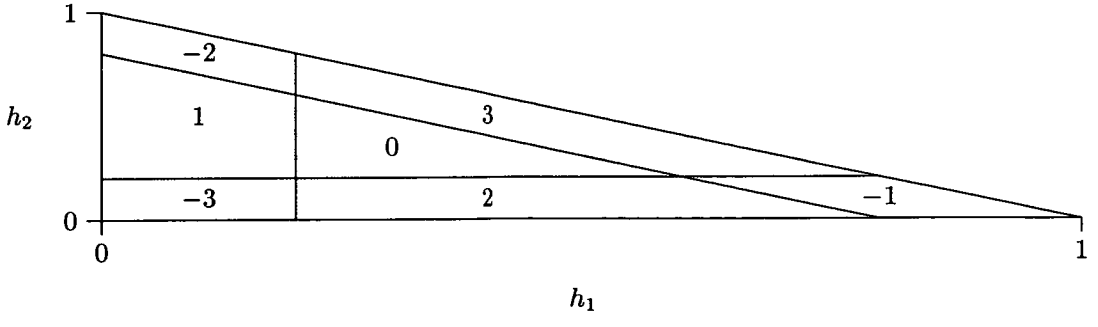

Figure 8.5: The Froude number condition at three points along the channel. From top to bottom at $x = 0$, i. e. at the sill and narrow, at $x = \pm 0.1$ and $x = \pm 0.5$. The criticality condition divides the the h_1-h_2-plane into seven distinct areas, labelled in the bottom figure. See text for details.

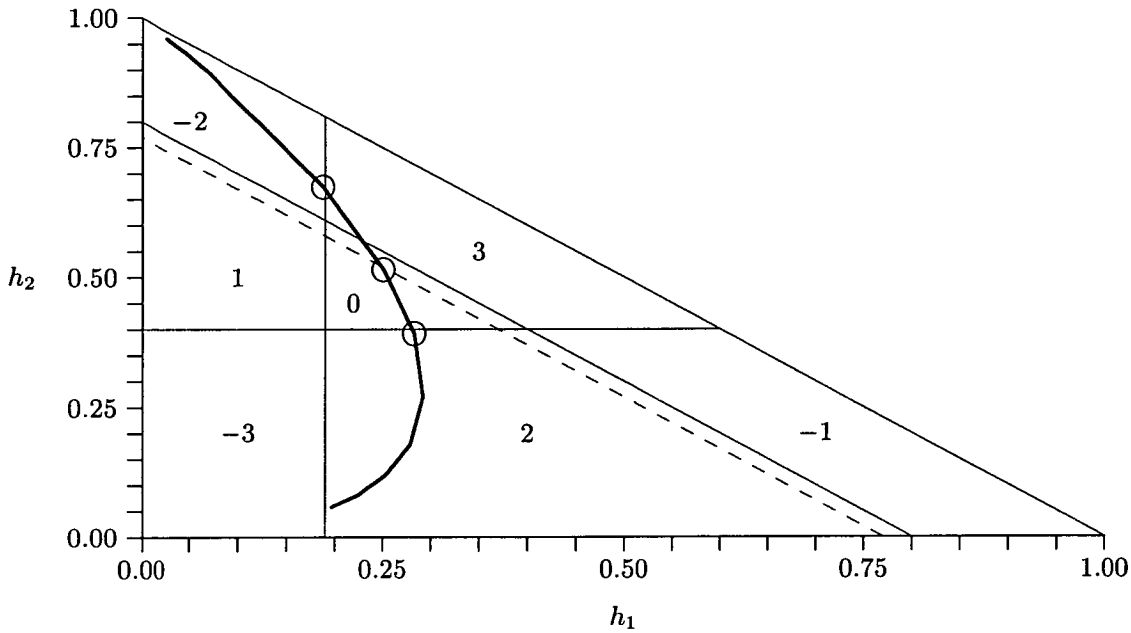

Figure 8.6: The solution from the example shown in figure 8.4 with its controls (circles), and the criticality condition for $x = \pm 0.1$ (solid) and $x = 0$ (dashed, only the 0-3-boundary). This path is classified as $[2, -2]$ as it connects the regimes 2 and -2. It passes through control points at $x = -0.12$ $(2 \to 0)$, at $x = 0$ $(0 \to 3)$ and $x = +0.14$ $(3 \to -2)$. The plot of the criticality condition is simplified from figure 8.5.

(i) refers to the Red Sea, and the second (j) to the Gulf of Aden.

To get all the flow types relevant for the study of the Red Sea, the following assumptions can be made:

- The lower interface drops to great depth in the Gulf of Aden, so that the regime in the Gulf of Aden is 3 if the interface between upper and middle layer is deep[4]; or -2 if the interface is shallower.

- Inside the Red Sea both interfaces do not drop significantly, whereas the bottom layer is very thick. This leads to the regime 1 if the upper layer is thin, 2 if the middle layer is thin, or -3 if both layers are thin.

The list of all possible 3-layer flow types given by Smeed (2000) excludes some combinations between these regimes, leaving only the types [-2,2], [1,3], [2,3] and [-3,3] as relevant for the Red Sea. These regimes are summarised in figure 8.7. In each case,

[4]The terms "deep", "shallow", "thin" cannot be quantified precisely at this point and should be seen as qualitative characterisations of the different regimes.

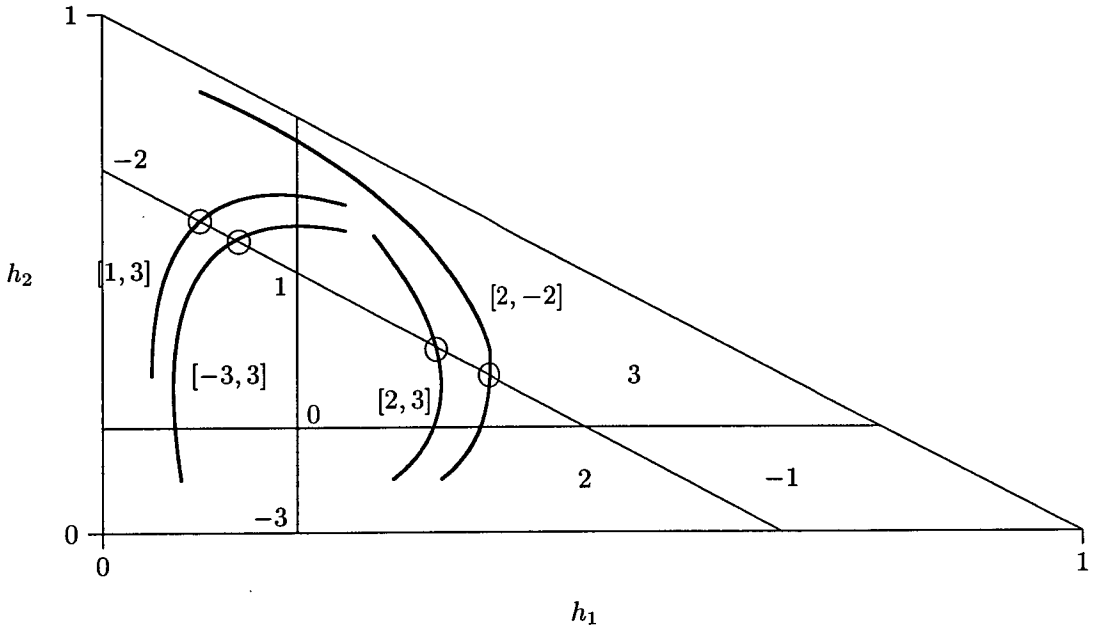

Regime	$[-3,3]$	$[1,3]$	$[2,3]$	$[2,-2]$
Control Red Sea (8.29)	×		×	×
Control Sill (8.30)	×	×	×	×
Control Gulf of Aden (8.31)	×	×		×
Regime Gulf of Aden	3			-2
Bernoulli upper interface	$h_{1\text{eff}} = h^*_{1g}$			
Regime Red Sea	-3	1	2	
Bernoulli lower interface		$h_{2\text{eff}} = h^*_{2r}$	$h_{2\text{eff}} = h^*_{2r} + \frac{h^*_{1r} - h^*_{1g}}{1-r}$	

Figure 8.7: The different flow types relevant for the Red Sea. The control at the sill is marked by circles in the h_1-h_2-diagram, other controls are at points where the path crosses to a different regime. The regime at the Strait entrances determines the type of the hydraulic jump and the Bernoulli constants. See text for details.

the regime at the strait entrances has one or two supercritical modes, and a hydraulic jump is necessary to connect the strait to the subcritical basins.

8.5 Solution method for the free surface problem

In this section, the strait equations are solved in order to obtain the flow rates from the boundary conditions. Similar to the 2-layer case, the hydraulic functional (8.2) and the control condition (8.15) give a set of coupled equations at three points along the channel, which then can be solved. While the 3-layer case with a rigid lid has been solved by Smeed (2000), here we use the full set of equations including a free surface.

8.5.1 The governing equations

For the following, the strait is assumed to be a channel of constant width, with a single sill at $x = 0$. At the ends the channel is connected to the much wider basins of the Gulf of Aden and the Red Sea. The sill is a single minimum, and the bottom depth falls to infinity towards both ends. In this geometry, the controls can only occur at the sill or at the channel entrances (Killworth 1992a) so that the location of the controls is known. Therefore it is sufficient to use the hydraulic functional at these three points, if it is checked – e. g. by the method shown above – that the solution can be matched through along the channel. In the following, the subscript $_r$ refers to quantities towards the Red Sea, $_s$ at the sill, and $_g$ towards the Gulf of Aden. Outside the strait, in the region where the narrow strait is connected to the wider basins, hydraulic jumps connect the flow to the boundary conditions in the basin. To distinguish between the layer thicknesses on both sides of the hydraulic jumps, the values in the basin are marked with an asterisk, so that e. g. h_{1g} is the thickness of the upper layer at the strait entrance, but h^*_{1g} is the thickness in the basin, with the hydraulic jump between them.

Furthermore, the assumption is made that the lower interface drops to great depth in the Gulf of Aden, so that $h_{2g} \to \infty$. In the Red Sea, neither interface drops significantly, while the bottom layer becomes infinitely thick ($h_{3r} \to \infty$). Under these assumptions the following equations hold:

$$0 = B_0 - \frac{1}{2}\left(\frac{q_1}{d_r b_r h_{1r}}\right)^2 + s d_r h_{0r} \tag{8.21}$$

$$0 = B_0 - \frac{1}{2}\left(\frac{q_1}{d_s b_s h_{1s}}\right)^2 + s d_s h_{0s} \tag{8.22}$$

$$0 = B_0 - \frac{1}{2}\left(\frac{q_1}{d_g b_g h_{1g}}\right)^2 + s d_g h_{0g} \tag{8.23}$$

$$0 = B_1 - \frac{1}{2}\left[\left(\frac{q_1}{d_r b_r h_{1r}}\right)^2 - \left(\frac{q_2}{d_r b_r h_{2r}}\right)^2\right] - r d_r (h_{1r} + h_{0r}) \tag{8.24}$$

$$0 = B_1 - \frac{1}{2}\left[\left(\frac{q_1}{d_s b_s h_{1s}}\right)^2 - \left(\frac{q_2}{d_s b_s h_{2s}}\right)^2\right] - r d_s (h_{1s} + h_{0s}) \tag{8.25}$$

$$0 = B_1 - \frac{1}{2}\left(\frac{q_1}{d_g b_g h_{1g}}\right)^2 - r d_g (h_{1g} + h_{0g}) \tag{8.26}$$

$$0 = B_2 - \frac{1}{2}\left(\frac{q_2}{d_r b_r h_{2r}}\right)^2 - (1-r) d_r (h_{2r} + h_{1r} + h_{0r}) \tag{8.27}$$

$$\begin{aligned} 0 = {} & B_2 - \frac{1}{2}\left[\left(\frac{q_2}{d_s b_s h_{2s}}\right)^2 - \left(\frac{q_3}{d_s b_s h_{3s}}\right)^2\right] \\ & -(1-r) d_s (h_{2s} + h_{1s} + h_{0s}) \end{aligned} \tag{8.28}$$

$$0 = -r^2 + r \cdot (1 + F_{1r}^2) - F_{1r}^2 - F_{2r}^2 + F_{1r}^2 F_{2r}^2 \tag{8.29}$$

$$\begin{aligned} 0 = {} & -r^2 + r \cdot (1 + F_{1s}^2 - F_{3s}^2) + F_{3s}^2 \cdot (F_{1s}^2 + F_{2s}^2) \\ & + F_{2s}^2 \cdot (F_{1s}^2 - 1) - F_{1s}^2 \end{aligned} \tag{8.30}$$

$$0 = r - F_{1g}^2 \tag{8.31}$$

$$F_{ix}^2 := \frac{q_i^2}{(d_x b_x h_{ix})^3} \quad \text{with} \quad i = 1,2,3 \quad \text{and} \quad x = r,s,g \tag{8.32}$$

The first eight equations give the Bernoulli function at the surface, upper interface and lower interface, each towards the Gulf of Aden, towards the Red Sea, and at the sill. The last three equations give the control condition at these three points. The number and position of the controls depends on the strait regime, so that not all three control conditions can be used for every flow type: Type [1, 3] only has controls at the Sill and the Gulf of Aden, so that the control condition towards the Red Sea (8.29) is not valid, and for type [2, 3] there is no control at the Gulf of Aden (8.31).

For the rigid lid approximation, Smeed (2000) solved a similar (but smaller) set of equations using a Newton iteration for the full set of variables. However, for the free surface problem this is impractical as the number of variables and possible solutions is larger. Instead, the equations are solved analytically as far as possible, and iteration schemes only employed for equations that cannot be solved analytically.

For each of the different flow types a different solution method has to be used, as

the number of controls and therefore the number of equations varies. Furthermore, the different flow types have different types of hydraulic jumps connecting the strait to the basin, so that a different set of boundary conditions is active in each case.

It is convenient to express the Bernoulli potentials in terms of effective layer thicknesses defined by

$$B_0 = -sdh_{0\text{eff}} \tag{8.33}$$

$$B_1 = rdh_{1\text{eff}} \tag{8.34}$$

$$B_2 = (1-r)d(h_{2\text{eff}} + h_{1\text{eff}}) \tag{8.35}$$

8.5.2 Boundary conditions: the connection to the reservoirs

The set of governing equations provides 10 or 11 equations (depending on the number of controls) containing 14 variables. 3 or 4 variables have to be determined from the boundary conditions in the basin. For the surface, the Bernoulli potential is determined by the upstream sea level, and the downstream sea level is continuous from the strait to the basin. Therefore

$$\left.\begin{aligned} h_{0\text{eff}} &= h^*_{0g} \\ h_{0r} &= h^*_{0r} \end{aligned}\right\} \quad \text{for surface inflow} \tag{8.36}$$

$$\left.\begin{aligned} h_{0\text{eff}} &= h^*_{0r} \\ h_{0g} &= h^*_{0g} \end{aligned}\right\} \quad \text{for surface outflow} \tag{8.37}$$

where the asterisk denotes the values in the basin.

Internal hydraulic jumps connect the supercritical regime at the strait entrances to the subcritical basins. Across the jump, there should be no energy gain. For the different regimes, this condition leads to hydraulic jumps at the two strait entrances as follows:

Regime 3 towards the Gulf of Aden: In this regime the hydraulic jump affects only the lower interface, so that the Bernoulli potential in the upper interface is determined by the potential in the Gulf of Aden:

$$h_{1\text{eff}} = h^*_{1g} \tag{8.38}$$

Regime −2 towards the Gulf of Aden: In this case, both modes are supercritical at the strait entrance and the hydraulic jump affects both interfaces, so that the Bernoulli potentials are not determined by the basin condition in the Gulf of Aden.

Regime 1 towards the Red Sea: There is a hydraulic jump in the upper interface to the Red Sea, but the Bernoulli potential in the lower interface is determined by the conditions in the Red Sea:

$$h_{2\text{eff}} = h^*_{2r} \tag{8.39}$$

Regime 2 towards the Red Sea: The hydraulic jump affects both interfaces. However, the first mode is not affected, so that across the hydraulic jump the hydrostatic assumption is valid:

$$h_{2\text{eff}} = h^*_{2r} + \frac{h^*_{1r} - h^*_{1g}}{1-r} \tag{8.40}$$

Regime −3 towards the Red Sea: for this regime, both modes are supercritical, and neither mode is continuous across the hydraulic jump. Therefore, the Bernoulli potentials cannot be determined from the basin conditions.

It is now possible to obtain all other variables from the set of equations (8.21-8.31).

8.5.3 Solution method

In the following, the governing equations are solved for each flow type. Only the solution for type [1, 3] is explained in detail here, while the solution for the other regimes is summarised in figure 8.8, with the equations given in appendix D.3.2.

Flow type [1, 3]. In this regime, there is inflow in the two upper layers. There are controls at the sill and towards the Gulf of Aden, but not towards the Red Sea, so that (8.29) cannot be used. The boundary conditions yield:

$$B_0 = -sd_g h^*_{0g} \quad \text{(see D.3.2 d73)} \tag{8.41}$$

$$B_1 = rd_g h1g^* \quad \text{(see D.3.2 d84)} \tag{8.42}$$

$$B_2 = (1-r)d_g\left(\frac{B_1}{rd_r} + h^*_{2r}\right) \quad \text{(see D.3.2 d86)} \tag{8.43}$$

$$h_{0r} = h^*_{0r} \quad \text{(see D.3.2 d174)} \tag{8.44}$$

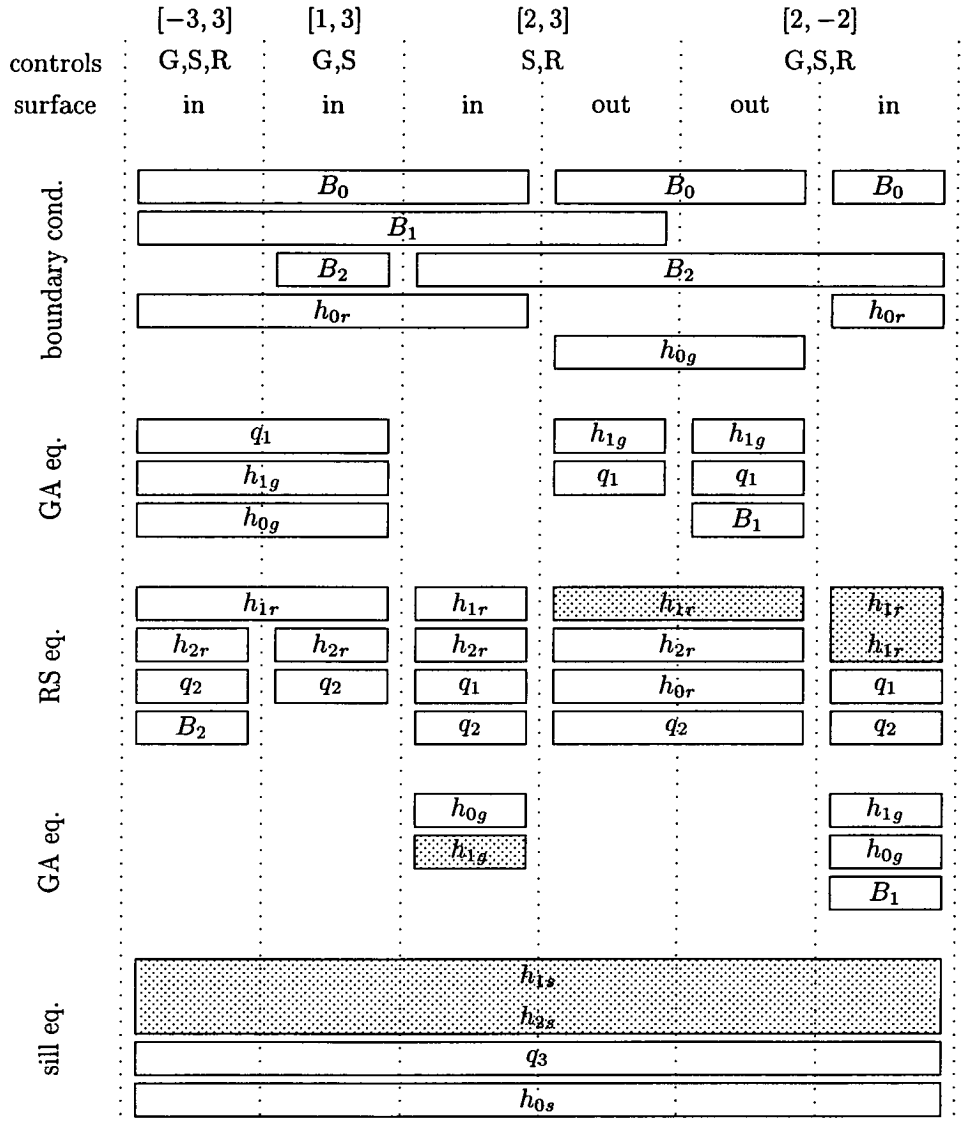

Figure 8.8: Overview of the solution used for the different regimes. Each column shows the order (from top to bottom) in which the variables can be calculated as functions of the variables above them. Boxes spanning different columns indicate that the same equation is used for different regimes. Variables in shaded boxes are implicitly defined by the roots of polynomial which is solved by a Newton algorithm, whereas variables in unshaded boxes are defined explicitly. The annotation on the left indicates the subset of the governing equations that is used to obtain the respective variables. All equations are listed in appendix D.3.2.

It is not necessary to solve all governing equations simultaneously. First the equations towards the Gulf of Aden (8.23, 8.26, 8.29) can be solved to give:

$$q_1^2 = \frac{8B_1^3 b_g}{27r^2} \quad \text{(see D.3.2 d136)} \tag{8.45}$$

$$h_{1g} = \frac{2B_1}{3rd_g} \quad \text{(see D.3.2 d138)} \tag{8.46}$$

$$h_{0g} = \frac{q_1^2}{2sd_g^3 b_g^2 h_{1g}^2} - \frac{B_0}{sd_g} \quad \text{(see D.3.2 d143)} \tag{8.47}$$

Now the set of equations for the Red Sea (8.21,8.24,8.27) give:

$$h_{1r} = \frac{q_1}{d_r b_r \sqrt{2(B_0 + sd_r h_{0r})}} \quad \text{(see D.3.2 d183)} \tag{8.48}$$

$$h_{2r} = \frac{2b_r^2(2d_r^3 h_{1r}^3 - (B_2 - B_1)d_r^2 h_{r1}^2) + q_1^2}{2(r-1)d_r^3 b_r^2 h_{1r}^2} \quad \text{(see D.3.2 d186)} \tag{8.49}$$

$$q_2^2 = \frac{h_{2r}^2}{h_{1r}^2}(2d_r^2 b_r^2 h_{1r}^2(rd_r h_{1r} - B_1) + q_1^2) \quad \text{(see D.3.2 d188)} \tag{8.50}$$

$$\tag{8.51}$$

At this point, all quantities at the basin entrances are known. Finally, the four sill equations (8.22,8.25,8.28,8.30) have to be solved for q_3, h_{0s}, h_{1s} and h_{2s}. The equations are combined to eliminate q_3 and h_{0s}, giving a coupled set of two equations in h_{1s} and h_{2s}:

$$0 = -s(2d_s^2 b_s^2 B_1 h_{2s}^2 + q_2^2)h_{1s}^2 + 2rsd_s^3 b_s^2 h_{1s}^3 h_{2s}^2 + sq_1^2 h_{2s}^2 \tag{8.52}$$

$$\begin{aligned}
0 = {} & q1^2 \\
& + h_{1s}^2 \cdot (-3d_r^3 h_{2s}^2 q_1^2 r b_r^2 + d_r^3 h_{2s} q_1^2 r b_r^2 + 3d_r^3 h_{2s}^2 q_1^2 b_r^2 \\
& \quad - d_r^3 h_{2s} q_1^2 b_r^2 - 2B_2 d_r^2 h_{2s} q_1^2 b_r^2 - 2B_1 d_r^2 q_1^2 b_r^2) \\
& + h_{1s}^3 \cdot (-6d_r^3 h_{2s} q_1^2 r b_r^2 + 2d_r^3 q_1^2 r b_r^2 + 6d_r^3 h_{2s} q_1^2 b_r^2 \\
& \quad - d_r^3 q_1^2 b_r^2 - 2B_2 d_r^2 q_1^2 b_r^2 - 2B_1 d_r^2 q_1^2 b_r^2) \\
& + h_{1s}^4 (3d_r^3 q_1^2 b_r^2) \\
& + h_{1s}^5 \cdot (3d_r^6 h_{2s}^2 r^2 b_r^4 - d_r^6 h_{2s} r^2 b_r^4 - 3d_r^6 h_{2s}^2 r b_r^4 \\
& \quad + d_r^6 h_{2s} r b_r^4 + 2B_2 d_r^5 h_{2s} r b_r^4 + 6B_1 d_r^5 h_{2s} r b_r^4 \\
& \quad - 6B_1 d_r^5 h_{2s} b_r^4 + 2B_1 d_r^5 b_r^4 + 4B_1 B_2 d_r^4 b_r^4 + 4B_1^2 d_r^4 b_r^4) \\
& + h_{1s}^6 \cdot (-3d_r^6 h_{2s} r^2 b_r^4 + 3d_r^6 h_{2s} r b_r^4 - 2d_r^6 r b_r^4 \\
& \quad - 4B_2 d_r^5 r b_r^4 - 4B_1 d_r^5 r b_r^4 - 6B_1 d_r^5 b_r^4)
\end{aligned} \tag{8.53}$$

$$+h_{1s}^7 \cdot (6d_r^6 r b_r^4)$$

This set of equations cannot be solved analytically, but is accessible to a two-dimensional Newton algorithm. With h_{1s} and h_{2s} known, h_{0s} and q_3 can be calculated:

$$h_{0s} = \frac{q_1^2}{2sd_s^3 b_s^2 h_{1s}^2} - \frac{B_0}{sd_s} \quad \text{(see D.3.2 d246)} \tag{8.54}$$

$$q_3^2 = \frac{(h_{2s} + h_{1s} - 1)^3}{rdbh_{1s}^3 h_{2S}^3 - h_{1s}^3 q_2^2 - h_{2S}^3 q_1^2} \cdot \tag{8.55}$$
$$\cdot \; (r^2 d_s^6 b_s^4 h_{1s}^3 h_{2s}^3 - r d_s^6 b_s^4 h_{1s}^3 h_{2s}^3 - r d_s^3 b_s^2 h_{2s}^2 q_1^2 + d_s^3 b_s^2 h_{1s}^3 q_2^2 + d_s^3 b_s^2 h_{2s}^3 q_1^2 - q_1^2 q_2^2)$$
(see D.3.2 d247)

This solution method is depicted graphically in the second column in figure 8.8.

Flow type $[-3, 3]$. This flow type is a limiting case for $[1, 3]$ with an additional control at the Red Sea, and – like $[1, 3]$ – with surface inflow. As the regime at the Red Sea is -3 and therefore has two supercritical modes, the Bernoulli potential of the lower interface B_2 is not determined by the reservoir conditions, but this additional variable can be solved for as there is the additional control condition at the Red Sea (8.29). The solution method for this type is summarised in the first column in figure 8.8, and the explicit equations given in appendix D.3.2.

Flow type $[2, 3]$. This flow type has one control at the sill and one in the Red Sea, but the control condition in the Gulf of Aden (8.31) may not be used. As the regime towards both reservoirs has one subcritical mode, all Bernoulli potentials are determined by the boundary conditions. For this flow type, the surface flow can be in both directions. As the surface boundary conditions depend on the direction of the flow (see section 8.5.2), the solution method for surface inflow is different than for surface outflow. The two solution methods are shown in the third and fourth column of figure 8.8.

Flow type $[2, -2]$. This flow type is a limiting case of $[2, 3]$ with one additional control at the Gulf of Aden. With two supercritical modes towards the Gulf of Aden (regime -2), the Bernoulli potential B_1 is not determined from the boundary conditions but can be calculated from the full set of equations following the method outlined in the

last two columns of figure 8.8. Again separate methods have to be used for inflow and outflow.

8.5.4 The selection of the correct type

Criteria are needed to decide which flow type is correct for a given set of boundary conditions, so that the correct solution method can be used. This has also been identified as an important problem by Lane-Serff et al. (2000). For the problem presented here, continuity arguments simplify the problem considerably. When the boundary conditions change, the solution may change continuously within one flow type, or the solution may switch to a different flow type. However, only a limited number of transitions are possible: Flow type $[-3,3]$, e. g., cannot be transformed into $[2,-2]$ without going through $[2,3]$. The possible transitions can easily be seen from figure 8.7, and the different flow types can only change along the sequence $[1,3] \leftrightarrow [-3,3] \leftrightarrow [2,3] \leftrightarrow [2,-2]$.

- In the transitions $[1,3] \leftrightarrow [-3,3]$, one additional control (dis-)appears, as $[1,3]$ has two controls (at the sill and the Gulf of Aden), whereas $[-3,3]$ has three controls. In $[-3,3]$ the control condition at the Red Sea (8.29) is identically 0, and for continuity it also has to approach 0 from $[1,3]$. Therefore the control condition is calculated from the values obtained by the solution method for type $[1,3]$, and the switch from $[1,3]$ to $[-3,3]$ can easily be found when it approaches 0. As can be seen in the h_1-h_2-plot (figure 8.7), this transition occurs when the middle layer in the Red Sea becomes thinner.

- For the transition $[2,3] \leftrightarrow [2,-2]$ the same argument applies with respect to the control condition in the Gulf of Aden (8.31). This transition occurs when the interface in the Gulf of Aden becomes very shallow.

- In the transition $[-3,3] \rightarrow [2,3]$, the control at the Gulf of Aden disappears. In channel geometries where the position of the control may vary, there are intermediate flow regimes: First the control towards the Gulf of Aden moves towards the Strait, eventually forming a second order control at the sill, which the splits into one control at the sill and one control that moves towards the Red Sea. In the simple channel geometry used here, controls can only be at the sill or channel

entrances. However, the transition can still be identified by a second order control at the sill. A second order control, i. e. two coincident controls, can be found by calculating the saddle points of the control condition (see also figure 8.5). This leads to the condition

$$0 = \frac{F_1^2}{h_1}(F_2^2 - 1 + r) + \frac{F_1^2 - r}{h_2}(F_1^2 - 1) \tag{8.56}$$

This transition can occur when the interfaces in the Red Sea rise or sink.

These conditions give sufficient criteria for the transition between the different flow types.

8.6 Conclusions and future work

The work presented here forms the basis for the strait submodel which can represent all relevant 3-layer flow types and improves the rigid lid model used by Smeed (2000) by including a free surface. Although some insight into the different flow types can be gained from the strait submodel alone, the results are not significantly different from the rigid lid results obtained by Smeed (2000): Without a corresponding box model, the free surface has to be set to values that lead to a specified net exchange, so that the model is essentially equivalent to the rigid lid model.

In future, this strait submodel will be connected to a box model similar to the HYCOBOX model described in chapter 3, but with an additional intermediate layer between the upper and the lower layer, connected to the middle layer in the strait. Its volume can approach 0 to model the 2-layer winter exchange as a limiting case of the 3-layer situation. As there is no outflow from the intermediate layer trough the strait, it loses water to the upper and lower layer through mixing and diffusion.

This model can be used for a variety of problems. Of immediate interest are the following:

- Can the observed cycle of the sea level in the Red Sea (Cromwell and Smeed 1998) be attributed to the internal dynamics alone, i. e. is the reversal of the surface flow driven by the sea level difference or directly by the wind? The model can be used to impose the sea level cycle in the Gulf of Aden and obtain the resulting sea level cycle in the Red Sea, which can be compared to observations.

- How much is the spreading of the tongue of GAIW in the Red Sea influenced by mixing between the layers? The model can be used to investigate different values of diffusion and mixing between the layers. A comparison with the observed size of the GAIW tongue leads to better understanding of the mixing processes.

- Under which circumstances is the present 3-layer/2-layer seasonal cycle possible? If the upwelling in the Gulf of Aden is weaker, does the seasonal cycle revert to a simple 2-layer flow? Has this occurred for situations in the past? This is particularly important, as the total exchange in the combined 3-layer/2-layer cycle is considerably less than in a simple 2-layer flow, with implications for the water properties of the Red Sea.

Chapter 9

Summary and conclusions

In this thesis, a range of studies is presented that were performed with the HYCOBOX model, a 3-box model of the Mediterranean Sea (or similar marginal basins) with a hydraulically controlled Strait of Gibraltar. Box models have the inherent problem that they are very coarse representations of complex systems in nature, and therefore cannot compete with General Circulation Models (GCMs) when precise numerical predictions are needed. However, the complexity of GCM studies also makes it difficult or impossible to interpret the results – one might say that they *describe* reality very well, but are less adequate for *explaining* it. Process studies using simpler models, on the other hand, focus on physical mechanisms. They can therefore give insight into fundamental constraints and overall behaviour of the system, but they also often yield surprising results and lead to new questions. The model presented here is no exception and offers both useful and robust "rules of thumb" and surprising new types of dynamical behaviour.

Firstly, the work presented here has produced some simple correlations that can be helpful for the investigation of similar systems. For example, section 3.5 discusses how realistic strait cross-sections can be approximated by simple rectangular cross-sections. This is useful for GCM experiments, where the representation of sea straits is notoriously difficult. For the geometry of Gibraltar, this method leads to a representation of the triangular strait by a rectangular strait with a sill depth of 208 m, considerably shallower than the true depth of 284 m.

More relevant for a wide range of applications, in the interpretation both of GCM

experiments and of observations in nature, is the SQE equation (5.13) in section 5.1. For a change in the freshwater budget, i. e. changes in evaporative losses or changes in freshwater input through precipitation or river runoff, this equation gives the resulting change in strait transport and basin salinity. The SQE equation is particularly useful as it is based on quite fundamental constraints and is therefore not sensitive to details of the basin processes. This is also confirmed by the set of experiments listed in table 5.3 and 5.4, which cover fundamentally different water formation processes.

A related result is the observation that a change in evaporative fluxes not only changes the salinity of the basin, but as a secondary effect also the temperature: For every 1 psu increase in the salinity of the bottom layer, its temperature increases by 0.7 °C (assuming that the heat budget remains unchanged). Similarly, a change in atmospheric heat loss with unchanged water budget primarily affects the temperature, but as a secondary effect the salinity also changes by about 0.06 psu for every 1 °C. These results are used to investigate the causes of observed changes in Mediterranean water properties in section 5.3, where it is found that the observed increase in temperature and salinity of the Mediterranean in the 20th century is not consistent with known changes in river runoff alone.

Besides these correlations, the study has also lead to challenging new types of behaviour, which may have to be investigated in more detail in future work. At least three situations have been identified in which the feedback between the basin and the strait leads to surprising dynamical behaviour, that has not received much attention by previous researchers. In these situations, the system responds to comparatively small disturbances with a significantly altered circulation for considerable periods on the order of centuries.

Firstly, the experiments in chapter 5 indicate that changing air-sea-fluxes do not always lead to a smooth transition from the old steady state to the new steady state. At least for some types of water formation parameterisations, the transitional period is characterised by a considerable movement of the interface depth: The interface drops when the net evaporation or the heat loss is reduced, and rises when either is increased, returning to almost the initial depth only after more than a century. Although the transitional phase is less visible in other quantities like the strait transport or the basin

average water properties, the change in interface depth is in itself significant, as the interface can be identified with the pycnocline, whose depth has profound influence on the nutrient availability in the photic zone and therefore on the biological productivity of the basin. However, it has not been established sufficiently whether this behaviour is relevant for real past or present situations. It may be possible in future to obtain sufficient observational data to detect this transitional signal in the movement of the pycnocline.

A second type of interesting dynamical behaviour is the reservoir effect discussed in section 6.3, where the effects of the rising sea level since the Last Glacial Maximum (LGM) are investigated. The long reaction time of the properties of the deep and intermediate water masses make the basin more stably stratified in times of comparatively rapid sea level change, providing a possible new mechanism for the collapse of the circulation that has lead to the formation of carbon-rich sediments at the pleistocene-holocene transition. The model allows this effect to be estimated in comparison to other proposed mechanisms, namely the inflow of additional freshwater through the opening of the Black Sea. The reservoir effect is found to be of comparable size. It can therefore be conjectured that it may indeed have played a role in the formation of sapropels in the Mediterranean Sea at the end of the pleistocene. This result also suggests that evidence for reduced circulation at the same time may be found in other marginal basins, as this mechanism is driven only by the global sea level change.

Finally, a challenging new type of complex behaviour is found in chapter 7, where new feedbacks are introduced into the system through a parameterisation of mixing in the hydraulic jump. It is assumed that a fraction of the inflowing water is entrained into the outflow, thus reducing the effective exchange with the basin. The entrainment rate depends on the height of the hydraulic jump. With these modifications, a new meta-stable state is possible. The system can move to this meta-stable state after a comparatively small perturbation, and the circulation in the basin may collapse for a period of the order of centuries. In other situations, the system can show oscillatory behaviour between a normal circulation and a stagnant basin, where the period of the oscillation is several centuries. This mechanism has not been noticed by previous researchers, and it may be a relevant factor in the explanation of past changes in the

circulation.

However, while this is the most surprising and complex behaviour found in this study, it is also the most speculative contribution to our understanding of the feedback, as fluid dynamical studies give only limited support to significant entrainment of inflowing water into the outflow. On the other hand, as is discussed in section 7.8, it is not entirely unrealistic either. Whether this behaviour is possible in natural systems cannot be established here, but it is shown in section 7.7 that it can occur in General Circulation Models. Therefore, even if it were an unrealistic scenario in nature, it could still help to understand and improve the representation of sea straits in General Circulation Models.

Although the amount of mixing can in principle be easily established from salinity measurements, for the qualitative dynamical behaviour the absolute value of the mixing is less important than the functional relation between mixing and the hydraulic regime in the strait. Therefore, measurements of the mixing are needed for both the submaximal and the maximal regime for a range of interface depths. Obviously the present day Mediterranean is not in the strong mixing/weak circulation regime, so present day observations cannot give much insight into this state. However, some information about the relation between strait regime and mixing can likely be obtained from a detailed analysis of observations of seasonal and tidal changes, where the strait regime may change on shorter timescales.

On a different line of argument, the Alboran Gyres may provide the mixing mechanism proposed here, if it can be shown that the maximal strait regime leads to stronger circulation in the gyres, and that stronger gyre circulation increases the entrainment of surface water into the outflow. Both theoretical studies and observations are needed to clarify these relations, and therefore a more detailed investigation of the Alboran Gyres may give important insights into the dynamics of the whole Mediterranean Sea.

Leaving the Mediterranean, the application of the ideas and results presented here to other marginal basins will be useful. Of foremost interest is the Red Sea with its shallow connection to the Gulf of Aden through the Strait of Bab al Mandab. However, the straightforward application of the HYCOBOX model poses some problems, as the exchange switches from the 2-layer system to a fundamentally different 3-layer exchange

in summer. Chapter 8 discusses the 3-layer case and identifies four different flow types that are relevant in the Red Sea. Previous work by Smeed (2000) on the 3-layer exchange is supplemented by the inclusion of a free surface, and a solution for each of the four flow types is given. This work forms the centrepiece of a future box model of the Red Sea, but considerable work is still necessary. The resulting model will be a useful tool to investigate the mechanisms of this fascinating seasonal cycle and to investigate different conditions in the past.

Appendix A

Symbols and Conventions

A.1 A note on the salinity units

According to the practical salinity scale (PSS), which has been adopted as standard on oceanographic research, salinities should be quoted as unitless numbers, e. g. "a salinity of 38 on the practical salinity scale". However, scientist's *horror vacui* demands that every measurement value is accompanied by a unit, so that the use of "practical salinity units" (psu) has found widespread use. Unitless salinities have more or less died out. In this text, the pragmatic approach was preferred over the fundamentalist, and the psu used as a "unit" for salinity.

In numerical terms, the values on the practical salinity scale are approximately equal to values measured in kg of salt per ton of water, or ‰.

A.2 Symbols used in this text

Quantities that are defined separately in each layer carry subscripts. Arabic numerals (0,1,2,3) refer to the quantities in the strait, capital Roman letters (A, F, U and L) refer to quantities in the basin, and small Roman letters (a, s, b) refer to different points in the strait.

The following symbols are used in the text:

$\tilde{\ }$ nondimensional quantities (only used where it is necessary to distinguish between dimensional and nondimensional quantities)

$\cdot_0$	refers to the sea level in the strait, only used for h_0
$\cdot_1$	quantities of the upper layer in the strait, i. e. the strait inflow
$\cdot_2$	quantities of the lower layer in the strait, i. e. the strait outflow
$\cdot_A$	quantities of the Atlantic (surface water)
$\cdot_F$	quantities of the water formation box F in the basin
$\cdot_U$	quantities of the upper layer box U in the basin
$\cdot_L$	quantities of the lower layer box L in the basin
$\cdot_s$	quantities at the sill
$\cdot_a$	quantities in the strait, at the entrance towards the Atlantic
$\cdot_b$	quantities in the strait, at the entrance towards the Mediterranean basin
α	coefficient for $\frac{\partial \rho}{\partial S}$ in the equation of state for sea water ($\approx 0.766 \frac{\text{kg}}{\text{m}^3\,\text{psu}}$)
α	parameter in the water formation parameterisation
β	coefficient for $-\frac{\partial \rho}{\partial T}$ in the equation of state for sea water ($\approx -0.244 \frac{\text{kg}}{\text{m}^3\,\text{K}}$)
β	parameter in the water formation parameterisation
μ	parameter in the water formation parameterisation
ν	parameter in the water formation parameterisation
ζ	parameter in the water formation parameterisation
η	parameter in the water formation parameterisation
$\tau_{h_{U'}}$	characteristic timescale (e-folding time) for changes in interface depth in the basin
τ_{h_0}	characteristic timescale for changes in sea level
τ_S	characteristic timescale for changes in salinity
τ_T	characteristic timescale for changes in temperature
A	area of the basin
a_{tot}	total cross-sectional area at the sill
a_i	cross-sectional area of layer i at the sill
$c(\cdot)$	dimensionalisation constants
c_{XY}	transport rate from box X to box Y, where X and Y can be F, U or L
D	sill depth
$d(x)$	channel depth
E	entrainment rate

E	evaporation
$E - P$	net evaporation (evaporation minus precipitation and river runoff)
H	total (effective) depth of the basin
H_{Atm}	heat loss to the atmosphere
h_0	sea level (positive values: sea level below reference level)
h_1	thickness of the top layer in the strait
h_2	thickness of the bottom layer (for 2-layer case) or the middle layer (for 3-layer case) in the strait
h_3	thickness of the bottom layer (3-layer case) in the strait
h_{ia}	layer thickness of layer i at the strait entrance towards the Atlantic
h_{ib}	layer thickness of layer i at the strait entrance towards the Mediterranean basin
h_{is}	layer thickness of layer i at the sill
$h_{ib}^{\max}$	basinside interface depth at which the strait regime becomes maximal
h_F	"thickness" of the water formation box F, i. e. its volume divided by the basin area A
h_L	thickness of the lower layer box L, i. e. its volume divided by the basin area A
h_U	"thickness" of the upper layer box U, i. e. its volume divided by the basin area A
$h_{U'}$	"thickness" of the effective upper layer box $U' = U + F$
h_{HJ}	"height" of the hydraulic jump between the strait and the basin
J	Hydraulic functional for the two-layer case
$J^{(3)}$	Hydraulic functional in the three-layer case
$J^{(2)}$	Hydraulic functional for three-layer case with rigid lid
k_{geom}	factor describing the strait geometry
k_{entr}	factor describing the mixing strength for entrainment in the hydraulic jump
Q	net strait exchange, $Q = q_1 + q_2 = \lvert q_1\rvert - \lvert q_2\rvert$
q	total transport in the strait, $q = q_1 - q_2 = \lvert q_1\rvert + \lvert q_2\rvert$
q_i	flow rate in layer i in the strait, $q_i > 0$ for inflow
q_1	upper layer inflow, generally $q_1 > 0$

q_2	lower layer outflow, generally $q_2 < 0$
$q_i^{\max}$	flow rate in layer i for the maximal regime
q_{entr}	entrainment from upper into lower layer in the hydraulic jump
q_i'	effective flow rate into (> 0) or out of (< 0) the basin in layer i
Q	net strait exchange, $Q = q_1 + q_2 = q_1 - \|q_2\|$
W	channel width at the narrows
W_s	channel width at the sill
x	alongchannel coordinate
z	vertical coordinate, measured downwards from the reference level

Appendix B

Equation of state for seawater

The equation of state for seawater

$$\rho(S,T) = 1028.125 - 0.0735T - 0.00469T^2 + (0.802 - 0.002T)(S - 35) \tag{B.1}$$

was used throughout this study, where the temperature is measured in °C, and the salinity in values on the practical salinity scale. Occasionally only the differential relation between salinity and density is needed, represented by the coefficient

$$\beta := \frac{\partial \rho}{\partial S} = 0.766 \, \frac{\text{kg}}{\text{m}^3 \, \text{psu}} \tag{B.2}$$

Similarly, the differential relation between density and temperature is

$$\alpha := -\frac{\partial \rho}{\partial T} = 0.244 \, \frac{\text{kg}}{\text{m}^3 \, ^\circ\text{C}} \tag{B.3}$$

where the numerical values are valid around $T = 18\,^\circ\text{C}$ and $S = 36\,\text{psu}$. Then

$$\Delta\rho = -\alpha\Delta T + \beta\Delta S \tag{B.4}$$

Appendix C

Parameters of HYCOBOX runs

In this Appendix, the parameters for all HYCOBOX runs used in this study are listed.

C.1 General

The following values were the default values used in every experiment, unless stated otherwise in the description of the individual experiments. In the tables for each experiment below, parameters that differ from the default values are marked with an asterisk (*).

Parameter	Symbol	Value
Sill depth	D	284 m
Width of Narrows	W	12 km
Basin Area	A	2.4×10^{12} m^2
Effective Basin Depth	H	1000 m
Salinity of the Atlantic inflow	S_1	36 psu
Temperature of the Atlantic inflow	T_1	16 °C
Net Evaporation	$E - P$	75 cm/year
Heat Loss	H_{Atm}	7 W/m^2

For the water formation parameterisations the following abbreviations are used:

Symbol	Description	Parameterisation
(I)	interface only	$c_{FL} = \alpha \cdot (h_U + h_F)$
(D)	density	$c_{FL} = \begin{cases} \mu \cdot (h_1 + h_F) \cdot (\rho_F - \rho_L) & \text{for } \rho_F > \rho_L \\ 0 & \text{for } \rho_F \leq \rho_L \end{cases}$
(E)	evaporation	$c_{FL} = \zeta \cdot (h_1 + h_F) \cdot (E - P)$

The parameters α, μ and ζ are quoted here in two different units. The first form can easily be interpreted, whereas the second form is the form used in the model, where all transports between the boxes are interpreted as "thickness transports" per year. The units and conversion factors (assuming $A = 2.4 \times 10^{12}\,\mathrm{m}^2$) are as follows:

Parameter	physical units	model units	conversion factor
α	m^2/s	$\mathrm{year}^{-1} \cdot A$	$\mathrm{year}^{-1} \cdot A = 7.72 \times 10^4\,\mathrm{m}^2/\mathrm{s}$
μ	$\mathrm{m}^5/(\mathrm{kg\ s})$	$\mathrm{m}^3/(\mathrm{kg\ year}) \cdot A$	$\mathrm{year}^{-1} \cdot A = 7.72 \times 10^4\,\mathrm{m}^2/\mathrm{s}$
ζ	m^{-1}	m^{-1}	

C.2 Individual experiments

The following tables give all the relevant parameters for each experiment in this study. Parameters that have the default value (see C.1) are not listed, parameters for which a different value than the default value was used are marked with an asterisk (*).

Section 4.1.2: Experiments to demonstrate maximal and submaximal situations, shown in figures 4.1, 4.2, 4.3 and 4.4, and further experiments summarised in figure 4.5. The experiments have identical initial external conditions and identical settings for all parameters except the water formation parameter α.

Parameter	Value
Cross section	rectangular
Sea level	constant
Heat Loss (*)	$H_{\text{Atm}} = 0\,\text{W/m}^2$
Water formation parameterisation	(I)
WFO parameter	$\alpha = \begin{cases} 0.12 & \text{submaximal exp.} \\ 0.25 & \text{maximal exp.} \end{cases}$
Basin Mixing	no
Initial interface depth	$h_{U'} = 0.6D = 170\,\text{m}$
Initial lower layer salinity	$S_L = 38\,\text{psu}$
Initial lower layer temperature	$T_L = 16\,^\circ\text{C}$

Section 4.2: Four experiments to demonstrate the typical timescales for different feedback mechanisms. The experiments are shown in figures 4.7, 4.9, 4.11 and 4.12. Each of the experiments was started with the same conditions:

Parameter	Value
Cross section	rectangular
Sea level	constant
Water formation parameterisation	(I), (D), (E)
WFO parameter	see table 5.2
Basin Mixing	no
Initial interface depth	$h_{U'} = 0.268D = 76.1\,\text{m}$
Initial lower layer salinity	$S_L = 37.44\,\text{psu}$
Initial lower layer temperature	$T_L = 13.4\,^\circ\text{C}$

The initial conditions were chosen close to the steady state such that the steady state is reached after less than 10 years, and the model run was run for 20 years ($t = -20$ to $t = 0$) before the following changes was introduced at $t = 0$:

Experiment	figure		steady state value	changed to
Sea level	4.7	$h_0 =$	16 cm	41 cm
Interface depth	4.9	$h_{U'} =$	76.2 m	56.6 m
Salinity	4.11	$S_L =$	37.42 psu	36.90 psu
Temperature	4.12	$T_L =$	13.44 °C	14.4 °C

Section 5.2: 24 experiments, in which the air-sea-flux was changed. Details of the experiments are listed in tables 5.1 and 5.2.

Parameter	Value
Cross-section	simplified Mediterranean

Two initial states were used, one in the maximal regime, and one in the submaximal regime. These are characterised as follows:

Maximal regime	
Steady state	$E - P = 75\,\text{cm/year} \cdot A = 0.058\,\text{Sv}$
	$H_{\text{Atm}} = 7\,\text{W/m}^2 \cdot A = 17 \times 10^{12}\,\text{W}$
	$h_{U'} = 60\,\text{m}$
	$q_2 = 1.057\,\text{Sv}$
	$\Delta S = 1.97\,\text{psu}$
	$\Delta T = -3.49\,^\circ\text{C}$
Water form. param.	$\alpha = 1.77 \times 10^4\,\text{m}^2/\text{s} = 0.229\,\text{year}^{-1} \cdot A$
	$\mu = 4.28 \times 10^4\,\text{m}^5\,\text{kg}^{-1}\,\text{s}^{-1} = 0.555\,\text{m}^3\,\text{kg}^{-1}\,\text{year}^{-1} \cdot A$
	$\zeta = 0.305\,\text{m}^{-1}$

Submaximal regime	
Steady state	$E - P = 75\,\text{cm/year} \cdot A = 0.058\,\text{Sv}$
	$H_{\text{Atm}} = 7\,\text{W/m}^2 \cdot A = 17 \times 10^{12}\,\text{W}$
	$h_{U'} = 100\,\text{m}$
	$q_2 = 0.989\,\text{Sv}$
	$\Delta S = 2.11\,\text{psu}$
	$\Delta T = -3.68\,^\circ\text{C}$
Water form. param.	$\alpha = 1.14 \times 10^4\,\text{m}^2/\text{s} = 0.128\,\text{year}^{-1} \cdot A$
	$\mu = 2.14 \times 10^4\,\text{m}^5\,\text{kg}^{-1}\,\text{s}^{-1} = 0.278\,\text{m}^3\,\text{kg}^{-1}\,\text{year}^{-1} \cdot A$
	$\zeta = 0.171\,\text{m}^{-1}$

Section 7.3: Experiments including entrainment in the hydraulic jump. The results are summarised in table 7.2.

Parameter	Value
Water formation parameterisation	(D)
Water formation parameter	$\mu = 3.1 \times 10^4\,\text{m}^5\,\text{kg}^{-1}\,\text{s}^{-1}$
	$= 0.4\,\text{m}^3\,\text{kg}^{-1}\,\text{year}^{-1} \cdot A$
Basin Mixing	yes
hydraulic jump entrainment	yes
entrainment parameter	$k_{\text{entr}} = 0;\ 0.2;\ 0.3;\ 0.35;\ 0.4;\ 0.5$

The steady state is characterised by the following values:

Variable	Value
Interface depth	$h_{U'} = 81\,\text{m}$
Outflow	$q_2 = 1.051\,\text{Sv}$
Salinity difference (Strait)	$\Delta S = 1.97\,\text{psu}$
Temperature difference (Strait)	$\Delta T = -3.47\,^\circ\text{C}$

Appendix D

Programme listings

D.1 HYCOBOX

HYCOBOX was programmed using the Modelmaker package by Cherwell Scientific Computing Ltd., Version 3.0.2. The Modelmaker software package is specifically designed to simplify the programming of box models and process studies which do not need much computing power.

The model is designed on a graphical user interface which displays the connection between the different variables. The figures on the following pages give the graphical representation of the model. The first figure on page 230 gives the overall design, followed by detailed views of the different sub-models.

The equations that define each of the model variables are listed in pages 240 to 249.

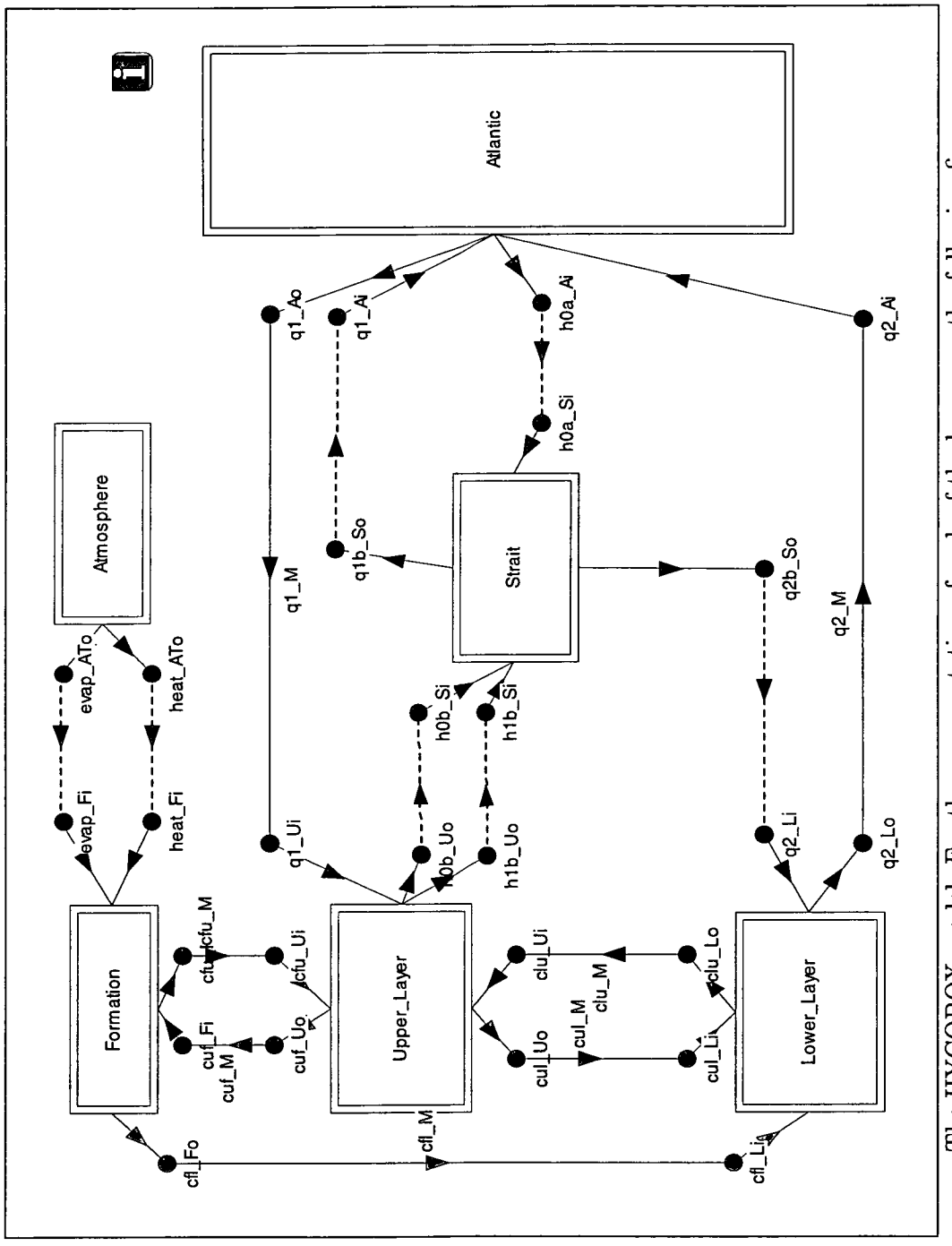

The HYCOBOX model. For the representation of each of the boxes see the following figures.

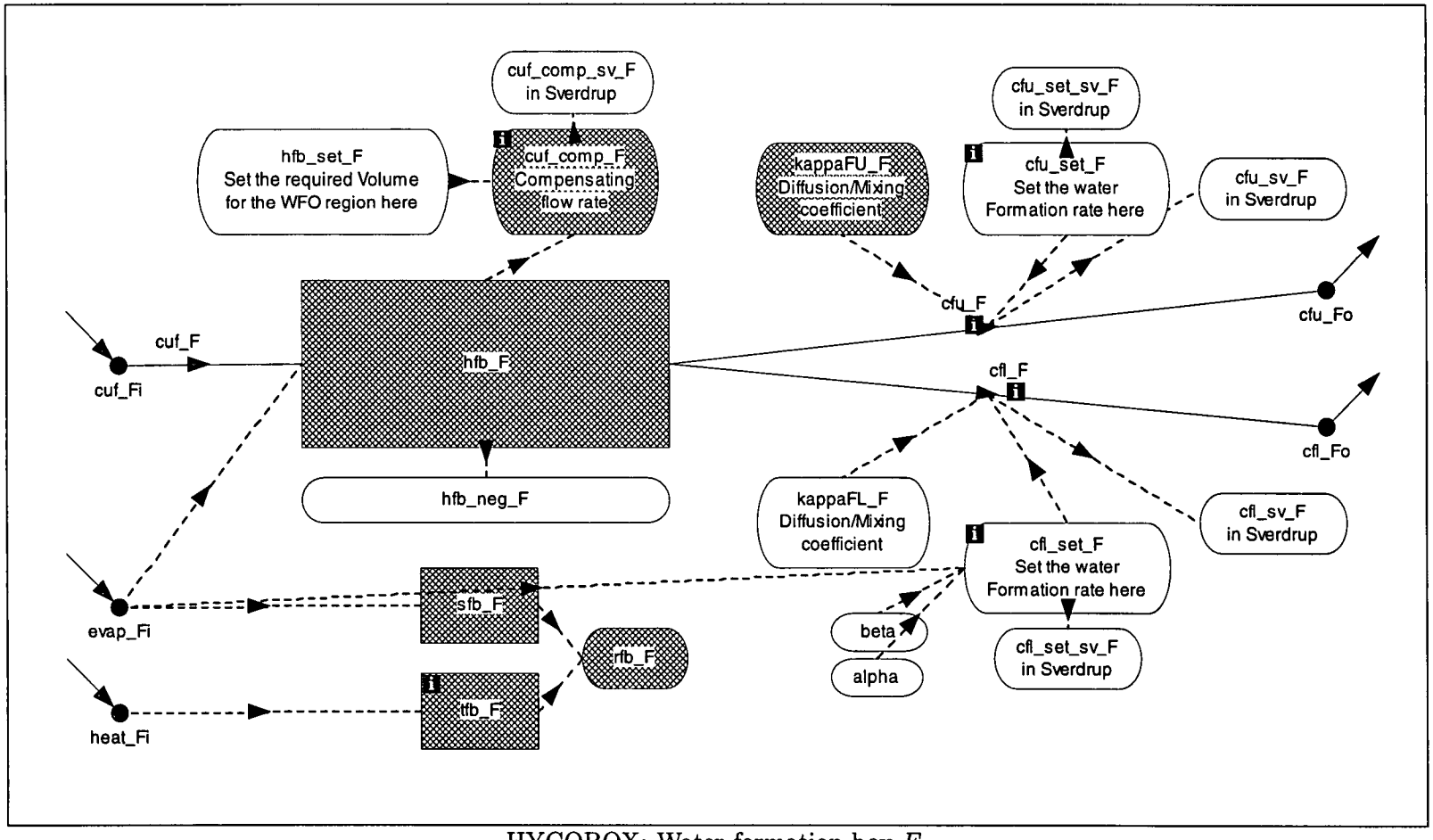

HYCOBOX: Water formation box F.

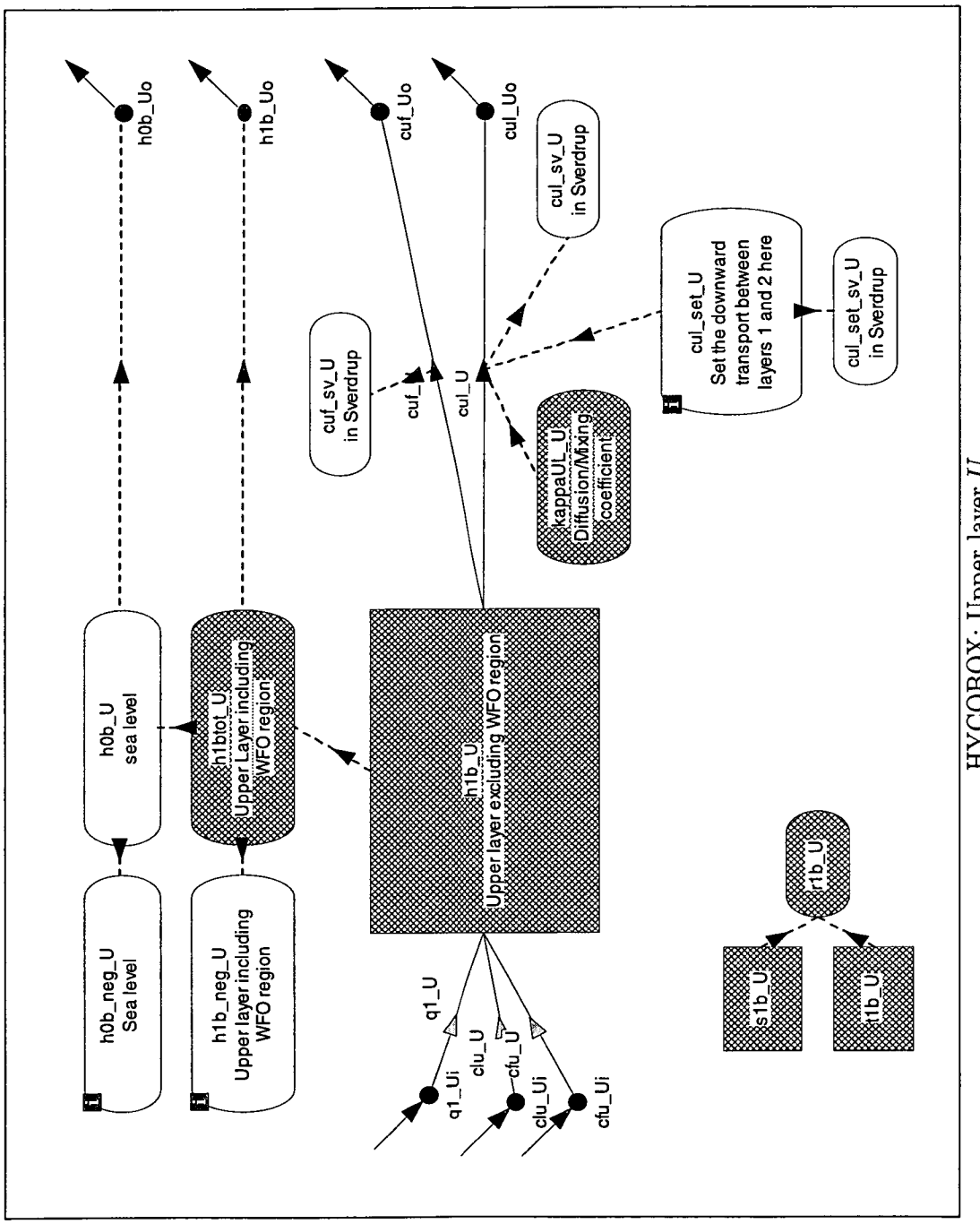

HYCOBOX: Upper layer U.

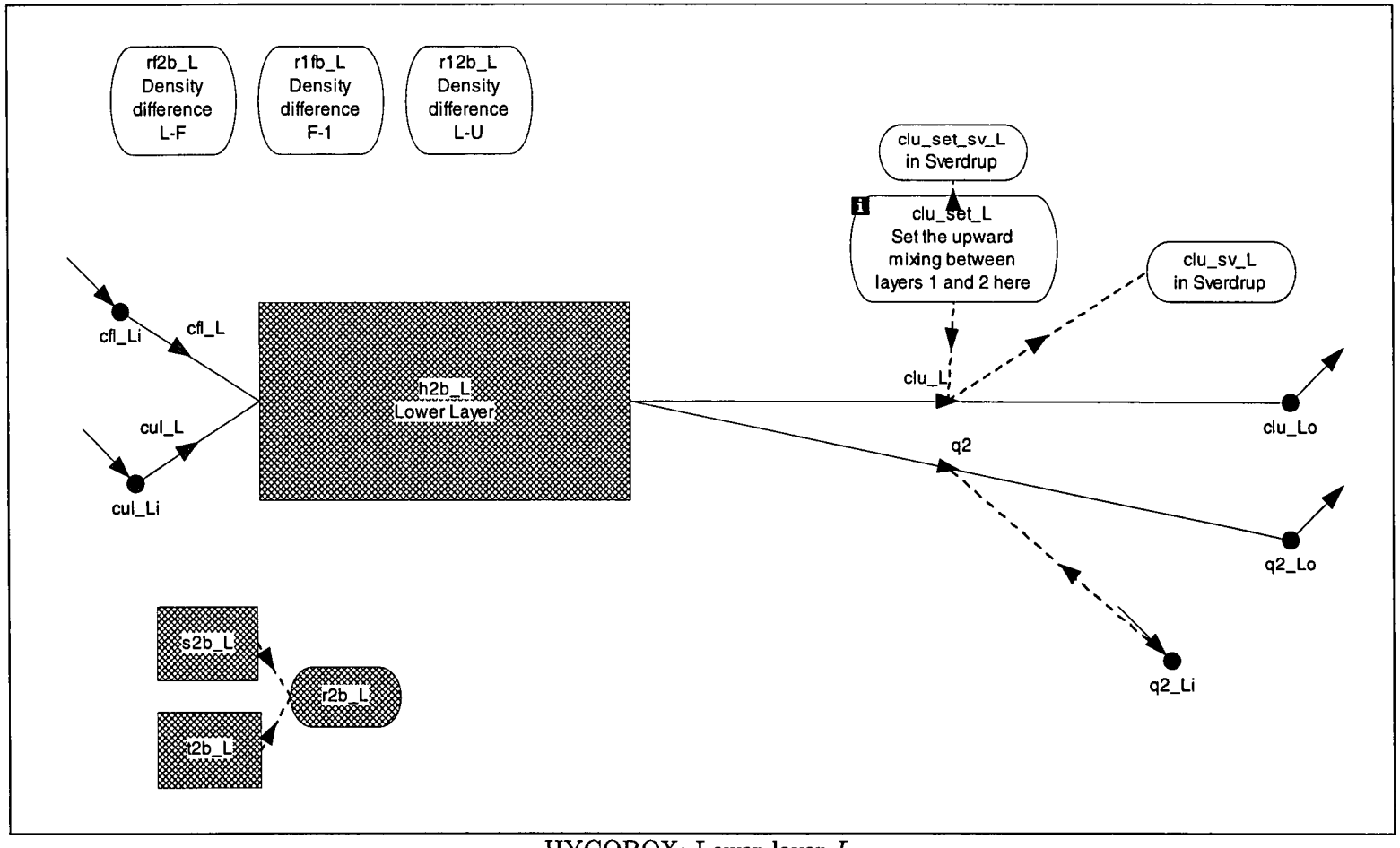

HYCOBOX: Lower layer L.

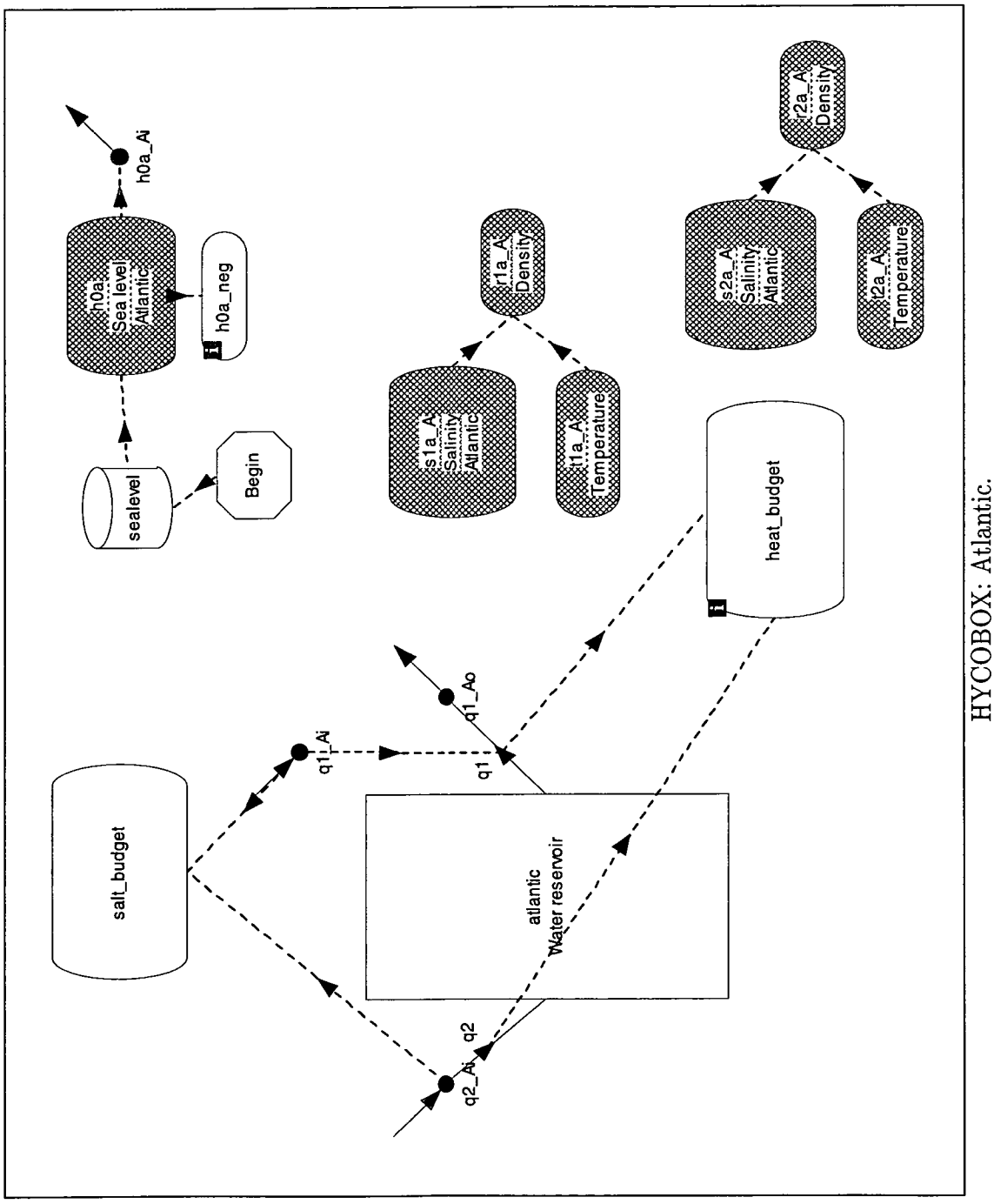

HYCOBOX: Atlantic.

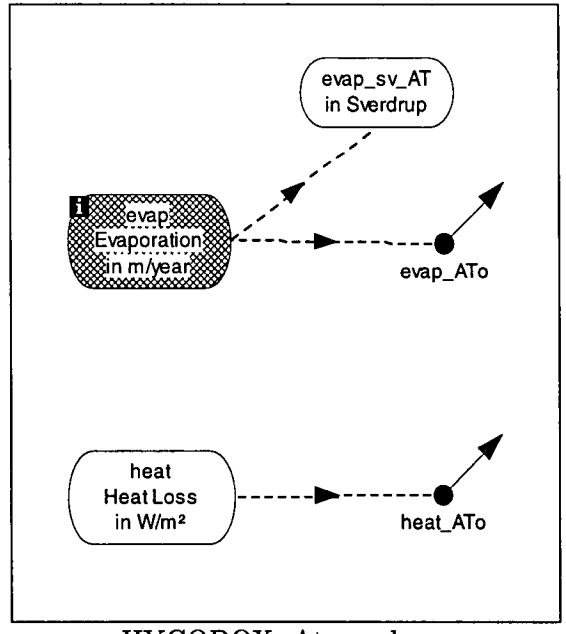

HYCOBOX: Atmosphere.

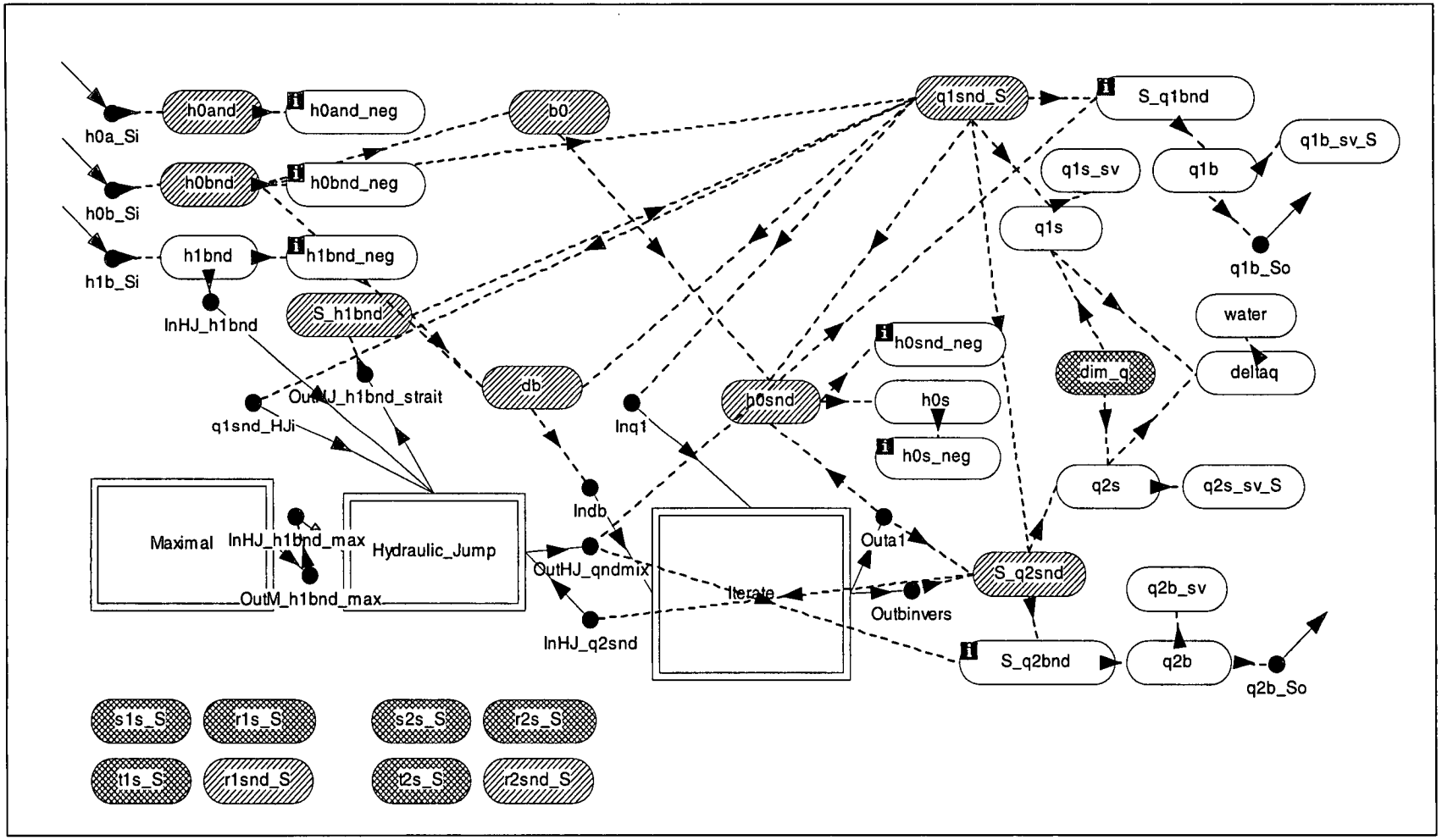

HYCOBOX: The Strait equations. The sub-box "Iterate" contains the the Newton-Raphson iteration (3.10). The sub-box "Maximal" calculates the maximal solution, and the sub-box "Hydraulic Jump" connects the interface in the basin with the interface in the strait according to the present strait regime.

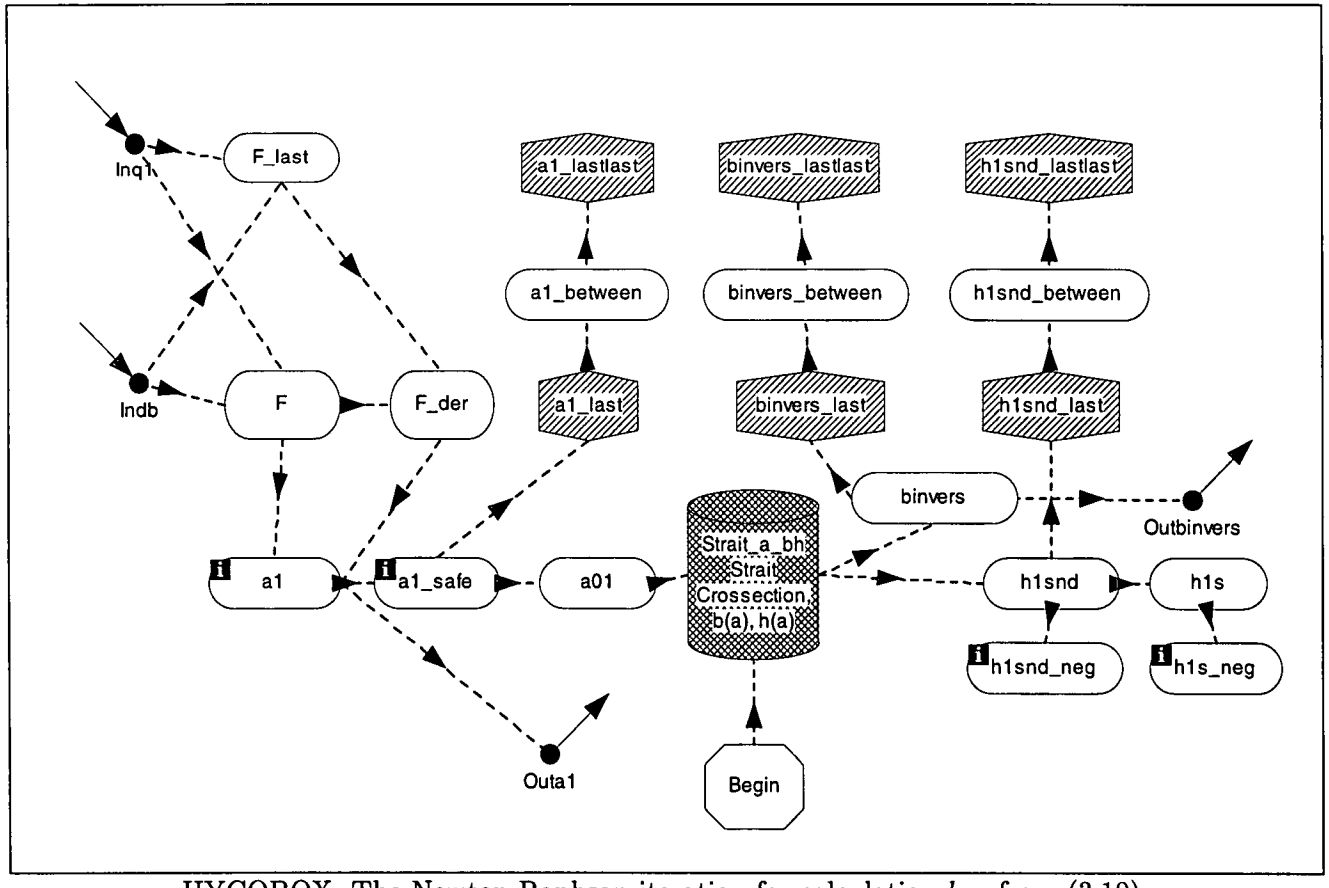

HYCOBOX: The Newton-Raphson iteration for calculation h_{1h} from (3.10).

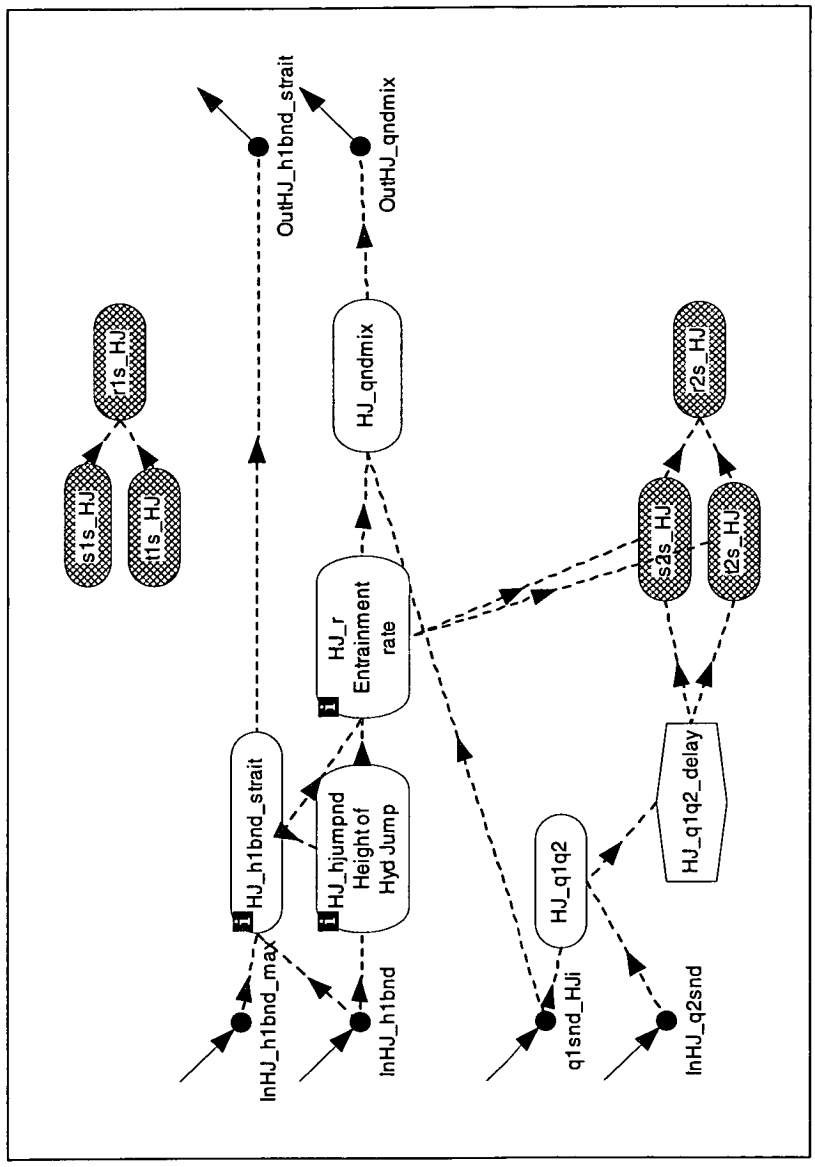

HYCOBOX: Hydraulic Jump.

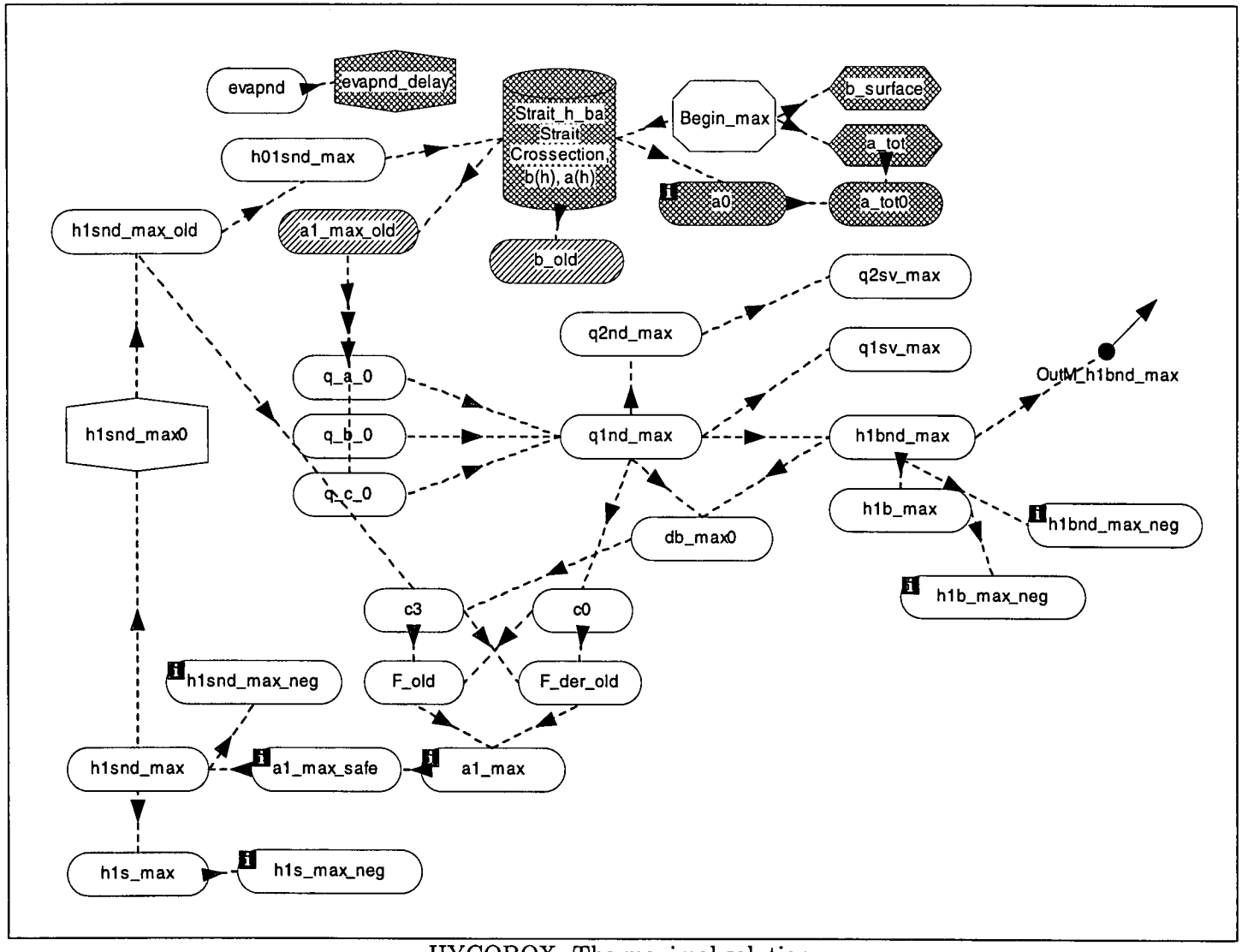

HYCOBOX: The maximal solution.

```
t                                   -100            0
Main
  alpha_ave                         0.4             0
    conversion coefficient in 1/year
  alpha_seas_amp                    0               0
  alpha_seas_phase                  0               0
  area                              2400000000000   0
    Area Basin
  Atlantic
    atlantic Unconditional
      Water reservoir
        datlantic/dt = -q1+q2
        Initial Value = 0.0
    Begin Active Reset
        Non-periodic triggers at:
          start
        Actions:
          GetFileName("Please enter data file containing sea level data", "Data file", sealevel);
    h0a Unconditional Universal
      Sea level Atlantic
        h0a = h0ext
    h0a_neg Unconditional
        Sea level in the Atlantic
          h0a_neg = -h0a
    heat_budget Unconditional
          heat_budget = (t1a_A*q1-tfb_F*evap*area-t2s_S*q2)*r_0*c_heat/(secyear*area)
    sealevel Sealevel.dat
        t Control
        h0ext Controlled by: t
            Linear interpolation
    q1 Unconditional
      Flow from atlantic to q1_a
        q1 = q1_Ai
    q2 Unconditional
      Flow from q2_a to atlantic
        q2 = q2_Ai
    r1a_A Unconditional Universal
      Density
        r1a_A = 1028.125-0.0735*t1a_A-0.00469*t1a_A^2+(0.802-0.002*t1a_A)*(s1a_A-35)
    r2a_A Unconditional Universal
      Density
        r2a_A = 1028.125-0.0735*t2a_A-0.00469*t2a_A^2+(0.802-0.002*t2a_A)*(s2a_A-35)
    s1a_A Unconditional Universal
      Salinity Atlantic
        s1a_A = s1a_ini
    s2a_A Unconditional Universal
      Salinity Atlantic
        s2a_A = s2b_ini
    salt_budget Unconditional
        salt_budget = (q1_Ai*s1a_A-q2_Ai*s2s_S)/secyear
    t1a_A Unconditional Universal
      Temperature
        t1a_A = t1a_ini+t1a_seas_amp*(cos(2*3.1415*(t-t1a_seas_phase)))
    t2a_A Unconditional Universal
      Temperature
        t2a_A = t1a_ini
  Atmosphere
    evap Conditional Universal
        Evaporation in m/year
          evap =
              evap_increase*evap_ave+evap_seas_amp*(cos(2*3.1415*(t-evap_seas_phase))) for
            t>evap_increase_time and t<evap_increase_time+evap_increase_period
              evap_ave+evap_seas_amp*(cos(2*3.1415*(t-evap_seas_phase))) by default
    evap_sv_AT Unconditional
      in Sverdrup
        evap_sv_AT = evap*area/secyear/1E6
    heat Conditional
      Heat Loss in W/m²
        heat =
            heat_ave for t<0
            heat_increase*(heat_ave+heat_seas_amp*(cos(2*3.1415*(t-heat_seas_phase)))) for
          t>heat_increase_time and t<heat_increase_time+heat_increase_period
```

heat_ave+heat_seas_amp*(cos(2*3.1415*(t-heat_seas_phase))) by default
beta_ave 0 0
conversion coefficient
beta_seas_amp 0 0
beta_seas_phase 0 0
c_heat 4200 0
Specific heat capacity of water in J/kg°C
cfl_M Unconditional
Flow from cfl_Fo to cfl_Li
cfl_M = cfl_Fo
cfu_M Unconditional
Flow from cfu_Fo to cfu_Ui
cfu_M = cfu_Fo
clu_M Unconditional
Flow from clu_Lo to clu_Ui
clu_M = clu_Lo
cuf_M Unconditional
Flow from cuf_Uo to cuf_Fi
cuf_M = cuf_Uo
cul_M Unconditional
Flow from c_u to cul_Li
cul_M = cul_Uo
diffdistFL 10 0
Typical diffusion distance between F and L
diffdistFU 20 0
Typical diffusion distance between F and U
diffdistUL 1000 0
Typical diffusion distance between U and L
ds 284 0
Depth Strait
evap_ave 0.75 0
Average evaporation in meter/year
evap_increase 1 0
Increase in evoparation at evap_increase_time
evap_increase_period 10 0
Period over which the evaporation increases
evap_increase_time 500 0
Time when evaporation changes
evap_seas_amp 0 0
Seasonal amplitude of evaporation
evap_seas_phase 0.5 0
Seasonal phase of evaporation (0: Winter maximum)
Formation
alpha Unconditional
alpha = alpha_ave+alpha_seas_amp*sin(6.2830*(t-alpha_seas_phase))
beta Unconditional
beta = beta_ave+beta_seas_amp*sin(6.2830*(t-beta_seas_phase))
cfl_F Conditional
Flow from hfb_F to cfl_Fo
cfl_F =
cfl_set_F for switch_waterformation=0
cfl_set_F for switch_waterformation=1
0 for switch_waterformation=2
cfl_set_F for switch_waterformation=3
cfl_set_F+kappaFL_F/diffdistFL*secyear by default
cfl_set_F Conditional
Set the water Formation rate here
cfl_set_F =
(alpha*h1btot_U+beta)*(rfb_F-r2b_L+rf2diff) for rfb_F-r2b_L>-rf2diff
0 by default
evap_Fi*(alpha*h1btot_U+beta) for 1>0
alpha*h1btot_U+beta by default
cfl_set_sv_F Unconditional
in Sverdrup
cfl_set_sv_F = cfl_set_F*area/secyear/1E6
cfl_sv_F Unconditional
in Sverdrup
cfl_sv_F = cfl_F*area/secyear/1E6
cfu_F Conditional
Flow from hfb_F to cfu_Fo
cfu_F =

```
            cfu_set_F for switch_waterformation=0
            0 for switch_waterformation=1
            kappaFU_F/diffdistFU*secyear for switch_waterformation=2
            0 for switch_waterformation=3
            cfu_set_F+kappaFU_F/diffdistFU*secyear by default
  cfu_set_F Unconditional
    Set the water Formation rate here
      cfu_set_F = 0
  cfu_set_sv_F Unconditional
    in Sverdrup
      cfu_set_sv_F = cfu_set_F*area/secyear/1E6
  cfu_sv_F Unconditional
    in Sverdrup
      cfu_sv_F = cfu_F*area/secyear/1E6
  cuf_comp_F Unconditional Universal
    Compensating flow rate
      cuf_comp_F = (hfb_set_F-hfb_F)/t_comp
  cuf_comp_sv_F Unconditional
    in Sverdrup
      cuf_comp_sv_F = cuf_comp_F*area/secyear/1E6
  cuf_F Unconditional Global
    Flow from cuf_Fi to hfb_F
      cuf_F = cuf_Fi
  hfb_F Unconditional Universal
    dhfb_F/dt = +cuf_F-cfl_F-evap_Fi-cfu_F
    Initial Value = 0.1
  hfb_neg_F Unconditional
    hfb_neg_F = -hfb_F
  hfb_set_F Unconditional
    Set the required Volume for the WFO region here
      hfb_set_F = 0.3*h1b_U
  kappaFL_F Conditional
    Diffusion/Mixing coefficient
      kappaFL_F =
        kappaFL_conv for rfb_F>r2b_L
        kappaFL_back by default
  kappaFU_F Conditional Universal
    Diffusion/Mixing coefficient
      kappaFU_F =
        kappaFU_conv for rfb_F>r1b_U
        kappaFU_back by default
  rfb_F Unconditional Universal
    rfb_F = 1028.125-0.0735*tfb_F-0.00469*tfb_F^2+(0.802-0.002*tfb_F)*(sfb_F-35)
  sfb_F Unconditional Universal
    dsfb_F/dt = (s1b_U-sfb_F)*cuf_F/hfb_F+sfb_F*evap_Fi/hfb_F
    Initial Value = s1b_ini
  tfb_F Unconditional Universal
    dtfb_F/dt = (t1b_U-tfb_F)*cuf_F/hfb_F-heat_Fi*secyear/(c_heat*r_0*hfb_F)
    Initial Value = t1b_ini
heat_ave                7                0
  Average heat loss in W/m² over the basin
heat_increase           1                0
  Increase in heat loss at heat_increase_time
heat_increase_period    0                0
  Period over which the heat loss increases
heat_increase_time      500              0
  Time at which the heat loss changes
heat_seas_amp           0                0
  Seasonal amplitude of heat loss
heat_seas_phase         0                0
  Seasonal phase of heat loss (0: Winter maximum)
htotb                   1000             0
  total depth of basin
ini_a1                  0.6              0
  Inital Area for iteration
ini_cluul               14               0
  Transport between 1 and 2
ini_h0b                 0.1              0
  initial sealevel in basin
ini_h0snd               0.02             0
  initial sealevel in strait
ini_h1bnd               0.3              0
```

```
    initial thickness of top layer in basin
  ini_h1snd                    0.5                  0
  kappaFL_back                 0                    0
    Diffusion coefficient between F and L in m²/s
  kappaFL_conv                 0.001                0
    Diffusion coefficient between F and L in m²/s during convection
  kappaFU_back                 0.0001               0
    Diffusion coefficient between F and U in m²/s
  kappaFU_conv                 0.1                  0
    Diffusion coefficient between F and U in m²/s during convection
  kappaUL_back                 0.0001               0
    Diffusion coefficient between U and L in m²/s
  kappaUL_conv                 0.1                  0
    Diffusion coefficient between U and L in m²/s during convection
Lower_Layer
  cfl_L Unconditional Global
    Flow from cfl_Li to h2b_L
      cfl_L = cfl_Li
  clu_L Conditional
    Flow from h2b_L to clu_Lo
      clu_L =
          clu_set_L for switch_waterformation=0
          0 for switch_waterformation=1
          kappaUL_U/diffdistUL*secyear for switch_waterformation=3
          kappaUL_U/diffdistUL*secyear for switch_waterformation=2
          clu_set_L+kappaUL_U/diffdistUL*secyear by default
  clu_set_L Unconditional
      Set the upward mixing between layers 1 and 2 here
        clu_set_L = ini_cluul
  clu_set_sv_L Unconditional
    in Sverdrup
      clu_set_sv_L = clu_set_L*area/secyear/1E6
  clu_sv_L Unconditional
    in Sverdrup
      clu_sv_L = clu_L*area/secyear/1E6
  cul_L Unconditional Global
    Flow from cul_Li to h2b_L
      cul_L = cul_Li
  h2b_L Unconditional Universal
    Lower Layer
      dh2b_L/dt = +cul_L-q2/area+cfl_L-clu_L
      Initial Value = htotb-ini_h1bnd*ds-ini_h0b
  q2 Unconditional
    Flow from h2b to q2_l
      q2 = q2_Li
  r12b_L Unconditional
    Density difference L-U
      r12b_L = r2b_L-r1b_U
  r1fb_L Unconditional
    Density difference F-1
      r1fb_L = rfb_F-r1b_U
  r2b_L Unconditional Universal
      r2b_L = 1028.125-0.0735*t2b_L-0.00469*t2b_L^2+(0.802-0.002*t2b_L)*(s2b_L-35)
  rf2b_L Unconditional
    Density difference L-F
      rf2b_L = r2b_L-rfb_F
  s2b_L Unconditional Universal
      ds2b_L/dt = (s1b_U-s2b_L)*cul_L/h2b_L+(sfb_F-s2b_L)*cfl_L/h2b_L
      Initial Value = s2b_ini
  t2b_L Unconditional Universal
      dt2b_L/dt = (t1b_U-t2b_L)*cul_L/h2b_L+(tfb_F-t2b_L)*cfl_L/h2b_L
      Initial Value = t2b_ini
q1_M Unconditional
  Flow from q1_a to q1_u
    q1_M = q1_Ao
q2_M Unconditional
  Flow from q2_Lo to q2_Ai
    q2_M = q2_Lo
r_0                            1028                 0
rf2diff                        0                    0
  Density difference between F and UL for which WFO sets in
```

```
s1a_ini                    36              0
  Initial Salinity Atlantic Surface
s1b_ini                    36              0
  Initial Sal Upper Layer Basin
s2b_ini                    38              0
  Initial Sal Lower Layer Basin
secyear                    31104000        0
  seconds per year
start                      -100            0
Strait
  b0 Conditional Global
    b0 =
      -(r1snd_S*h0bnd)/(r2snd_S-r1snd_S) for h0and>h0bnd
      -(r1snd_S*h0and)/(r2snd_S-r1snd_S) by default
  db Unconditional Global
    db = (q1snd_S/S_h1bnd)^2/2+S_h1bnd+h0bnd
  deltaq Unconditional
    deltaq = (q1s-q2s)/area
  dim_q Unconditional Universal
    dim_q = ws*sqrt(ds^3*9.81*2*(r2s_S-r1s_S)/(r1s_S+r2s_S))*secyear
  h0and Unconditional Global
    h0and = h0a_Si/ds
  h0and_neg Unconditional
      h0and_neg = -h0and
  h0bnd Unconditional Global
    h0bnd = h0b_Si/ds
  h0bnd_neg Unconditional
    Sea level in Basin
      h0bnd_neg = -h0bnd
  h0s Unconditional
    h0s = h0snd*ds
  h0s_neg Unconditional
    Sea level in the Strait
      h0s_neg = -h0s
  h0snd Unconditional Global
    h0snd = (r2snd_S-r1snd_S)/r1snd_S * ((q1snd_S/Outa1)^2/2-b0)
  h0snd_neg Unconditional
    Sea level in the Strait, nondimensional
      h0snd_neg = -h0snd
  h1bnd Unconditional
    h1bnd = h1b_Si/ds
  h1bnd_neg Unconditional
    Upper layer thickness in the Basin, nondimensional
      h1bnd_neg = -h1bnd
  Hydraulic_Jump
    HJ_h1bnd_strait Unconditional
        HJ_h1bnd_strait = max(lnHJ_h1bnd,lnHJ_h1bnd_max)
    HJ_hjumpnd Unconditional
      Height of Hyd Jump
        HJ_hjumpnd = HJ_h1bnd_strait-lnHJ_h1bnd
    HJ_q1q2 Unconditional
      HJ_q1q2 = q1snd_HJi/lnHJ_q2snd
    HJ_q1q2_delay
      Delay = 0
      Initial Value = 1
      Maximum Delay = 1
    HJ_qndmix Unconditional
      HJ_qndmix = q1snd_HJi*HJ_r
    HJ_r Unconditional
      Entrainment rate
        HJ_r = min(mix_maximum,mix_strength*HJ_hjumpnd/HJ_h1bnd_strait)
    mix_maximum            0.7             0
      Maximal mixing ratio
    mix_strength           0               0
      Proportion of water across HJ height mixed into lower layer
    r1s_HJ Unconditional Universal
      r1s_HJ = 1028.125-0.0735*t1s_HJ-0.00469*t1s_HJ^2+(0.802-0.002*t1s_HJ)*(s1s_HJ-35)
    r2s_HJ Unconditional Universal
      r2s_HJ = 1028.125-0.0735*t2s_HJ-0.00469*t2s_HJ^2+(0.802-0.002*t2s_HJ)*(s2s_HJ-35)
    s1s_HJ Unconditional Universal
      s1s_HJ = s1a_A
    s2s_HJ Unconditional Universal
```

```
        s2s_HJ = s1s_HJ*HJ_r*HJ_q1q2_delay+s2b_L*(1-HJ_r*HJ_q1q2_delay)
    t1s_HJ Unconditional Universal
        t1s_HJ = t1a_A
    t2s_HJ Unconditional Universal
        t2s_HJ = t1s_HJ*HJ_r*HJ_q1q2_delay+t2b_L*(1-HJ_r*HJ_q1q2_delay)
Iterate
    a01 Unconditional
        a01 = a1_safe+a0
    i a1 Conditional
            a1 =
                (a1_last+a_tot0)/2 for F_der<0
                a1_last-F/F_Der by default
    a1_between Unconditional
        a1_between = a1_last
    a1_last Global
        Delay = 0
        Initial Value = ini_a1*a_tot
        Maximum Delay = 1
    a1_lastlast Global
        Delay = 0
        Initial Value = ini_a1*a_tot*0.99
        Maximum Delay = 1
    i a1_safe Conditional
            a1_safe =
                0.5*a_tot0 for a1<0
                0.5*a_tot0 for a1>a_tot0
                a1 by default
    binvers Unconditional
        binvers = 1/Lookup1b
    binvers_between Unconditional
        binvers_between = binvers_last
    binvers_last Global
        Delay = 0
        Initial Value = 1/b_surface
        Maximum Delay = 1
    binvers_lastlast Global
        Delay = 0
        Initial Value = 1/b_surface
        Maximum Delay = 1
    Begin Active Reset
        Non-periodic triggers at:
          start
        Actions:
          GetFileName("Please enter data file containing Strait cross-section", "Data file", Strait_a_bh);
    F Unconditional
        F =
        binvers_last*a1_last^4+(2*h1snd_last+2*h0and-2*Indb-a_tot0*binvers_last)*a1_last^3+a_tot0*Inq
    F_der Unconditional
        F_der = (F-F_last)/(a1_last-a1_lastlast)
    F_last Unconditional
        F_last =
        binvers_lastlast*a1_lastlast^4+(2*h1snd_lastlast+2*h0and-2*Indb-a_tot0*binvers_lastlast)*a1_lastl
    h1s Unconditional
        h1s = h1snd*ds
    i h1s_neg Unconditional
          Upper layer thickness in the Strait
            h1s_neg = -h1s
    h1snd Unconditional
        h1snd = Lookup1h-h0and
    h1snd_between Unconditional
        h1snd_between = h1snd_last
    h1snd_last Global
        Delay = 0
        Initial Value = ini_h1snd
        Maximum Delay = 1
    h1snd_lastlast Global
        Delay = 0
        Initial Value = 1
        Maximum Delay = 1
    i h1snd_neg Unconditional
          Upper layer thickness in the Strait, nondimensional
```

```
        h1snd_neg = -h1snd
    Strait_a_bh strait.dat
      Strait Crossection, b(a), h(a)
        Lookup1h Controlled by: a01 Universal
          Linear interpolation
        Lookup1b Controlled by: a01
          Linear interpolation
        a01 Control
  Maximal
    a_tot Unconditional Universal
      a_tot = 1
    a_tot0 Unconditional Universal
      a_tot0 = a_tot-a0
    i a0 Unconditional Universal
      a0 = lookup(Lookup2a,h0and)
    i a1_max Conditional
      a1_max =
        min(a_tot0,(a1_max_old+a_tot0)/2) for F_der_old<0
        min(a_tot0,a1_max_old-F_old/F_der_old) by default
    a1_max_old Unconditional Global
      a1_max_old = Lookup2a-a0
    i a1_max_safe Conditional
      a1_max_safe =
        0.5*a_tot0 for a1_max<0
        0.5*a_tot0 for a1_max>a_tot0
        a1_max by default
    b_old Unconditional Global
      b_old = Lookup2b
    b_surface Unconditional Universal
      b_surface = 1
    Begin_max Active Reset
      Non-periodic triggers at:
        start
      Actions:
        GetFileName("Please enter data file containing Strait cross-section", "Data file", Strait_h_ba);
        b_surface=lookup(Lookup2b,0);
        a_tot=lookup(Lookup2a,1);
    c0 Unconditional
      c0 = a_tot0*b_old*q1nd_max^2
    c3 Unconditional
      c3 = b_old*(2*h1snd_max_old-2*db_max0)-a_tot0
    db_max0 Unconditional
      db_max0 = (q1nd_max/h1bnd_max)^2/2+h1bnd_max
    evapnd Unconditional
      evapnd = evap*area/dim_q
    evapnd_delay Universal
      Delay = 0
      Initial Value = 0
      Maximum Delay = 1
    F_der_old Unconditional
      F_der_old = 6*a1_max_old^3+3*c3*a1_max_old^2
    F_old Unconditional
      F_old = a1_max_old^4+c3*a1_max_old^3+c0
    h01snd_max Unconditional
      h01snd_max = h1snd_max_old+h0and
    h1b_max Unconditional
      h1b_max = h1bnd_max*ds
    i h1b_max_neg Unconditional
      Upper layer thickness in the Basin for maxinal exchange
        h1b_max_neg = -h1b_max
    h1bnd_max Unconditional
      h1bnd_max = q1nd_max^(2/3)
    i h1bnd_max_neg Unconditional
      Uper layer thickness in the Basin for maxinal exchange, nondimensional
        h1bnd_max_neg = -h1bnd_max
    h1s_max Unconditional
      h1s_max = h1snd_max*ds
    i h1s_max_neg Unconditional
      Upper layer thickness in the Strait for maxinal exchange
        h1s_max_neg = -h1s_max
    h1snd_max Unconditional
      h1snd_max = lookup(Lookup1h,a1_max_safe+a0)-h0and
```

```
h1snd_max_neg Unconditional
    Upper layer thickness in the Strait for maxinal exchange, nondimensional
      h1snd_max_neg = -h1snd_max
h1snd_max_old Unconditional
    h1snd_max_old = h1snd_max0
h1snd_max0
    Delay = 0
    Initial Value = .95
    Maximum Delay = 1
Strait_h_ba strait.dat
  Strait Crossection, b(h), a(h)
    h01snd_max Control
    Lookup2b Controlled by: h01snd_max Global
      Linear interpolation
    Lookup2a Controlled by: h01snd_max Global
      Linear interpolation
q_a_0 Unconditional
    q_a_0 = (a_tot0-a1_max_old)^3+a1_max_old^3
q_b_0 Unconditional
    q_b_0 = -2*evapnd_delay*a1_max_old^3
q_c_0 Unconditional
    q_c_0 = a1_max_old^3*(evapnd_delay^2-(1/b_old)*(a_tot0-a1_max_old)^3)
q1nd_max Unconditional
    q1nd_max = (-q_b_0+sqrt(q_b_0^2-4*q_a_0*q_c_0))/(2*q_a_0)
q1sv_max Unconditional
    q1sv_max = q1nd_max*dim_q/secyear/1E6
q2nd_max Unconditional
    q2nd_max = q1nd_max-evapnd_delay
q2sv_max Unconditional
    q2sv_max = q2nd_max*dim_q/secyear/1E6
q1b Unconditional
  q1b = S_q1bnd*dim_q
q1b_sv_S Unconditional
  q1b_sv_S = q1b/secyear/1E6
q1s Unconditional
  q1s = q1snd_S*dim_q
q1s_sv Unconditional
  q1s_sv = q1s/secyear/1E6
q1snd_S Conditional Global
  q1snd_S =
     -S_h1bnd*sqrt(r1snd_S/(r2snd_S-r1snd_S)*(h0and-h0bnd)) for h0and>h0bnd
     S_h1bnd*sqrt(r1snd_S/(r2snd_S-r1snd_S)*(h0bnd-h0and)) by default
q2b Unconditional
  q2b = S_q2bnd*dim_q
q2b_sv Unconditional
  q2b_sv = q2b/secyear/1E6
q2s Unconditional
  q2s = S_q2snd*dim_q
q2s_sv_S Unconditional
  q2s_sv_S = q2s/secyear/1E6
r1s_S Unconditional Universal
  r1s_S = 1028.125-0.0735*t1s_S-0.00469*t1s_S^2+(0.802-0.002*t1s_S)*(s1s_S-35)
r1snd_S Unconditional Global
  r1snd_S = 2*r1s_S/(r1s_S+r2s_S)
r2s_S Unconditional Universal
  r2s_S = 1028.125-0.0735*t2s_S-0.00469*t2s_S^2+(0.802-0.002*t2s_S)*(s2s_S-35)
r2snd_S Unconditional Global
  r2snd_S = 2*r2s_S/(r1s_S+r2s_S)
S_h1bnd Unconditional Global
  S_h1bnd = OutHJ_h1bnd_strait
S_q1bnd Unconditional
  Flow rate upstream of HJ
    S_q1bnd =-q1snd_S-OutHJ_qndmix
S_q2bnd Unconditional
  Flow rate upstream of HJ
    S_q2bnd = S_q2snd-OutHJ_qndmix
S_q2snd Unconditional Global
  S_q2snd = sqrt(abs((a_tot0-Outa1)^3*(Outbinvers-q1snd_S^2/Outa1^3)))
s1s_S Unconditional Universal
  s1s_S = s1a_A
s2s_S Unconditional Universal
```

```
    s2s_S = s2s_HJ
  t1s_S Unconditional Universal
    t1s_S = t1s_HJ
  t2s_S Unconditional Universal
    t2s_S = t2s_HJ
  water Unconditional
    water = (deltaq*area-evapnd_delay*dim_q)/secyear
switch_waterformation 3 0
  Sets the type of Water Formation Parameterization
t_comp 0.1 0
  Timescale for compensating flow into WFO region in years
t1a_ini 16 0
  Initial Temp Atlantic Surface
t1a_seas_amp 0 0
t1a_seas_phase 0.75 0
t1b_ini 16 0
  Initial Temp Upper Layer Basin
t2b_ini 12.5 0
  Initial Temp Lower Layer Basin
Upper_Layer
  cfu_U Unconditional Global
  Flow from cfu_Ui to h1b_U
    cfu_U = cfu_Ui
  clu_U Unconditional Global
  Flow from clu_Ui to h1b_U
    clu_U = clu_Ui
  cuf_sv_U Unconditional
  in Sverdrup
    cuf_sv_U = cuf_U*area/secyear/1E6
  cuf_U Conditional
  Flow from h1b_U to cuf_Uo
    cuf_U =
        cuf_comp_F for switch_waterformation=0
        cuf_comp_F for switch_waterformation=1
        cuf_comp_F+kappaFU_F/diffdistFU*secyear for switch_waterformation=2
        cuf_comp_F for switch_waterformation=3
        cuf_comp_F+kappaFU_F/diffdistFU*secyear by default
  cul_set_sv_U Unconditional
  in Sverdrup
    cul_set_sv_U = cul_set_U*area/secyear/1E6
  cul_set_U Unconditional
    Set the downward transport between layers 1 and 2 here
      cul_set_U = ini_cluul
  cul_sv_U Unconditional
  in Sverdrup
    cul_sv_U = cul_U*area/secyear/1E6
  cul_U Conditional
  Flow from h1b_U to cul_Uo
    cul_U =
        cul_set_U for switch_waterformation=0
        0 for switch_waterformation=1
        cul_set_U+kappaUL_U/diffdistUL*secyear for switch_waterformation=2
        kappaUL_U/diffdistUL*secyear for switch_waterformation=3
        cul_set_U+kappaUL_U/diffdistUL*secyear by default
  h0b_neg_U Unconditional
    Sea level
      h0b_neg_U = -h0b_U
  h0b_U Unconditional
  sea level
    h0b_U = htotb-h1btot_U-h2b_L
  h1b_neg_U Unconditional
    Upper layer including WFO region
      h1b_neg_U = -h1btot_U
  h1b_U Unconditional Universal
  Upper layer excluding WFO region
    dh1b_U/dt = +q1_U/area-cul_U-cuf_U+clu_U+cfu_U
    Initial Value = ini_h1bnd*ds
  h1btot_U Unconditional Universal
  Upper Layer including WFO region
    h1btot_U = h1b_U+hfb_F
  kappaUL_U Conditional Universal
  Diffusion/Mixing coefficient
```

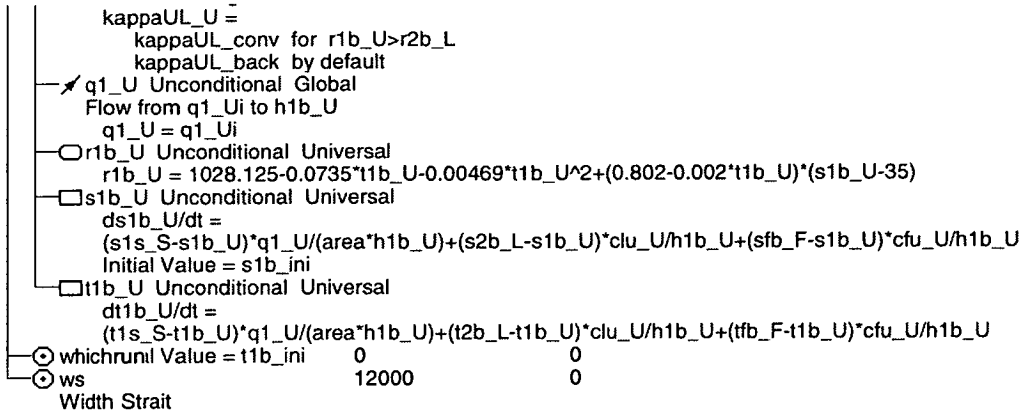
kappaUL_U =
kappaUL_conv for r1b_U>r2b_L
kappaUL_back by default
q1_U Unconditional Global
Flow from q1_Ui to h1b_U
q1_U = q1_Ui
r1b_U Unconditional Universal
r1b_U = 1028.125-0.0735*t1b_U-0.00469*t1b_U^2+(0.802-0.002*t1b_U)*(s1b_U-35)
s1b_U Unconditional Universal
ds1b_U/dt =
(s1s_S-s1b_U)*q1_U/(area*h1b_U)+(s2b_L-s1b_U)*clu_U/h1b_U+(sfb_F-s1b_U)*cfu_U/h1b_U
Initial Value = s1b_ini
t1b_U Unconditional Universal
dt1b_U/dt =
(t1s_S-t1b_U)*q1_U/(area*h1b_U)+(t2b_L-t1b_U)*clu_U/h1b_U+(tfb_F-t1b_U)*cfu_U/h1b_U
whichrunI Value = t1b_ini 0 0
ws 12000 0
Width Strait

D.2 Stability analysis

The Macsyma-code used for the stability analysis in chapter 7.4 is shown on the following pages.

Stephan Matthiesen D:\SM\Beruf\PHD\Hycobox\HJ-mix\HJ-mix-stability.mfe

Mixing in the Hydraulic jump - stability analysis

Find the functions c(h) (water formation rate) and q(h) (strait transport) and plot them. The steady state is the intersection between the curves. For different paramters, there might be multiple equilibria.

Strait transport

Maximal part:

(c1) q(h):=0.1255*(1-k+k*h/0.26)^(3/2)

(d1) $$q(h) := 0.1255\left(1 - k + \frac{k\,h}{0.26}\right)^{3/2}$$

For simplicity, the submaximal part is defined explicitly:

(c2) qsubmax:[0, 0.0546199,0.103109, 0.123455,0.125262,0.125476]

(d2) [0, 0.05462, 0.10311, 0.12345, 0.12526, 0.12548]

(c3) hsubmax:[1,0.547792,0.392114,0.296796,0.272177,0.25973]

(d3) [1, 0.54779, 0.39211, 0.2968, 0.27218, 0.25973]

Water formation rate

First the explicit form

(c4) konstant: mu*sqrt(rl)/(W*sqrt(D*g))

(d4) $$\frac{\mu\sqrt{rl}}{\sqrt{d\,g}\,w}$$

(c5) eq1: cf=h*(rf-rl)/sqrt(rl-r1)*konstant

(d5) $$cf = \frac{h\,\mu\,(rf - rl)\sqrt{rl}}{\sqrt{d\,g}\sqrt{rl - r1}\,w}$$

(c6) define(cf0(h),part(eq1,2))

(d6) $$cf0(h) := \frac{h\,\mu\,(rf - rl)\sqrt{rl}}{\sqrt{d\,g}\sqrt{rl - r1}\,w}$$

On the other hand, rf changes when the water formation changes. We want to remove this effect for the plot. The assumption is made that the density of the water formation layer is in steady state, so that diff(rf,t)=0. Therefore:

(c7) eq2:0=(ru-rf)*cf+fluxes

(d7) $$0 = cf\ (ru - rf) + fluxes$$

Later the flux constant is calculated from the present water formation rate and densities:

(c8) fluxes0:rhs(first(solve(eq2,fluxes))),cf:cf0

(d8) $$cf0\ rf - cf0\ ru$$

Now solve eq2 for rf, and combine it with eq1 to obtain a relation between the water formation rate and the interface depth.

(c9) solve(eq2,rf-ru)

(d9) $$\left[rf - ru = \frac{fluxes}{cf}\right]$$

(c10) subst(solve(eq2,rf),eq1)

(d10) $$cf = \frac{h\,\mu\sqrt{rl}\left(\frac{cf\ ru + fluxes}{cf} - rl\right)}{\sqrt{d\,g}\sqrt{rl - r1}\,w}$$

(c11) fullratsimp(%)

(d11) $$cf = \frac{\sqrt{rl}\,(cf\,h\,\mu\,ru - cf\,h\,\mu\,rl + fluxes\,h\,\mu)}{cf\sqrt{d\,g}\sqrt{rl - r1}\,w}$$

(c12) eq3:multthru(%,denom(rhs(%)))

(d12) $$cf^2\sqrt{d\,g}\sqrt{rl - r1}\,w = \sqrt{rl}\,(cf\,h\,\mu\,ru - cf\,h\,\mu\,rl + fluxes\,h\,\mu)$$

It is easier - and sufficient for the plot - to define h(cf) rather cf(h)

(c13) solution1:solve(eq3,h)

(d13) $$\left[h = \frac{cf^2 \sqrt{d\,g} \sqrt{rf - rl}\, w}{cf\,\mu\sqrt{rl}\,ru - cf\,\mu\,rl^{3/2} + fluxes\,\mu\sqrt{rl}}\right]$$

(c14) define(h(cf),part(solution1,1,2))

(d14) $$h(cf) := \frac{cf^2 \sqrt{d\,g} \sqrt{rf - rl}\, w}{cf\,\mu\sqrt{rl}\,ru - cf\,\mu\,rl^{3/2} + fluxes\,\mu\sqrt{rl}}$$

Plotting the solution

Define the function "makeplot", which takes a number of variables and plots the cf- and q-curves. Also, it calculates values for cf(h) which then can be used for PiCTeX.

(c15)
```
makeplot(mu0,k,cf0,rl,rf,ru,rl):= block(
    numer:true, xmin:0, ymin:0,
    mu:mu0*7.72E4,
    fluxes:fluxes0,
    cfvalues:[
        last(realroots(eval(h(cf)-0.01))),
        last(realroots(eval(h(cf)-0.02))),
        last(realroots(eval(h(cf)-0.04))),
        last(realroots(eval(h(cf)-0.08))),
        last(realroots(eval(h(cf)-0.16))),
        last(realroots(eval(h(cf)-0.32))),
        last(realroots(eval(h(cf)-0.64))),
        last(realroots(eval(h(cf)-1.00)))
    ],
    disp(cfvalues),
    plot(eval(cf0(h)),h,0,1,[2],first),
    paramplot(eval(h(cf)),cf,cf,0,0.15,[1],same),
    graph(hsubmax,qsubmax,[0],same),
    plot(eval(q(h)),h,0,0.26,[0],last)
) $
```

Some constants have to be given numerical values:

(c16) [w,d,g]:[12000,284,10]

(d16) [12000, 284, 10]

Results

Some example situations.

(c17)
```
/* The steady state for k=0.4 and mu=0.4 */
makeplot(0.4,0.4,0.1255,1026.518 ,1029.201,1026.927, 1028.781), xmax:0.4, ymax:0.2
```

[cf = 0.04549, cf = 0.05991, cf = 0.07676, cf = 0.09492, cf = 0.1125, cf = 0.12738, cf = 0.13829, cf = 0.1432]

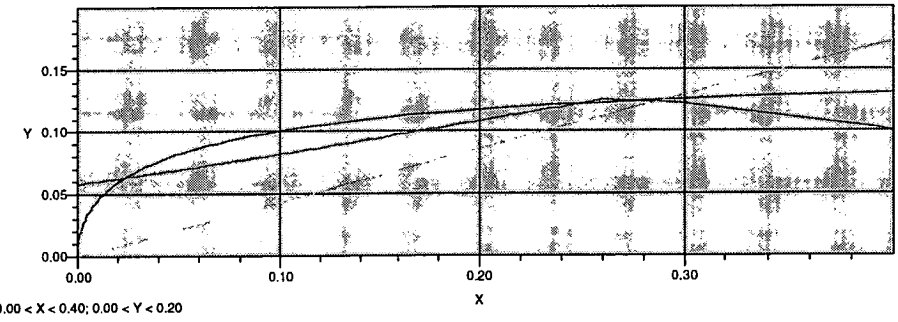

0.00 < X < 0.40; 0.00 < Y < 0.20

(d17) done

(c18)
```
/* The steady state for k=0.2 and mu=0.4, otherwise the same values as above*/
makeplot(0.4,0.2,0.1255,1026.518 ,1029.201,1026.927, 1028.781), xmax:0.4, ymax:0.2
```

[cf = 0.04549, cf = 0.05991, cf = 0.07676, cf = 0.09492, cf = 0.1125, cf = 0.12738, cf = 0.13829, cf = 0.1432]

Stephan Matthiesen D:\SM\Beruf\PHD\Hycobox\HJ-mix\HJ-mix-stability.mfe

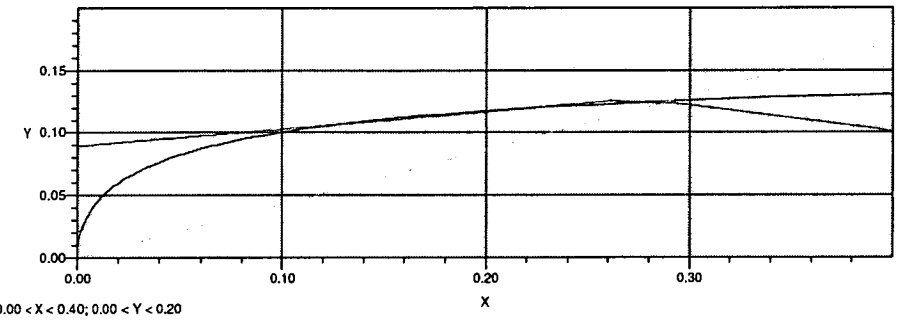

0.00 < X < 0.40; 0.00 < Y < 0.20

(d18) done

(c19) /* The situation for k=0.4 and mu=0.4, but increased evaporation */
makeplot(0.4,0.4,0.1255,1026.518 ,1029.301,1026.927, 1028.781), xmax:0.4, ymax:0.2

[cf = 0.04666, cf = 0.06153, cf = 0.07899, cf = 0.09792, cf = 0.11638, cf = 0.13214, cf = 0.1438, cf = 0.14909]

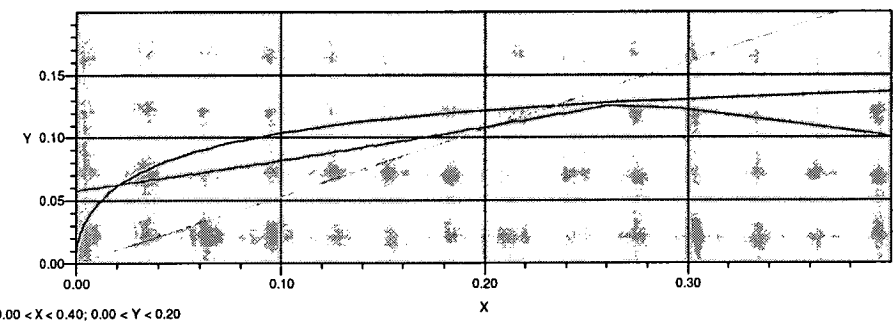

0.00 < X < 0.40; 0.00 < Y < 0.20

(d19) done

(c20)

D.3 3-layer theory

The 3-layer system was mainly investigated using the computer algebra system *Macsyma*. Two scripts were used, one for producing h_1-h_2-plots of different quantities, and one solving the equations for the free surface system.

D.3.1 Rigid lid approximation and h_1-h_2-plots

The following *Macsyma* script defines a number of functions for producing h_1-h_2-plots. In particular, it provides functions for the following:

- The function *plot_roots* that finds the roots of the hydraulic functional by a Newton search algorithm at one point along the channel.
- The function *plot_roots_all* that uses *plot_roots* to plot the roots at different points along the channel, producing a path in the h_1-h_2-diagram.
- The function *plot_froude* which plots the Froude number condition.

Stephan Matthiesen D:\SM\Beruf\RedSea\Macsyma\Def 3-layer plots.mfe

The 3-layer problem - Solutions along the channel

Introduction

This script tries to clarify what the solutions are for the 3-layer system are. If we only solve the set of equations at the three points, it is possible that we get solutions which cannot be connected through. This is a real danger, as the numerical solution depends on finding roots of polynomials.

It is therefore desirable to know the solutions along the channel (at least for a simple channel geometry).

Here the system of equations is solved, so that - ideally - if we know the boundary conditions in the two reservoirs, this Macsyma script will produce a plot of the solution along the channel as well as values for all the parameters that occur in the Modelmaker programme. This is done in two (independent?) ways:

- by producing a contour plot of the hydraulic functional

- by deriving a differential equation, which is then solved numerically.

Definitions

These parameters and variables are used (in **bold**: parameters imposed by the boundary conditions):

x_rs, x_s, x_ga: position of the control points towards Red Sea, at the Sill and towards Gulf of Aden

h0, h1, h2, h3: layer thicknesses (general).

h0_rs, etc.: layer thicknesses at the entrance or the virtual control towards the Red Sea

h0_rsx, etc,: layer thicknesses in the Red Sea

h0_ga, etc.: layer thicknesses at the entrance or the virtual control towards the Gulf of Aden

h0_gax, etc: layer thicknesses in the Gulf of Aden

h0_s, etc,: layer thicknesses at the sill=geometric control point

rho1, rho2, rho3: layer densities

b0_hj, b1_hj, b2_hj: Bernoulli potentials when a hydraulic jump is present

Normalization

The layer thicknesses are normalized "twice": hi(x) [meter] = ds(x) [meter] * d(x) * h(x), where ds(meter) is the depth at the sill in meter, and d(x) is the nondimensional channel depth with d(x_sill)=1. Therefore always 0<h(x)<1, but the h(x) at two different points are not directly comparable.

Basic definitions

Bernoulli equations

Starting point are the Bernoulli equations. We have one for the surface, and two which represent the difference in Bernoulli potential across the two interfaces. They are taken from David Cobby's thesis.

All are in nondimensional form, in which d(x) is the nondimensional channel depth along the channel, w(x) is the channel width. Both can be explicitly defined later.

(c1) `fun0(x,h0,h1,h2,h3,b0) := 1/(2*w(x)^2*d(x)^2) * (q1/h1)^2 - s * d(x)*h0 - b0`

(d1)
$$\mathrm{fun0}(x, h0, h1, h2, h3, b0) := \frac{\left(\frac{q1}{h1}\right)^2}{2\,w^2(x)\,d^2(x)} - s\,d(x)\,h0 - b0$$

(c2) `fun1(x,h0,h1,h2,h3,b1) := 1/(2*w(x)^2*d(x)^2) * ((q1/h1)^2 - (q2/h2)^2) + r*d(x)*(h0+h1) -h1`

(d2)
$$\mathrm{fun1}(x, h0, h1, h2, h3, b1) := \frac{\left(\frac{q1}{h1}\right)^2 - \left(\frac{q2}{h2}\right)^2}{2\,w^2(x)\,d^2(x)} + r\,d(x)\,(h0 + h1) - b1$$

(c3) `fun2(x,h0,h1,h2,h3,b2) := 1/(2*w(x)^2*d(x)^2) * ((q2/h2)^2 - (q3/h3)^2) + (1-r)*d(x)*(h0+h1+h2)-h2`

(d3)
$$\mathrm{fun2}(x, h0, h1, h2, h3, b2) := \frac{\left(\frac{q2}{h2}\right)^2 - \left(\frac{q3}{h3}\right)^2}{2\,w^2(x)\,d^2(x)} + (1 - r)\,d(x)\,(h0 + h1 + h2) - b2$$

Froude numbers

(c4) `froude1(x,h1):= q1^2/(w(x)^2*d(x)^3*h1^3) $`

(c5) `froude2(x,h2):= q2^2/(w(x)^2*d(x)^3*h2^3) $`

(c6) `froude3(x,h3):= q3^2/(w(x)^2*d(x)^3*h3^3) $`

System of equations

(c7) `eq_1rs: 0=factor(fun1(x_rs,h0_rs,h1_rs,h2_rs,inf,b1)*2*(d(x_rs)*w(x_rs)*h1_rs*h2_rs)^2), h0_rs:0`

(d7)
$$0 = 2\,h1\_rs^3\,h2\_rs^2\,r\,d^3(x\_rs)\,w^2(x\_rs) - 2\,b1\,h1\_rs^2\,h2\_rs^2\,d^2(x\_rs)\,w^2(x\_rs) - h1\_rs^2\,q2^2 + h2\_rs^2\,q1^2$$

(c8) `eq_2rs: 0=-factor(limit(fun2(x_rs,h0_rs,h1_rs,h2_rs,inf,h2)*2*(d(x_rs)*w(x_rs)*h2_rs)^2)), h0_rs:0`

$$0 = 2\,h2\_rs^3\,r\,d^3(x\_rs)\,w^2(x\_rs) + 2\,h1\_rs\,h2\_rs^2\,r\,d^3(x\_rs)\,w^2(x\_rs) - 2\,h2\_rs^3 * d^3(x\_rs)\,w^2(x\_rs) - 2\,h1\_rs\,h2\_rs^2\,d^3(x\_rs)\,w^2(x\_rs) + 2\,b2\,h2\_rs^2\,d^2(x\_rs) * w^2(x\_rs) - q2^2 \tag{d8}$$

(c9) eq_1s: 0=factor(fun1(x_s,h0_s,h1_s,h2_s,1-h0_s-h1_s-h2_s,b1)*2*(d(x_s)*w(x_s)*h1_s*h2_s)^2), h0_s:0

$$0 = 2\,h1\_s^3\,h2\_s^2\,r\,d^3(x\_s)\,w^2(x\_s) - 2\,b1\,h1\_s^2\,h2\_s^2\,d^2(x\_s)\,w^2(x\_s) - h1\_s^2\,q2^2 + h2\_s^2\,q1^2 \tag{d9}$$

(c10) eq_2s: 0=-factor(subst(q3=-q1-q2,fun2(x_s,h0_s,h1_s,h2_s,1-h0_s-h1_s-h2_s,h2)*2*(d(x_s)*w(x_s)*(1-h1_s-h2_s)*h2_s)^2)), h0_s:0

$$\begin{aligned}0 &= 2\,h2\_s^5\,r\,d^3(x\_s)\,w^2(x\_s) + 6\,h1\_s\,h2\_s^4\,r\,d^3(x\_s)\,w^2(x\_s) - 4\,h2\_s^4\,r\,d^3(x\_s)\,w^2(x\_s) + 6\,h1\_s^2\,h2\_s^3\,r\,d^3(x\_s) * w^2(x\_s) - 8\,h1\_s\,h2\_s^3\,r\,d^3(x\_s)\,w^2(x\_s) + 2\,h2\_s^3\,r\,d^3(x\_s)\,w^2(x\_s) + 2\,h1\_s^3\,h2\_s^2\,r\,d^3(x\_s)\,w^2(x\_s) - 4\,h1\_s^2\,h2\_s^2 * r\,d^3(x\_s)\,w^2(x\_s) + 2\,h1\_s\,h2\_s^2\,r\,d^3(x\_s)\,w^2(x\_s) - 2\,h2\_s^5\,d^3(x\_s)\,w^2(x\_s) - 6\,h1\_s\,h2\_s^4\,d^3(x\_s)\,w^2(x\_s) + 4\,h2\_s^4 * d^3(x\_s)\,w^2(x\_s) - 6\,h1\_s^2\,h2\_s^3\,d^3(x\_s)\,w^2(x\_s) + 8\,h1\_s\,h2\_s^3\,d^3(x\_s)\,w^2(x\_s) - 2\,h2\_s^3\,d^3(x\_s)\,w^2(x\_s) - 2\,h1\_s^3 * h2\_s^2\,d^3(x\_s)\,w^2(x\_s) + 4\,h1\_s^2\,h2\_s^2\,d^3(x\_s)\,w^2(x\_s) - 2\,h1\_s\,h2\_s^2\,d^3(x\_s)\,w^2(x\_s) + 2\,b2\,h2\_s^4\,d^2(x\_s)\,w^2(x\_s) + 4\,b2\,h1\_s\,h2\_s^3\,d^2(x\_s)\,w^2(x\_s) - 4\,b2\,h2\_s^3\,d^2(x\_s)\,w^2(x\_s) + 2\,b2\,h1\_s^2\,h2\_s^2\,d^2(x\_s)\,w^2(x\_s) - 4\,b2\,h1\_s\,h2\_s^2 * d^2(x\_s)\,w^2(x\_s) + 2\,b2\,h2\_s^2\,d^2(x\_s)\,w^2(x\_s) - 2\,h1\_s\,h2\_s\,q2^2 + 2\,h2\_s\,q2^2 - h1\_s^2\,q2^2 + 2\,h1\_s\,q2^2 - q2^2 + 2\,h2\_s^2\,q1\,q2 + h2\_s^2\,q1^2\end{aligned} \tag{d10}$$

(c11) eq_1ga: 0=factor(limit(fun1(x_ga,h0_ga,h1_ga,inf,inf,b1)*2*(d(x_ga)*w(x_ga)*h1_ga)^2)), h0_ga:0

$$0 = 2\,h1\_ga^3\,r\,d^3(x\_ga)\,w^2(x\_ga) - 2\,b1\,h1\_ga^2\,d^2(x\_ga)\,w^2(x\_ga) + q1^2 \tag{d11}$$

(c12) froude_s: 0 =-factor(subst(q3=-q1-q2,(froude2(x_s,h2_s)^2 - (r- froude1(x_s,h1_s)-froude2(x_s,h2_s)) * (1-r-froude2(x_s,h2_s)-froude3(x_s,1-h1_s-h2_s)))*d(x_s)^6*w(x_s)^4*h1_s^3*h2_s^3*(1-h1_s-h2_s)^3))

$$\begin{aligned}0 &= h1\_s^3\,h2\_s^6\,r^2\,d^6(x\_s)\,w^4(x\_s) + 3\,h1\_s^4\,h2\_s^5\,r^2\,d^6(x\_s)\,w^4(x\_s) - 3\,h1\_s^3\,h2\_s^5\,r^2\,d^6(x\_s)\,w^4(x\_s) + 3\,h1\_s^5\,h2\_s^4\,r^2 * d^6(x\_s)\,w^4(x\_s) - 6\,h1\_s^4\,h2\_s^4\,r^2\,d^6(x\_s)\,w^4(x\_s) + 3\,h1\_s^3\,h2\_s^4\,r^2\,d^6(x\_s)\,w^4(x\_s) + h1\_s^6\,h2\_s^3\,r^2\,d^6(x\_s)\,w^4(x\_s) - 3\,h1\_s^5\,h2\_s^3\,r^2\,d^6(x\_s)\,w^4(x\_s) + 3\,h1\_s^4\,h2\_s^3\,r^2\,d^6(x\_s)\,w^4(x\_s) - h1\_s^3\,h2\_s^3\,r^2\,d^6(x\_s)\,w^4(x\_s) - h1\_s^3\,h2\_s^6\,r * d^6(x\_s)\,w^4(x\_s) - 3\,h1\_s^4\,h2\_s^5\,r\,d^6(x\_s)\,w^4(x\_s) + 3\,h1\_s^3\,h2\_s^5\,r\,d^6(x\_s)\,w^4(x\_s) - 3\,h1\_s^5\,h2\_s^4\,r\,d^6(x\_s)\,w^4(x\_s) + 6 * h1\_s^4\,h2\_s^4\,r\,d^6(x\_s)\,w^4(x\_s) - 3\,h1\_s^3\,h2\_s^4\,r\,d^6(x\_s)\,w^4(x\_s) - h1\_s^6\,h2\_s^3\,r\,d^6(x\_s)\,w^4(x\_s) + 3\,h1\_s^5\,h2\_s^3\,r\,d^6(x\_s) * w^4(x\_s) - 3\,h1\_s^4\,h2\_s^3\,r\,d^6(x\_s)\,w^4(x\_s) + h1\_s^3\,h2\_s^3\,r\,d^6(x\_s)\,w^4(x\_s) - h1\_s^3\,h2\_s^3\,q2^2\,r\,d^3(x\_s)\,w^2(x\_s) - 2\,h1\_s^3 * h2\_s^3\,q1\,q2\,r\,d^3(x\_s)\,w^2(x\_s) - h2\_s^6\,q1^2\,r\,d^3(x\_s)\,w^2(x\_s) - 3\,h1\_s\,h2\_s^5\,q1^2\,r\,d^3(x\_s)\,w^2(x\_s) + 3\,h2\_s^5\,q1^2\,r\,d^3(x\_s) * w^2(x\_s) - 3\,h1\_s^2\,h2\_s^4\,q1^2\,r\,d^3(x\_s)\,w^2(x\_s) + 6\,h1\_s\,h2\_s^4\,q1^2\,r\,d^3(x\_s)\,w^2(x\_s) - 3\,h2\_s^4\,q1^2\,r\,d^3(x\_s)\,w^2(x\_s) - 2 * h1\_s^3\,h2\_s^3\,q1^2\,r\,d^3(x\_s)\,w^2(x\_s) + 3\,h1\_s^2\,h2\_s^3\,q1^2\,r\,d^3(x\_s)\,w^2(x\_s) - 3\,h1\_s\,h2\_s^3\,q1^2\,r\,d^3(x\_s)\,w^2(x\_s) + h2\_s^3\,q1^2\,r * d^3(x\_s)\,w^2(x\_s) + h1\_s^3\,h2\_s^3\,q2^2\,d^3(x\_s)\,w^2(x\_s) + 3\,h1\_s^4\,h2\_s^2\,q2^2\,d^3(x\_s)\,w^2(x\_s) - 3\,h1\_s^3\,h2\_s^2\,q2^2\,d^3(x\_s) * w^2(x\_s) + 3\,h1\_s^5\,h2\_s\,q2^2\,d^3(x\_s)\,w^2(x\_s) - 6\,h1\_s^4\,h2\_s\,q2^2\,d^3(x\_s)\,w^2(x\_s) + 3\,h1\_s^3\,h2\_s\,q2^2\,d^3(x\_s)\,w^2(x\_s) + h1\_s^6\,q2^2\,d^3(x\_s)\,w^2(x\_s) - 3\,h1\_s^5\,q2^2\,d^3(x\_s)\,w^2(x\_s) + 3\,h1\_s^4\,q2^2\,d^3(x\_s)\,w^2(x\_s) - h1\_s^3\,q2^2\,d^3(x\_s)\,w^2(x\_s) + h2\_s^6\,q1^2\,d^3(x\_s)\,w^2(x\_s) + 3\,h1\_s\,h2\_s^5\,q1^2\,d^3(x\_s)\,w^2(x\_s) - 3\,h2\_s^5\,q1^2\,d^3(x\_s)\,w^2(x\_s) + 3\,h1\_s^2\,h2\_s^4\,q1^2\,d^3(x\_s) * w^2(x\_s) - 6\,h1\_s\,h2\_s^4\,q1^2\,d^3(x\_s)\,w^2(x\_s) + 3\,h2\_s^4\,q1^2\,d^3(x\_s)\,w^2(x\_s) + h1\_s^3\,h2\_s^3\,q1^2\,d^3(x\_s)\,w^2(x\_s) - 3\,h1\_s^2 * h2\_s^3\,q1^2\,d^3(x\_s)\,w^2(x\_s) + 3\,h1\_s\,h2\_s^3\,q1^2\,d^3(x\_s)\,w^2(x\_s) - h2\_s^3\,q1^2\,d^3(x\_s)\,w^2(x\_s) - h1\_s^3\,q2^2\,d^3(x\_s)\,w^2(x\_s) + 3\,h1\_s^2\,h2\_s^2\,q1^2\,q2^2 - 3 * h1\_s\,h2\_s^2\,q1^2\,q2^2 + 3\,h2\_s^2\,q1^2\,q2^2 - 3\,h1\_s^2\,h2\_s\,q1^2\,q2^2 + 6\,h1\_s\,h2\_s\,q1^2\,q2^2 - 3\,h2\_s\,q1^2\,q2^2 + 3\,h1\_s^2\,q1^2\,q2^2 - 3\,h1\_s * q1^2\,q2^2 + q1^2\,q2^2 + 2\,h2\_s^3\,q1^3\,q2 + h2\_s^3\,q1^4\end{aligned} \tag{d12}$$

(c13) froude_rs: 0 = factor((-r*(1-r) + froude2(x_rs,h2_rs) - (1-r)*froude1(x_rs,h1_rs) - froude1(x_rs,h1_rs) *froude2(x_rs,h2_rs)) * h1_rs^3*h2_rs^3*d(x_rs)^6*w(x_rs)^4)

$$0 = h1\_rs^3\,h2\_rs^3\,r^2\,d^6(x\_rs)\,w^4(x\_rs) - h1\_rs^3\,h2\_rs^3\,r\,d^6(x\_rs)\,w^4(x\_rs) + h2\_rs^3\,q1^2\,r * d^3(x\_rs)\,w^2(x\_rs) + h1\_rs^3\,q2^2\,d^3(x\_rs)\,w^2(x\_rs) - h2\_rs^3\,q1^2\,d^3(x\_rs)\,w^2(x\_rs) - q1^2\,q2^2 \tag{d13}$$

Hydraulic functional

Now define the hydraulic functional. I define two forms: One for a free surface, and a simplified version assuming a rigid lid. The rigid-lid version is the one investigated by Smeed.

(c14) fun2d(x,h0,h1,h2,h3,b1,b2):=matrix([fun1(x,h0,b1,h2,h3,b1)],[fun2(x,h0,h1,h2,h3,b2)]) $

(c15) fun2d_simp(x,h1,h2,b1,h2):=fun2d(x,0,h1,h2,1-h1-h2,b1,h2) $

(c16) fun2d(x,h0,h1,h2,h3,b1,h2)

$$\begin{bmatrix} \dfrac{\dfrac{q1^2}{h1^2} - \dfrac{q2^2}{h2^2}}{2\,d^2(x)\,w^2(x)} + (h1 + h0)\,r\,d(x) - b1 \\ \dfrac{\dfrac{q2^2}{h2^2} - \dfrac{q3^2}{h3^2}}{2\,d^2(x)\,w^2(x)} + (h2 + h1 + h0)\,(1 - r)\,d(x) - h2 \end{bmatrix} \tag{d16}$$

(c17) fun2d_simp(x,h1,h2,b1,h2)

(d17)
$$\begin{bmatrix} \dfrac{\dfrac{q1^2}{h1^2}-\dfrac{q2^2}{h2^2}}{2\,d^2(x)\,w^2(x)}+h1\,r\,d(x)-b1 \\ \dfrac{\dfrac{q2^2}{h2^2}-\dfrac{q3^2}{(-h2-h1+1)^2}}{2\,d^2(x)\,w^2(x)}+(h2+h1)\,(1-r)\,d(x)-b2 \end{bmatrix}$$

Criticality condition

Control points are points at which different solution sheets of the Bernoulli equations meet, and the solutions are regular. Different sheets meet when the determinant of the gradient matrix vanishes.

(c18)
```
m(x,h0,h1,h2,h3,b1,b2):=
    addrow(diff(fun2d(x,h0,h1,h2,h3,b1,b2)^`,b1),diff(fun2d(x,h0,h1,h2,h3,b1,b2)^`,h2)) $
```

(c19)
```
m_simp(x,h1,h2,b1,b2):=
    addrow(diff(fun2d_simp(x,h1,h2,b1,b2)^`,h1),diff(fun2d_simp(x,h1,h2,b1,b2)^`,h2)) $
```

(c20)
```
n(x,h0,h1,h2,h3,b1,b2):=
    addrow(diff(fun2d(x,h0,h1,h2,h3,b1,b2)^`,w(x)),diff(fun2d(x,h0,h1,h2,h3,b1,b2)^`,d(x))) $
```

(c21)
```
n_simp(x,h1,h2,b1,b2):=
    addrow(diff(fun2d_simp(x,h1,h2,b1,b2)^`,w(x)),diff(fun2d_simp(x,h1,h2,b1,b2)^`,d(x))) $
```

(c22)
```
m_simp(x,h1,h2,b1,b2)
```

(d22)
$$\begin{bmatrix} r\,d(x)-\dfrac{q1^2}{h1^3\,d^2(x)\,w^2(x)} & (1-r)\,d(x)-\dfrac{q3^2}{(-h2-h1+1)^3\,d^2(x)\,w^2(x)} \\ \dfrac{q2^2}{h2^3\,d^2(x)\,w^2(x)} & -\dfrac{\dfrac{2\,q3^2}{(-h2-h1+1)^3}-\dfrac{2\,q2^2}{h2^3}}{2\,d^2(x)\,w^2(x)}+(1-r)\,d(x) \end{bmatrix}$$

(c23)
```
n_simp(x,h1,h2,b1,b2)
```

(d23)
$$\begin{bmatrix} -\dfrac{\dfrac{q1^2}{h1^2}-\dfrac{q2^2}{h2^2}}{d^2(x)\,w^3(x)} & -\dfrac{\dfrac{q2^2}{h2^2}-\dfrac{q3^2}{(-h2-h1+1)^2}}{d^2(x)\,w^3(x)} \\ h1\,r-\dfrac{\dfrac{q1^2}{h1^2}-\dfrac{q2^2}{h2^2}}{d^3(x)\,w^2(x)} & (h2+h1)\,(1-r)-\dfrac{\dfrac{q2^2}{h2^2}-\dfrac{q3^2}{(-h2-h1+1)^2}}{d^3(x)\,w^2(x)} \end{bmatrix}$$

And now the differential equation:

(c24)
```
depends([h1,h2,d,w],x)
```

(d24)
$$[h1(x),\,h2(x),\,d(x),\,w(x)]$$

(c25)
```
diffeqn1: 0=diff(fun2d_simp(x,h1,h2,b1,b2)[1],x)
```

(d25)
$$0=-\frac{\left(\dfrac{q1^2}{h1^2}-\dfrac{q2^2}{h2^2}\right)\dfrac{d}{dx}(w(x))}{d^2(x)\,w^3(x)}-\frac{\left(\dfrac{q1^2}{h1^2}-\dfrac{q2^2}{h2^2}\right)\dfrac{d}{dx}(d(x))}{d^3(x)\,w^2(x)}+h1\,r\,\frac{d}{dx}(d(x))+\frac{\dfrac{2\,\dfrac{dh2}{dx}\,q2^2}{h2^3}-\dfrac{2\,\dfrac{dh1}{dx}\,q1^2}{h1^3}}{2\,d^2(x)\,w^2(x)}+\frac{dh1}{dx}\,r\,d(x)$$

(c26)
```
diffeqn2: 0=diff(fun2d_simp(x,h1,h2,b1,b2)[2],x)
```

(d26)
$$0=-\frac{\left(\dfrac{q2^2}{h2^2}-\dfrac{q3^2}{(-h2-h1+1)^2}\right)\dfrac{d}{dx}(w(x))}{d^2(x)\,w^3(x)}-\frac{\left(\dfrac{q2^2}{h2^2}-\dfrac{q3^2}{(-h2-h1+1)^2}\right)\dfrac{d}{dx}(d(x))}{d^3(x)\,w^2(x)}$$
$$+(h2+h1)\,(1-r)\,\frac{d}{dx}(d(x))+\frac{\dfrac{2\left(-\dfrac{dh2}{dx}-\dfrac{dh1}{dx}\right)q3^2}{(-h2-h1+1)^3}-\dfrac{2\,\dfrac{dh2}{dx}\,q2^2}{h2^3}}{2\,d^2(x)\,w^2(x)}+\left(\frac{dh2}{dx}+\frac{dh1}{dx}\right)(1-r)\,d(x)$$

(c27)
```
detm(x,h0,h1,h2,h3):=determinant(m(x,h0,h1,h2,h3,b1,b2)) $
```

(c28)
```
detm_simp(x,h1,h2):=determinant(m_simp(x,h1,h2,b1,b2)) $
```

(c29)
```
detm(x,h0,h1,h2,h3)
```

(d29)
$$\left(r\,d(x)-\frac{q1^2}{h1^3\,d^2(x)\,w^2(x)}\right)\left((1-r)\,d(x)-\frac{q2^2}{h2^3\,d^2(x)\,w^2(x)}\right)-\frac{q2^2\,(1-r)}{h2^3\,d(x)\,w^2(x)}$$

(c30)
```
detm_simp(x,h1,h2)
```

Stephan Matthiesen D:\SM\Beruf\RedSea\Macsyma\Def 3-layer plots.mfe

(d30)
$$\left(r\,d(x)-\frac{q1^2}{h1^3\,d^2(x)\,w^2(x)}\right)\left(\frac{-\frac{2\,q3^2}{(-h2-h1+1)^3}-\frac{2\,q2^2}{h2^3}}{2\,d^2(x)\,w^2(x)}+(1-r)\,d(x)\right)-\frac{q2^2\left((1-r)\,d(x)-\frac{q3^2}{(-h2-h1+1)^3\,d^2(x)\,w^2(x)}\right)}{h2^3\,d^2(x)\,w^2(x)}$$

(c31)
```
froude(x,h0,h1,h2):= diff(fun1(x,h0,h1,h2,1-h0-h1-h2,h1),h1) * diff((fun2(x,h0,h1,h2,1-h0-h1-h2,h2),h2) -
        diff(fun2(x,h0,h1,h2,1-h0-h1-h2,h2),h1) * diff(fun1(x,h0,h1,h2,1-h0-h1-h2,h1),h2) $
```

(c32)
```
froude(x,h0,h1,h2)
```

(d32)
$$\left(r\,d(x)-\frac{q1^2}{h1^3\,d^2(x)\,w^2(x)}\right)\left(\frac{-\frac{2\,q3^2}{(-h2-h1-h0+1)^3}-\frac{2\,q2^2}{h2^3}}{2\,d^2(x)\,w^2(x)}+(1-r)\,d(x)\right)-\frac{q2^2\left((1-r)\,d(x)-\frac{q3^2}{(-h2-h1-h0+1)^3\,d^2(x)\,w^2(x)}\right)}{h2^3\,d^2(x)\,w^2(x)}$$

(c33)
```
froude1(x,h1):= q1^2/(w(x)^2*d(x)^3*h1^3) $
```

(c34)
```
froude2(x,h2):= q2^2/(w(x)^2*d(x)^3*h2^3) $
```

(c35)
```
froude3(x,h3):= q3^2/(w(x)^2*d(x)^3*h3^3) $
```

Connection to the basin: the Bernoulli potentials bi

The Bernoulli potentials are determined from the reservoir conditions. The functional form of this relation, however, depends on the presence or absence of the hydraulic jump.

(c36)
```
eq_hj1: b1= r* d(x_ga)*(h1_gax)
```

(d36)
$$b1 = h1\_gax\,r\,d(x\_ga)$$

(c37)
```
eq_hj2: b2=-b1+ d(x_rs)*(h1_rsx + (1-r)* h2_rsx)
```

(d37)
$$h2 = (h2\_rsx\,(1-r)+h1\_rsx)\,d(x\_rs) - b1$$

Model channel geometry

In order to solve along the channel, depth and width have to specified.

(c38)
```
d(x):=5-4* exp(-x^2) $
```

(c39)
```
w(x):=5-4* exp(-x^2) $
```

Find the solutions: find_solution_brute

This defines a function that calculates the q1,q2,q3,b1,b2 from the basin conditions. Note that the q's can be plus or minus - the original symmetry was lost due to the assumption q1+q2+q3=1 used in deriving the equations. However, this doesn't work very well, as a huge number of operations are involved.

(c40)
```
find_solution_brute(h1_rsx_fs,h2_rsx_fs,h1_gax_fs,x_rs_fs,x_s_fs,x_ga_fs,r,start):=block(
        [h1_rsx,h2_rsx,h1_gax,x_ga,x_s,x_ga,eqnlist,varlist],
        h1_rsx: h1_rsx_fs,
        h2_rsx: h2_rsx_fs,
        h1_gax: h1_gax_fs,
        x_rs: x_rs_fs,
        x_s: x_s_fs,
        x_ga: x_ga_fs,
        varlist: [q1,q2,h1_rs,h2_rs,b1_s,b2_s,b1_ga],
        b1:ev(assoc('b1,[eq_hj1])),
        b2:ev(assoc('b2,[eq_hj2])),
        eqnlist:ev([eq_1rs,eq_2rs,eq_1s,eq_2s,eq_1ga,froude_s,froude_rs]), /* use the eqn at GA explicitly */
        display(eqnlist),
        display(x_rs,x_s,x_ga,b1,h2),
        newton_optimize:true,
        solution: newton(               /* attempt to find the numerical roots */
                eqnlist,
                varlist,
                start
        ),
        display(solution)
) $
```

Alongchannel plot: plot_channel_diff

This defines a function that takes the important parameters, integrates the differential form of the equations and plots the solution along the channel, so that it is easier to try out different situations. This is called by:

plot_channel_diff(q1,q2,b1,b2,r,x_min,x_max,h1_bc,h2_bc,stepsize)

The variables are:
q1, q2: flow rates (with appropriate sign); q3 is calculated from q1+q2+q3=0
b1, b2: Bernoulli differences
r: density ratio
x_min, x_max: channel boundaries
h1_bc, h2_bc: boundary conditions for h1, h2 at x=x_min, **normalized to the depth at x_min**
stepsize: stepsize for the integration

Note the normalization of all depth variables in the graph-function: for the plot, everything is normalized to sill depth, not to local channel depth.

```
plot_channel_diff(q1_pc,q2_pc,b1_pc,b2_pc,r_pc,x_min,x_max,h1_bc,h2_bc,stepsize):=block([q1,q2,q3,b1,b2,r,ymax],
        q1: q1_pc,
        q2: q2_pc,
        q3: -q1-q2,
        b1: b1_pc,
        b2: b2_pc,
        r: r_pc,
```

(c41)
```
        solution:ode_numsol(
                [ev(diffeqn1,nouns),ev(diffeqn2,nouns)],
                ['h1,'h2],
                's,
                ['at(h1,s=s_min)=h1_bc,'at(h2,s=s_min)=h2_bc],
                s_min,
                s_max,
                stepsize
        ),
        ymax:0,
        graph(assoc('x,solution),[
                -d(assoc('x,solution)),
                -assoc('h1,solution)*d(assoc('x,solution)),
                -(assoc('h1,solution)+assoc('h2,solution))*d(assoc('x,solution))
        ])
)$
```

Plot of solutions at different points: plot_roots

The hydraulic functional fun2d_simp(x,h1,h2,b1,b2) is a function R^3 -> R^2. Unfortunately it is difficult to produce a contour plot of fun2d_simple along the channel, as we now have 2 vertical variables (h1, h2). However, for given b1, b1, q1, q2, q3, it is possible to plot the solution into a h1-h2-diagramme for any given point x.

The following defines a function that plots the root of the hydraulic functional at different points. This is called by:

plot_roots(q1,q2,b1,b2,r,x)

The variables are:
q1, q2: flow rates (with appropriate sign); q3 is calculated from q1+q2+q3=0
b1, b2: Bernoulli differences
r: density ratio
x: point along the channel
num_intervals: number of intervals for the search

Before the plot function can be defined, we need an auxiliary function which transforms the numerical results into a list that can be plottet.

(c42)
```
produce_plotlist(inputlist):=block([list1,list2],          /*inputlist: [[h1=a,h2=b],[h1=c,h2=d],...] */
        kill(list1,list2),                                 /*output: [[a,c,...],[b,d,...]] */
        list1: [],
        list2: [],
        for i:1 thru length(inputlist) do block(
                list1:append(list1,[part(inputlist,i,1,2)]),
                list2:append(list2,[part(inputlist,i,2,2)])
        ),
        [list1,list2]
)$
```

And now the definition fo the plot function.

(c43)
```
plot_roots(q1_pr,q2_pr,b1,b2,r,x,num_intervals):=block([q1,q2,q3,list1,list2,solution,contours,xlabel,ylabel],
        q1: q1_pr,
        q2: q2_pr,
        q3: -q1-q2,
        solution: newton_search(                           /* attempt to find the numerical roots */
                [fun2d_simp(x,h1,h2,b1,b2)[1],fun2d_simp(x,h1,h2,b1,b2)[2]],
                [h1,h2],
                [0.01,0.01],
                [1,1],
                [num_intervals,num_intervals]              /* the number of interval for the search */
        ),
        contours:[0],
        xlabel:"h1",ylabel:"h2",
        title: concat("b1=",b1, "; b2=", b2, "; q1=", q1,  "; q2=", q2, "; q3=", q3, "; r=", r," ; x=",x),
        combine_plots(                                     /* produce two plots */
                contourplot([                              /* plot the 0-contour of the two components */
                        fun2d_simp(x,h1,h2,b1,b2)[1],
                        fun2d_simp(x,h1,h2,b1,b2)[2]
                ],h1,0.01,1,h2,0.01,1),
                graph(                                     /* plot the numerical roots */
                        produce_plotlist(solution)[1],
                        produce_plotlist(solution)[2],
                        [19]                               /* circles, no line */
                ),
                graph([0,1],[1,0],[2])                     /* the diagonal */
        ),
        solution
)$
```

Plot of the roots: plot_roots_all

A similar function, but this plots only the roots (not the full contours), but for different points along the channel. This is called by:

plot_roots_all(q1,q2,b1,b2,r,x_min,x_max,stepsize)

The variables are:
q1, q2: flow rates (with appropriate sign); q3 is calculated from q1+q2+q3=0
b1, b2: Bernoulli differences
r: density ratio
x_min, x_max: channel boundaries
stepsize: stepsize
num_intervals: number of intervals for the search

```
plot_roots_all(q1_pr,q2_pr,b1,b2,r,x_min,x_max,stepsize,num_intervals):=block([q1,q2,q3,x,solution,solution1,xlabel,ylabel],
        q1: q1_pr,
        q2: q2_pr,
```

```
        q3: -q1-q2,
        xlabel:"h1 - normalized to total depth at x",ylabel:"h2 - normalized to total depth at x",                    /* set the axes labels */
        title: concat("q1=", q1,  "; q2=", q2, "; q3=", q3, "; b1=",b1, "; b2=", b2, "; r=", r, "; x=[",x_min,"...",x_max,"]; dx=",stepsize),
        grapb([0,1],[1,0],[2],first),                    /* plot the diagonal (only points below diagonal are relevant) */
        for x:x_min step stepsize while x <= x_max do block(          /* calculate solution for points along the channel */
                solution: newton_search(                 /* attempt to find the numerical roots */
                        [fun2d_simp(x,b1,b2,b1,b2)[1],fun2d_simp(x,b1,b2,b1,b2)[2]],
                        [b1,b2],
                        [0.01,0.01],
                        [1,1],
                        [num_intervals,num_intervals]
                ),
                if x=x_min then solution1:solution,
                if x=x_min then graph(                   /* plot the solution at x_min with a different symbol */
                        produce_plotlist(solution)[1],
(c44)                   produce_plotlist(solution)[2],
                        [69],                            /* plot crosses, no line */
                        same                             /* plot into the same plot */
                ),
                else graph(                              /* plot the numerical roots */
                        produce_plotlist(solution)[1],
                        produce_plotlist(solution)[2],
                        [99],                            /* dots, no line */
                        same                             /* plot into the same plot */
                )
        ),
        graph(                                           /* plot the last solution again with different symbol*/
                produce_plotlist(solution)[1],
                produce_plotlist(solution)[2],
                [19],                                    /* circles, no line */
                same, last                               /* the last plot in this series */
        ),
        display(x_min,solution1,x_max,solution)
)$
```

Plot of the roots: plot_roots_all_d

Essentially the same function, but the plot is normalized to sill depth, whereas plot_roots_all is normalized to actual depth at each point. This can be useful, because it is easier to sea how the layer thicknesses change.

This is called by:

plot_roots_all_d(q1,q2,b1,b2,r,x_min,x_max,stepsize)

The variables are:
q1, q2: flow rates (with appropriate sign); q3 is calculated from q1+q2+q3=0
b1, b2: Bernoulli differences
r: density ratio
x_min, x_max: channel boundaries
stepsize: stepsize
num_intervals: number of intervals for the search

```
plot_roots_all_d(q1_pr,q2_pr,b1,b2,r,x_min,x_max,stepsize,num_intervals):=block([q1,q2,q3,x,solution,xlabel,ylabel],
        q1: q1_pr,
        q2: q2_pr,
        q3: -q1-q2,
        xlabel:"h1 - normalized to sill depth",ylabel:"h2 - normalized to sill depth",                    /* set the axes labels */
        title: concat("q1=", q1,  "; q2=", q2, "; q3=", q3, "; b1=",b1, "; b2=", b2, "; r=", r, "; x=[",x_min,"...",x_max,"]; dx=",stepsize),
        for x:x_min step stepsize while x <= x_max do block(          /* calculate solution for points along the channel */
                solution: d(x)*newton_search(            /* attempt to find the numerical roots */
                        [fun2d_simp(x,b1,b2,b1,b2)[1],fun2d_simp(x,b1,b2,b1,b2)[2]],
                        [b1,b2],
                        [0.01,0.01],
                        [1,1],
                        [num_intervals,num_intervals]
                ),
                if x=x_min then graph(                   /* plot the solution at x_min with a different symbol */
                        produce_plotlist(solution)[1],
(c45)                   produce_plotlist(solution)[2],
                        [69],                            /* plot crosses, no line */
                        first                            /* first plot in a series */
                ),
                else graph(                              /* plot the numerical roots */
                        produce_plotlist(solution)[1],
                        produce_plotlist(solution)[2],
                        [99],                            /* dots, no line */
                        same                             /* plot into the same plot */
                )
        ),
        graph(                                           /* plot the last solution again with different symbol*/
                produce_plotlist(solution)[1],
                produce_plotlist(solution)[2],
                [19],                                    /* circles, no line */
                same, last                               /* the last plot in this series */
        )
)$
```

Another plot along the channel: plot_channel_plain

This solves the Bernoulli equation numerically for [h1,h2] at different points and plots it inot a h1-h2 diagram. thus it is not necessary to integrate the differential form of the equation.

The following defines a function that plots the root of the hydraulic functional at different points. This is called by:

plot_channel_plain(q1,q2,b1,b2,r,x_min,x_max,stepsize)

The variables are:

q1, q2: flow rates (with appropriate sign); q3 is calculated from q1+q2+q3=0
b1, b2: Bernoulli differences
r: density ratio
x_min, x_max: channel boundaries
stepsize: stepsize for the integration

Note the normalization of all depth variables in the graph-function: for the plot, everything is normalized to sill depth, not to local channel depth.
Technical notes: Newton_search gives the solution in the form
[[h1=h1_a, h2=h2_a], [h1=h1_b, h2=h2_b], ...] for every x. However, for plotting with the graph command the best form would be to have lists [x1,x2,x3,...], [h1_a(x1), h1_a(x2),...], [h2_a(x1), h2_a(x2),...], [h1_b(x1), h1_b(x2),....], [h2_b(x1), h2_b(x2),...], ordered according to size: h1_a<h1_b<h1_c .... Unfortunately we don't know in advance how many roots there are for every points, and the system should still hold if some roots dissappear. This will take some reorganizing of the data before they can be plotted.

```
plot_channel_plain(q1_pc,q2_pc,b1_pc,b2_pc,r_pc,x_min,x_max,stepsize):=block(
        q1: q1_pc,
        q2: q2_pc,
        q3: -q1-q2,
        b1: b1_pc,
        b2: b2_pc,
        r: r_pc,
(c46)   for x:x_min while x <= x_max do block(          /* calculate solution for points along the channel  */
                solution: newton_search(          /* attempt to find the numerical roots */
                        [fun2d_simp(x,h1,h2,b1,b2)[1],fun2d_simp(x,h1,h2,b1,b2)[2]],
                        [h1,h2],
                        [0.01,0.01],
                        [1,1]
                )
        )
)$
```

Plot of the Froude number: plot_froude

The following defines a function that plots the root of the determinant. This is called by:

plot_froude(q1,q2,r,x)

The variables are:
q1, q2: flow rates (with appropriate sign); q3 is calculated from q1+q2+q3=0
r: density ratio
x: point along the channel
num_intervals: number of intervals for the search

And now the definition of the plot function.

```
plot_froude(q1_pr,q2_pr,r,x):=block(
        [q1,q2,q3,h1_temp,h2_temp,list1,list2,solution,contours,xlabel,ylabel],
        q1: q1_pr,
        q2: q2_pr,
        q3: -q1-q2,
        contours:[0], labelcontours:false,
(c47)   xlabel:"h1 - normalized to total depth at x",ylabel:"h2 - normalized to total depth at x",
        title: concat("q1=", q1,  "; q2=", q2, "; q3=", q3, "; r=", r," ; x=",x),
        contourplot(
                at(froude(x,0,h1_temp,h2_temp),[h1_temp=h1,h2_temp=h2])
                ,h1,0.01,1,h2,0.01,1
        )
)$
```

End of definitions

Now all the functions are defined and can be used to investigate different situations.

(c48)

D.3.2 Macsyma: Different solution regimes for the 3-layer case with free surface

The following *Macsyma* script solves the governing equations for the free surface system, see section 8.5.3

Stephan Matthiesen D:\SM\Beruf\RedSea\Macsyma\Def 3-layer.mfe

The 3-layer problem - different solution regimes

Summary and Introduction

This Macsyma Script derives the equations used in the 3-layer Modelmaker programme. It also provides a number of functions that solve the system numerically and produce different plots.

The Bernoulli equations and appropriate Froude number conditions are calculated ar three points along the channel. The Bernoulli potentials are obtained from the basin conditions, with appropriate considerations for hydraulic jumps.

(c69) stardisp:true /* Macsyma: display a star instead of space as multiplication symbol */ $

Definitions

These parameters and variables are used (in **bold**: parameters imposed by the boundary conditions):

xrs, xs, xga: position of the control points towards Red Sea, at the Sill and towards Gulf of Aden

h0, h1, h2, h3: layer thicknesses (general).

h0rs, etc.: layer thicknesses at the entrance or the virtual control towards the Red Sea

h0rsx, etc,: layer thicknesses in the Red Sea

h0ga, etc.: layer thicknesses at the entrance or the virtual control towards the Gulf of Aden

h0gax, etc: layer thicknesses in the Gulf of Aden

h0s, etc,: layer thicknesses at the sill=geometric control point

r, s: density ratios

b0, b1, b2: Bernoulli potentials

h0eff, h1eff, h2eff: Effective layer thicknesses, David Smeed's "h1-hat, h2-hat". A different way of expressing the Bernoulli-Potentials, these can be interpreted as the layer thicknesses if all energy was potential energy.

Normalization

The layer thicknesses are normalized "twice": hi(x) [meter] = ds(x) [meter] * d(x) * h(x), where ds(meter) is the depth at the sill in meter, and d(x) is the nondimensional channel depth with d(x_sill)=1. Therefore always 0<h(x)<1, but the h(x) at two different points are not directly comparable.

Bernoulli potentials and effective layer thicknesses

Effective layer thicknesses are a differnet way of expressing Bernoulli potentials. The relation is as follows (assuming that h0<<h1):

(c70) relation_b0_heff: b0=s*h0eff*d(x)

(d70) $$b0 = h0eff*s*d(x)$$

(c71) relation_b1_heff: b1=r*h1eff*d(x)

(d71) $$b1 = h1eff*r*d(x)$$

(c72) relation_b2_heff: b2=(1-r)*(h1eff+h2eff)*d(x)

(d72) $$b2 = (h2eff + h1eff)*(1 - r)*d(x)$$

Solution Regimes

Relevant for the situation at the Bab-el-Mandab are four different solution regimes (we think...). We label them according to Smeed's classification with two numbers, the first number characterizes the condition at the RS, the second number at the GA. Also, for the purpose of this calculation, we use small letters (a,b,c,d) as a handy index.

The four regimes are:

(a) [-3,3]: 3 controls: RS ([-3]-[1]), Sill ([1]-[-2]), GA ([-2]-[3])

(b) [1,3]: 2 controls: Sill ([1]-[-2]), GA ([-2]-[3])

(c) [2,3]: 2 controls: RS ([2]-[0]), Sill ([0]-[3])

(d) [2,-2]: 3 controls: RS ([2]-[0]), Sill ([0]-[3]), GA ([3]-[-2])

Obviously [-3,3] is a limiting case of [1,3] with one additional control, but otherwise equal situation. Similarly [2,-2] is a limiting case of [2,3].

Hydraulic jump at the surface

The Bernoulli constant b0 is determined by the upstream sea level:

(c73) sol_b0i: b0=-h0gax*s*d(x), x:xga

(d73) $$b0 = - h0gax*s*d(xga)$$

(c74) sol_b0o: b0=-h0rsx*s*d(x), x:xrs

(d74) $$b0 = - h0rsx*s*d(xrs)$$

Hydraulic jumps and connection to the basin

The type of the Hydraulic jumps, and therefore the appropriate equation for connecting the Strait to the Basins, depend on the flow regime at each end. Note that if the flow regime has one supercritical mode [+i], then it is the second mode (Smeed's conjecture). Note also that generally the Bernoulli in the upper interface is determined in the GA, the lower in the RS (Why?).

[3] at GA (a,b,c): hydraulic jump in the lower layer (does not concern us here), Bernoulli in upper interface is directly determined from the GA conditions.

(c75) connection_ga3: h1eff=h1gax

(d75) $$h1eff = h1gax$$

(c76) connection_ga3b: subst(connection_ga3,relation_b1_heff), x:xga

(d76) $$b1 = h1gax*r*d(xga)$$

[-2] at GA (d): with two supercritical modes, the Bernoulli in upper interface is not determined, but has to be calculated using the additional control condition.

[1] at RS (b): hydraulic jump in the upper layer , Bernoulli in lower interface is directly determined from the RS conditions.

(c77) connection_rs1: h2eff=h2rsx

(d77) $$h2eff = h2rsx$$

(c78) connection_rs1b: subst(solve(relation_b1_heff,h1eff),subst(connection_rs1,relation_b2_heff)), x:xrs

(d78) $$b2 = (1 - r)*\left(\frac{b1}{r*d(xrs)} + h2rsx\right)*d(xrs)$$

[2] at RS (c,d): second mode HJ in the RS

(c79) connection_rs2: h1eff+(1-r)*h2eff=h1rsx+(1-r)*h2rsx

(d79) $$h2eff*(1 - r) + h1eff = h2rsx*(1 - r) + h1rsx$$

(c80) connection_rs2b: partfrac(subst(solve(connection_rs2,h2eff),relation_b2_heff),h2rsx), x:xrs

(d80) $$b2 = (h1rsx - h1eff*r)*d(xrs) + h2rsx*(1 - r)*d(xrs)$$

[-3] at RS (a): with two supercritical modes, the Bernoulli in the lower interface is not determined, but has to be calculated using the additional control condition.

Summing up for each of the cases:

[-3,3] (a): No information about h2eff and b2, but h1eff and b1 are determined from the GA conditions:

(c81) connection_a1h: connection_ga3

(d81) $$h1eff = h1gax$$

(c82) connection_a1b: connection_ga3b

(d82) $$b1 = h1gax*r*d(xga)$$

[1,3] (b) Both Bernoulli functions are defined

(c83) connection_b1h: connection_ga3

(d83) $$h1eff = h1gax$$

(c84) connection_b1b: connection_ga3b

(d84) $$b1 = h1gax*r*d(xga)$$

(c85) connection_b2h: subst(connection_ga3,connection_rs1)

(d85) $$h2eff = h2rsx$$

(c86) connection_b2b: subst(connection_ga3,connection_rs1b)

(d86) $$b2 = (1 - r)*\left(\frac{b1}{r*d(xrs)} + h2rsx\right)*d(xrs)$$

[2,3] (c) Both Bernnoulli potentials are defined:

(c87) connection_c1h: connection_ga3

(d87) $$h1eff = h1gax$$

(c88) connection_c1b: connection_ga3b

(d88) $$b1 = h1gax*r*d(xga)$$

(c89) connection_c2h: partfrac(first(solve(subst(connection_ga3,connection_rs2),h2eff)),r)

(d89) $$h2eff = \frac{h1gax - h1rsx}{r - 1} + h2rsx$$

(c90) connection_c2b: factorsum(ratsubst(solve(relation_b1_heff,h1eff),connection_rs2b)), x:xrs

(d90) $$b2 = -\left((h2rsx*(r - 1) - h1rsx)*d(xrs) + b1\right)$$

[2,-2] (d) The upper Bernoulli potential is not determined from the basin condition. The lower Bernoulli potential is given by

(c91) connection_d2h: partfrac(first(solve(connection_rs2,h2eff)),r)

(d91) $$h2eff = \frac{h1eff - h1rsx}{r - 1} + h2rsx$$

(c92) connection_d2b: factorsum(ratsubst(solve(relation_b1_heff,h1eff),connection_rs2b)), x:xrs

(d92) $$b2 = -\left((h2rsx*(r-1)-h1rsx)*d(xrs)+b1\right)$$

Conditions for each regime

There are two conditions that establich which regime is appropriate

1) h1rsx<h1gax for (a,b) - h1rsx>h1gax for (c,d)

2) 2 controls for (b,c) - 3 controls for (a,d)

To determine the correct regime, we therefore proceed as follows:

1) Check h1rsx/h1gax. Establishes whether it is (a,b) or (c,d)

2) Assume it is (b) or (c) respectively and calculate solution.

3) Check the Froude number condition to see if a 3rd control is necessary. This establishes the correct regime.

Outline of solution

Basic definitions

Bernoulli equations

Starting point are the Bernoulli equations. We have one for the surface, and two which represent the difference in Bernoulli potential across the two interfaces. They are taken from David's thesis.

All are in nondimensional form, in which d(x) is the nondimensional channel depth along the channel, w(x) is the channel width. Both can be explicitly defined later.

(c93) fun0(x,h0,h1,h2,h3,b0) := 1/(2*w(x)^2*d(x)^2) * (q1/h1)^2 - s * d(x)*h0 - b0

(d93) $$fun0(x,h0,h1,h2,h3,b0) := \frac{\left(\frac{q1}{h1}\right)^2}{2*w^2(x)*d^2(x)} - s*d(x)*h0 - b0$$

(c94) fun1(x,h0,h1,h2,h3,b1) := 1/(2*w(x)^2*d(x)^2) * ((q1/h1)^2 - (q2/h2)^2) + r*d(x)*(h0+h1) -b1

(d94) $$fun1(x,h0,h1,h2,h3,b1) := \frac{\left(\frac{q1}{h1}\right)^2 - \left(\frac{q2}{h2}\right)^2}{2*w^2(x)*d^2(x)} + r*d(x)*(h0+h1) - b1$$

(c95) fun2(x,h0,h1,h2,h3,b2) := 1/(2*w(x)^2*d(x)^2) * ((q2/h2)^2 - (q3/h3)^2) + (1-r)*d(x)*(h0+h1+h2)-b2

(d95) $$fun2(x,h0,h1,h2,h3,b2) := \frac{\left(\frac{q2}{h2}\right)^2 - \left(\frac{q3}{h3}\right)^2}{2*w^2(x)*d^2(x)} + (1-r)*d(x)*(h0+h1+h2) - b2$$

The rigid lid approximation is used in the derivation of some equations, mainly the Froude number conditions. However, we will not assume the rigid lid approximation for calculating the solution.

(c96) rigid_lid: 1=h1+h2+h3

(d96) $$1 = h3 + h2 + h1$$

Hydraulic functional

Now define the hydraulic functional. I define two forms: One for a free surface, and a simplified version assuming a rigid lid. The rigid-lid version is the one investigated by Smeed.

(c97) fun2d(x,h0,h1,h2,h3,b1,b2):=matrix([fun1(x,h0,h1,h2,h3,b1)],[fun2(x,h0,h1,h2,h3,b2)]) $

(c98) fun2d(x,h0,h1,h2,h3,b1,b2)

(d98) $$\begin{bmatrix} \frac{\frac{q1^2}{h1^2} - \frac{q2^2}{h2^2}}{2*d^2(x)*w^2(x)} + (h1+h0)*r*d(x) - b1 \\ \frac{\frac{q2^2}{h2^2} - \frac{q3^2}{h3^2}}{2*d^2(x)*w^2(x)} + (h2+h1+h0)*(1-r)*d(x) - b2 \end{bmatrix}$$

Use the rigid lid approximation to map this functional onto a functional on the 2-dimensional subspace of (h1,h2,h3) defined by the rigid lid condition.

(c99) fun2d_simp(x,h1,h2,b1,b2):=fun2d(x,0,h1,h2,1-h1-h2,b1,b2) $

(c100) fun2d_simp(x,h1,h2,b1,b2)

Stephan Matthiesen D:\SM\Beruf\RedSea\Macsyma\Def 3-layer.mfe

(d100)
$$\begin{bmatrix} \dfrac{\dfrac{q1^2}{h1^2}-\dfrac{q2^2}{h2^2}}{2*d^2(x)*w^2(x)}+h1*r*d(x)-b1 \\ \dfrac{\dfrac{q2^2}{h2^2}-\dfrac{q3^2}{(-h2-h1+1)^2}}{2*d^2(x)*w^2(x)}+(h2+h1)*(1-r)*d(x)-b2 \end{bmatrix}$$

And now the full 3-dimensional version

(c101) fun3d(x,h0,h1,h2,h3,b0,b1,b2,b3):=matrix([fun0(x,h0,h1,h2,h3,b0)],[fun1(x,h0,h1,h2,h3,b1)],[fun2(x,h0,h1,h2,h3,h2)]) $

(c102) fun3d(x,h0,h1,h2,h3,b0,b1,b2,b3)

(d102)
$$\begin{bmatrix} \dfrac{q1^2}{2*h1^2*d^2(x)*w^2(x)}-h0*s*d(x)-b0 \\ \dfrac{\dfrac{q1^2}{h1^2}-\dfrac{q2^2}{h2^2}}{2*d^2(x)*w^2(x)}+(h1+h0)*r*d(x)-b1 \\ \dfrac{\dfrac{q2^2}{h2^2}-\dfrac{q3^2}{h3^2}}{2*d^2(x)*w^2(x)}+(h2+h1+h0)*(1-r)*d(x)-b2 \end{bmatrix}$$

(c103) fun3d_simp(x,h0,h1,h2,b0,b1,b2,b3):=fun3d(x,h0,h1,h2,1-h0-h1-h2,b0,b1,b2,b3) $

(c104) fun3d_simp(x,h0,h1,h2,b0,b1,b2,b3)

(d104)
$$\begin{bmatrix} \dfrac{q1^2}{2*h1^2*d^2(x)*w^2(x)}-h0*s*d(x)-b0 \\ \dfrac{\dfrac{q1^2}{h1^2}-\dfrac{q2^2}{h2^2}}{2*d^2(x)*w^2(x)}+(h1+h0)*r*d(x)-b1 \\ \dfrac{\dfrac{q2^2}{h2^2}-\dfrac{q3^2}{(-h2-h1-h0+1)^2}}{2*d^2(x)*w^2(x)}+(h2+h1+h0)*(1-r)*d(x)-b2 \end{bmatrix}$$

Criticality condition for rigid lid

Control points are points at which different solution sheets of the Bernoulli equations meet, and the solutions are regular. Different sheets meet when the determinant of the gradient matrix vanishes.

(c105) m2d(x,h1,h2):=at(jacobian(flatten(args(fun2d_simp(x,a,b,b1,b2))),[a,b]),[a=h1,b=h2]) $

(c106) m2d(x,h1,h2)

(d106)
$$\begin{bmatrix} r*d(x)-\dfrac{q1^2}{h1^3*d^2(x)*w^2(x)} & \dfrac{q2^2}{h2^3*d^2(x)*w^2(x)} \\ (1-r)*d(x)-\dfrac{q3^2}{(-h2-h1+1)^3*d^2(x)*w^2(x)} & \dfrac{-\dfrac{2*q3^2}{(-h2-h1+1)^3}-\dfrac{2*q2^2}{h2^3}}{2*d^2(x)*w^2(x)}+(1-r)*d(x) \end{bmatrix}$$

(c107) froude_temp(x,h1,h2):=determinant(m2d(x,h1,h2))$

(c108) froude_temp(x,h1,h2)

(d108)
$$\left(r*d(x)-\frac{q1^2}{h1^3*d^2(x)*w^2(x)}\right)*\left(\frac{-\dfrac{2*q3^2}{(-h2-h1+1)^3}-\dfrac{2*q2^2}{h2^3}}{2*d^2(x)*w^2(x)}+(1-r)*d(x)\right)-\frac{q2^2*\left((1-r)*d(x)-\dfrac{q3^2}{(-h2-h1+1)^3*d^2(x)*w^2(x)}\right)}{h2^3*d^2(x)*w^2(x)}$$

A better, more familiar form:

(c109) froude(x,h1,h2):=expandwrt(distrib(froude_temp(x,h1,h2)/d(x)^2),d,2) $

(c110) froude(x,h1,h2)

(d110)
$$-\frac{q3^2*r}{(-h2-h1+1)^3*d^3(x)*w^2(x)}-\frac{q2^2*r}{h2^3*d^3(x)*w^2(x)}-\frac{q2^2*(1-r)}{h2^3*d^3(x)*w^2(x)}-\frac{q1^2*(1-r)}{h1^3*d^3(x)*w^2(x)}$$
$$+\frac{q2^2*q3^2}{(-h2-h1+1)^3*h2^3*d^6(x)*w^4(x)}+\frac{q1^2*q3^2}{h1^3*(-h2-h1+1)^3*d^6(x)*w^4(x)}+\frac{q1^2*q2^2}{h1^3*h2^3*d^6(x)*w^4(x)}+(1-r)*r$$

Bring this into simpler form by defining

```
slfroude:[
        f1=q1^2/(h1^3*d(x)^3*w(x)^2),
(c111)  f2=q2^2/(h2^3*d(x)^3*w(x)^2),
        f3=q3^2/(h3^3*d(x)^3*w(x)^2)
]
```

(d111)
$$\left[f1 = \frac{q1^2}{h1^3 d^3(x) w^2(x)},\ f2 = \frac{q2^2}{h2^3 d^3(x) w^2(x)},\ f3 = \frac{q3^2}{h3^3 d^3(x) w^2(x)} \right]$$

(c112) fullratsubst(ineq_reverse(slfroude),subst(h3,1-h1-h2,froude(x,h1,h2)))

(d112)
$$-r^2 + (-f3 + f1 + 1)r + (f2 + f1)f3 + (f1 - 1)f2 - f1$$

Control condition for the free surface

The same for the full equations.

(c113) m3d(x,h0,h1,h2):=at(jacobian(flatten(args(fun3d_simp(x,a,b,c,b0,b1,b2,b3))),[a,b,c]),[a=h0,b=h1,c=h2]) $

(c114) m3d(x,h0,h1,h2)

(d114)
$$\begin{bmatrix} -s\,d(x) & -\dfrac{q1^2}{h1^3 d^2(x) w^2(x)} & 0 \\ r\,d(x) & r\,d(x) - \dfrac{q1^2}{h1^3 d^2(x) w^2(x)} & \dfrac{q2^2}{h2^3 d^2(x) w^2(x)} \\ (1-r)\,d(x) - \dfrac{q3^2}{(-h2-h1-h0+1)^3 d^2(x) w^2(x)} & (1-r)\,d(x) - \dfrac{q3^2}{(-h2-h1-h0+1)^3 d^2(x) w^2(x)} & \dfrac{-\dfrac{2q3^2}{(-h2-h1-h0+1)^3} - \dfrac{2q2^2}{h2^3}}{2 d^2(x) w^2(x)} + \end{bmatrix}$$

(c115) froude3d_temp(x,h0,h1,h2):=determinant(m3d(x,h0,h1,h2))$

(c116) froude3d_temp(x,h0,h1,h2)

(d116)
$$\frac{q1^2 \left(r\,d(x) \left(\dfrac{-\dfrac{2q3^2}{(-h2-h1-h0+1)^3} - \dfrac{2q2^2}{h2^3}}{2 d^2(x) w^2(x)} + (1-r)\,d(x) \right) - \dfrac{q2^2 \left((1-r)\,d(x) - \dfrac{q3^2}{(-h2-h1-h0+1)^3 d^2(x) w^2(x)} \right)}{h2^3 d^2(x) w^2(x)} \right)}{h1^3 d^2(x) w^2(x)} - s\,d(x) \left(\left(r\,d(x) - \dfrac{q1^2}{h1^3 d^2(x) w^2(x)} \right) \left(\dfrac{-\dfrac{2q3^2}{(-h2-h1-h0+1)^3} - \dfrac{2q2^2}{h2^3}}{2 d^2(x) w^2(x)} + (1-r)\,d(x) \right) - \dfrac{q2^2 \left((1-r)\,d(x) - \dfrac{q3^2}{(-h2-h1-h0+1)^3 d^2(x) w^2(x)} \right)}{h2^3 d^2(x) w^2(x)} \right)$$

(c117) froude3d(x,h0,h1,h2,h3):=expand(subst(h3,1-h0-h1-h2,froude3d_temp(x,h0,h1,h2))/(d(x)^3)) $

(c118) froude3d(x,h0,h1,h2,h3)

(d118)
$$\frac{q3^2 r s}{h3^3 d^3(x) w^2(x)} - \frac{q1^2 r s}{h1^3 d^3(x) w^2(x)} + \frac{q2^2 s}{h2^3 d^3(x) w^2(x)} + \frac{q1^2 s}{h1^3 d^3(x) w^2(x)} - \frac{q1^2 r^2}{h1^3 d^3(x) w^2(x)} + \frac{q1^2 r}{h1^3 d^3(x) w^2(x)} - \frac{q2^2 q3^2 s}{h2^3 h3^3 d^6(x) w^4(x)} - \frac{q1^2 q3^2 s}{h1^3 h3^3 d^6(x) w^4(x)} - \frac{q1^2 q2^2 s}{h1^3 h2^3 d^6(x) w^4(x)} - \frac{q1^2 q3^2 r}{h1^3 h3^3 d^6(x) w^4(x)} - \frac{q1^2 q2^2}{h1^3 h2^3 d^6(x) w^4(x)} + \frac{q1^2 q2^2 q3^2}{h1^3 h2^3 h3^3 d^9(x) w^6(x)} + r^2 s - r s$$

(c119) fullratsubst(ineq_reverse(slfroude),froude3d(x,h0,h1,h2,h3))

(d119)
$$\left(r^2 + (f3 - f1 - 1)r + (-f2 - f1)f3 + (1 - f1)f2 + f1\right)s - f1 r^2 + (f1 - f1 f3)r + f1 f2 f3 - f1 f2$$

The bracket in the first term is equivalent to the 2-dimensioanl situation. As s>>r, the both versions are approximately equal.

(c267) remfunction(froude_temp,froude3d_temp)

(d267) [froude_temp, froude3d_temp]

The equations in explicit form

Stephan Matthiesen D:\SM\Beruf\RedSea\Macsyma\Def 3-layer.mfe

The flow rates can be determined by solving a set of equations at the three control points (or, for [0,-2], for the geometric control and the strait entrances).

For the rigid lid with prescribed net flux, there are 8 equations for the 8 variables q1, q2, q3, h1_rs, h2_rs, h1_s, h2_s, h1_ga. These are the equations below, excluding eq0_rs, eq0_s and eq0_ga, plus q=q1+q2+q3.

For the free surface we have 10 equations for the 10 quantities q1, q2, q3, h0_rs, h1_rs, h2_rs, h0_s, h1_s, h2_s, h1_ga.

(c120) eq_0rs: 0=fun0(xrs,h0rs,h1rs,h2rs,inf,b0)

(d120)
$$0=\frac{q1^2}{2*h1rs^2*d^2(xrs)*w^2(xrs)}-h0rs*s*d(xrs)-b0$$

(c121) eq_1rs: 0=fun1(xrs,h0rs,h1rs,h2rs,inf,b1)

(d121)
$$0=\frac{\frac{q1^2}{h1rs^2}-\frac{q2^2}{h2rs^2}}{2*d^2(xrs)*w^2(xrs)}+(h1rs+h0rs)*r*d(xrs)-b1$$

(c122) eq_2rs: 0=fun2(xrs,h0rs,h1rs,h2rs,inf,b2)

(d122)
$$0=\frac{\frac{q2^2}{h2rs^2}-\frac{q3^2}{\infty^2}}{2*d^2(xrs)*w^2(xrs)}+(h2rs+h1rs+h0rs)*(1-r)*d(xrs)-b2$$

(c123) eq_0s: 0=fun0(xs,h0s,h1s,h2s,1-h0s-h1s-h2s,b0)

(d123)
$$0=\frac{q1^2}{2*h1s^2*d^2(xs)*w^2(xs)}-h0s*s*d(xs)-b0$$

(c124) eq_1s: 0=fun1(xs,h0s,h1s,h2s,1-h0s-h1s-h2s,b1)

(d124)
$$0=\frac{\frac{q1^2}{h1s^2}-\frac{q2^2}{h2s^2}}{2*d^2(xs)*w^2(xs)}+(h1s+h0s)*r*d(xs)-b1$$

(c125) eq_2s: 0=fun2(xs,h0s,h1s,h2s,1-h0s-h1s-h2s,b2)

(d125)
$$0=\frac{\frac{q2^2}{h2s^2}-\frac{q3^2}{(-h2s-h1s-h0s+1)^2}}{2*d^2(xs)*w^2(xs)}+(h2s+h1s+h0s)*(1-r)*d(xs)-b2$$

(c126) eq_0ga: 0=fun0(xga,h0ga,h1ga,inf,inf,b0)

(d126)
$$0=\frac{q1^2}{2*h1ga^2*d^2(xga)*w^2(xga)}-h0ga*s*d(xga)-b0$$

(c127) eq_1ga: 0=fun1(xga,h0ga,h1ga,inf,inf,b1)

(d127)
$$0=\frac{\frac{q1^2}{h1ga^2}-\frac{q2^2}{\infty^2}}{2*d^2(xga)*w^2(xga)}+(h1ga+h0ga)*r*d(xga)-b1$$

(c128) froude_s: 0=froude(xs,h1s,h2s)

(d128)
$$0=-\frac{q3^2*r}{(-h2s-h1s+1)^3*d^3(xs)*w^2(xs)}-\frac{q2^2*r}{h2s^3*d^3(xs)*w^2(xs)}-\frac{q2^2*(1-r)}{h2s^3*d^3(xs)*w^2(xs)}-\frac{q1^2*(1-r)}{h1s^3*d^3(xs)*w^2(xs)}$$
$$+\frac{q2^2*q3^2}{(-h2s-h1s+1)^3*h2s^3*d^6(xs)*w^4(xs)}+\frac{q1^2*q3^2}{h1s^3*(-h2s-h1s+1)^3*d^6(xs)*w^4(xs)}+\frac{q1^2*q2^2}{h1s^3*h2s^3*d^6(xs)*w^4(xs)}+(1-r)*r$$

(c129) froude_rs: 0=expand(limit((froude(xrs,h1rs,h2rs),1-h1rs-h2rs,inf))

(d129)
$$0=\frac{q1^2*r}{h1rs^3*d^3(xrs)*w^2(xrs)}-\frac{q2^2}{h2rs^3*d^3(xrs)*w^2(xrs)}-\frac{q1^2}{h1rs^3*d^3(xrs)*w^2(xrs)}+\frac{q1^2*q2^2}{h1rs^3*h2rs^3*d^6(xrs)*w^4(xrs)}-r^2+r$$

(c130) froude_ga: 0=expand(ratsimp(limit(froude(xga,h1ga,h2ga),h2ga,inf)/(1-r)))

(d130)
$$0=r-\frac{q1^2}{h1ga^3*d^3(xga)*w^2(xga)}$$

Or, in a more familar form:

(c131) fullratsubst(ineq_reverse(slfroude),subst([h1s=h1,h2s=h2,xs=x],subst(h3,1-h1s-h2s,froude_s)))

(d131)
$$0=-r^2+(-f3+f1+1)*r+(f2+f1)*f3+(f1-1)*f2-f1$$

(c132) fullratsubst(ineq_reverse(slfroude),subst([h1rs=h1,h2rs=h2,xrs=x],froude_rs))

(d132) $$0 = -r^2 + (f1 + 1)*r + (f1 - 1)*f2 - f1$$

(c133) fullratsubst(ineq_reverse(slfroude),subst([h1ga=h1,xga=x],froude_ga))

(d133) $$0 = r - f1$$

Solution for the different regimes

Solve the equations for each regime. From the way the variables occur in the equations, it is natural to start with the GA equations, then the RS, and finally the sill equations. For the two interfaces, we assume that h0(<<h1) can be neglected.

GA solutions

Start by solving the equations at the GA for as many variables as possible in each case.

Cases (a) and (b), GA solution

(c134) eqnlist_gaab:limit(subst(q1sq,q1^2,[eq_1ga,froude_ga])), h0ga:0

(d134) $$\left[0 = \frac{\left(2*h1ga^3*r*d^3(xga) - 2*b1*h1ga^2*d^2(xga)\right)*w^2(xga) + q1sq}{2*h1ga^2*d^2(xga)*w^2(xga)}, 0 = r - \frac{q1sq}{h1ga^3*d^3(xga)*w^2(xga)}\right]$$

(c135) sol_q1h1ga_ab: solve(eqnlist_gaab,[q1sq,h1ga])

(d135) $$\left[[h1ga = 0, q1sq = 0], \left[q1sq = \frac{8*b1^3*w^2(xga)}{27*r^2}, h1ga = \frac{2*b1}{3*r*d(xga)}\right]\right]$$

(c136) sol_q1_a: part(sol_q1h1ga_ab,2,1)

(d136) $$q1sq = \frac{8*b1^3*w^2(xga)}{27*r^2}$$

(c137) sol_q1_b:sol_q1_a $

(c138) sol_h1ga_a: part(sol_q1h1ga_ab,2,2)

(d138) $$h1ga = \frac{2*b1}{3*r*d(xga)}$$

(c139) sol_h1ga_b:sol_h1ga_a $

(c140) remvalue(eqnlist_gaab,sol_q1h1ga_ab) $

For outflow in top layer, h0ga is equal to the GA value, for inflow it has to be calculated from the Bernoulli

Note: for outflow this does not lead to consistent equations! However, there should be no outflow in this situation. For the model, it is best to use the same surface connection for in- and outflow (but check whether the model has outflow in these cases).

(c141) sol_h0ga_ao: h0ga=h0gax

(d141) $$h0ga = h0gax$$

(c142) sol_h0ga_bo: sol_h0ga_ao $

(c143) temp: first(expand(solve(eq_0ga,h0ga)))

(d143) $$h0ga = \frac{q1^2}{2*h1ga^2*s*d^3(xga)*w^2(xga)} - \frac{b0}{s*d(xga)}$$

(c144) sol_h0ga_a: subst(sol_q1_a,subst(sol_h1ga_a, subst(q1sq,q1^2,temp)))

(d144) $$h0ga = \frac{b1}{3*s*d(xga)} - \frac{b0}{s*d(xga)}$$

(c145) sol_h0ga_b: sol_h0ga_a $

(c146) remvalue(temp) $

For cases (a) and (b), we now have the following quantities: b0, b1, q1, h1ga, h0ga. For (b) also b2.

Note: strictly this is only true for inflow. However, the outflow is irrelevant, so for reasons of simplicity and model stability it is best to assume that in- and outflow follow the same equations.

Case (c), GA solution, outflow

(c147) temp: eliminate(limit([eq_0ga,eq_1ga]),[q1])

C:\Programme\Macsyma\Macsyma2\share\elim.fas being loaded.
C:\Programme\Macsyma\Macsyma2\library\result.fas being loaded.

(d147) $$\left[4*h1ga^4*d^4(xga)*\left((h0ga*s + h1ga*r + h0ga*r)*d(xga) - b1 + b0\right)^2*w^4(xga)\right]$$

(c148) sol_h0ga_co: h0ga=h0gax

(d148) $$h0ga = h0gax$$

(c149) sol_h1ga_co: first(solve(temp,h1ga))

(d149) $$h1ga = -\frac{(h0ga*s + h0ga*r)*d(xga) - b1 + b0}{r*d(xga)}$$

(c150) sol_q1_co: first(solve(subst(q1sq,q1^2,limit(eq_1ga)),q1sq))

(d150) $$q1sq = \left(\left(-2*h1ga^3 - 2*h0ga*h1ga^2\right)*r*d^3(xga) + 2*b1*h1ga^2*d^2(xga)\right)*w^2(xga)$$

(c151) sol_q1_co2: factorsum(subst(sol_h1ga_co,sol_q1ga_co))

(d151) sol_q1ga_co

(c152) remvalue(temp)$

For case (c), outflow, we now have the following quantities: b0, b1, b2, q1, h1ga, h0ga.

Case (c), GA solution, inflow

In this case, h0ga is not determined in the basin, but has to be calculated. With only two equations, we cannot solve for q1. h0ga and h1ga can only be calculated after the RS equations have been solved (they are not needed for the RS equations)

(c153) sol_h0ga_ci: subst(q1sq,q1^2,first(expand(solve(eq_0ga,h0ga))))

(d153) $$h0ga = \frac{q1sq}{2*h1ga^2*s*d^3(xga)*w^2(xga)} - \frac{b0}{s*d(xga)}$$

(c154) temp: subst(q1sq,q1^2,limit(eq_1ga)), h0ga:0

(d154) $$0 = \frac{\left(2*h1ga^3*r*d^3(xga) - 2*b1*h1ga^2*d^2(xga)\right)*w^2(xga) + q1sq}{2*h1ga^2*d^2(xga)*w^2(xga)}$$

(c155) sol_h1ga_ci_imp: collectterms(expand(multthru(temp,denom(last(temp)))),h1ga)

C:\Programme\Macsyma\Macsyma2\share\facex1.fas being loaded.
C:\Programme\Macsyma\Macsyma2\share\FACEXP.fas being loaded.
C:\Programme\Macsyma\Macsyma2\share\GNDECL.fas being loaded.

(d155) $$0 = 2*h1ga^3*r*d^3(xga)*w^2(xga) - 2*b1*h1ga^2*d^2(xga)*w^2(xga) + q1sq$$

(c156) remvalue(temp) $

For case (c) inflow, we have now an implicit expression for h1ga (to be solved by a Newton Raphson method), and an explicit equation for h0ga, both under the assumption that q1 is known.

Case (d), GA solution, outflow

On this case, b1 is not known from the basin conditions, i.e. there are now 3 unknowns (b1,q1,h1ga) which have to be solved using the three available equations.

(c157) sol_h0ga_do: h0ga=h0gax

(d157) $$h0ga = h0gax$$

(c158) temp: limit([eq_1ga,froude_ga]), h0ga:0

(d158) $$\left[0 = \frac{\left(2*h1ga^3*r*d^3(xga) - 2*b1*h1ga^2*d^2(xga)\right)*w^2(xga) + q1^2}{2*h1ga^2*d^2(xga)*w^2(xga)}, 0 = r - \frac{q1^2}{h1ga^3*d^3(xga)*w^2(xga)}\right]$$

(c159) eqnlist_gad: subst(q1sq,q1^2,cons(eq_0ga,temp))

(d159) $$\left[0 = \frac{q1sq}{2*h1ga^2*d^2(xga)*w^2(xga)} - h0ga*s*d(xga) - b0,\ 0 = \frac{\left(2*h1ga^3*r*d^3(xga) - 2*b1*h1ga^2*d^2(xga)\right)*w^2(xga) + q1sq}{2*h1ga^2*d^2(xga)*w^2(xga)},\ 0 = r - \frac{q1sq}{h1ga^3*d^3(xga)*w^2(xga)}\right]$$

(c160) temp:solve(eqnlist_gad,[b1,h1ga,q1sq])

$$[[b1 = \%r1,\ h1ga = 0,\ q1sq = 0],$$

(d160)

$$\left[q1sq = \frac{\left(8*h0ga^3*s^3*d^3(xga) + 24*b0*h0ga^2*s^2*d^2(xga) + 24*b0^2*h0ga*s*d(xga) + 8*b0^3\right)*w^2(xga)}{r^2},\right.$$

$$h1ga = \frac{2*h0ga*s*d(xga) + 2*b0}{r*d(xga)},$$

$$\left.b1 = r^2*\left(\frac{\left(8*h0ga^3*s^3*d^3(xga) + 24*b0*h0ga^2*s^2*d^2(xga) + 24*b0^2*h0ga*s*d(xga) + 8*b0^3\right)*w^2(xga)}{r^2} + \frac{2*\left(2*h0ga*s*d(xga) + 2*b0\right)^3*w^2(xga)}{r^2}\right) \Big/ \left(2*\left(2*h0ga*s*d(xga) + 2*b0\right)^2*w^2(xga)\right)\right]]$$

This tells me that there is a solution, however the given solution is not very helpful...

(c161) sol_h1ga_do: part(temp,2,2)

(d161)

$$h1ga = \frac{2*h0ga*s*d(xga) + 2*b0}{r*d(xga)}$$

(c162) sol_q1_do: first(solve(last(eqnlist_gad),q1sq))

(d162)

$$q1sq = h1ga^3*r*d^3(xga)*w^2(xga)$$

(c163) sol_b1_do: first(expand(solve(part(eqnlist_gad,2),b1)))

(d163)

$$b1 = \frac{q1sq}{2*h1ga^2*d^2(xga)*w^2(xga)} + h1ga*r*d(xga)$$

(c164) remvalue(temp)$

For case (d) outflow, we now have the following quantities: b0, b1, b2, q1, h1ga, h0ga.

Case (d), GA solution, inflow

On this case, neither b1 nor h0ga are not known from the basin conditions, i.e. there are now 4 unknowns (b1,q1,h1ga, h0ga) with three equations. These equations cannot be solved unless q1 is known.

(c165) sol_h1ga_di: last(solve(last(eqnlist_gad), h1ga))

(d165)

$$h1ga = \frac{q1sq^{1/3}}{r^{1/3}*d(xga)*w^{2/3}(xga)}$$

(c166) sol_h0ga_di: first(expand(solve(first(eqnlist_gad),h0ga)))

(d166)

$$h0ga = \frac{q1sq}{2*h1ga^2*s*d^3(xga)*w^2(xga)} - \frac{b0}{s*d(xga)}$$

(c167) sol_b1_di: first(expand(solve(part(eqnlist_gad,2),b1)))

(d167)

$$b1 = \frac{q1sq}{2*h1ga^2*d^2(xga)*w^2(xga)} + h1ga*r*d(xga)$$

We should eliminate all GA quantities to obtain a relation between b1 and q1sq, to use it in the RS solutions:

(c168) rel_b1q1_di: 0=first(eliminate([sol_h1ga_di,sol_b1_di], [h1ga]))/d(xga)^3

(d168)

$$0 = 2*b1*q1sq^{2/3}*r^{1/3}*w^{8/3}(xga) - 3*q1sq*r*w^2(xga)$$

(c169) remvalue(eqnlist_gad)$

For case (d) inflow, we now have explicit equations for h0ga, h1ga, b1, assuming that q1 is known, and a relation between b1 and q1 involving only known quantities.

RS equations

We want to get to a situation where the following quantities are known: b0, b1, b2, q1, q2, h0ga, h0rs, h1ga, h1rs, h2rs. The 4 equations at the sill can then be used to solve for: q3, h0s, h1s, h2s.

Stephan Matthiesen D:\SM\Beruf\RedSea\Macsyma\Def 3-layer.mfe

Current Situation:

For cases (a,b) the following quantities are known: b0, b1, q1, h0ga, h1ga, h0rs.

For cases (c out, d out) the following quantities are known: b0, b1, q1, h0ga, h1ga.

For case (c in) the following quantities are known: b0, b1, h0rs. (h1ga, h0ga can be calculated when q1 is known)

For case (d in) the following quantities are known: b0, h0rs, and a relation q1-b1. (b1, h1ga, h0ga can be calculated when q1 is known)

It may be possible to combine the last two cases by taking b1 from the last timestep in the RS for (d in).

First define the list of equations that we can use.

(c170) temp: limit([eq_1rs,eq_2rs,froude_rs]), h0rs:0

(d170)

$$\left[0 = -\frac{q2^2}{2*h2rs^2*d^2(xrs)*w^2(xrs)} + \frac{q1^2}{2*h1rs^2*d^2(xrs)*w^2(xrs)} + h1rs*r*d(xrs) - b1,\right.$$

$$0 = -\frac{\left(\left(\left(2*h2rs^3 + 2*h1rs*h2rs^2\right)*r - 2*h2rs^3 - 2*h1rs*h2rs^2\right)*d^3(xrs) + 2*b2*h2rs^2*d^2(xrs)\right)*w^2(xrs) - q2^2}{2*h2rs^2*d^2(xrs)*w^2(xrs)},$$

$$\left.0 = \frac{q1^2*r}{h1rs^3*d^3(xrs)*w^2(xrs)} - \frac{q2^2}{h2rs^3*d^3(xrs)*w^2(xrs)} - \frac{q1^2}{h1rs^3*d^3(xrs)*w^2(xrs)} + \frac{q1^2*q2^2}{h1rs^3*h2rs^3*d^6(xrs)*w^4(xrs)} - r^2 + r\right]$$

(c171) eqnlist_rsacd: subst(q2sq,q2^2,subst(q1sq,q1^2,cons(eq_0rs,temp)))

(d171)

$$\left[0 = \frac{q1sq}{2*h1rs^2*d^2(xrs)*w^2(xrs)} - h0rs*s*d(xrs) - b0,\right.$$

$$0 = -\frac{q2sq}{2*h2rs^2*d^2(xrs)*w^2(xrs)} + \frac{q1sq}{2*h1rs^2*d^2(xrs)*w^2(xrs)} + h1rs*r*d(xrs) - b1,$$

$$0 = -\frac{\left(\left(\left(2*h2rs^3 + 2*h1rs*h2rs^2\right)*r - 2*h2rs^3 - 2*h1rs*h2rs^2\right)*d^3(xrs) + 2*b2*h2rs^2*d^2(xrs)\right)*w^2(xrs) - q2sq}{2*h2rs^2*d^2(xrs)*w^2(xrs)},$$

$$\left.0 = \frac{q1sq*r}{h1rs^3*d^3(xrs)*w^2(xrs)} - \frac{q2sq}{h2rs^3*d^3(xrs)*w^2(xrs)} - \frac{q1sq}{h1rs^3*d^3(xrs)*w^2(xrs)} + \frac{q1sq*q2sq}{h1rs^3*h2rs^3*d^6(xrs)*w^4(xrs)} - r^2 + r\right]$$

(c172) eqnlist_rsb: rest(eqnlist_rsacd,-1)

(d172)

$$\left[0 = \frac{q1sq}{2*h1rs^2*d^2(xrs)*w^2(xrs)} - h0rs*s*d(xrs) - b0,\right.$$

$$0 = -\frac{q2sq}{2*h2rs^2*d^2(xrs)*w^2(xrs)} + \frac{q1sq}{2*h1rs^2*d^2(xrs)*w^2(xrs)} + h1rs*r*d(xrs) - b1,$$

$$\left.0 = -\frac{\left(\left(\left(2*h2rs^3 + 2*h1rs*h2rs^2\right)*r - 2*h2rs^3 - 2*h1rs*h2rs^2\right)*d^3(xrs) + 2*b2*h2rs^2*d^2(xrs)\right)*w^2(xrs) - q2sq}{2*h2rs^2*d^2(xrs)*w^2(xrs)}\right]$$

(c173) remvalue(temp) $

Case (a), RS solution

Known: b0, b1, q1, h0rs. Wanted: h2, q2, h1ra, h2rs

(c174) sol_h0rs_a: h0rs=h0rsx

(d174) $h0rs = h0rsx$

(c175) sol_h1rs_a: h1rs=max(map(rhs,solve(first(eqnlist_rsacd),h1rs)))

(d175)

$$h1rs = \max\left(\frac{\sqrt{\frac{q1sq}{h0rs*s*d(xrs) + b0}}}{\sqrt{2}*d(xrs)*w(xrs)}, -\frac{\sqrt{\frac{q1sq}{h0rs*s*d(xrs) + b0}}}{\sqrt{2}*d(xrs)*w(xrs)}\right)$$

(c176) temp:eliminate(part(eqnlist_rsacd,[2,4]),[q2sq])

(d176)

$$\left[h2rs^2*\left(\left(\left(h1rs^5*h2rs*r^2 + \left(2*h1rs^6 - h1rs^5*h2rs\right)*r\right)*d^6(xrs) - 2*b1*h1rs^5*d^5(xrs)\right)*w^4(xrs)\right.$$

$$+\left(\left(\left(-h1rs^2*h2rs - 2*h1rs^3\right)*q1sq*r + \left(h1rs^2*h2rs + h1rs^3\right)*q1sq\right)*d^3(xrs) + 2*b1*h1rs^2*q1sq*d^2(xrs)\right)$$

$$\left.*w^2(xrs) - q1sq^2\right)\Big]$$

(c177) temp2:temp/(h2rs^max(powers(temp,h2rs)))

C:\Programme\Macsyma\Macsyma2\share\powers.fas being loaded.

(d177)
$$\left[\left(\left(h1rs^5*h2rs*r^2+\left(2*h1rs^6-h1rs^5*h2rs\right)*r\right)*d^6(xrs)-2*b1*h1rs^5*d^5(xrs)\right)*w^4(xrs)+\left(\left(\left(-h1rs^2*h2rs-2*h1rs^3\right)*q1sq*r+\left(h1rs^2*h2rs+h1rs^3\right)*q1sq\right)*d^3(xrs)+2*b1*h1rs^2*q1sq*d^2(xrs)\right)*w^2(xrs)-q1sq^2\right]_j$$

(c178) sol_h2rs_a: first(factorsum(solve(temp2,h2rs)))

(d178)
$$h2rs=-\frac{\left(h1rs^3*d^3(xrs)*w^2(xrs)-q1sq\right)*\left(2*h1rs^2*d^2(xrs)*(h1rs*r*d(xrs)-b1)*w^2(xrs)+q1sq\right)}{h1rs^2*(r-1)*d^3(xrs)*w^2(xrs)*\left(h1rs^3*r*d^3(xrs)*w^2(xrs)-q1sq\right)}$$

(c179) remvalue(temp,temp2)$

(c180) sol_q2_a: factorsum(first(solve(part(eqnlist_rsacd,2),q2sq)))

(d180)
$$q2sq=\frac{h2rs^2*\left(2*h1rs^2*d^2(xrs)*(h1rs*r*d(xrs)-b1)*w^2(xrs)+q1sq\right)}{h1rs^2}$$

(c181) sol_b2_a: factorsum(first(solve(part(eqnlist_rsacd,3),b2)))

(d181)
$$b2=-\frac{2*h2rs^2*(h2rs+h1rs)*(r-1)*d^3(xrs)*w^2(xrs)-q2sq}{2*h2rs^2*d^2(xrs)*w^2(xrs)}$$

For case (a), we now have all 10 variables: b0, b1, h0rs (from boundary); q1, h0ga, h1ga (from GA) and b2, q2, h1rs, h2rs (from RS)

Case (b), RS solution

Known: b0, b1, b2, q1, h0rs. Wanted: q2, h1ra, h2rs

(c182) sol_h0rs_b: h0rs=h0rsx

(d182)
$$h0rs=h0rsx$$

(c183) sol_h1rs_b: h1rs=max(map(rhs,solve(first(eqnlist_rsb),h1rs)))

(d183)
$$h1rs=\max\left(\frac{\sqrt{\frac{q1sq}{h0rs*s*d(xrs)+b0}}}{\sqrt{2}*d(xrs)*w(xrs)},-\frac{\sqrt{\frac{q1sq}{h0rs*s*d(xrs)+b0}}}{\sqrt{2}*d(xrs)*w(xrs)}\right)$$

(c184) temp:eliminate(rest(eqnlist_rsb),[q2sq])

(d184)
$$\left[h2rs^2*\left(\left(\left(2*h1rs^2*h2rs*r-2*h1rs^2*h2rs-2*h1rs^3\right)*d^3(xrs)+\left(2*b2+2*b1\right)*h1rs^2*d^2(xrs)\right)*w^2(xrs)-q1sq\right)\right]_j$$

(c185) temp2:temp/(h2rs^max(powers(temp,h2rs)))

(d185)
$$\left[\left(\left(2*h1rs^2*h2rs*r-2*h1rs^2*h2rs-2*h1rs^3\right)*d^3(xrs)+\left(2*b2+2*b1\right)*h1rs^2*d^2(xrs)\right)*w^2(xrs)-q1sq\right]_j$$

(c186) sol_h2rs_b: first(solve(temp2,h2rs))

(d186)
$$h2rs=\frac{\left(2*h1rs^3*d^3(xrs)+\left(-2*b2-2*b1\right)*h1rs^2*d^2(xrs)\right)*w^2(xrs)+q1sq}{\left(2*h1rs^2*r-2*h1rs^2\right)*d^3(xrs)*w^2(xrs)}$$

(c187) remvalue(temp,temp2)$

(c188) sol_q2_b: factorsum(first(solve(part(eqnlist_rsb,2),q2sq)))

(d188)
$$q2sq=\frac{h2rs^2*\left(2*h1rs^2*d^2(xrs)*(h1rs*r*d(xrs)-b1)*w^2(xrs)+q1sq\right)}{h1rs^2}$$

For case (b), we now have all 10 variables: b0, b1, b2, h0rs (from boundary); q1, h0ga, h1ga (from GA) and q2, h1rs, h2rs (from RS)

(c189) remvalue(eqnlist_rsb) $

Case (c) inflow, RS solution

Known: b0, b1, b2, h0rs. Wanted: b2, q1, q2, h1ra, h2rs

(c190) sol_h0rs_ci: h0rs=h0rsx

(d190)
$$h0rs=h0rsx$$

(c191) temp: factor(eliminate(eqnlist_rsacd,[q1sq,q2sq]))

$$\left[h1rs^4*h2rs^2*d^4(xrs)*\left(4*h0rs^2*s^2*d^2(xrs)+2*h0rs*h2rs*r*s*d^2(xrs)+4*h0rs*h1rs*r*s*d^2(xrs)-2*h0rs*h2rs*s*d^2(xrs)-2*h0rs*h1rs*s*d^2(xrs)-h1rs*h2rs*r^2*d^2(xrs)+h1rs*h2rs*r*d^2(xrs)-2*h1rs^2*r*d^2(xrs)-4*b1*h0rs*s*d(xrs)+8*b0*h0rs*s*d(xrs)+2*b0*h2rs*r*d(xrs)+4*b0*h1rs*r*d(xrs)-2*b0*h2rs*d(xrs)+2*b1*h1rs*d(xrs)-2*b0*h1rs*d(xrs)-4*b0*b1+4*b0^2\right)*w^4(xrs),h1rs^2*h2rs^2*d^4(xrs)*\left(6*h0rs*h2rs*r*s*d^2(xrs)+4*h0rs*h1rs*r*s*d^2(xrs)-6*h0rs*h2rs*s*d^2(xrs)-4*h0rs*h1rs*s*d^2(xrs)-h1rs*h2rs*r^2*d^2(xrs)-h1rs*h2rs*r*d^2(xrs)-2*h1rs^2*r*d^2(xrs)+2*h1rs*h2rs*d^2(xrs)+2*h1rs^2*d^2(xrs)+4*b2*h0rs*s*d(xrs)+6*b0*h2rs*r*d(xrs)+4*b0*h1rs*r*d(xrs)-6*b0*h2rs*d(xrs)-2*b2*h1rs*d(xrs)-4*b0*h1rs*d(xrs)+4*b0*b2\right)*w^4(xrs)\right]_1^1 \tag{d191}$$

(c192) temp1: 0=first(temp) $

(c193) temp2: 0=last(temp) $

(c194) temp1

$$0=h1rs^4*h2rs^2*d^4(xrs)*\left(4*h0rs^2*s^2*d^2(xrs)+2*h0rs*h2rs*r*s*d^2(xrs)+4*h0rs*h1rs*r*s*d^2(xrs)-2*h0rs*h2rs*s*d^2(xrs)-2*h0rs*h1rs*s*d^2(xrs)-h1rs*h2rs*r^2*d^2(xrs)+h1rs*h2rs*r*d^2(xrs)-2*h1rs^2*r*d^2(xrs)-4*b1*h0rs*s*d(xrs)+8*b0*h0rs*s*d(xrs)+2*b0*h2rs*r*d(xrs)+4*b0*h1rs*r*d(xrs)-2*b0*h2rs*d(xrs)+2*b1*h1rs*d(xrs)-2*b0*h1rs*d(xrs)-4*b0*b1+4*b0^2\right)*w^4(xrs) \tag{d194}$$

(c195) temp3:temp1/part(temp1,2,allbut(4))

$$0=4*h0rs^2*s^2*d^2(xrs)+2*h0rs*h2rs*r*s*d^2(xrs)+4*h0rs*h1rs*r*s*d^2(xrs)-2*h0rs*h2rs*s*d^2(xrs)-2*h0rs*h1rs*s*d^2(xrs)-h1rs*h2rs*r^2*d^2(xrs)+h1rs*h2rs*r*d^2(xrs)-2*h1rs^2*r*d^2(xrs)-4*b1*h0rs*s*d(xrs)+8*b0*h0rs*s*d(xrs)+2*b0*h2rs*r*d(xrs)+4*b0*h1rs*r*d(xrs)-2*b0*h2rs*d(xrs)+2*b1*h1rs*d(xrs)-2*b0*h1rs*d(xrs)-4*b0*b1+4*b0^2 \tag{d195}$$

(c196) temp2

$$0=h1rs^2*h2rs^2*d^4(xrs)*\left(6*h0rs*h2rs*r*s*d^2(xrs)+4*h0rs*h1rs*r*s*d^2(xrs)-6*h0rs*h2rs*s*d^2(xrs)-4*h0rs*h1rs*s*d^2(xrs)-h1rs*h2rs*r^2*d^2(xrs)-h1rs*h2rs*r*d^2(xrs)-2*h1rs^2*r*d^2(xrs)+2*h1rs*h2rs*d^2(xrs)+2*h1rs^2*d^2(xrs)+4*b2*h0rs*s*d(xrs)+6*b0*h2rs*r*d(xrs)+4*b0*h1rs*r*d(xrs)-6*b0*h2rs*d(xrs)-2*b2*h1rs*d(xrs)-4*b0*h1rs*d(xrs)+4*b0*b2\right)*w^4(xrs) \tag{d196}$$

(c197) temp4: temp2/part(temp2,2,allbut(4))

$$0=6*h0rs*h2rs*r*s*d^2(xrs)+4*h0rs*h1rs*r*s*d^2(xrs)-6*h0rs*h2rs*s*d^2(xrs)-4*h0rs*h1rs*s*d^2(xrs)-h1rs*h2rs*r^2*d^2(xrs)-h1rs*h2rs*r*d^2(xrs)-2*h1rs^2*r*d^2(xrs)+2*h1rs*h2rs*d^2(xrs)+2*h1rs^2*d^2(xrs)+4*b2*h0rs*s*d(xrs)+6*b0*h2rs*r*d(xrs)+4*b0*h1rs*r*d(xrs)-6*b0*h2rs*d(xrs)-2*b2*h1rs*d(xrs)-4*b0*h1rs*d(xrs)+4*b0*b2 \tag{d197}$$

The best way to proceed is probably to take h2 from previous step, then solve one of the equations for h1, and then the other for h2

(c198) sol_h2rs_ci: factorsum(first(solve(temp4,h2rs)))

$$h2rs=-\frac{2*(h1rs*(r-1)*d(xrs)+b2)*((2*h0rs*s-h1rs)*d(xrs)+2*b0)}{(r-1)*d(xrs)*(6*h0rs*s*d(xrs)-h1rs*r*d(xrs)-2*h1rs*d(xrs)+6*b0)} \tag{d198}$$

(c199) temp5: multthru(denom(rhs(sol_h2rs_ci)),subst(sol_h2rs_ci,temp3))

$$\begin{aligned}0=&-4*h0rs*r*s*d^2(xrs)*(h1rs*(r-1)*d(xrs)+b2)*((2*h0rs*s-h1rs)*d(xrs)+2*b0)+4*h0rs*s*d^2(xrs)\\&*(h1rs*(r-1)*d(xrs)+b2)*((2*h0rs*s-h1rs)*d(xrs)+2*b0)+2*h1rs*r^2*d^2(xrs)*(h1rs*(r-1)*d(xrs)+b2)\\&*((2*h0rs*s-h1rs)*d(xrs)+2*b0)-2*h1rs*r*d^2(xrs)*(h1rs*(r-1)*d(xrs)+b2)*((2*h0rs*s-h1rs)*d(xrs)+2*b0)-4*b0*r\\&*d(xrs)*(h1rs*(r-1)*d(xrs)+b2)*((2*h0rs*s-h1rs)*d(xrs)+2*b0)+4*b0*d(xrs)*(h1rs*(r-1)*d(xrs)+b2)\\&*((2*h0rs*s-h1rs)*d(xrs)+2*b0)+4*h0rs^2*(r-1)*s^2*d^3(xrs)*(6*h0rs*s*d(xrs)-h1rs*r*d(xrs)-2*h1rs*d(xrs)+6*b0)+4*h0rs\\&*h1rs*(r-1)*r*s*d^3(xrs)*(6*h0rs*s*d(xrs)-h1rs*r*d(xrs)-2*h1rs*d(xrs)+6*b0)-2*h0rs*h1rs*(r-1)*s*d^3(xrs)\\&*(6*h0rs*s*d(xrs)-h1rs*r*d(xrs)-2*h1rs*d(xrs)+6*b0)-2*h1rs^2*(r-1)*r*d^3(xrs)\\&*(6*h0rs*s*d(xrs)-h1rs*r*d(xrs)-2*h1rs*d(xrs)+6*b0)-4*b1*h0rs*(r-1)*s*d^2(xrs)\\&*(6*h0rs*s*d(xrs)-h1rs*r*d(xrs)-2*h1rs*d(xrs)+6*b0)+8*b0*h0rs*(r-1)*s*d^2(xrs)\\&*(6*h0rs*s*d(xrs)-h1rs*r*d(xrs)-2*h1rs*d(xrs)+6*b0)+4*b0*h1rs*(r-1)*r*d^2(xrs)\\&*(6*h0rs*s*d(xrs)-h1rs*r*d(xrs)-2*h1rs*d(xrs)+6*b0)+2*b1*h1rs*(r-1)*d^2(xrs)\\&*(6*h0rs*s*d(xrs)-h1rs*r*d(xrs)-2*h1rs*d(xrs)+6*b0)-2*b0*h1rs*(r-1)*d^2(xrs)\\&*(6*h0rs*s*d(xrs)-h1rs*r*d(xrs)-2*h1rs*d(xrs)+6*b0)-4*b0*b1*(r-1)*d(xrs)\\&*(6*h0rs*s*d(xrs)-h1rs*r*d(xrs)-2*h1rs*d(xrs)+6*b0)+4*b0^2*(r-1)*d(xrs)\\&*(6*h0rs*s*d(xrs)-h1rs*r*d(xrs)-2*h1rs*d(xrs)+6*b0)\end{aligned} \tag{d199}$$

(c200) temp6: solve(temp5,h1rs)

Stephan Matthiesen D:\SM\Beruf\RedSea\Macsyma\Def 3-layer.mfe

$$h1rs = -\left(\sqrt{\left(9*h0rs^2*r^2 + 72*h0rs^2*r\right)*s^2*d^2(xrs) + \left((6*b2 + 6*b1 + 18*b0)*h0rs*r^2 + (-24*b2 - 60*b1 + 144*b0)*h0rs*r\right)*s*d(xrs) + \left(b2^2 + (2*b1 + 6*b0)*b2 + b1^2 + 6*b0*b1 + 9*b0^2\right)*r^2 + \left((4*b1 - 24*b0)*b2 + 4*b1^2 - 60*b0*b1 + 72*b0^2\right)*r + 4*b - 3*h0rs*r*s*d(xrs) + (-b2 - b1 - 3*b0)*r - 2*b1}\right)/(6*r*d(xrs))$$

(d200)

$$h1rs = \left(\sqrt{\left(9*h0rs^2*r^2 + 72*h0rs^2*r\right)*s^2*d^2(xrs) + \left((6*b2 + 6*b1 + 18*b0)*h0rs*r^2 + (-24*b2 - 60*b1 + 144*b0)*h0rs*r\right)*s*d(xrs) + \left(b2^2 + (2*b1 + 6*b0)*b2 + b1^2 + 6*b0*b1 + 9*b0^2\right)*r^2 + \left((4*b1 - 24*b0)*b2 + 4*b1^2 - 60*b0*b1 + 72*b0^2\right)*r + 4*b1^2 + 3*h0rs*r*s*d(xrs) + (b2 + b1 + 3*b0)*r + 2*b1}\right)/(6*r*d(xrs))$$

$$h1rs = \frac{2*h0rs*s*d(xrs) + 2*b0}{d(xrs)}$$

(c201) sol_h1rs_ci: part(temp6,2)

(d201)

$$h1rs = \left(\sqrt{\left(9*h0rs^2*r^2 + 72*h0rs^2*r\right)*s^2*d^2(xrs) + \left((6*b2 + 6*b1 + 18*b0)*h0rs*r^2 + (-24*b2 - 60*b1 + 144*b0)*h0rs*r\right)*s*d(xrs) + \left(b2^2 + (2*b1 + 6*b0)*b2 + b1^2 + 6*b0*b1 + 9*b0^2\right)*r^2 + \left((4*b1 - 24*b0)*b2 + 4*b1^2 - 60*b0*b1 + 72*b0^2\right)*r + 4*b1^2 + 3*h0rs*r*s*d(xrs) + (b2 + b1 + 3*b0)*r + 2*b1}\right)/(6*r*d(xrs))$$

(c202) remvalue(temp, temp1, temp2, temp3, temp4, temp5, temp6) $

(c203) sol_q2_ci: factor(first(solve(part(eqnlist_rsacd,3),q2sq)))

(d203) $$q2sq = 2*h2rs^2*d^2(xrs)*(h2rs*r*d(xrs) + h1rs*r*d(xrs) - h2rs*d(xrs) - h1rs*d(xrs) + b2)*w^2(xrs)$$

(c204) sol_q1_ci: factor(first(solve(part(eqnlist_rsacd,1),q1sq)))

(d204) $$q1sq = 2*h1rs^2*d^2(xrs)*(h0rs*s*d(xrs) + b0)*w^2(xrs)$$

For case (c) inflow, we now have all 10 variables: b0, b1, b2, h0rs (from boundary); q1, q2, h1rs, h2rs (from RS); h0ga, h1ga (from GA)

Case (c) and (d) outflow, RS solution

Known: b0, b1, q1. Wanted: b2, q2, h0rs, h1rs, h2rs

(c205) sol_b2_co: connection_d2b

(d205) $$b2 = -\left((h2rsx*(r - 1) - h1rsx)*d(xrs) + b1\right)$$

(c206) sol_b2_do: sol_b2_co$

(c207) sol_q2_co: factor(first(solve(part(eqnlist_rsacd,2),q2sq)))

(d207) $$q2sq = \frac{h2rs^2*\left(2*h1rs^3*r*d^3(xrs)*w^2(xrs) - 2*b1*h1rs^2*d^2(xrs)*w^2(xrs) + q1sq\right)}{h1rs^2}$$

(c208) sol_q2_do: sol_q2_co $

(c209) temp:subst(sol_q2_co,part(eqnlist_rsacd,[3,4]))

Stephan Matthiesen D:\SM\Beruf\RedSea\Macsyma\Def 3-layer.mfe

$$\left[0 = -\frac{\left(\left(\left(2*h2rs^3 + 2*h1rs*h2rs^2\right)*r - 2*h2rs^3 - 2*h1rs*h2rs^2\right)*d^3(xrs) + 2*b2*h2rs^2*d^2(xrs)\right)*w^2(xrs) - \frac{h2rs^2*\left(2*h1rs^3*r*d^3(xrs)*w^2(xrs) - 2*b1*h1rs^2*d^2(xrs)*w^2(xrs) + q1sq\right)}{h1rs^2}}{2*h2rs^2*d^2(xrs)*w^2(xrs)}\right],$$

(d209)
$$0 = -\frac{2*h1rs^3*r*d^3(xrs)*w^2(xrs) - 2*b1*h1rs^2*d^2(xrs)*w^2(xrs) + q1sq}{h1rs^2*h2rs*d^3(xrs)*w^2(xrs)}$$
$$+\frac{q1sq*\left(2*h1rs^3*r*d^3(xrs)*w^2(xrs) - 2*b1*h1rs^2*d^2(xrs)*w^2(xrs) + q1sq\right)}{h1rs^5*h2rs*d^6(xrs)*w^4(xrs)} + \frac{q1sq*r}{h1rs^3*d^3(xrs)*w^2(xrs)}$$
$$\left. - \frac{q1sq}{h1rs^3*d^3(xrs)*w^2(xrs)} - r^2 + r \right]$$

(c210) temp2: 0=factor(first(eliminate(temp,[h2rs])))

(d210)
$$0 = h1rs^2*(r - 1)*d^3(xrs)*w^2(xrs)*\left(6*h1rs^6*r*d^6(xrs)*w^4(xrs) - 2*b2*h1rs^5*r*d^5(xrs)\right.$$
$$\left.*w^4(xrs) - 2*b1*h1rs^5*r*d^5(xrs)*w^4(xrs) - 4*b1*h1rs^5*d^5(xrs)*w^4(xrs) - 3*h1rs^3*q1sq*r\right.$$
$$\left.*d^3(xrs)*w^2(xrs) + 2*b2*h1rs^2*q1sq*d^2(xrs)*w^2(xrs) + 6*b1*h1rs^2*q1sq*d^2(xrs)*w^2(xrs) - 3*q1sq^2\right)$$

(c211) sol_h1rs_co_imp: multthru(1/part(temp2,2,allbut(5)),temp2)

(d211)
$$0 = 6*h1rs^6*r*d^6(xrs)*w^4(xrs) - 2*b2*h1rs^5*r*d^5(xrs)*w^4(xrs) - 2*b1*h1rs^5*r*d^5(xrs)*w^4(xrs) - 4*b1*h1rs^5*d^5(xrs)$$
$$*w^4(xrs) - 3*h1rs^3*q1sq*r*d^3(xrs)*w^2(xrs) + 2*b2*h1rs^2*q1sq*d^2(xrs)*w^2(xrs) + 6*b1*h1rs^2*q1sq*d^2(xrs)*w^2(xrs) - 3*q1sq^2$$

(c212) sol_h1rs_do_imp: sol_h1rs_co_imp $

(c213) sol_h2rs_co: first(solve(first(temp),h2rs))

(d213)
$$h2rs = \frac{\left(2*h1rs^3*d^3(xrs) + \left(-2*b2 - 2*b1\right)*h1rs^2*d^2(xrs)\right)*w^2(xrs) + q1sq}{\left(2*h1rs^2*r - 2*h1rs^2\right)*d^3(xrs)*w^2(xrs)}$$

(c214) sol_h2rs_do: sol_h2rs_co $

(c215) remvalue(temp, temp1, temp2)$

(c216) sol_h0rs_co: expand(first(solve(first(eqnlist_rsacd),h0rs)))

(d216)
$$h0rs = \frac{q1sq}{2*h1rs^2*s*d^3(xrs)*w^2(xrs)} - \frac{b0}{s*d(xrs)}$$

(c217) sol_h0rs_do: sol_h0rs_co $

For cases (c, d) outflow, we now have all 10 variables: b0, b1, b2, h0ga (from boundary); q1, h1ga (from GA); q2, h0rs, h1rs, h2rs (from RS)

Case (d) inflow, RS solution

Known: b0, h0rs, and a relation between q1 and b1. Wanted: b1, b2, q1, q2, h1rs, h2rs

For case (d) inflow, we now have all 10 variables: b0, h0rs (from boundary); (from RS) b1, h0ga, h1ga (from GA)

(c218) sol_h0rs_di: h0rs=h0rsx

(d218)
$$h0rs = h0rsx$$

(c219) eqnlist_rsdi: append(eqnlist_rsacd,[rel_b1q1_di, connection_d2h])$

(c220) dispterms(eqnlist_rsdi)

$$|$$

$$0 = \frac{q1sq}{2*h1rs^2*d^2(xrs)*w^2(xrs)} - h0rs*s*d(xrs) - b0$$

$$0 = -\frac{q2sq}{2*h2rs^2*d^2(xrs)*w^2(xrs)} + \frac{q1sq}{2*h1rs^2*d^2(xrs)*w^2(xrs)} + h1rs*r*d(xrs) - b1$$

Stephan Matthiesen D:\SM\Beruf\RedSea\Macsyma\Def 3-layer.mfe

$$0 = -\frac{\left(\left(\left(2*h2rs^3 + 2*h1rs*h2rs^2\right)*r - 2*h2rs^3 - 2*h1rs*h2rs^2\right)*d^3(xrs) + 2*b2*h2rs^2*d^2(xrs)\right)*w^2(xrs) - q2sq}{2*h2rs^2*d^2(xrs)*w^2(xrs)}$$

$$0 = \frac{q1sq*r}{h1rs^3*d^3(xrs)*w^2(xrs)} - \frac{q2sq}{h2rs^3*d^3(xrs)*w^2(xrs)} - \frac{q1sq}{h1rs^3*d^3(xrs)*w^2(xrs)} + \frac{q1sq*q2sq}{h1rs^3*h2rs^3*d^6(xrs)*w^4(xrs)} - r^2 + r$$

$$0 = 2*h1*q1sq^{2/3}*r^{1/3}*w^{8/3}(xga) - 3*q1sq*r*w^2(xga)$$

$$b2 = -\left((h2rsx*(r-1) - h1rsx)*d(xrs) + b1\right)$$

(d220) done

(c221) temp: factor(eliminate(eqnlist_rsdi,[b1,b2])) $

(c222) dispterms(temp)

$$f$$

$$2*h0rs*h1rs^2*s*d^3(xrs)*w^2(xrs) + 2*b0*h1rs^2*d^2(xrs)*w^2(xrs) - q1sq$$

$$*\left(\begin{array}{c} -2*h2rs^4*d^2(xrs)*w^2(xrs) \\ 2*h1rs^2*h2rsx*r*d^3(xrs)*w^2(xrs) - 2*h1rs^2*h2rs*r*d^3(xrs)*w^2(xrs) - 2*h1rs^2*h2rsx*d^3(xrs)*w^2(xrs) \\ +2*h1rs^2*h2rs*d^3(xrs)*w^2(xrs) - 2*h1rs^2*h1rsx*d^3(xrs)*w^2(xrs) + 2*h1rs^3*d^3(xrs)*w^2(xrs) + q1sq \end{array}\right)$$

$$\begin{array}{c} h1rs^3*h2rs^3*r^2*d^6(xrs)*w^4(xrs) - h1rs^3*h2rs^3*r*d^6(xrs)*w^4(xrs) - h2rs^3*q1sq*r \\ *d^3(xrs)*w^2(xrs) + h1rs^3*q2sq*d^3(xrs)*w^2(xrs) + h2rs^3*q1sq*d^3(xrs)*w^2(xrs) \\ -q1sq*q2sq \end{array}$$

$$-2*\left(\begin{array}{c} 2*h1rs^3*h2rs^2*q1sq^{2/3}*r^{4/3}*w^{8/3}(xga)*d^3(xrs)*w^2(xrs) - 3*h1rs^2*h2rs^2*q1sq*r \\ *w^2(xga)*d^2(xrs)*w^2(xrs) - h1rs^2*q1sq^{2/3}*q2sq*r^{1/3}*w^{8/3}(xga) + h2rs^2*q1sq^{5/3}*r^{1/3} \\ *w^{8/3}(xga) \end{array}\right)$$

(d222) done

(c223) sol_q1_di: factorsum(first(solve(first(temp),q1sq)))

(d223) $q1sq = 2*h1rs^2*d^2(xrs)*(h0rs*s*d(xrs) + b0)*w^2(xrs)$

(c224) temp2: factor(subst(sol_q1_di,rest(temp))) $

(c225) dispterms(temp2)

[

$$- 4*h1rs^2*h2rs^4*d^4(xrs)$$
$$*(h0rs*s*d(xrs) + h2rsx*r*d(xrs) - h2rs*r*d(xrs) - h2rsx*d(xrs) + h2rs*d(xrs) - h1rsx*d(xrs) + h1rs*d(xrs) + b0)*w^4(xrs)$$

$$- h1rs^2*d^2(xrs)*w^2(xrs)$$
$$*\left(\begin{array}{l} 2*h0rs*h2rs^3*r*s*d^4(xrs)*w^2(xrs) - 2*h0rs*h2rs^3*s*d^4(xrs)*w^2(xrs) - h1rs*h2rs^3*r^2*d^4(xrs)*w^2(xrs) + h1rs*h2rs^3*r*d^4(xrs) \\ *w^2(xrs) + 2*b0*h2rs^3*r*d^3(xrs)*w^2(xrs) - 2*b0*h2rs^3*d^3(xrs)*w^2(xrs) + 2*h0rs*q2sq*s*d(xrs) - h1rs*q2sq*d(xrs) + 2*b0*q2sq \end{array}\right)$$

$$2*\left(6*h0rs*h1rs^4*h2rs^2*r*s*w^2(xga)*d^5(xrs)*w^4(xrs) + 6*b0*h1rs^4*h2rs^2*r*w^2(xga)*d^4(xrs)*w^4(xrs) - 2*2^{2/3}\right.$$
$$*h1rs^{10/3}*h2rs^2*r^{1/3}*w^{8/3}(xga)*d^{10/3}(xrs)*(h0rs*s*d(xrs) + b0)^{5/3}*w^{10/3}(xrs) - 2*2^{2/3}*h1rs^{13/3}*h2rs^2*r^{4/3}*w^{8/3}(xga)$$
$$\left.*d^{13/3}(xrs)*(h0rs*s*d(xrs) + b0)^{2/3}*w^{10/3}(xrs) + 2^{2/3}*h1rs^{10/3}*q2sq*r^{1/3}*w^{8/3}(xga)*d^{4/3}(xrs)*(h0rs*s*d(xrs) + b0)^{2/3}*w^{4/3}(xrs)\right)$$

(d225) done

(c226) sol_q2_di: first(solve(part(temp2,2),q2sq))

(d226) $$q2sq = -\frac{\left(\left(\left(2*h0rs*h2rs^3*r - 2*h0rs*h2rs^3\right)*s - h1rs*h2rs^3*r^2 + h1rs*h2rs^3*r\right)*d^4(xrs) + \left(2*b0*h2rs^3*r - 2*b0*h2rs^3\right)*d^3(xrs)\right)*w^2(xrs)}{(2*h0rs*s - h1rs)*d(xrs) + 2*b0}$$

(c227) temp3: factor(subst(sol_q2_di,part(temp2,[1,3])))

$$\left. - 4*h1rs^{2}*h2rs^{4}*d^{4}(xrs) \right]$$

(d227)

$$*(h0rs*s*d(xrs) + h2rsx*r*d(xrs) - h2rs*r*d(xrs) - h2rsx*d(xrs) + h2rs*d(xrs) - h1rsx*d(xrs) + h1rs*d(xrs) + b0)$$

$$*w^{4}(xrs), \frac{2*h2rs^{2}*\left(\begin{array}{c} 12*h0rs^{2}*h1rs^{4}*r*s^{2}*w^{2}(xga)*d^{6}(xrs)*w^{4}(xrs) - 6*h0rs*h1rs^{5}*r*s*w^{2}(xga)*d^{6}(xrs)*w^{4}(xrs) + 24*b0*h0rs*h1rs^{4}*r*s \\ *w^{2}(xga)*d^{5}(xrs)*w^{4}(xrs) - 6*b0*h1rs^{5}*r*w^{2}(xga)*d^{5}(xrs)*w^{4}(xrs) + 12*b0^{2}*h1rs^{4}*r*w^{2}(xga)*d^{4}(xrs)*w^{4}(xrs) - 4*2^{2/3} \\ *h0rs*h1rs^{10/3}*r^{1/3}*s*w^{8/3}(xga)*d^{13/3}(xrs)*(h0rs*s*d(xrs) + b0)^{5/3}*w^{10/3}(xrs) + 2*2^{2/3}*h1rs^{13/3}*r^{1/3}*w^{8/3}(xga)*d^{13/3}(xrs) \\ *(h0rs*s*d(xrs) + b0)^{5/3}*w^{10/3}(xrs) - 4*2^{2/3}*b0*h1rs^{10/3}*r^{1/3}*w^{8/3}(xga)*d^{10/3}(xrs)*(h0rs*s*d(xrs) + b0)^{5/3}*w^{10/3}(xrs) - 2 \\ *2^{2/3}*h0rs*h1rs^{10/3}*h2rs*r^{4/3}*s*w^{8/3}(xga)*d^{16/3}(xrs)*(h0rs*s*d(xrs) + b0)^{2/3}*w^{10/3}(xrs) - 4*2^{2/3}*h0rs*h1rs^{13/3}*r^{4/3}*s \\ *w^{8/3}(xga)*d^{16/3}(xrs)*(h0rs*s*d(xrs) + b0)^{2/3}*w^{10/3}(xrs) + 2*2^{2/3}*h0rs*h1rs^{10/3}*h2rs*r^{1/3}*s*w^{8/3}(xga)*d^{16/3}(xrs) \\ *(h0rs*s*d(xrs) + b0)^{2/3}*w^{10/3}(xrs) + 2^{2/3}*h1rs^{13/3}*h2rs*r^{7/3}*w^{8/3}(xga)*d^{16/3}(xrs)*(h0rs*s*d(xrs) + b0)^{2/3}*w^{10/3}(xrs) - 2^{2/3} \\ *h1rs^{13/3}*h2rs*r^{4/3}*w^{8/3}(xga)*d^{16/3}(xrs)*(h0rs*s*d(xrs) + b0)^{2/3}*w^{10/3}(xrs) + 2*2^{2/3}*h1rs^{16/3}*r^{4/3}*w^{8/3}(xga)*d^{16/3}(xrs) \\ *(h0rs*s*d(xrs) + b0)^{2/3}*w^{10/3}(xrs) - 2*2^{2/3}*b0*h1rs^{10/3}*h2rs*r^{4/3}*w^{8/3}(xga)*d^{13/3}(xrs)*(h0rs*s*d(xrs) + b0)^{2/3}*w^{10/3}(xrs) \\ - 4*2^{2/3}*b0*h1rs^{13/3}*r^{4/3}*w^{8/3}(xga)*d^{13/3}(xrs)*(h0rs*s*d(xrs) + b0)^{2/3}*w^{10/3}(xrs) + 2*2^{2/3}*b0*h1rs^{10/3}*h2rs*r^{1/3}*w^{8/3}(xga) \\ *d^{13/3}(xrs)*(h0rs*s*d(xrs) + b0)^{2/3}*w^{10/3}(xrs) \end{array}\right)}{2*h0rs*s*d(xrs) - h1rs*d(xrs) + 2*b0}$$

(c228) reveal(temp3,3)

(d228)

$$\left[- Product(6), \frac{Product(3)}{Sum(3)} \right]$$

(c229) powers(expand(temp3),h1rs)

(d229)

$$\left[[2, 3], \left[\frac{10}{3}, 4, \frac{13}{3}, 5, \frac{16}{3}\right]\right]$$

(c230) sol_h1rs_di: first(solve(first(temp3),h1rs))

(d230)

$$h1rs = - \frac{(h0rs*s + (h2rsx - h2rs)*r - h2rsx + h2rs - h1rsx)*d(xrs) + b0}{d(xrs)}$$

(c231) temp4: num(last(temp3)) $

(c232) powers(expand(temp4),h2rs)

(d232)

$$[2, 3]$$

(c233) temp5: temp4/h2rs^2 $

(c234) temp6: factor(fullratsimp(first(solve(temp5,h2rs))))

(d234)

$$h2rs = \frac{\left(\begin{array}{c} 2*(2*h0rs*s*d(xrs) - h1rs*d(xrs) + 2*b0) \\ *\left(\begin{array}{c} 3*h0rs*h1rs*r*s*d^{2}(xrs)*w(xrs) + 3*b0*h1rs*r*d(xrs)*w(xrs) - 2^{2/3}*h0rs*h1rs^{1/3}*r^{1/3}*s \\ *w^{2/3}(xga)*d^{4/3}(xrs)*(h0rs*s*d(xrs) + b0)^{2/3}*w^{1/3}(xrs) - 2^{2/3}*h1rs^{4/3}*r^{4/3}*w^{2/3}(xga)*d^{4/3}(xrs) \\ *(h0rs*s*d(xrs) + b0)^{2/3}*w^{1/3}(xrs) - 2^{2/3}*b0*h1rs^{1/3}*r^{1/3}*w^{2/3}(xga)*d^{1/3}(xrs) \\ *(h0rs*s*d(xrs) + b0)^{2/3}*w^{1/3}(xrs) \end{array}\right) \end{array}\right)}{2^{2/3}*h1rs^{1/3}*(r - 1)*r^{1/3}*w^{2/3}(xga)*d^{4/3}(xrs)*(h0rs*s*d(xrs) + b0)^{2/3}*(2*h0rs*s*d(xrs) - h1rs*r*d(xrs) + 2*b0)*w^{1/3}(xrs)}$$

(c235) reveal(temp6,4)

(d235)
$$h2rs = \frac{2*Sum(3)*Sum(5)}{Expt*Expt*Sum(2)*Expt*Expt*Expt*Expt*Sum(3)*Expt}$$

(c236) temp7:scanmap(undistrib,temp6)

(d236)
$$h2rs = \frac{\left(\begin{array}{c} 2*(2*h0rs*s*d(xrs) - h1rs*d(xrs) + 2*b0) \\ * \left(\begin{array}{c} 3*h0rs*h1rs^{2/3}*r^{2/3}*s*d^{5/3}(xrs)*w^{2/3}(xrs) + 3*b0*h1rs^{2/3}*r^{2/3}*d^{2/3}(xrs)*w^{2/3}(xrs) - 2^{2/3}*h0rs*s*w^{2/3}(xga)*d(xrs) \\ *(h0rs*s*d(xrs) + b0)^{2/3} - 2^{2/3}*h1rs*r*w^{2/3}(xga)*d(xrs)*(h0rs*s*d(xrs) + b0)^{2/3} - 2^{2/3}*b0*w^{2/3}(xga) \\ *(h0rs*s*d(xrs) + b0)^{2/3} \end{array}\right) \end{array}\right)}{2^{2/3}*(r - 1)*w^{2/3}(xga)*d(xrs)*(h0rs*s*d(xrs) + b0)^{2/3}*(2*h0rs*s*d(xrs) - h1rs*r*d(xrs) + 2*b0)}$$

See if it is possible to cancel common factors:

(c237)
```
for i:1 thru 6 do block([temp1,temp2],
    temp1: expand([num(rhs(temp7)),denom(rhs(temp7))]),
    temp2: factor(denom(rhs(temp7))),
    print(part(temp2,i,1)),
    print(powers(temp1,part(temp2,i,1)))
)
```

2

$$\left[\left[0, \frac{2}{3}, 1\right]_f, \left[\frac{2}{3}, 1\right]\right]$$

r

$$\left[\left[0, \frac{2}{3}, 1\right]_f, [0, 1, 2]\right]$$

w(xga)

$$\left[\left[0, \frac{2}{3}\right]_f, \left[\frac{2}{3}\right]\right]$$

xrs

[[0], [0]]

h0rs*s*d(xrs) + b0

$$\left[\left[0, \frac{2}{3}\right]_f, \left[\frac{2}{3}\right]\right]$$

2*h0rs*s*d(xrs)

[[0], [0]]

(d237) done

Apparently no simple common factors.

(c238) sol_h2rs_di: map(factorsum,temp7)

(d238)
$$h2rs = \frac{\left(\begin{array}{c} 2*((2*h0rs*s - h1rs)*d(xrs) + 2*b0) \\ * \left(\begin{array}{c} 3*h0rs*h1rs^{2/3}*r^{2/3}*s*d^{5/3}(xrs)*w^{2/3}(xrs) + 3*b0*h1rs^{2/3}*r^{2/3}*d^{2/3}(xrs)*w^{2/3}(xrs) - 2^{2/3}*h0rs*s*w^{2/3}(xga)*d(xrs) \\ *(h0rs*s*d(xrs) + b0)^{2/3} - 2^{2/3}*h1rs*r*w^{2/3}(xga)*d(xrs)*(h0rs*s*d(xrs) + b0)^{2/3} - 2^{2/3}*b0*w^{2/3}(xga) \\ *(h0rs*s*d(xrs) + b0)^{2/3} \end{array}\right) \end{array}\right)}{2^{2/3}*(r - 1)*w^{2/3}(xga)*d(xrs)*(h0rs*s*d(xrs) + b0)^{2/3}*(2*h0rs*s*d(xrs) - h1rs*r*d(xrs) + 2*b0)}$$

Clean up the temporary variables.

(c239) remvalue(temp, temp2, temp3, temp4, temp5, temp6, temp7)

(d239) [temp, temp2, temp3, temp4, temp5, temp6, temp7]

(c240) sol_b1_di

(d240)
$$b1 = \frac{q1sq}{2*h1ga^2*d^2(xga)*w^2(xga)} + h1ga*r*d(xga)$$

(c241) sol_b2_di: connection_d2b

(d241)
$$b2 = -\left((h2rsx*(r - 1) - h1rsx)*d(xrs) + b1\right)$$

(c242) remvalue(eqnlist_rsacd,eqnlist_rsdi) $

For case (d) inflow, we now have all 10 variables: b0, h0rs (from boundary); q1, q2, h1rs, h2rs (from RS); h0ga, h1ga, b1 (from GA), b2 (from boundary)

Sill equations

For each of the cases we now have the following quantities: h0, h1, h2, q1, q2, h0ga, h1ga, h0rs, h1rs, h2rs.

The 4 sill equations have to be solved for: q3, h0s, h1s, h2s

(c243) temp: limit([eq_1s,eq_2s,froude_s]), h0s:0

(d243)
$$\left[0 = -\frac{q2^2}{2*h2s^2*d^2(xs)*w^2(xs)} + \frac{q1^2}{2*h1s^2*d^2(xs)*w^2(xs)} + h1s*r*d(xs) - b1,\right.$$
$$0 = -\frac{q3^2}{2*(-h2s-h1s+1)^2*d^2(xs)*w^2(xs)} + \frac{q2^2}{2*h2s^2*d^2(xs)*w^2(xs)} - h2s*r*d(xs) - h1s*r*d(xs) + h2s*d(xs)$$
$$+ h1s*d(xs) - b2, 0 = -\frac{q3^2*r}{(-h2s-h1s+1)^3*d^3(xs)*w^2(xs)} + \frac{q1^2*r}{h1s^3*d^3(xs)*w^2(xs)} - \frac{q2^2}{h2s^3*d^3(xs)*w^2(xs)}$$
$$\left. - \frac{q1^2}{h1s^3*d^3(xs)*w^2(xs)} + \frac{q2^2*q3^2}{(-h2s-h1s+1)^3*h2s^3*d^6(xs)*w^4(xs)} + \frac{q1^2*q3^2}{h1s^3*(-h2s-h1s+1)^3*d^6(xs)*w^4(xs)} + \frac{q1^2*q2^2}{h1s^3*h2s^3*d^6(xs)*w^4(xs)} - r^2 + r\right]$$

(c244) eqnlist_s: subst(q3sq,q3^2,(subst(q2sq,q2^2,subst(q1sq,q1^2,cons(eq_0s,temp))))) $

(c245) dispterms(eqnlist_s)

|

$$0 = \frac{q1sq}{2*h1s^2*d^2(xs)*w^2(xs)} - h0s*s*d(xs) - b0$$

$$0 = -\frac{q2sq}{2*h2s^2*d^2(xs)*w^2(xs)} + \frac{q1sq}{2*h1s^2*d^2(xs)*w^2(xs)} + h1s*r*d(xs) - b1$$

$$0 = -\frac{q3sq}{2*(-h2s-h1s+1)^2*d^2(xs)*w^2(xs)} + \frac{q2sq}{2*h2s^2*d^2(xs)*w^2(xs)} - h2s*r*d(xs) - h1s*r*d(xs) + h2s*d(xs) + h1s*d(xs) - b2$$

$$0 = -\frac{q3sq*r}{(-h2s-h1s+1)^3*d^3(xs)*w^2(xs)} + \frac{q1sq*r}{h1s^3*d^3(xs)*w^2(xs)} - \frac{q2sq}{h2s^3*d^3(xs)*w^2(xs)} - \frac{q1sq}{h1s^3*d^3(xs)*w^2(xs)}$$
$$+ \frac{q2sq*q3sq}{(-h2s-h1s+1)^3*h2s^3*d^6(xs)*w^4(xs)} + \frac{q1sq*q3sq}{h1s^3*(-h2s-h1s+1)^3*d^6(xs)*w^4(xs)} + \frac{q1sq*q2sq}{h1s^3*h2s^3*d^6(xs)*w^4(xs)} - r^2 + r$$

(d245) done

(c246) sol_h0s: expand(first(solve(first(eqnlist_s),h0s)))

(d246)
$$h0s = \frac{q1sq}{2*h1s^2*s*d^3(xs)*w^2(xs)} - \frac{b0}{s*d(xs)}$$

(c247) sol_q3: factorsum(first(solve(last(eqnlist_s), q3sq)))

(d247)
$$q3sq = \frac{(h2s+h1s-1)^3*\left(\begin{array}{c} h1s^3*h2s^3*r^2*d^6(xs)*w^4(xs) - h1s^3*h2s^3*r*d^6(xs)*w^4(xs) - h2s^3*q1sq*r \\ *d^3(xs)*w^2(xs) + h1s^3*q2sq*d^3(xs)*w^2(xs) + h2s^3*q1sq*d^3(xs)*w^2(xs) \\ - q1sq*q2sq \end{array}\right)}{h1s^3*h2s^3*r*d^3(xs)*w^2(xs) - h1s^3*q2sq - h2s^3*q1sq}$$

(c248) temp: subst(sol_q3,part(eqnlist_s,[2,3]))

Stephan Matthiesen D:\SM\Beruf\RedSea\Macsyma\Def 3-layer.mfe

(d248)
$$\left[0 = -\frac{q2sq}{2*h2s^2*d^2(xs)*w^2(xs)} + \frac{q1sq}{2*h1s^2*d^2(xs)*w^2(xs)} + h1s*r*d(xs) - b1,\right.$$
$$0 = -\frac{(h2s+h1s-1)^3*\left(\begin{array}{c} h1s^3*h2s^3*r^2*d^6(xs)*w^4(xs) - h1s^3*h2s^3*r*d^6(xs)*w^4(xs) - h2s^3*q1sq*r \\ *d^3(xs)*w^2(xs) + h1s^3*q2sq*d^3(xs)*w^2(xs) + h2s^3*q1sq*d^3(xs)*w^2(xs) \\ - q1sq*q2sq \end{array}\right)}{2*(-h2s-h1s+1)^2*d^2(xs)*w^2(xs)*\left(h1s^3*h2s^3*r*d^3(xs)*w^2(xs) - h1s^3*q2sq - h2s^3*q1sq\right)}$$
$$\left.+\frac{q2sq}{2*h2s^2*d^2(xs)*w^2(xs)} - h2s*r*d(xs) - h1s*r*d(xs) + h2s*d(xs) + h1s*d(xs) - b2\right]$$

(c249) powers(expand(temp),h1s)

(d249) [[0] = [-2, 0, 1], [0] = [0, 1, 2, 3, 4, 5, 6]]

(c250) powers(expand(temp),h2s)

(d250) [[0] = [-2, 0], [0] = [-2, 0, 1, 2, 3, 4, 5, 6]]

(c251) sol_h1s_imp:facsum(expand(first(temp)*(h1s*h2s*d(xs)*w(xs))^2*2*s),h1s)

C:\Programme\Macsyma\Macsyma2\share\index.fas being loaded.

(d251) $0 = -h1s^2*s*\left(2*b1*h2s^2*d^2(xs)*w^2(xs) + q2sq\right) + 2*h1s^3*h2s^2*r*s*d^3(xs)*w^2(xs) + h2s^2*q1sq*s$

(c252) temp2: first(eliminate(temp,[q2sq]))

(d252)
$$-h1s^2*h2s^4*\left(\begin{array}{c} \left(\left(3*h1s^5*h2s^2 + \left(-3*h1s^6 - h1s^5\right)*h2s\right)*r^2 + \left(-3*h1s^5*h2s^2 + \left(3*h1s^6 + h1s^5\right)*h2s + 6*h1s^7 - 2*h1s^6\right)*r\right)*d^6(xs) \\ + \left(\left((2*b2 + 6*b1)*h1s^5*h2s + \left(-4*b2 - 4*b1\right)*h1s^6\right)*r - 6*b1*h1s^5*h2s - 6*b1*h1s^6 + 2*b1*h1s^5\right)*d^5(xs) + \left(4*b1*b2 + 4*b1^2\right)*h \\ *w^4(xs) + \left(\left(\left(-3*h1s^2*h2s^2 + \left(h1s^2 - 6*h1s^3\right)*h2s + 2*h1s^3\right)*q1sq*r + \left(3*h1s^2*h2s^2 + \left(6*h1s^3 - h1s^2\right)*h2s + 3*h1s^4 - h1s^3\right)\right.\right. \\ \left.\left.*d^3(xs) + \left(-2*b2*h1s^2*h2s + \left(-2*b2 - 2*b1\right)*h1s^3 - 2*b1*h1s^2\right)*q1sq*d^2(xs)\right) \\ *w^2(xs) + q1sq^2 \end{array}\right)$$

(c253) temp3: expand(temp2) $

(c254) powers(temp3,h2s)

(d254) [4, 5, 6]

(c255) powers(temp3,h1s)

(d255) [2, 4, 5, 6, 7, 8, 9]

(c256) powers(temp3,d(xs))

(d256) [0, 2, 3, 4, 5, 6]

(c257) powers(temp3,w(xs))

(d257) [0, 2, 4]

(c258) powers(temp3,r)

(d258) [0, 1, 2]

(c259) temp4: -temp2/(h1s^2*h2s^4)

(d259)
$$\left(\begin{array}{c} \left(\left(3*h1s^5*h2s^2 + \left(-3*h1s^6 - h1s^5\right)*h2s\right)*r^2 + \left(-3*h1s^5*h2s^2 + \left(3*h1s^6 + h1s^5\right)*h2s + 6*h1s^7 - 2*h1s^6\right)*r\right)*d^6(xs) \\ + \left(\left((2*b2 + 6*b1)*h1s^5*h2s + \left(-4*b2 - 4*b1\right)*h1s^6\right)*r - 6*b1*h1s^5*h2s - 6*b1*h1s^6 + 2*b1*h1s^5\right)*d^5(xs) + \left(4*b1*b2 + 4*b1^2\right)*h1s^5*d^4(xs) \\ *w^4(xs) + \left(\left(\left(-3*h1s^2*h2s^2 + \left(h1s^2 - 6*h1s^3\right)*h2s + 2*h1s^3\right)*q1sq*r + \left(3*h1s^2*h2s^2 + \left(6*h1s^3 - h1s^2\right)*h2s + 3*h1s^4 - h1s^3\right)*q1sq\right)\right. \\ \left.*d^3(xs) + \left(-2*b2*h1s^2*h2s + \left(-2*b2 - 2*b1\right)*h1s^3 - 2*b1*h1s^2\right)*q1sq*d^2(xs)\right) \\ *w^2(xs) + q1sq^2 \end{array}\right)$$

(c260) sol_h2s_imp: 0=facsum(temp4,h2s)

Stephan Matthiesen D:\SM\Beruf\RedSea\Macsyma\Def 3-layer.mfe

$$0 = -h1s^2*h2s*d^2(xs)*w^2(xs)*\begin{pmatrix} 3*h1s^4*r^2*d^4(xs)*w^2(xs) + h1s^3*r^2*d^4(xs)*w^2(xs) - 3*h1s^4*r*d^4(xs)*w^2(xs) - h1s^3*r \\ *d^4(xs)*w^2(xs) - 2*b2*h1s^3*r*d^3(xs)*w^2(xs) - 6*b1*h1s^3*r*d^3(xs)*w^2(xs) + 6*b1*h1s^3 \\ *d^3(xs)*w^2(xs) + 6*h1s*q1sq*r*d(xs) - q1sq*r*d(xs) - 6*h1s*q1sq*d(xs) + q1sq*d(xs) + 2*b2*q1sq \end{pmatrix}$$

(d260)
$$+ \left(3*h1s^4*d^3(xs)*w^2(xs) - h1s^3*d^3(xs)*w^2(xs) - 2*b2*h1s^3*d^2(xs)*w^2(xs) - 2*b1*h1s^3*d^2(xs)*w^2(xs) + q1sq\right)$$
$$*\left(2*h1s^3*r*d^3(xs)*w^2(xs) - 2*b1*h1s^2*d^2(xs)*w^2(xs) + q1sq\right) + 3*h1s^2*h2s^2*(r-1)*d^3(xs)*w^2(xs)$$
$$*\left(h1s^3*r*d^3(xs)*w^2(xs) - q1sq\right)$$

(c261) remvalue(eqnlist_s,temp,temp2,temp3,temp4) $

(c262) sol_h2s_coeff0: collectterms(expandwrt(factorsum(coeff(sol_h2s_imp,h2s,0)),h1s),h1s)

(d262) $$0 = \left(h1s^3*d^2(xs)*\left((3*h1s-1)*d(xs) - 2*(b2+b1)\right)*w^2(xs) + q1sq\right)*\left(2*h1s^2*d^2(xs)*(h1s*r*d(xs) - b1)*w^2(xs) + q1sq\right)$$

(c263) sol_h2s_coeff1: collectterms(expandwrt(factorsum(coeff(sol_h2s_imp,h2s,1)),h1s),h1s)

(d263) $$0 = -h1s^2*d^2(xs)*w^2(xs)*\begin{pmatrix} 3*h1s^4*r^2*d^4(xs)*w^2(xs) + h1s^3*r^2*d^4(xs)*w^2(xs) - 3*h1s^4*r*d^4(xs)*w^2(xs) - h1s^3*r \\ *d^4(xs)*w^2(xs) - 2*b2*h1s^3*r*d^3(xs)*w^2(xs) - 6*b1*h1s^3*r*d^3(xs)*w^2(xs) + 6*b1*h1s^3 \\ *d^3(xs)*w^2(xs) + 6*h1s*q1sq*r*d(xs) - q1sq*r*d(xs) - 6*h1s*q1sq*d(xs) + q1sq*d(xs) + 2*b2*q1sq \end{pmatrix}$$

(c264) sol_h2s_coeff2: collectterms(expandwrt(factorsum(coeff(sol_h2s_imp,h2s,2)),h1s),h1s)

(d264) $$0 = 3*h1s^2*(r-1)*d^3(xs)*w^2(xs)*\left(h1s^3*r*d^3(xs)*w^2(xs) - q1sq\right)$$

Now all the equations have been solved.

(c268)

Bibliography

A. E. Aksu, D. Yaşar, and P. J. Mudie. Paleoclimatic and paleoceanographic conditions leading to development of sapropel layer S1 in the Aegean Sea. *Palaeogeography, Palaeoclimatology, Palaeoecology*, 116:71–101, 1995.

J. R. Apel. *Principles of Ocean Physics*, volume 38 of *International Geophysics Series.* Academic Press, 24-28 Oval Road, London NW1 7DX, United Kingdom, 1 edition, 1987. ISBN 0-12-058866-8.

L. Armi. The hydraulics of two flowing layers with different densities. *J. Fluid Mech.*, 163:27–58, 1986.

L. Armi and D. M. Farmer. The internal hydraulics of the Strait of Gibraltar and associated sills and narrows. *Oceanolog. Acta*, 8:37–46, 1985.

L. Armi and D. M. Farmer. Maximal 2-layer exchange through a contraction with barotropic net flow. *J. Fluid Mech.*, 164:27–51, 1986.

L. Armi and D. M. Farmer. A generalization of the concept of maximal exchange in a strait. *J. Geophys. Res.*, 92(10C):14697–14680, 1987.

L. Armi and D. M. Farmer. The flow of Mediterranean water through the Strait of Gibraltar. *Prog. Oceanog.*, 21:1–105, 1988.

L. Armi and R. Williams. The hydraulics of a stratified fluid flowing through a contraction. *J. Fluid Mech.*, 251:355–375, 1993.

G. Assaf and A. Hecht. Sea straits: a dynamical model. *Deep-Sea Research*, 21:947–958, 1974.

P. G. Baines. *Topographic Effects in Stratified Flows.* Cambridge Monographies on Mechanics. Cambridge University Press, 1995.

M. O. Baringer and J. F. Price. Mixing and spreading of the Mediterranean outflow. *J. Phys. Oceanogr.*, 27:1654–1677, 1997.

M. O. Baringer and J. F. Price. A review of the physical oceanography of the Mediterranean outflow. *Marine Geology*, 155:63–82, 1999.

J. Bethoux. Budgets of the Mediterranean Sea: Their dependence on the local climate and on the characteristics of the Atlantic water. *Oceanolog. Acta*, 21:1–105, 1979.

J. Bethoux, B. Gentili, J. Raunet, and D. Taillez. Warming trend in the Western Mediterranean Deep Water. *Nature*, 347:660–662, 1990.

J. P. Bethoux. Paleoceanographic changes in the Mediterranean Sea in the last 20,000 years. *Oceanologica Acta*, 7:43–48, 1984.

J. P. Bethoux. Mediterranean sapropel formation, dynamic and climatic viewpoints. *Oceanologica Acta*, 16:127–133, 1993.

M. Bormans and C. Garrett. The effect of rotation on the surface inflow through the Strait of Gibraltar. *J. Phys. Oceanogr.*, 19:1535–1542, 1989a.

M. Bormans and C. Garrett. The effects of nonrectangular cross section, friction, and barotropic fluctuations on the exchange through the Strait of Gibraltar. *J. Phys. Oceanogr.*, 19:1543–1557, 1989b.

M. Bormans and C. Garrett. A simple criterion for gyre formation by the surface outflow from a strait, with application to the Alboran Sea. *J. Geophys. Res.*, 94(C9): 12637–12644, 1989c.

B. Boudreau. A simple evolutionary model for water and salt in the Black Sea. *Paleoceanography*, 4(2):157–166, 1989.

J. M. Brankart and P. Brasseur. The general circulation in the Mediterranean Sea: a climatological approach. *J. Marine Systems*, 18:41–70, 1998.

P. Brasseur, J. M. Beckers, J. Brankart, and R. Schoenauen. Seasonal temperature and salinity fields in the Mediterranean Sea: Climatological analysis of a historical data set. *Deep-Sea Research*, 43:159–192, 1996.

N. Bray, J. Ochoa, and T. H. Kinder. The role of the interface in exchange through the Strait of Gibraltar. *J. Geophys. Res.*, 100(C6):10755–10776, 1995.

H. L. Bryden. Recent progress in strait dynamics. *Rev. Geophysics*, 29:617–631, 1991.

H. L. Bryden, J. Candela, and T. H. Kinder. Exchange through the Strait of Gibraltar. *Prog. Oceanog.*, 33:201–248, 1994.

H. L. Bryden and T. H. Kinder. Steady 2-layer exchange through the Strait of Gibraltar. *Deep-Sea Research Part A-Oceanographic Research Papers*, 38:S 445–S 463, 1991.

H. L. Bryden and H. Stommel. Origin of the Mediterranean outflow. *J. Mar. Res.*, 40: 55–71, 1982.

H. L. Bryden and H. M. Stommel. Limiting processes that determine basic features of the circulation in the Mediterranean Sea. *Oceanolog. Acta*, 7:289–296, 1984.

J. Candela. The Gibraltar Strait and its role in the dynamics of the Mediterranean Sea. *Dynamics of Atmosphere and Ocean*, 15:267–299, 1991.

A. Cramp and M. Collins. A late Pleistocene-Holocene sapropelic layer in the northwest Aegean Sea, Eastern Mediterranean. *Geo-Marine Letters*, 8:19–23, 1988.

A. Cramp, M. Collins, and R. West. Late Pleistocene-Holocene sedimentation in the NW Aegean Sea: a palaeoclimatic palaeoceanographic reconstruction. *Palaeogeography, Palaeoclimatology, Palaeoecology*, 68:61–77, 1988.

D. Cromwell and D. A. Smeed. Altimetric observations of sea level cycles near the Strait of Bab al Mandab. *Int. J. Remote Sensing*, 1998(8):1561–1578, 1998.

S. B. Dalziel. Two-layer hydraulics: a functional approach. *J. Fluid Mech.*, 223:135–163, 1991.

S. B. Dalziel. Maximal exchange in channels with nonrectangular cross sections. *J. Phys. Oceanogr.*, 22:1188–1206, 1992.

S. B. Dalziel and G. F. Lane-Serff. The hydraulics of doorway exchange flows. *Building Environment*, 26:121–135, 1991.

P. A. Davies, A. M. Folkard, and G. C. Dhieres. Remote-sensing observations of filament formation along the Almeria-Oran front. *Annales Geophysicae-Atmospheres Hydrospheres Space Sciences*, 11:419–430, 1993.

G. J. Delange and H. L. Tenhaven. Recent sapropel formation in the Eastern Mediterranean. *Nature*, 305:797–798, 1983.

EUROMODEL Group. Progress from 1982 to 1992 in understanding the circulation of the Western Mediterranean. *Oceanologica Acta*, 18(2):255–271, 1995.

R. G. Fairbanks. A 17.000 year glacio-eustatic sea level record: Influence of glacial melting rates on the Younger Dryas Event and deep ocean circulation. *Nature*, 342: 637–642, 1989.

D. M. Farmer. Hydraulic control in a sill fjord. *Ocean Management*, 6:244–244, 1981.

D. M. Farmer and L. Armi. Maximal 2-layer exchange over a sill and through the combination of a sill and contraction with barotropic flow. *J. Fluid Mech.*, 164:53, 1986.

D. M. Farmer and L. Armi. The flow of Atlantic water through the Strait of Gibraltar - the flow of Mediterranean water through the Strait of Gibraltar. *Progress Oceanography*, 21:1, 1988.

D. M. Farmer and R. A. Denton. Hydraulic control of flow over the sill in Observatory Inlet. *J. Geophysical Research-Oceans*, 90:9051–9068, 1985.

H. J. S. Fernando. Turbulent mixing in stratified fluids. *Annual Review Fluid Mechanics*, 23:455–493, 1991.

M. Gacic, M. Astraldi, and P. E. La Violette. The Mediterranean Sea - circulation, strait exchange and dense water formation processes - preface. *J. Marine Systems*, 20:R7–R9, 1999.

C. Garrett, M. Bormans, and K. Thompson. Is the exchange throught the Strait of Gibraltar maximal or submaximal? In L. Pratt, editor, *The Physical Oceanography of Sea Straits*, pages 271–294. Kluwer Academic Publishers, 1990.

A. Gill. The hydraulics of rotating-channel flow. *J. Fluid Mech.*, 80(4):641–671, 1977.

K. R. Helfrich. Time-dependent 2-layer hydraulic exchange flows. *J. Phys. Oceanography*, 25:359–373, 1995.

T. S. Hopkins. The thermohaline forcing of the Gibraltar exchange. *J. Marine Systems*, 20:1–31, 1999.

J. A. Jenkins and D. F. Williams. Nile water as a cause of eastern Mediterranean sapropel formation - evidence for and against. *Marine Micropaleontology*, 8:521–534, 1984.

G. C. Johnson and D. R. Ohlsen. Frictionally modified rotating hydraulic channel exchange and ocean outflows. *J. Phys. Oceanography*, 24:66–78, 1994.

R. Johnson. Climate control requires a dam at the Strait of Gibraltar. *Eos, Transactions of the American Geophysical Union*, 78(27):277,280–281, 1997.

G. A. Jones and A. R. Gagnon. Radiocarbon chronology of Black Sea sediments. *Deep-Sea Research Part I-Oceanographic Research Papers*, 41:531–557, 1994.

N. Kallel, M. Paterne, J. C. Duplessy, C. Vergnaud-Grazzini, C. Pujol, L. Labeyrie, M. Arnold, M. Fontugne, and C. Pierre. Enhanced rainfall in the Mediterranean region during the last sapropel event. *Oceanologica Acta*, 20:697–712, 1997.

A. Kemp, I. Koizumi, J. Pike, and S. Rance. The role of mat-forming diatoms in the formation of Mediterranean sapropels. *Nature*, 398:57–61, 1999.

P. D. Killworth. Flow properties in rotating, stratified hydraulics. *J. Phys. Oceanography*, 22:997–1017, 1992a.

P. D. Killworth. On hydraulic control in a stratified fluid. *J. Fluid Mech.*, 237:605–626, 1992b.

P. D. Killworth. Hydraulic control and maximal flow in rotating stratified hydraulics. *Deep-Sea Research Part I-Oceanographic Research Papers*, 42:859–871, 1995.

T. H. Kinder and G. Parilla. Yes, some of the Mediterranean outflow does come from great depth. *J. Geophys. Res.*, 92(C3):2901–2906, 1987.

B. Klein, W. Roether, B. B. Manca, D. Bregant, V. Beitzel, V. Kovacevic, and A. Luchetta. The large deep water transient in the Eastern Mediterranean. *Deep-Sea Research Part I-Oceanographic Research Papers*, 46:371–414, 1999.

J. B. Klemp, R. Rotunno, and W. C. Skamarock. On the propagation of internal hydraulic bores. *J. Fluid Mech.*, 331:81–106, 1997.

P. E. La Violette and R. A. Arnone. A tide-generated internal waveform in the western approaches to the Strait of Gibraltar. *J. Geophys. Res. - Oceans*, 93(C12):15653–15667, 1988.

J. G. Lafuente, N. Cano, M. Vargas, J. P. Rubin, and A. Hernandezguerra. Evolution of the Alboran Sea hydrographic structures during July 1993. *Deep-Sea Research Part I-Oceanographic Research Papers*, 45:39–65, 1998.

J. M. G. Lafuente and N. C. Lucaya. Tidal dynamics and associated features of the northwestern shelf of the Alboran Sea. *Continental Shelf Research*, 14:1–21, 1994.

G. F. Lane-Serff, E. J. Rohling, H. L. Bryden, and H. Charnock. Postglacial connection of the Black Sea to the Mediterranean and its relation to the timing of sapropel formation. *Paleoceanography*, 12:169–174, 1997.

G. F. Lane-Serff, D. A. Smeed, and C. R. Postlethwaite. Multi-layer hydraulic exchange flows. *J. Fluid Mech.*, 416:269–296, 2000.

P.-Y. Le Traon and P. Gauzelin. Response of the Mediterranean mean sea level to atmospheric pressure forcing. *J. Geophys. Res.*, 102(C1):973–984, 1997.

M. Li and P. C. Cummins. A note on hydraulic theory of internal bores. *Dynamics of Atmosphere and Ocean*, 28:1–7, 1998.

J. J. Lowe and M. J. C. Walker. *Reconstructing Quaternary Environments.* Longman, 2nd edition, 1997. ISBN 0-582-10166-2.

J.-M. Martin and J. D. Milliman. EROS 2000 (European River Ocean System). the Western Mediterranean: An introduction. *Deep-Sea Research*, 44(3-4):521–529, 1997.

C. Millot. Circulation in the Western Mediterranean Sea. *J. Marine Systems*, 20: 423–442, 1999.

P. G. Myers and K. Haines. Stability of the Mediterranean's thermohaline circulation under modified evaporative fluxes. *J. Geophys. Res.*, submitted, 2001.

P. G. Myers, K. Haines, and S. Matthiesen. Multiple equilibria of the thermohaline circulation of the Mediterranean in an ocean general circulation model. in preparation, 2001.

P. G. Myers, K. Haines, and E. J. Rohling. Modeling the paleocirculation of the Mediterranean: The last glacial maximum and the Holocene with emphasis on the formation of sapropel S1. *Paleoceanography*, 13:586–606, 1998.

S. Narimousa and H. J. S. Fernando. On the sheared density interface of an entraining stratified fluid. *J. Fluid Mechanics*, 174:1–22, 1987.

T. Oğuz, E. Özsoy, M. A. Latif, H. I. Sur, and Ü. Ünlüata. Modeling of hydraulically controlled exchange flow in the Bosporus Strait. *J. Phys. Oceanography*, 20:945–965, 1990.

T. Oğuz and H. I. Sur. A 2-layer model of water exchange through the Dardanelles Strait. *Oceanologica Acta*, 12:23–31, 1989.

L. Padman and I. Jones. Richardson number statistics in the seasonal thermocline. *J. Phys. Oceanogr.*, 15(7):844–854, 1985.

W. Patzert. Wind-induced reversal in Red Sea circulation. *Deep-Sea Research*, 21: 109–121, 1974.

J. Pedlosky. *Ocean Circulation Theory.* Springer Verlag, Berlin, 1996. ISBN 3-540-60489-8.

O. Peyron, J. Guiot, R. Cheddadi, P. Tarasov, M. Reille, J. L. Debeaulieu, S. Bottema, and V. Andrieu. Climatic reconstruction in Europe for 18,000 yr B.P. from pollen data. *Quaternary Research*, 49:183–196, 1998.

P. Pistek and P. E. La Violette. Observations of the suppression of tide-generated nonlinear internal wave packets in the Strait of Gibraltar. *J. Marine Systems*, 20: 113–128, 1999.

W. Pitman and W. Ryan. *Noah's Flood. The New Scientific Discoveries About the Event That Changes History.* Simon & Schuster, New York, 1998.

L. J. Pratt. Hydraulic control of sill flow with bottom friction. *J. Phys. Oceanography*, 16:1970–1980, 1986.

S. Rahmstorf. Influence of Mediterranean outflow on climate. *Eos, Transactions of the American Geophysical Union*, 79(24):281–282, 1998.

J. Reid. On the contribution of the Mediterranean Sea outflow to the Norwegian-Greenland Sea. *Deep-Sea Research*, 26:1199–1223, 1979.

A. R. Robinson, P. Malanotte-Rizzoli, A. Hecht, A. Michelato, W. Roether, A. Theocharis, Ü. Ünlüata, N. Pinardi, A. Artegiani, A. Bergamasco, J. Bishop, S. Brenner, S. Christianidis, M. Gacic, D. Georgopoulos, M. Golnaraghi, M. Hausmann, H. G. Junghaus, A. Lascaratos, M. A. Latif, W. G. Leslie, C. J. Lozano, T. Oğuz, E. Özsoy, E. Papageorgiou, E. Paschini, Z. Rozentroub, E. Sansone, P. Scarazzato, R. Schlitzer, G. C. Spezie, E. Tziperman, G. Zodiatis, L. Athanassiadou, M. Gerges, and M. Osman. General-circulation of the eastern Mediterranean. *Earth-Science Rev.*, 32:285–309, 1992.

E. J. Rohling. Shoaling of the eastern mediterranean pycnocline due to reduction of excess evaporation: Implications for sapropel formation. *Paleoceanography*, 6(6): 747–753, 1991a.

E. J. Rohling. A simple two-layered model for shoaling of the Eastern Mediterranean pycnocline due to glacio-eustatic sea level lowering. *Paleoceanography*, 6(4):537–541, 1991b.

E. J. Rohling. Glacial conditions in the Red Sea. *Paleoceanography*, 9:653–660, 1994a.

E. J. Rohling. Review and new aspects concerning the formation of eastern Mediterranean sapropels. *Marine Geology*, 122:1–28, 1994b.

E. J. Rohling and H. L. Bryden. Man-induced salinity and temperature increases in Western Mediterranean deep-water. *J. Geophys. Res. - Oceans*, 97:11191–11198, 1992.

E. J. Rohling and H. L. Bryden. Estimating past changes in the eastern Mediterranean fresh-water budget, using reconstructions of sea-level and hydrography. *Proceedings Koninklijke Nederlandse Akademie Van Wetenschappen-Biological Chem. Geological Phys. Medical Sciences*, 97:201–217, 1994.

E. J. Rohling and W. W. C. Gieskes. Late quaternary changes in Mediterranean Intermediate Water density and formation rate. *Paleoceanography*, 4:747–753, 1989.

E. J. Rohling and F. J. Hilgen. The eastern Mediterranean climate at times of sapropel formation - a review. *Geologie En Mijnbouw*, 70:253–264, 1991.

E. J. Rohling and W. J. Zachariasse. Red-sea outflow during the last glacial maximum. *Quaternary International*, 31:77–83, 1996.

M. Rossignol-Strick. Mediterranean quaternary sapropels, an immediate response of the african monsoon to variations of insolation. *Palaeogeography, Palaeoclimatology, Palaeoecology*, 49:237–263, 1985.

M. Rossignol-Strick, W. Nesteroff, P. Olive, and C. Vergnaud-Grazzini. After the deluge - Mediterranean stagnation and sapropel formation. *Nature*, 295:105–110, 1982.

W. B. F. Ryan, W. C. Pitman, C. O. Major, K. Shimkus, V. Moskalenko, G. A. Jones, P. Dimitrov, N. Gorur, M. Sakinc, and H. Yuce. An abrupt drowning of the Black Sea shelf. *Marine Geology*, 138:119–126, 1997.

D. A. Smeed. Seasonal variation of the flow in the Strait of Bab al Mandab. *Oceanolog. Acta*, 20(6):773–781, 1997.

D. A. Smeed. Hydraulic control of three-layer exchange flows: Application to the Bab al Mandab Strait. *J. Phys. Oceanogr.*, 30:2574–2588, 2000.

S. Speich, G. Madec, and M. Crepon. A strait outflow circulation process study - the case of the Alboran Sea. *J. Phys. Oceanography*, 26:320–340, 1996.

H. Stommel and H. Farmer. Control of salinity in an estuary by a transition. *J. Mar. Res.*, 12:13–20, 1953.

M. Stuiver, G. W. Pearson, and T. Braziunas. Radiocarbon age calibration of marine samples back to 9000 cal yr BP. *Radiocarbon*, 28:980–1021, 1986.

R. B. Thorpe and G. R. Bigg. Two layer channel flow in ocean general circulation models with application to the Strait of Gibraltar. *J. Phys. Oceanogr.*, submitted, 1998.

R. C. Thunell and D. F. Williams. Glacial-Holocene salinity changes in the Mediterranean Sea - hydrographic and depositional effects. *Nature*, 338:493–496, 1989.

J. Tintore, P. E. La Violette, I. Blade, and A. Cruzado. A study of an intense density front in the Eastern Alboran Sea: The Almeria-Oran Front. *J. Phys. Oceanogr.*, 18: 1384–1397, 1988.

M. Tomczak and J. S. Godfrey. *Regional Oceanography: An Introduction.* Pergamon Press, Oxford, New York, Tokyo, 1994.

S. R. Troelstra and J. E. Vanhinte. The Younger Dryas sapropel S1 connection in the Mediterranean Sea. *Geologie En Mijnbouw*, 74:275–280, 1995.

E. Tziperman and K. Speer. A study of water mass transformation in the Mediterranean Sea: Analysis of climatological data and a simple three-box model. *Dynamics of Atmosphere and Ocean*, 21:53–82, 1994.

A. Viudez and J. Tintore. Time and space variability in the Eastern Alboran Sea from March to May 1990. *J. Geophysical Research-Oceans*, 100:8571–8586, 1995.

D. P. Wang. The Strait of Gibraltar model - internal tide, diurnal inequality and fortnightly modulation. *Deep-Sea Research Part I-Oceanographic Research Papers*, 40:1187–1203, 1993.

J. C. Wesson and M. C. Gregg. Mixing at Camarinal Sill in the Strait of Gibraltar. *J. Geophys. Res. – Oceans*, 99:9847–9878, 1994.

J. A. Whitehead. Internal hydraulic control in rotating fluids - applications to oceans. *Geophysical Astrophysical Fluid Dynamics*, 48:169–192, 1989.

J. A. Whitehead. Topographic control of oceanic flows in deep passages and straits. *Rev. Geophysics*, 36:423–440, 1998.

J. A. Whitehead and R. Kimura. Rotating hydraulic models of fronts at the continental-shelf break and in circular eddies. *Geophysical Astrophysical Fluid Dynamics*, 76: 1–27, 1994.

J. A. Whitehead, A. Leetma, and R. A. Knox. Rotating hydraulics of strait and sill flows. *Geophysical Fluid Dynamics*, 6:101–125, 1974.

I. Wood and J. Simpson. Jumps in layered miscible fluids. *J. Fluid Mech.*, 140:329–342, 1984.